# COMPUTATIONAL MECHANICS OF SENSORY PROCESSING

NICOLAS RAULT

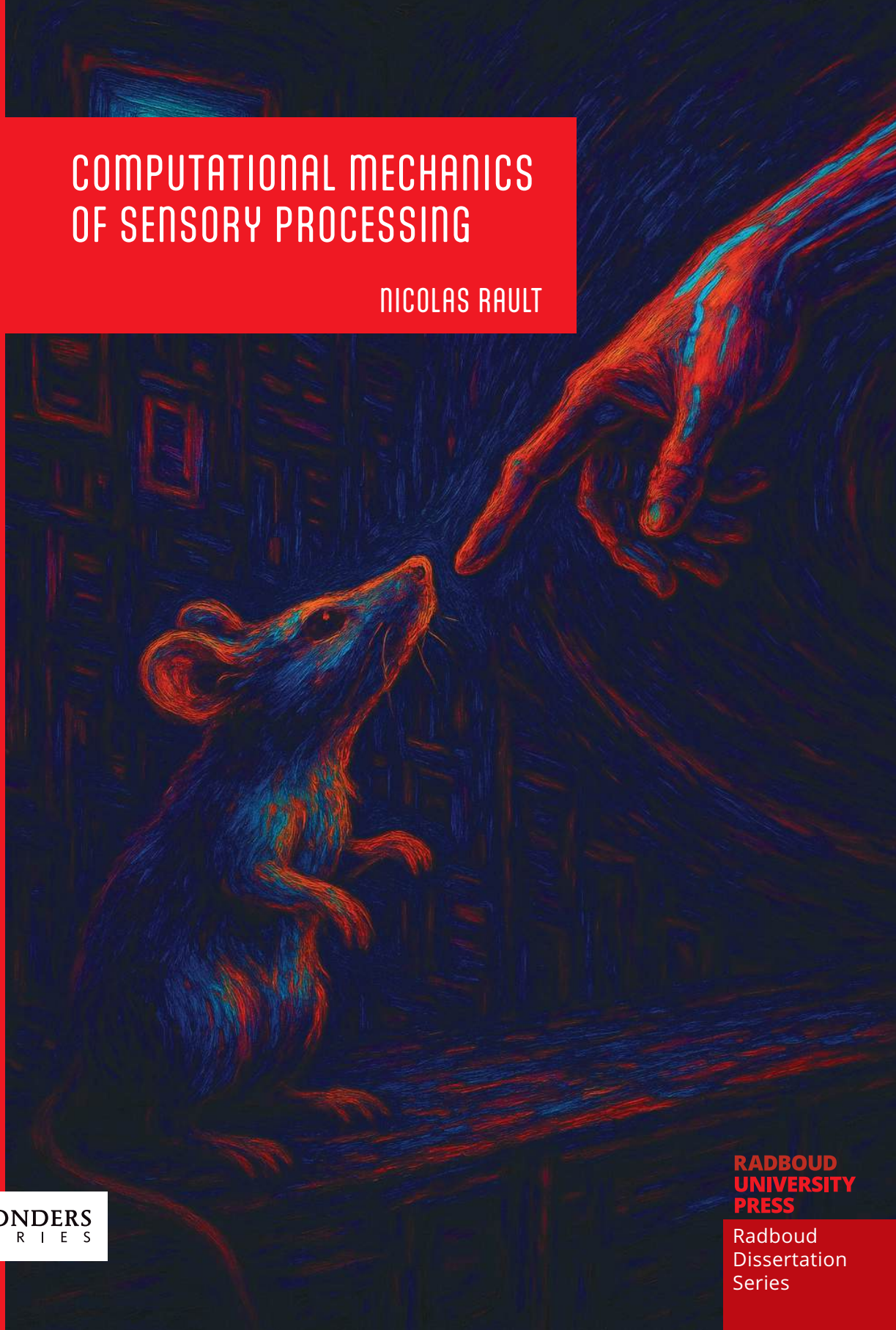

DONDERS SERIES

RADBOUD UNIVERSITY PRESS

Radboud Dissertation Series

# Computational Mechanics of Sensory Processing: Modelling and Computation for Next-Generation Artificial Sensing

**Nicolas Rault**

**Computational Mechanics of Sensory Processing: Modelling and Computation for Next-Generation Artificial Sensing**
**Nicolas Rault**

Radboud Dissertation Series
ISSN: 2950-2772 (Online); 2950-2780 (Print)

Published by RADBOUD UNIVERSITY PRESS
Postbus 9100, 6500 HA Nijmegen, The Netherlands
www.radbouduniversitypress.nl

Design: Proefschrift AIO | Guus Gijben
Cover: Nicolas Rault
Printing: DPN Rikken/Pumbo

ISBN: 9789465152578
DOI: 10.54195/9789465152578
Free download at: https://doi.org/10.54195/9789465152578



RADBOUD
UNIVERSITY
PRESS

**Computational Mechanics of Sensory Processing: Modelling and Computation for Next-Generation Artificial Sensing**

Proefschrift ter verkrijging van de graad van doctor
aan de Radboud Universiteit Nijmegen
op gezag van de rector magnificus prof. dr. J.M. Sanders,
volgens besluit van het college voor promoties
in het openbaar te verdedigen op

woensdag 6 mei 2026
om 16.30 uur precies

door

Nicolas Hubert RAULT
geboren op 27 augustus 1997
te Orsay (Frankrijk)

**Promotor:**
Prof. dr. T. Celikel

**Copromotor:**
Dr. F. Zeldenrust

**Manuscriptcommissie:**
Prof. dr. P.H.E. Tiesinga
Dr. B. Englitz
Prof. dr. R. Petersen (University of Manchester, Verenigd Koninkrijk)

Computational Mechanics of Sensory Processing: Modelling and Computation for Next-Generation Artificial Sensing

Dissertation to obtain the degree of doctor
from Radboud University Nijmegen
on the authority of the Rector Magnificus prof. dr. J.M. Sanders,
according to the decision of the Doctorate Board
to be defended in public on

Wednesday, May 6, 2026
at 4:30 pm

by

Nicolas Hubert RAULT
born on August 27, 1997
in Orsay (France)

**PhD supervisor:**
Prof. dr. T. Celikel

**PhD co-supervisor:**
Dr. F. Zeldenrust

**Manuscript Committee:**
Prof. dr. P.H.E. Tiesinga
Dr. B. Englitz
Prof. dr. R. Petersen (University of Manchester, United Kingdom)

# Table of contents

Chapter 1

# Introduction
# Foundation of Mechanosensation

The study of perception is a cornerstone of epistemology, probing how we come to know the world. In his *Meditation on First Philosophy* [1], René Descartes wondered, 'What can be more easily perceived than the perception of touch, sight, and hearing?' Yet, he doubted the certainty of sensory knowledge, as the senses may be deceived and thus cannot be fully trusted. For Descartes, knowledge is only obtained through reason, as the information we gather from the world through our senses is unreliable. In this way, the senses become the boundary between us and the world, made flesh, imperfect, and deceptive, shaping our experience of reality but not providing absolute truth. The position of Immanuel Kant does not go as far as denying the veracity of the existence of the outside world, yet in his *Critique of Pure Reason* [2], he makes the dichotomy between things-in-themselves, and things as they are perceived to be. For Kant, this distinction arises from the mind's innate structures, which shape our access to *phenomena*. Together, these thinkers framed the ongoing debate: Is perception a direct reflection of the external world, or a subjective construction of the mind? This thesis is inscribed in the continuity of this question, as we do not only propose the analysis of the information flow within the central nervous system but also, through the modeling of the receptors, the transduction of a force into neural activity. By quantifying the amount of information retained at each stage, we provide a quantitative difference between the raw stimulus and the *phenomena* of the stimulus – i.e., the experience of the stimulus. In this introduction, I would like to take you through the different types of mechanoreceptors playing an active role in shaping our tactile experience of the surrounding world and their mechanisms of activation.

Touch cells can respond to vibration, texture, and pressure [3] from a tactile stimulus, and they can be impacted by heat. Thus, mechanosensitive cells' activity can inform about the presence of a stimulus, its direction, its speed, the force with which it is applied, and for how long it is applied. Several physical properties of this population determine the information that is conveyed to the brain. Firstly, pressure that results when skin is touched spreads over the skin due to its elastic properties, which dampens the intensity of the stimulus [4]. Consequently, the intensity of a stimulus depends on the distance between the point of contact and the position of the touch cell. Secondly, not only does the *distance* to the contact point matter, but the *depth* of the receptor within the skin also plays a role in the information received by these cells [5]. Finally, the varying density of the receptors over different locations of the body also influences the information that is received by this system, making, for instance, the signals from the fingertips highly reliable as they provide a higher resolution than other limbs [6].

The mechanoreceptors compose the avant-garde of the nervous system as the first layer to transduce the stimulus – e.i, conversion of a mechanical stimulus into electrical signals (action potentials). These cells consist of various types, which differ in several electrophysiological properties. Strikingly, these cell types and their relative distributions appear to be shared across mammals [7]. They receive information through nerve endings, the shape of which depends on the depth within the skin and the part of the body considered. In hairy skin, the shaft of a hair can be surrounded by filiform structures called lanceolate endings or palisades called circumferential endings [8]. Their elongated shape allows them to bend in the same way as the hair. Glabrous (hairless) skin, on the other hand, can contain touch domes, free nerves, or club-like structures. The information from both these nerve endings is transmitted to touch cells through myelinated (namely: Aβ, Aδ) or unmyelinated (namely: C) fibers, classified based on their conducting properties. These fibers connect to Ruffini corpuscles, Meissner corpuscles, Pacini corpuscles, and Merkel cells.

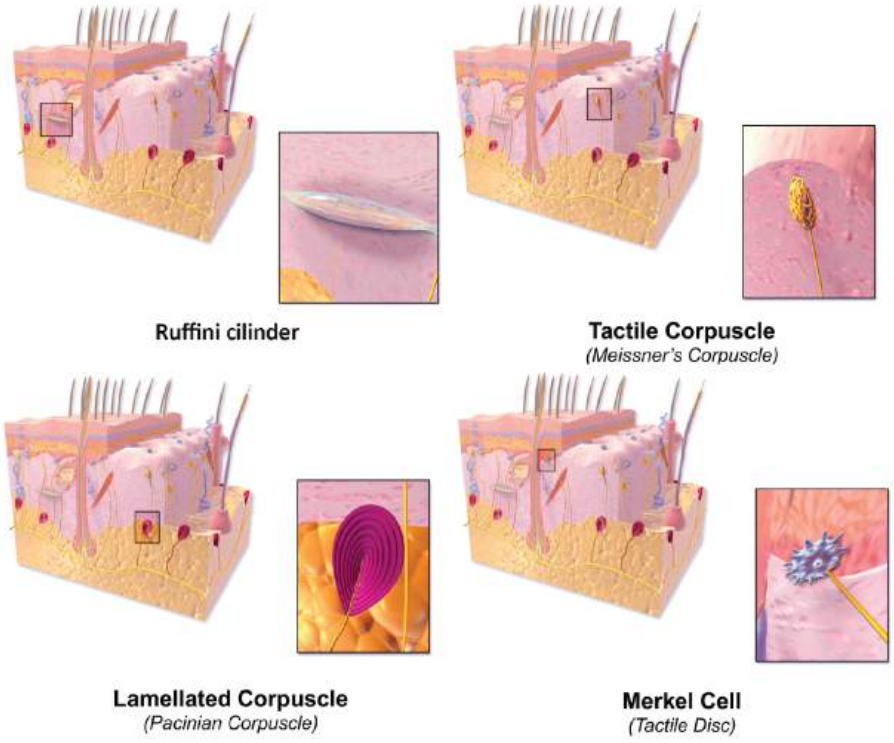


**Figure 1 - Side view of the skin with the different types of touch cells within.** The insets are zooms on the touch cell of interest. Top left: Zoom on a Ruffini Corpuscle. Top right: Zoom on a Meissner Corpuscle. Bottom left: Zoom on a Pacinian Corpuscle. Bottom right: Zoom on a Merkel cell. Original illustration from [9].

Ruffini corpuscles (**Figure 1**) are found in the glabrous skin and respond to stretch information with a slowly adapting type 2 (SA2) pattern of activity in response to a sustained stimulus[8], characterized by a sharp increase of activity at the beginning of a stimulus presentation and a slow decline toward a plateau. Meissner corpuscles (**Figure 1**) are specific to glabrous skin and are found mainly in parts of the mammalian body that require high accuracy, such as mouse paws or human fingertips. These cells provide a low resolution in stimulus direction, but are quite sensitive to pressure. They are believed to play an important role in prehension (seizing or grasping an object). Their association with rapidly adapting (RA) afferents enforces this hypothesis [10, 11]. Pacinian corpuscles (**Figure 1**) exhibit rapidly adapting type 2 (RA2) patterns of activity and are found in the hypodermis [8]. Both RA and RA2 fire at the onset and offset of a stimulus. Finally, Merkel cells (**Figure 1**) are present in whisker follicles as well as fingertips; they connect to slowly adapting afferents to form the Merkel neural complexes, which exhibit irregular spiking patterns. Maksimovic et al. propose the hypothesis that the afferents respond to dynamic stimuli, while the Merkel cells per se transduce static information such as pressure [12], explaining the slowly adapting type 1 (SA1) pattern of activity that they exhibit, in which the presentation of a stimulus induces a sharp increase of spiking activity followed by a sharp decrease toward an irregular plateau activity. In both compartments of this complex, piezo2 mechanosensitive ion channels allow for the transduction of a force into spiking activity [12, 13].

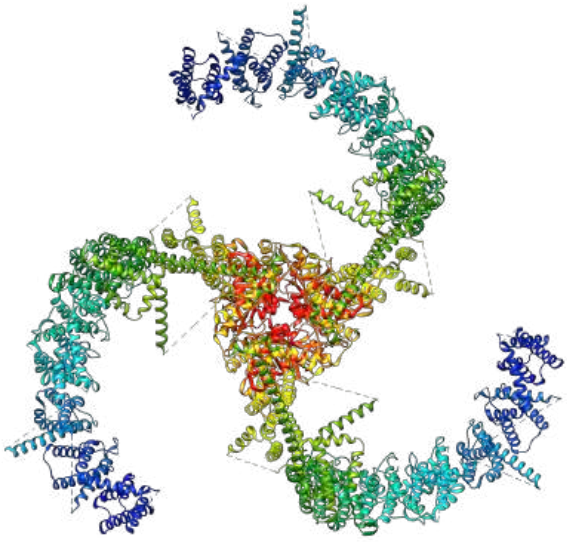

**Figure 2 - Schematic of a Piezo2 ion channel structure.** The three-helix structure acts as a lever, opening a pore in response to membrane tension, allowing a calcium ion influx (original illustration from [14]).

Mechanosensitive ion channels are the founding stones of mechanotransduction. As far as we know, 4 types of such ion channels play an important role in touch sensation, namely, the Piezo (**Figure 2**), TRP, K2P, and DEG/ENaC ion channels. While the molecular structures of these ion channels vary, the mechanism of activation remains the same: when pressure is applied, this results in a stretch of the tissue around the ion channel or a pressure applied directly to it. This pressure applied on the bilayer lipid membrane of the cell allows ions to enter. Piezo channels 1 and 2 are structures composed of three helices, linked to the structure's center by beams acting like levers on a cap, allowing calcium ions to enter the cell through a porous section hidden below once the cap has been `lifted' (Figure 2). They are found in diverse systems such as the bladder or the blood. They allow information about a push or stretch of surrounding tissue to be transformed into electrical activity. Piezo2 channels were found to be necessary for Merkel cells to conduct mechanotransduction [12]. TRP channels are activated by stretch and non-noxious heat. They are composed of four intertwined sub-units. Upon the stretch of the surrounding tissue, the lipid layers of the membrane of the cell are deformed, resulting in a separation of the sub-units, which in turn allows for a calcium ion influx into the cell [15]. TREK-1 ion channels are composed of two subunits, which, upon application of pressure, open, allowing potassium ions to enter the cell [16]. DEG/ENaC channels share a common structure composed of three subunits that act as springs. When pressure is applied perpendicular to the membrane, springs that are perpendicular to the cell membrane transfer the force to springs that are within the cell membrane, parallel to it, opening the membrane, thereby allowing sodium ions to enter the cell.

To summarize, when pressure is applied to the skin, it will stretch the membrane of the sensory cells, resulting in the opening of mechano-gated channels, allowing an influx of ions into the touch cells. This either happens directly on the touch cells' somata or in their end organs (touch dome, club-like endings, etc), in which case the change in pressure will be communicated to the touch cells through nerve fibers with different conducting properties. This intricate pressure-to-electrical-activity mechanism is the first step toward tactile sensation in the nervous system and builds upon a heterogeneous population of end organs, touch cells, nerve fibers, and ion channels. This thesis focuses on the information flow into the central nervous system and the transduction of a force into neural activity. We start by modeling the output of the touch cells, using their established response properties to understand their role in tactile encoding and information propagation of the resulting activity in the tactile system, which we will describe in Chapter 2.

In the second Chapter, I will take you through the somatosensory system, which receives information from the aforementioned mechanoreceptors by drawing the connectome of the whisker system of the rodent, relying on the extensive tracing experiments performed by the Allen Brain Institute on more than 2700 mice from more than 180 transgenic lines. Using the available 2-photon imaging data, I will focus on a subset of 18 nuclei that are essential for the whisker system with the aim of identifying key network motifs and potential computational roles of these early processing stages. I will show that the early stages of the central nervous system, through an intricate network, are more than mere relay stations for the information.

In the third Chapter, I will model the mechanoreceptors and quantify the information they allow the periphery to convey to the central nervous system by fitting a neuron model to electrophysiological recordings of such cells. Through an analysis of human reaction time and ability to distinguish between two tactile stimuli durations applied to their fingertips, we hypothesize that the tactile system is split into two pathways, one to detect a stimulus and one to distinguish between stimuli. Relying on the mechanoreceptors model, we conclude that the two pathways originate from the periphery itself. Leveraging information theory, I will investigate the encoding mechanisms in the early stages of the sensory system, as we hypothesize that the information encoding properties are distinct across these two pathways.

In the fourth Chapter, I will dive deeper into the specific representations of different stimuli that can be applied to whiskers. We expect to find that different stimulus features are encoded by distinct combinations of mechanoreceptor activity. To asses this hypothesis, we rely on a newly developed interface between a whisker model [17] and the mechanoreceptor model developed in the previous chapter. I will 1) apply forces with different directions, amplitudes, speeds, frequencies, and distances to the whisker basis on the modeled whisker, 2) assess the representation of each of these variables as well as quantify the information transfer between the mechanoreceptors and the brainstem and 3) deduce the encoding strategies in each layer of this network.

In the fifth Chapter, to conclude the modelling work of this thesis, I will complete the previous model by including a model of the thalamus and of the granular and supragranular layers 4, 3, and 2 of the somatosensory cortex [18]. We predict that information will be progressively refined and transformed as it ascends the pathway, leading to more abstract representations in higher cortical areas. To assess this hypothesis, I will decode the stimuli presented to the model, quantify

the information transfer between the stimulus and the different structures of the ascending somatosensory pathway, and unveil the evolution of coding patterns as it progresses through the ascending somatosensory pathway.

To conclude, I will take you through the advancement this thesis brings to the field of sensory neurosciences and its implications in the fields of neuroprosthetics and sensory integration. Through the lens of information theory, we will take a look at how touch sensation is represented in the different stages of tactile integration, the different strategies adopted by the layers of the network, and their consequences for neuromorphic sensors and sensory neuroprosthetics.

# References


[1] René Descartes: Meditations on First Philosophy. (2013). In Cambridge University Press eBooks. https://doi.org/10.1017/cbo9781139042895

[2] Kant, I. (1998). Critique of Pure Reason. In *Cambridge University Press eBooks*. https://doi.org/10.1017/cbo9780511804649

[3] J.M. Loomis, S.J. Lederman, K.R. Boff, L. Kaufman, J.P. Thomas (Eds.), Cognitive processes and performance, Handbook of perception and human performance, Vol. 2, John Wiley & Sons, New York (1986), pp. 31.1-31.41 (chap. 31)

[4] Deflorio, D., Di Luca, M., & Wing, A. M. (2022b). Skin and Mechanoreceptor Contribution to Tactile Input for Perception: A Review of Simulation Models. *Frontiers in Human Neuroscience*, *16*. https://doi.org/10.3389/fnhum.2022.862344

[5] Quindlen, J. C., Lai, V. K., & Barocas, V. H. (2015). Multiscale Mechanical Model of the Pacinian Corpuscle Shows Depth and Anisotropy Contribute to the Receptor's Characteristic Response to Indentation. *PLoS Computational Biology*, *11*(9), e1004370. https://doi.org/10.1371/journal.pcbi.1004370

[6] Johansson, R. S., & Vallbo, A. B. (1979). Tactile sensibility in the human hand: relative and absolute densities of four types of mechanoreceptive units in glabrous skin. *The Journal Of Physiology*, *286*(1), 283–300. https://doi.org/10.1113/jphysiol.1979.sp012619

[7] Maricich, S. M., Morrison, K. M., Mathes, E. L., & Brewer, B. M. (2012). Rodents Rely on Merkel Cells for Texture Discrimination Tasks. *Journal Of Neuroscience*, *32*(10), 3296–3300. https://doi.org/10.1523/jneurosci.5307-11.2012

[8] Cobo, R., García-Piqueras, J., García-Mesa, Y., Feito, J., García-Suárez, O., & Vega, J. A. (2020). Peripheral Mechanobiology of Touch—Studies on Vertebrate Cutaneous Sensory Corpuscles. *International Journal Of Molecular Sciences*, *21*(17), 6221. https://doi.org/10.3390/ijms21176221

[9] Blausen.com staff (29 August 2014)."Medical gallery of Blausen Medical 2014".WikiJournal of Medicine **1** (2). doi:10.15347/WJM/2014.010.Wikidata Q44276831. ISSN 2002-4436.

[10] Nikolaev, Y. A., Ziolkowski, L. H., Pang, S., Li, W., Feketa, V. V., Xu, C. S., Gracheva, E. O., & Bagriantsev, S. N. (2023). 3D architecture and a bicellular mechanism of touch detection in mechanosensory corpuscle. *Science Advances*, *9*(37). https://doi.org/10.1126/sciadv.adi4147

[11] Neubarth, N. L., Emanuel, A. J., Liu, Y., Springel, M. W., Handler, A., Zhang, Q., Lehnert, B. P., Guo, C., Orefice, L. L., Abdelaziz, A., DeLisle, M. M., Iskols, M., Rhyins, J., Kim, S. J., Cattel, S. J., Regehr, W., Harvey, C. D., Drugowitsch, J., & Ginty, D. D. (2020). Meissner corpuscles and their spatially intermingled afferents underlie gentle touch perception. *Science*, *368*(6497). https://doi.org/10.1126/science.abb2751

[12] Maksimovic, S., Nakatani, M., Baba, Y., Nelson, A. M., Marshall, K. L., Wellnitz, S. A., Firozi, P., Woo, S., Ranade, S., Patapoutian, A., & Lumpkin, E. A. (2014b). Epidermal Merkel cells are mechanosensory cells that tune mammalian touch receptors. *Nature*, *509*(7502), 617–621. https://doi.org/10.1038/nature13250

[13] Ranade, S. S., Woo, S., Dubin, A. E., Moshourab, R. A., Wetzel, C., Petrus, M., Mathur, J., Bégay, V., Coste, B., Mainquist, J., Wilson, A. J., Francisco, A. G., Reddy, K., Qiu, Z., Wood, J. N., Lewin, G. R., & Patapoutian, A. (2014). Piezo2 is the major transducer of mechanical forces for touch sensation in mice. *Nature*, *516*(7529), 121–125. https://doi.org/10.1038/nature13980

[14] Goutard59, Wikipedia contributor.*PIEZO2*. (Created: 9 October 2023, Accessed: 4 April 2024). Wikipedia. https://en.wikipedia.org/wiki/PIEZO2#

[15] Cao, E. (2020). Structural mechanisms of transient receptor potential ion channels. *The Journal Of General Physiology*, *152*(3). https://doi.org/10.1085/jgp.201811998

[16] Sorum, B., Docter, T., Panico, V., Rietmeijer, R. A., & Brohawn, S. G. (2024). Tension activation of mechanosensitive two-pore domain K+ channels TRAAK, TREK-1, and TREK-2. *Nature Communications*, *15*(1). https://doi.org/10.1038/s41467-024-47208-5

[17] Zweifel, N. O., Bush, N. E., Abraham, I., Murphey, T. D., & Hartmann, M. J. Z. (2021). A dynamical model for generating synthetic data to quantify active tactile sensing behavior in the rat. *Proceedings Of The National Academy Of Sciences*, *118*(27). https://doi.org/10.1073/pnas.2011905118

[18] Tompos, T., Zeldenrust, F., Celikel, T. (2025).Stability and Adaptability in Balance: A Dual Mechanism for Metaplasticity in Cortical Networks. bioRxiv. https://doi.org/10.1101/2025.04.02.646896

Chapter 2

# Where top-down meets bottom-up: Cell-type specific connectivity map of the whisker system

Rault, N., Bergmans, T., Delfstra, N., Kleijnen, B. J., Zeldenrust, F., & Celikel, T. (2024). Where top-down meets bottom-up: Cell-type specific connectivity map of the whisker system. *Neuroinformatics*, *22*(3), 251-268.

## Abstract

Sensorimotor computation integrates bottom-up world state information with top-down knowledge and task goals to form action plans. In the rodent whisker system, a prime model of active sensing, evidence shows that neuromodulatory neurotransmitters shape whisker control, affecting whisking frequency and amplitude. Since neuromodulatory neurotransmitters are mostly released from subcortical nuclei and have long-range projections that reach the rest of the central nervous system, mapping the circuits of top-down neuromodulatory control of sensorimotor nuclei will help to systematically address the mechanisms of active sensing. Therefore, we developed a neuroinformatic target discovery pipeline to mine the Allen Institute's Mouse Brain Connectivity Atlas. Using network connectivity analysis, we identified new putative connections along the whisker system and anatomically confirmed the existence of 42 previously unknown monosynaptic connections. Using this data, we updated the sensorimotor connectivity map of the mouse whisker system and developed the first cell-type-specific map of the network. The map includes 157 projections across 18 principal nuclei of the whisker system and neuromodulatory neurotransmitter-releasing. Performing a graph network analysis of this connectome, we identified cell-type-specific hubs, sources, and sinks, provided anatomical evidence for monosynaptic inhibitory projections into all stages of the ascending pathway, and showed that neuromodulatory projections improve network-wide connectivity. These results argue that, beyond the modulatory chemical contributions to information processing and transfer in the whisker system, the circuit connectivity features of the neuromodulatory networks position them as nodes of sensory and motor integration.


### List of abbreviations

TG - Trigeminal Ganglion
PSV - Principal sensory nucleus
SPVO, SPVI, SPVC - spinal nucleus of the trigeminal oralis, interpolaris, caudalis
VPM - ventral posteromedial nucleus
PO - posterior complex of the thalamus
RT (nRT) - Reticular Nucleus of the thalamus
bfd - barrel field of the primary somatosensory cortex
MOp (M1) - primary motor cortex
SC - Superior Colliculus
VII - Facial Motor nucleus
ZI - Zona Incerta
SI - Substantia Innominata
DR - Dorsal raphe nucleus
LC - Locus coeruleus
PPN - Pedunculopontine nucleus
VTA - Ventral tegmental area
TM - Tuberomammillary nucleus

## Introduction

In the wild, whisking rodents are subterranean mammals that live in dark and narrow environments. They heavily rely on the rhythmic protraction and retraction of their whiskers to navigate their natural habitat. Organized as closed-loop circuits (Kleinfeld et al., 1999), distributed networks in the brain control whisking as an adaptive sensorimotor computation while they encode sensory information originating from the sensory periphery and compute the future position of the whiskers as an iterative process (Voigt et al., 2008, Voigt et al., 2015, McElvain et al., 2018).

The neural circuits that contribute to the sensory representations acquired through whisker contacts and the positional controls of whiskers were last summarized more than a decade ago (Bosman et al., 2011). Building on (1) the first comprehensive sensorimotor circuit map in the whisker system (Kleinfeld et al., 1999), (2) the fundamental experimental work that described the lemniscal and paralemniscal ascending neural circuits (Chial et al., 1991, Lu and Lin, 1992), and (3) the descending projections originating from the motor cortex (Ashwell, 1982, Hemelt and Keller, 2008), Bosman and colleagues described the connectome between 43 nuclei contributing to the sensorimotor integration in the whisker system. In particular, 12 of the nuclei described in their studies, as well as 6 brainstem regions that release neuromodulatory transmitters, showed 74 connections (Supplemental Figure 1, for the complete network, Supplemental Figure 2).

Over the last decade, new experimental studies have provided direct evidence that the network connectivity along the whisker system is more expansive than previously shown. For example, a study by Jeong et al. (2016), focusing on the motor nuclei in the mouse, in particular MOp (M1), revealed projections to PO and VPM, as well as to the contralateral PSV, SPV, and VTA. (Mu˜noz-Casta˜neda et al., 2021) confirmed both this last connection and the monosynaptic Mop (M1) projections to PPN and SPVi. In parallel, direct monosynaptic projections originating from bfd and targeting TM, RT (nRT), and ZI (Zakiewicz et al., 2014), ZI projections to VII (Takatoh et al., 2021), VII innervation of SPVi (Bellavance et al., 2017), VPM to Mop (M1) connections (Hooks et al., 2013), and bidirectional communication between Mop (M1) and RT (nRT) were shown (Yang et al., 2022).

New monosynaptic projections along the sensorimotor pathways were also discovered to originate from several neuromodulatory neurotransmitter-releasing nuclei. Hosp et al., 2011 identified a projection between the VTA and Mop (M1), showing the contribution of dopaminergic connections originating from the

VTA in motor skill learning. Other studies showed that the VTA serves as a hub of divergence with projections to SI, LC, DR, RT (nRT) (Dunigan et al., 2021), and bfd (Aransay et al., 2015), all critical for the information processing in the whisker system. Finally, the novel discoveries along the neuromodulatory circuits and their integration with nuclei in the whisker system are not limited to the dopaminergic system. Monosynaptic cholinergic projections to RT (nRT) (Sokhadze et al., 2018), SI projections to ZI (Zhou et al., 2018), ZI projections to VTA (An et al., 2021), reciprocal connections between PO and SC (Benavidez et al., 2021), SI projections to PSV, VTA, VPM, SI (Benavidez et al., 2021), and DR (Benavidez et al., 2021; Dorocic et al., 2014) all provide anatomical evidence for neuromodulatory contributions to sensorimotor control.

The newly found connections mentioned above require an update of the previously drawn connectivity map of the rodent whisker system. In this study, by leveraging the connectivity data in the Allen Mouse Brain Atlas (Oh et al., 2014), we update the previously reported connectome (Bosman et al., 2011), develop the first-generation cell-type specific connectivity map along the mouse whisker system and investigate the contribution of neuromodulator-releasing nuclei to top-down regulation and information propagation in this network. In addition to the nuclei from the ascending somatosensory pathway and the motor cortex, we consider the following networks in our updated whisker system connectivity map: The facial motor nucleus (VII), as it contains the motoneurons innervating the muscle situated in the whisker pad (Ashwell, 1982). The Superior Colliculus (SC) is targeted by connections from the trigeminal nuclei and targets VII (Hemelt and Keller, 2008). The reticular nucleus of the thalamus (RT (nRT)) is added as the main source of inhibition of the thalamic nuclei (Pinault et al., 1995). The Zona Incerta (ZI) is included in the map for its role in the paralemniscal pathway (Urbain and Deschˆenes, 2007a) and its somatotopic map representation of whiskers (Nicolelis et al., 1992).

By analyzing 732 anterograde tracing experiments performed in 95 wild-type and transgenic lines using the open-source toolbox we developed (https://github.com/DepartmentofNeurophysiology/NeuralNet-ABC), we determine the connectivity along the ascending, descending, and neuromodulator pathways. We show that the sensorimotor circuits in the whisker system include 157 projections; 42 of these projections had not been described in the literature previously, but are confirmed anatomically herein. Additionally, 40 connections are identified as plausible monosynaptic projections and reported here as putative connections. By performing graph network analysis, we further identify cell-type-specific hubs,

sources, and sinks in this connectome and, finally, show that neuromodulatory projections improve network-wide connectivity.



## Materials & Methods

### Experimental pipeline

All experimental data (https://connectivity.brain-map.org/) and our custom-written toolbox for analysis (https://github.com/DepartmentofNeurophysiology/NeuralNet-ABC) are available online. Experimental procedures for data acquisition have been detailed by the Allen Brain Institute before (Oh et al., 2014). In short, genetically encoded fluorescent proteins were expressed in anatomically targeted regions using cell-type-specific or non-specific promoters in transgenic and wild-type mice. The resulting anterograde projection labeling was visualized using serial two-photon tomography. The data were projected onto a 3D normal brain built upon a volumetric average template from 1,675 wild-type mice with 10 µm isotropic voxel resolution. The 3D reference brain was then parcellated into 43 isocortical areas, 329 subcortical gray matters structures, 81 fiber tracts, and 8 ventricular structures for each hemisphere to identify the main anatomical origin and target areas based on a standard atlas (Wang et al., 2020). For each structure, four variables were extracted: the volume, the intensity, the density, and the energy. The volume represents the volume of tracer solution in mm3 present in a brain structure; the intensity is the sum of the brightness of every pixel in a given structure (the tracer producing a fluorescent reaction); the density is the number of pixels considered as expressing the gene divided by the total number of pixels present in the structure, and the energy is the sum of pixel intensities divided by the number of pixels in the structure. The results were stored in a JSON format containing a list of structures with their associated extracted variables. To build our connectivity matrices, we first downloaded the data using Allen Brain Institute's API (Figure 1), and identified experiments that targeted 57 target nuclei, which have been experimentally identified as a part of the sensorimotor circuits in the rodent brain (Supplemental Figure 1). From these experiments, we filtered out those with less than 50% of the viral solution injected in the targeted area (i.e., where more than half of the solution missed the targeted area). Each experiment was saved in a JSON file containing a list of structures (723 per hemisphere) and the measures of the projection volume, intensity, density, and energy. Next, we grouped the experiments per transgenic line and projected the data from each experiment onto a 723x1446 matrix (723 structures for each hemisphere), with the sources of the experiments as rows and the structures receiving the connections as columns (Figure 1).

## Specificity Calculation

To quantify the percentage of solution injected in the target area, we downloaded for each experiment a 3D representation of the animal's brain, in which every voxel's value represents the density of solution within the area with the voxel's coordinate. The area of injection was manually annotated by the Allen Brain Institute, and every voxel's value outside of the injection zone was set to 0. We downloaded a 3D mask of the injection structure for each experiment. This consists of a 3D matrix representing the mouse brain where only the voxel within the coordinates of the targeted structure is equal to one, and every voxel outside of the structure is set to 0. We performed a pairwise multiplication between the mask and the injection density matrix, giving us only the part of the injection within the targeted structure. We binarized the result by setting every voxel above 0 to 1 and did the same for the injection density. We finally divided the masked injection density (binarized injection density that has been multiplied by the mask) by the binarized injection density. These results give us the percentage of injection within the targeted area, called specificity. As stated in the experimental pipeline, we used this value to filter out experiments with less than 50% specificity. To validate the newly found connections, we relied on the Allen Brain Institute's specificity calculation and accepted only the anatomical validation from experiments with a specificity above 75%. This value is obtained through the same process as described previously, only without binarization of the voxel's value.

## Transgenic categorization

Transgenic lines were considered "excitatory" if presented as such in the literature or if the marked cells were glutamatergic, i.e., for example, expressed glutamate or vesicular glutamate transporters and other proteins necessary for glutamatergic signaling. "Inhibitory" cells were classified as cells expressing Gamma-Aminobutyric Acid (GABA), glycine neurotransmitters, or other proteins related to inhibitory signaling, such as GABA receptors. Transgenic lines were classified as "uncategorized" if marked cells expressed both excitatory and inhibitory proteins, or if they expressed neither (e.g., dopamine, adrenaline, serotonin, or other neuromodulatory proteins with no direct excitatory or inhibitory effect). See Supplemental Table 1 for the list and the corresponding citations.

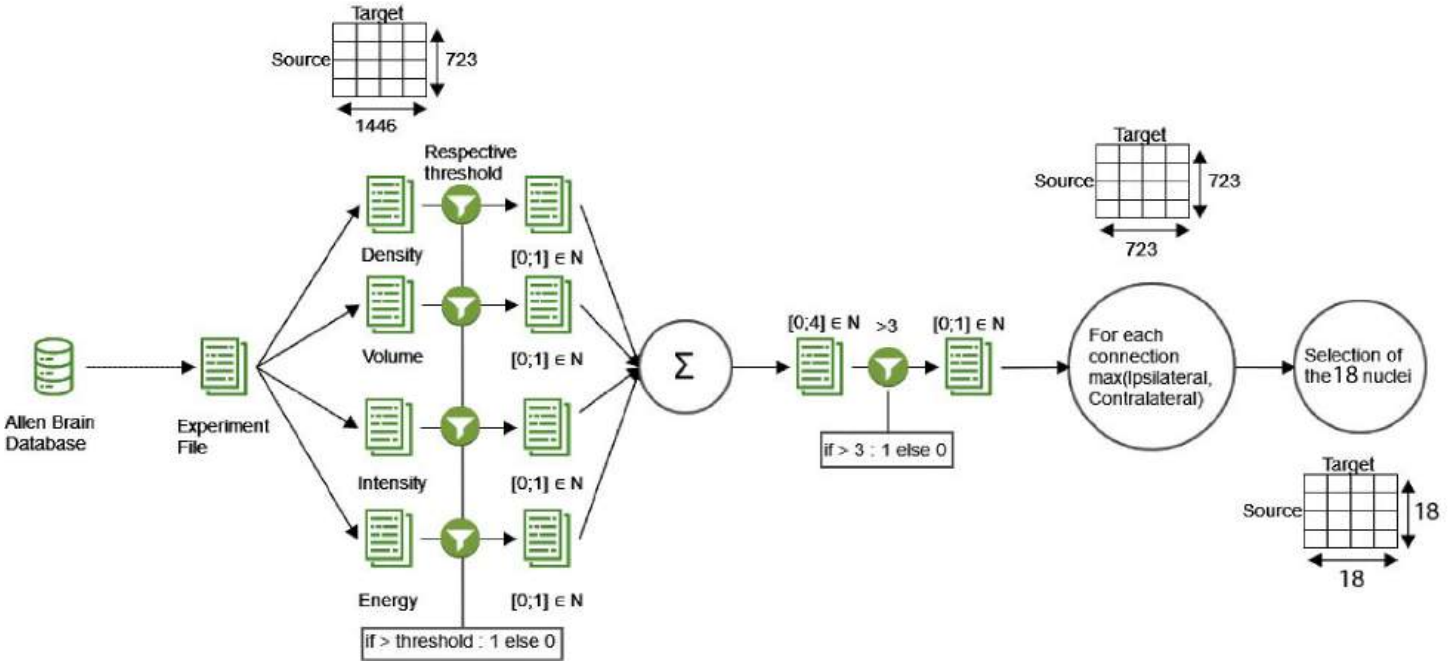


**Figure 1 - The data processing pipeline.** For each transgenic line, the data were downloaded from the Allen Brain database. Each experiment file was split into 4 matrices of size 723x1446 (see section 2.2), one per variable (density, volume, intensity, and energy). A threshold specific to each variable (see Connectivity Validation) was applied and 4 matrices with values of either zero or one were retrieved. These matrices were summed and a threshold equal to 4 was applied, so that only the connections that satisfied the conditions on all 4 variables remained. This way, a matrix composed of zeros and ones was obtained. Due to the sparse nature of contralateral hemispheric projections, which will increase the false negative rate, the connectomes across the hemispheres were merged by selecting the highest value. From the resulting matrix of size 723x723, we retrieved the connections for the nuclei of interest (see Supplemental Figure 1.b and 1.c). This resulted in a binary connectivity matrix with 324 (18x18) possible edges.

## Connectivity validation

To validate the connections identified in the connectivity matrices derived from the Allen Brain Institute's experiments, we compared them to a subset (N=34) of connections previously reported by Bosman et al. (2011) between a subset of 18 nuclei discussed in the introduction. For each variable, we determined a variable-specific threshold by systematically increasing the threshold until one of the 34 reference connections was no longer detected in the wild-type experiments. The last value for which we found 100% of true positives was considered the correct threshold. This process yielded four distinct thresholds, which were applied to each transgenic line (density threshold: $9 \times 10{-}5$ (a.u.), intensity threshold: 222 (a.u.), energy threshold: $2891 \times 10{-}2$ (a.u.), volume threshold: $395 \times 10{-}4$ (in mm3)).

A connection was considered valid only if it appeared on each variable-specific matrix after threshold application. This approach ensured that we retained previously known connections while avoiding assumptions about the underlying connectivity that might have arisen from minimizing false positives. By focusing solely on true positives, we did not impose any preconceived notions about the pattern of connectivity between different nuclei. Cross-validating our connections with the four available variables minimized the likelihood of false negatives. As an additional safeguard, we verified that the genes marked by the transgenic lines in the Allen Brain Institute's experiments were indeed expressed in the targeted structure using the transgenic characterization tool available on the Allen Brain Institute's website. Applying these thresholds resulted in four connectivity matrices: one for the wild type and one for each transgenic characterization (excitatory, inhibitory, or uncategorized), combined in one (Figure 2.b and Supplemental Figure 3) and compiled into connectivity maps (Figure 2.a and 3, Supplemental Figure 4 and 5). To corroborate the connections, calculations were repeated across animal lines. We reviewed the literature and identified new connections from our results (Figure 4). The density of these connections was normalized for every connection source so that the total density projected from a node sums to 1. We then analyzed the distribution of outgoing density amongst targeted nodes to assess the sparsity of the projections originating from each nucleus (Figure 5 and 6). New connections were validated through anatomical confirmation using the imaging data available in the Allen Brain Database from experiments with at least 75% of the viral solution injected in the targeted structure as calculated by the Allen Brain Institute. Finally, we constructed a summary map that includes previously established and newly discovered connections (Figure 4 and 7). For anatomical validation of the identified connections, we superimposed the results from the 2-photon imaging experiments onto a mean model of the mouse brain. The two images for each connection were

manually aligned using fiducial markers such as the hippocampus or the outline of the brain. The limitations of this approach are discussed in the discussion section.

To summarize, in order to identify new connections, we 1) used our calculated connectivity map as a ”hypothesis generation” tool to find likely projections across the connectivity map using experimental data with 50% specificity, which means that at least half of the injection volume is inside the target nucleus boundary. We 2) identified all experiments that met a secondary criterion (i.e., 75% or better specificity), anatomically confirmed the data, and provided the data as supplemental material (Supplemental Figures 6 to 35). And finally, 3) we built a summary matrix based on the results of Step 2 with “anatomically confirmed” connections. The remaining projections identified in Step 1 are presented as “putative connections”.

## Network analysis

Based on the obtained connectivity maps, we analyzed the network properties of neuromodulator-releasing nuclei and their contribution to the overall connectivity of the sensorimotor circuit. To assess the small-world nature of our network, we compared our summary graph to an Erdos-Renyi (ER) graph. First, we determined the total number of connections in our summary map and calculated the probability of a connection. We then constructed an ER graph with the same number of edges, nodes, and connection probability. Using theGRETNA toolbox (Wang et al., 2015), we computed the clustering coeffi cient and the shortest path for both the original and the ER graph. According to Watts and Strogatz (1998), a small-world network exhibits higher clustering values and a lower shortest path length compared to ordered and random networks. We therefore considered our summary network to be a small-world network if its clustering coefficient was higher than that of the ER graph and its average shortest path was lower than that of the ER graph.

In addition to the ER network, we constructed a summary graph without the neuromodulator-releasing nuclei. We then computed the nodal clustering coefficient, the nodal shortest path, the degree centrality, the nodal efficiency, the nodal local efficiency, and the betweenness centrality for both networks.

To determine whether the neuromodulator-releasing nuclei had an impact on the network structure, we compared the distributions of these values using a permutation test with 10,000 permutations. Finally, we assessed the presence of hubs in the extended network (57x57, Supplemental Figure 2). To do that, we first computed the out-degree as the sum of output and the in-degree as the sum of

input for each node. The sum of those two variables gives the degree of centrality. We considered every node with a degree centrality above the average plus one standard deviation as a hub (Figure 6).

## Results

We analyzed data from 162 experiments on wild-type mice and 570 experiments on 94 different transgenic lines. Of these 732 experiments, 501 presented at least 50% specificity. Focusing on the 18-nuclei subnetwork, out of the $18 \times 18 = 324$ possible connections for each type of mouse, 237 connections were identified in the wild-type strain. Experiments on the transgenic lines revealed 151 excitatory connections, 198 inhibitory connections, and 211 uncategorized connections exhibiting values above 0 without threshold application. Among these 797 connections, 44% (i.e., 351 projections) met the criteria for anatomical connections (see Materials and Methods for details) and originated from experiments with at least 50% specificity. For the 18-nuclei sub-network, Bosman et al. (2011) observed 74 connections (Supplemental Figure 1.b, 1.c). Our study identified 108 connections in the wild type (Figure 2.a, 2.b) and 243 connections in transgenic lines. The identified connections are distributed across the different cell-type-specific connectivity maps. Among these connections, 58 are excitatory (Figure 2.b; Supplemental Figure 4), 84 are inhibitory (Figure 2.b; Figure 3), and 101 are uncategorized (Figure 2; Supplemental Figure 5), with 27 of these not appearing on either excitatory or inhibitory connectivity maps (Figure 2).

Among the structures presented in this study, the tuberomammillary nucleus, the locus coeruleus, and the oral part of the spinal nucleus have not been targeted by experiments in the Allen Brain database, resulting in a lack of connectivity data for these structures. Additionally, on the wild-type map, connectivity data is not available for the tuberomammillary nucleus, the pedunculopontine nucleus, the locus coeruleus, and the dorsal nucleus raphe.

In the next sections, we will discuss the connections originating from each of the 18 nuclei, validated by our methods.

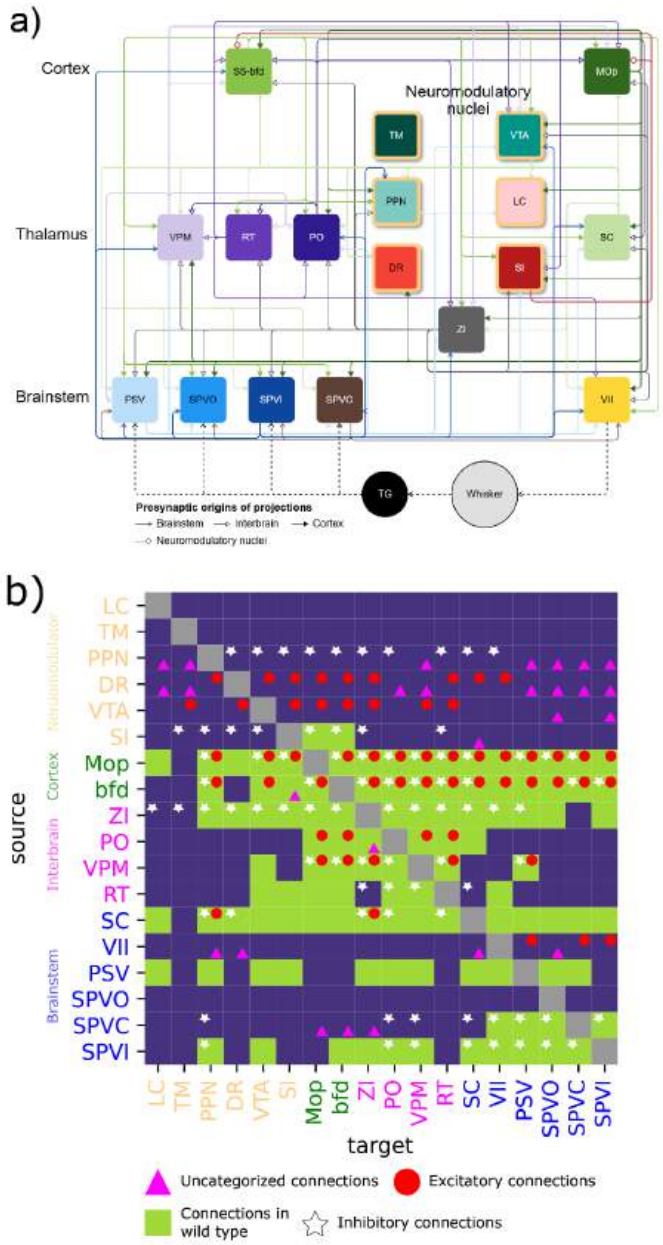


**Figure 2 - Sensorimotor connectivity map of the whisker system in wild-type mice.** a) Connectivity map across 18 nuclei with 108 connections computed from wild-type experiments in the Allen Brain database. A dashed line represents a flow of information outside of the central nervous system. The neuromodulatory structures are represented with yellow borders. b) Binary representation of the connectivity matrix combining wild, excitatory, inhibitory and unclassified transgenic lines. LC, TM, PPN, and DR were not targeted in wild-type animals, thus, their projections to the rest of the network are not shown. See Figure 7 for the updated connectome.

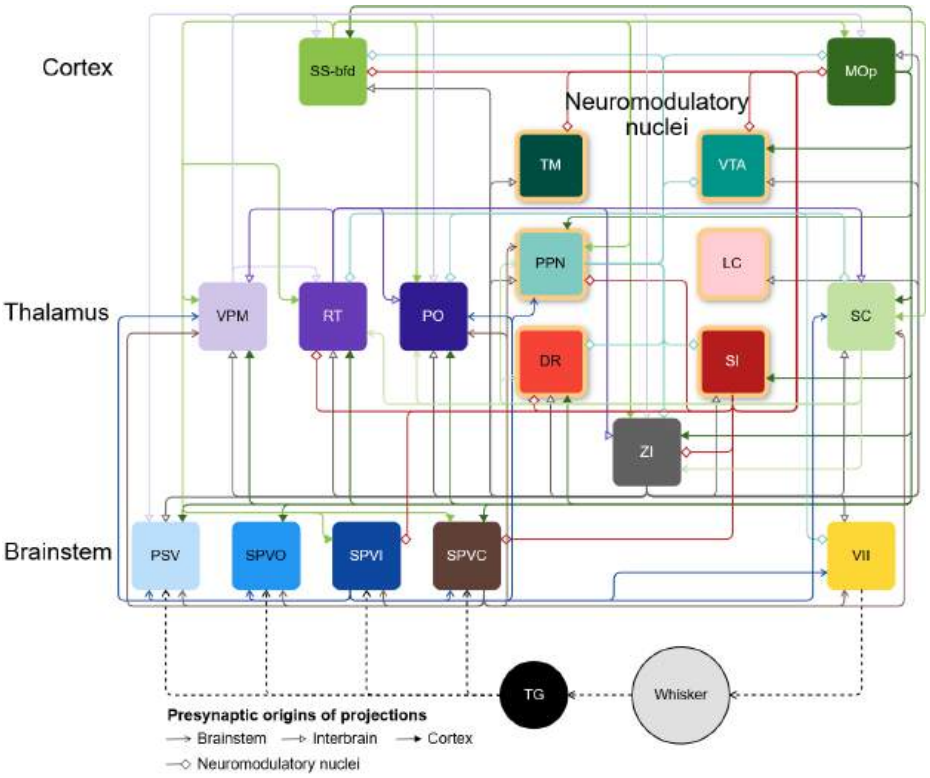


**Figure 3 - The connectome of the inhibitory projections in the mouse whisker system.** The connectivity map includes 84 connections. A dashed line represents the flow of information outside of the central nervous system. The nodes with yellow borders are neuromodulatory structures.

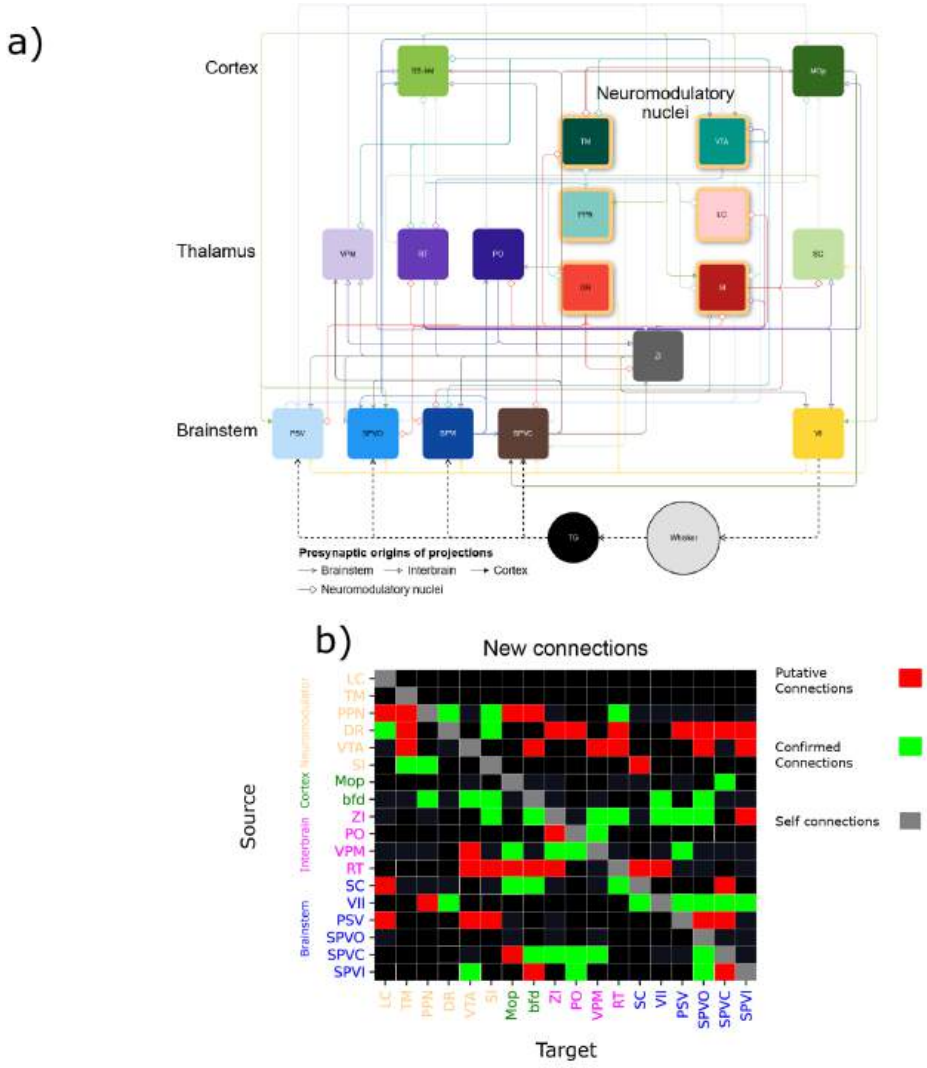


**Figure 4 - Newly discovered monosynaptic projections across the sensorimotor map of the mouse whisker system.** a) A graphical representation of the connectome. A dashed line represents the flow of information outside of the central nervous system. The neuromodulatory structures are represented with yellow borders. b) 42 of the 82 identified in the experiments from the Allen Brain database were anatomically confirmed and included in the summary map (Figure 7). The vertical axis represents the source of the connection, and the horizontal axis the target. Red cells indicate putative connections, green cells anatomically validated connections, black cells represent previously reported connections or lack of connections, whereas gray cells represent self-connections that were not considered in this study.

## Trigeminal nuclei

The information originating from whisker contact with a surface propagates along the brainstem, the thalamus, and the primary somatosensory cortex while making closed-loop connections with the motor system (Kleinfeld et al., 1999). This information is not solely transmitted via excitatory connections, as inhibition is observed early in the sensory pathway (Kleinfeld et al., 1999). In line with this, our findings reveal the presence of inhibitory presynaptic cells in SPVi and SPVc. This suggests that both inhibitory and excitatory activity play a role in processing tactile information as early as the brainstem (Figure 2).

Our findings reveal an inhibitory connection originating from SPVi targeting SC. The inhibitory nature of synaptic projections from SPVi to trigeminal nuclei and VII suggests an inhibitory control of touch processing already at the brainstem level. Moreover, SPVi inhibitory projections to PO and VPM further emphasize the brainstem's role in whisker information processing. The presence of this ascending inhibition implies that SPVi not only relays information but also filters it. Additionally, SPVi inhibits PPN, hinting at a potential role in modulating cholinergic neurons. Connections toward VTA, bfd, and ZI were identified in wild-type mice.

Connections to VTA, (PO), and SPVo were anatomically confirmed; the connections toward bfd and SPVc remain putative.

SPVi is not the only structure that targets cholinergic neurons. We demonstrated that inhibitory presynaptic cells in the trigeminal complex target other trigeminal nuclei and establish long-range connections to low-level structures of the motor pathway and acetylcholine-releasing nucleus. As described by Esmaeili et al. (2020), acetylcholine is thought to play a role in associating a whisker stimulus with a reward expectation. Through a direct connection from the trigeminal nuclei to PPN, low-level structures of the ascending somatosensory pathways can modulate cholinergic reward signals.

Our findings showed that SPVc inhibits the trigeminal nuclei, PO, SC, VPM, VII, and PPN. Uncategorized connections were found targeting ZI, MOp, and bfd. Connections toward bfd, ZI, PO, VPM, and SPVo were anatomically validated. These findings corroborate previous observations by Jacquin et al. (1990), who demonstrated dense intersubnuclear connections in the rat's trigeminal complex. Finally, the presence of inhibition in the trigeminal nuclei suggests a significant role for this node in filtering information in these early sensory structures. We could confirm anatomical projections toward bfd, ZI, PO, VPM, and SPVo. A long-

range direct projection from SPVc to bfd was shown, even though it is sparse. The connection to MOp remains putative for now.

The experiments targeting PSV had a specificity below 75%, therefore, we can only report putative connections from wild-type mice. Projections towards LC, VTA, SI, SPVo, and SPVc were found, but couldn't be confirmed.



## Thalamus

Traditionally, thalamic nuclei of the somatosensory system are considered as relay nuclei that contribute to the spatiotemporal representation of touch (Ahissar and Arieli, 2001, Azarfar et al., 2018). It is widely accepted that feed-forward excitatory projections originating from the ventral posteromedial (VPM) and posterior medial (PoM) nuclei, targeting the barrel field cortical columns and septa, respectively, constitute the primary pathway for information flow (Kleinfeld et al., 1999). However, our surprising findings argue that these projections not only include feed-forward excitation but also incorporate feed-forward inhibition. This finding has significant implications, as it reshapes our understanding of intrathalamic communication between the VPM and PoM nuclei.

Long-range connections from VPM originate from both excitatory and inhibitory cells. In addition to directly exciting bfd, Mop (M1), ZI and RT (nRT), VPM sends top-down excitatory projections to PSV. Direct inhibition (Supplemental Figures 7 and 34) of Mop (M1), bfd, ZI, RT (nRT), and PO has been demonstrated to originate from VPM. A connection toward VTA was only found in wild mice. The connections originating in VPM and targeting Mop (M1), ZI, PO, and PSV were anatomically confirmed. The projection to VTA remains putative. These findings suggest that VPM plays a complex role in shaping sensory information flow and sensorimotor transformations within the thalamus.

PO exhibits excitatory connections with RT (nRT), VPM, bfd, and Mop (M1). Uncategorized connections were also identified between ZI. A connection toward SC was seen only in wild mice. The connections targeting VPM were anatomically confirmed, whereas projections toward ZI remain putative.

Inhibitory connections originating from RT (nRT) target ZI, PO, SC, and VPM. Connections in wild mice were shown to target VTA, SI, MOp (M1), bfd, and VII. All connections originating from RT (nRT) were results found in an experiment with a specificity below 75% specificity; consequently, they remain putative.

While inhibition of the somatosensory thalamus is generally attributed to the activity of ZI and RT (nRT) (Barth´o et al., 2002), our findings reveal the presence of presynaptic inhibitory neurons in VPM, specifically connecting to PO. Further physiological investigations are warranted to determine whether these projections mediate the inhibition of the paralemniscal pathway by the lemniscal pathway.

## Barrel field of the primary somatosensory cortex

The conventional understanding of whisker information processing depicts a bottom-up integration followed by a top-down propagation of neural activity, ultimately leading to the activation of facial muscles. However, our study reveals a more nuanced picture, demonstrating a bidirectional flow of information, with top-down regulation of sensory information from Bfd to the brainstem and thalamus through both excitatory and inhibitory monosynaptic connections.

Bfd extends long-range connections to lower-level structures within the whisker system. Parallel excitatory and inhibitory pathways target MOp (M1), ZI, PO, SC, VPM, PPN, SPVc, SPVi and RT (nRT). Additionally, VTA, VII, PSV, and SPVo are excited by bfd, and an uncategorized connection targeting SI was identified.

All new connections originating from bfd were anatomically confirmed; those include PPN, VTA, SI, VII, and SPVo projections, demonstrating top-down modulation of the trigeminal nucleus and facial motor nucleus by Bfd.

## Primary Motor cortex

Primary motor cortex extensively targets nuclei across the cerebellar cortex and subcortical regions (see e.g., Bisman et al., 2011, Jeong et al., 2016, Muñoz-Castañeda et al., 2021). Our results show that there are parallel (i.e., excitatory and inhibitory) pathways of projections originating from the primary motor cortex and target bfd, PO, PPN, VTA, SC, VPM, RT (nRT), and ZI from Mop (M1). Monosynaptic projections into these target nuclei have been described before (Bisman et al., 2011; Jeong et al., 2016; Muñoz-Castañeda et al., 2021). SI, PSV, SPVo, and SPVc also receive excitatory and inhibitory projections. The connection toward SPVc has been anatomically validated.

In addition to the aforementioned projections, excitatory connections were found to target VII and SPVi. Connections toward LC and DR, however, were witnessed only in wild-type mice. The observations on the parallel feed-forward excitatory and feed-forward inhibitory projections argue that the role of the motor cortical projections might have a differential contribution to neural processing along ascending and descending pathways.

### Superior Colliculus

In the map previously described by Bosman et al. (2011), the superior colliculus contribution to sensorimotor integration in the 18 nuclei map was limited to connections to ZI, PPN, and VII. Our study revealed that the SC not only inhibits these nuclei but is also the source of inhibition toward PO, RT, and DR. PPN and ZI also appear to receive excitatory connections from the SC. Wild-type connections, however, span the entire sub-network except for TM, which doesn't appear to be targeted by the SC. The newly reported connections toward Mop (M1), RT (nRT), and bfd were anatomically confirmed. Projections toward LC and SPVc remain putative.

### Facial motor nucleus

The facial motor nucleus, a key component of the descending motor pathway, is composed of motoneurons and sends commands to the periphery to produce whisker movement (Ashwell, 1982).

In this study, we found anatomically confirmed connections originating from VII targeting the trigeminal nuclei and the SC. These structures, being the first nuclei to integrate whisker information in the brain, are also targeting VII (see section 3.1 Trigeminal nuclei). The interplay between VII and the trigeminal nuclei might be part of a low-level loop integrating sensory information and producing whisker movement without requiring activity from higher structures.

More precisely, the motor nucleus excites PSV, SPVc, and SPVi. Connections that could not be definitively classified as excitatory or inhibitory (i.e., uncategorized) were found to target SPVo, SC, PPN, and DR. The connection toward DR was anatomically validated, while a connection toward PPN remains putative.

Reciprocal connections between the trigeminal nuclei and VII should be further investigated to understand the role of such low-level loops in the whisker system of the rodent. As VII does not send any inhibitory connections, based on the currently available data, one can assume the purely excitatory nature of the projections to SC. The postsynaptic target of the facial motor nucleus projections into SC is not clear. If this connection targets the sensory area of SC, this suggests the possibility of an efference copy, a signal sent to SC to inform it about the action taken by the whisker and therefore, to adjust its internal representation based on previous movements. The same hypothesis can be made for the trigeminal nuclei interaction.

## Zona Incerta

The zona incerta is described as one of the main sources of inhibition in the rodent whisker system (Venkataraman et al., 2021). Therefore, unsurprisingly, we found inhibitory presynaptic cells projecting to almost all nuclei of the sub-network. These connections were found to target Mop (M1), the thalamic nuclei, PSV, VTA, SI, LC, SC, TM, VII, PPN, RT(nRT,) and DR. Wild-type projections connect to SPVo and SPVi. New connections targeting bfd, PSV, SI, SPVo, VPM, VII, SPVc, and RT (nRT) were anatomically confirmed. A connection toward SPVi, on the other hand, remains putative.

In line with most studies targeting ZI reporting GABAergic connections (Ficalora and Mize, 1989; Nicolelis et al., 1992; Nicolelis et al., 1990), we didn't find any excitatory presynaptic cells in ZI projecting to the sensorimotor system. Furthermore, the extensive connectome of ZI spanning the somatosensory pathway and in particular low-level structures such as the trigeminal nuclei and VII hint at a prominent role played by ZI in low-level sensorimotor integration.

## Neuromodulatory projections

The VTA has a role in learning the association of a whisker stimulus with a potential reward (Esmaeili et al., 2020). Our results revealed that the VTA's contribution to the whisker system's function is not necessarily solely mediated by dopaminergic connections; excitatory presynaptic neurons in the VTA also target other nuclei. The VTA sends excitatory connections to TM, DR, SI, MOp (M1), bfd, ZI, VPM, and RT (nRT). Projections toward SPVo and SPVi were identified, but the transgenic line showing those connections couldn't be categorized as either excitatory or inhibitory. Each of the new connections reported herein towards bfd, SPVo, TM, VPM, RT, and SPVi remains putative.

Cholinergic connections have been hypothesized to play a role in transforming whisker sensations into a motor action (e.g., licking behavior (Esmaeili et al., 2020)). Consequently, it is not surprising to see connections originating from SI that target bfd and Mop (M1). However, as for VTA, we observed a large number of connections, mainly inhibitory, targeting other neuromodulator-releasing nuclei. This shows that SI can regulate the activity of other nuclei in the neuromodulatory system. In particular, SI inhibits PPN, another cholinergic nucleus, TM, VTA, as well as MOp (M1), bfd, ZI, RT (nRT), and DR. One connection with non-specific presynaptic cells was unveiled toward SC. New connections to TM and PPN were anatomically confirmed. The connection toward SC remains putative.

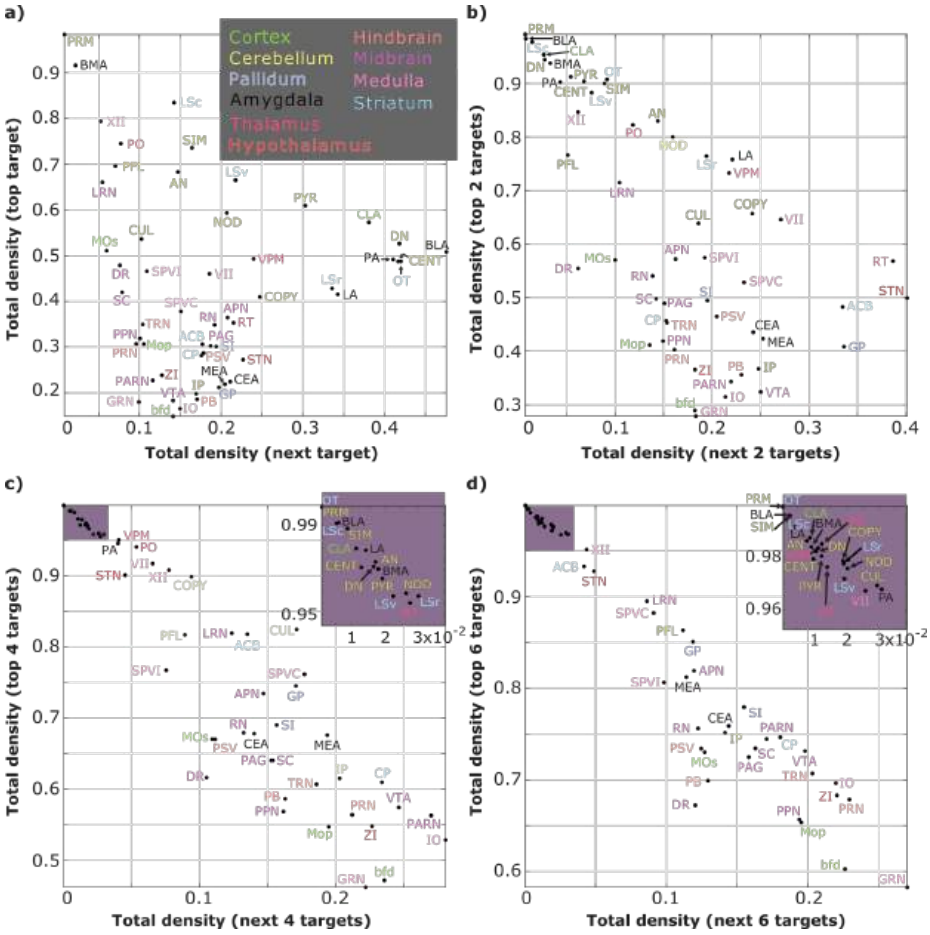


**Figure 5 - Relative density of outgoing connections.** Connections were ordered by the density of outgoing connections and plotted against the x-axis, next densest connections for comparison. This shows the skewness of the distribution. The color scale represents the anatomical structure to which the nuclei belong. a) The density of incoming connections as a function of the density of the next incoming connection (in order of magnitude). b) Same as a), but now for the next 2 connections. c) Same as a), but now for the next 4 connections. d) Same as a), but now for the next 6 connections. Onsets in c) and d) are a zoom-in on the nodes on the top-left corner. FN, LC, TM, and SPVo were not included as no connections originating from those nuclei were found, due to a lack of experiments targeting these nodes.

Excitatory connections from DR were found to target PPN, VTA, SI, MOp(M1), bfd, ZI, RT, SC, VII. Uncategorized connections towards PO, PSV, SPVo, LC, TM, VPM, SPVc, and SPVi were identified. The connections targeting LC and SI were anatomically confirmed. Projections toward TM, ZI, PO, RT, PSV, SPVo, SPVi, and SPVc remain putative.

Inhibitory connections originating within PPN were identified to project to MOp (M1), ZI, PO, bfd, VTA, SI, SC, VII, RT (nRT), and DR. Connections with uncategorized presynaptic cells target PSV, SPVo, LC, TM, VPM, SPVc, and SPVi. PPN targets DR, SI, and RT (anatomically confirmed). Putative connections toward LC, TM, MOp, and bfd were discovered but couldn't be validated.

## Density distribution

To elucidate connectivity patterns within and between structures in the sensorimotor pathway, we conducted an analysis of the density, defined as the percentage of outgoing connections originating from a single source, for each of the 57 nuclei. This examination revealed distinctive connectivity profiles, with the cortex displaying sparse outgoing connections to a multitude of nuclei. The top 6 connections from MOp, MOs, and bfd accounted for at most 78% of the outgoing density (Figure 5), emphasizing the distributed nature of cortical inputs. Contrastingly, the Thalamus exhibited a more specialized pattern, with the top 4 of its outgoing projections accounting for over 94% of all of their projections (Figure 5).

When focusing on the ascending somatosensory pathway, a discernible pattern emerges. The trigeminal nuclei, serving as the initial nodes for whisker information, project sparsely to a diverse array of nuclei. Their top 6 projection targets explain approximately 74% of the outgoing projections (Figure 5). Subsequently, the pathway narrows as it targets the thalamus, projecting to fewer post-synaptic nuclei, with 94% of their outgoing density explained by only 4 projections (Figure 5). Finally, the cortical information flow displays a divergent pattern, with only 60% of outgoing density distributed among 6 nuclei (Figure 5).

This observed pattern along the ascending somatosensory pathway underscores a dynamic process: the brainstem initially projects broadly, supporting a divergent network formation, followed by a sharp reduction of the target nuclei of the thalamus. The pathway then broadens again as cortical projections target a diverse set of nodes. This highlights the thalamus's specific role as a crucial node for routing sensory information. Coupled with inhibitory processes, the thalamus emerges as a key filter, emphasizing its pivotal role in shaping and modulating sensory inputs.

## Network analysis

To assess the role of neuromodulator-releasing nuclei in shaping the network structure and to investigate their potential facilitation of communication within the network, we conducted a permutation test with 10,000 permutations on the 57-nuclei adjacency matrix (Supplemental Figure 2). Comparisons between the

network with and without neuromodulator-releasing nuclei revealed no discernible differences in terms of the distribution of betweenness centrality, degree centrality, nodal clustering, nodal efficiency, or local nodal efficiency. However, a notable distinction emerged in the comparison of nodal shortest path lengths. Specifically, the network without neuromodulator-releasing nuclei exhibited a significantly higher mean value (0.8969 ±0.1093 std) compared to the network with neuromodulators (0.8577 ±0.1063 std; p-value = 0.0011). These findings underscore the nuanced impact of neuromodulator-releasing nuclei on the structural dynamics of the network, particularly in terms of nodal shortest path lengths.

To determine if the network presented small-world properties, we compared the clustering coefficient and the shortest path between a structured graph (ER) and the 57x57 network resulting from our analysis of the Allen Brain Database. This analysis revealed a significantly higher average shortest path for our network (mean ER = 0.7159 ±0.0447 std; mean summary graph = 0.8577 ±0.1063 std; p-value = 9.999×10−5 ) and a significantly higher clustering coef- ficient for our network (mean ER = 0.1241 ±0.288 std; mean summary graph = 0.1726 ±0.1107 std; p-value = 0.0015 ). Given that our network presents a higher shortest path than an Erdos-Renyi graph (see Materials and Methods), we conclude that the studied network doesn't present a small-world structure.

Next, we computed the degree centrality of each nucleus of the network (see section 2.5). This analysis revealed that the majority of connections targeted and originated from the midbrain, which represents 21% of all connections. In particular, DR, PPN, SC, PAG, and RN appear to be hubs. The Medulla, while representing 11% of all connections, appears to have evenly distributed connections along all its nuclei. In the hindbrain, PB is the only hub despite the hindbrain representing 11% of total connections. The striatum appears to concentrate 9% of connection mainly targeting and originating from the only hub of this structure, CP. The cortex represents only 10% of all connections, but MOs, MOp, and bfd appear to be hubs, only CLA doesn't satisfy the criterion. No hubs were identified in either the Cerebellum (10% of connections), the Amygdala (8% of connections), or the Thalamus (5% of connections). In the Hypothalamus (6% of connections), ZI is a hub, and the only node that we considered from the Pallidum (5% of connections), GP, is considered a hub. Amongst the nodes, VTA, GRN, PRN, SI, CEA, and IP appear slightly below the threshold to be considered a hub. More experiments performed on these nuclei might increase their degree centrality (Figure 6).

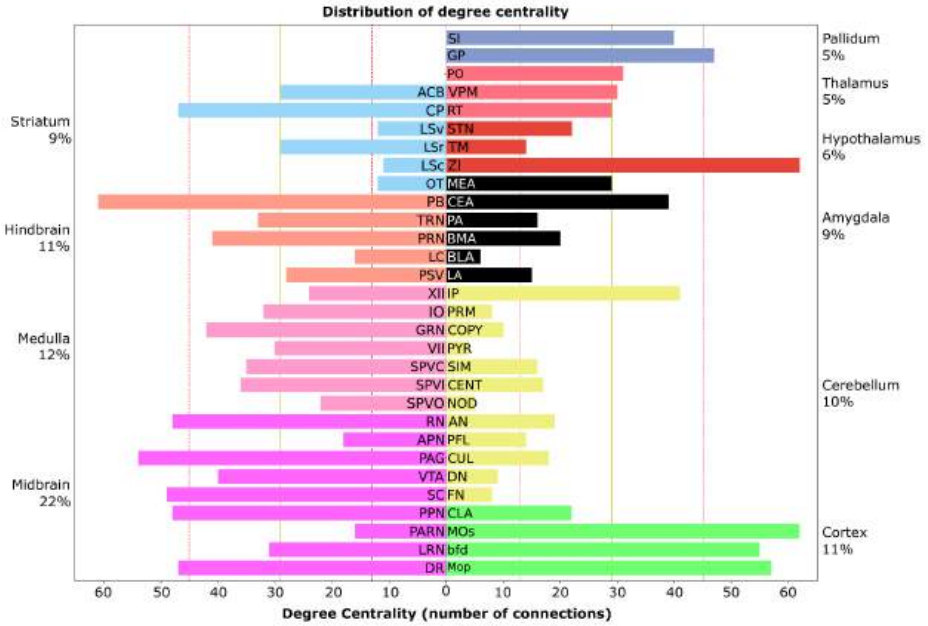


**Figure 6 - Degree centrality of the 57-node network.** The yellow line represents the mean of the distribution, and the red dotted lines represent the mean ± the standard deviation. We consider every node above the mean + standard deviation to be a hub.

## Discussion

We extended the established connectome of the mouse whisker system (Bosman et al., 2011) by incorporating 42 additional connections (Figure 7). We substantiated the presence of these connections through anatomical evidence (Supplementary Material - Fig.6 to Fig.35). Within this framework, we identified cell-type-specific connections and hubs, revealing intricate connectivity patterns along the ascending somatosensory pathway.

We reported a total of 157 connections, constituting 48.4% of all possible connections within this 18x18 subnetwork. Notably, 42 of these connections were not previously described in the literature, to the best of our knowledge. The 18 nuclei were chosen because they were experimentally shown to contribute to sensorimotor integration, which might explain the high level of connectivity described herein. These findings suggest that even if some nuclei were "cut off" from the network, information flow could persist, underscoring the robustness of the network organization. Conversely, the analysis of shortest-path length

highlights the importance of neuromodulator-releasing nuclei in facilitating faster communication between network nodes. The average shortest path length significantly increases in the absence of neuromodulatory nuclei.

The connectivity pattern of the ascending somatosensory pathway follows an hourglass shape, with divergent brainstem projections, followed by convergence of thalamic projections into only a few targets in the cortex. Once the sensory information reaches the cortex, the divergence of projections once again allows the distribution of the sensory information across a large number of nuclei. This is further supported by the results shown from our analysis of outgoing densities (Figure 5, also see Figure 6). In fact, this analysis demonstrates that the trigeminal nuclei are nodes that distribute information beyond the sensory thalamus. Meanwhile, the narrowing of the pathway at the level of the thalamus through denser and fewer connections, together with the presence of inhibition in this structure, might hint at a filtering role of the somatosensory thalamus, as it appears to be highly specialized given the few strong connections originating from this structure (Figure 5). Further widening of the projections in the cortex points to possible parallel processing of sensory information along the downstream nuclei.

## Prominent inhibitory projections in every stage of the ascending pathway

Inhibition is a pervasive phenomenon at every level in the whisker system. Our study reveals inhibitory contributions from nodes not previously identified as sources of inhibition. A notable example is the inhibitory connection from VPM to PO, as illustrated in the Ppp1r17-Cre-NL1 animal line (Supplemental Figure 6). This discovery challenges the notion that RT (nRT) is the sole source of inhibition in the somatosensory thalamus. The inhibitory pathway from VPM may even play a role in disinhibition, given its targeting of RT nRT) and ZI, which, in turn, influence the thalamic nuclei of the ascending somatosensory pathway (Figure 3). This suggests a nuanced filtering or processing role for VPM beyond its traditional role as a relay station.

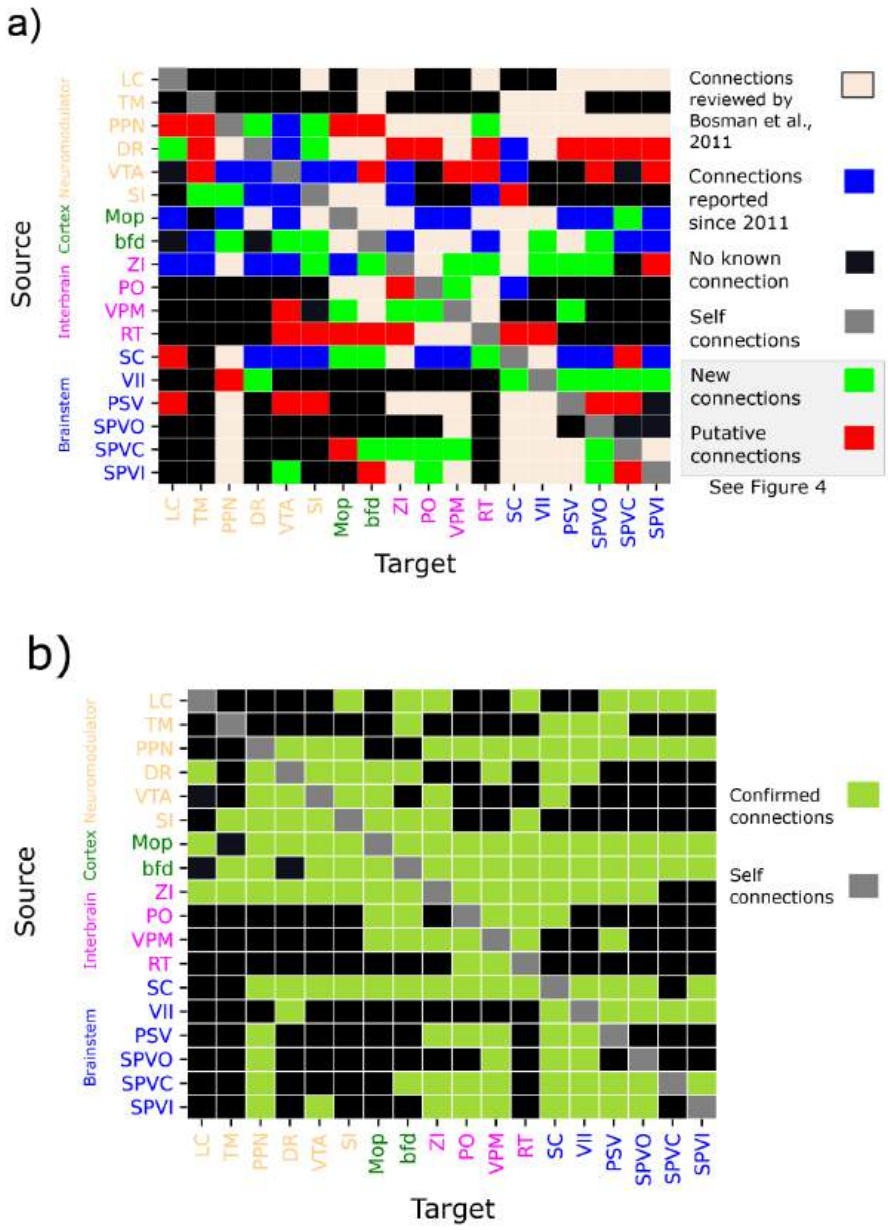


**Figure 7 - The sensorimotor connectivity map of the mouse whisker system.** Summary of data from all animal lines combined. a) A total of 157 connections were found and confirmed either by previous work or through anatomical validation. See Figure 4 for new and putative connections only. b) A binary connectivity matrix that summarizes the pairwise connectivity in the network with only previously reported or anatomically confirmed connections.

Inhibition is not confined to higher levels; it is also observed in the trigeminal nuclei, which send inhibitory connections (Figure 3). While these connections primarily target other trigeminal nuclei, especially VII, they may play a crucial role in modulating whisker movement amplitude following contact with an object during free whisking. Descending projecting connections from higher-level structures could then further modulate whisking behavior during active exploration. This low-level loop in the whisker system underscores the ability of trigeminal nuclei to reduce the whisking amplitude upon contact with an object. Furthermore, ascending inhibitory connections from the somatosensory brainstem (trigeminal nuclei) target VPM and PPN, suggesting a multifaceted role for the trigeminal nuclei beyond a simple relay station in the whisker system. In conclusion, our analysis points to extensive and intricate processing that involves both excitatory and inhibitory projections in the early phases of the somatosensory pathway, as it was previously described in invertebrates for sensorimotor control (Hughes and Celikel, 2019).

## Top-down modulation of sensorimotor integration: a primer

While the structures under consideration play a role in sensorimotor integration, it is plausible that some of the identified connections may not directly contribute to sensorimotor processing. Notably, certain structures (Supplementary Material - Table 2), such as neuromodulator-releasing nuclei, were targeted by only a few, if any, experiments. These connections warrant further investigation to better understand their functional significance. However, to ensure the robustness of our findings and mitigate potential biases from false positives or negatives, we confirmed the connections through anatomical validation (Figure 4).

The Pedunculopontine Nucleus (PPN) is the most interconnected node among neuromodulatory nuclei, it appears to send connections to every node of the somatosensory system, with the exception of the cortex. Interestingly, the somatosensory thalamus doesn't appear to project to PPN. The Dorsal Raphe nucleus (DR) stands out amongst the neuromodulator-releasing nuclei as a node that doesn't receive direct input from the sensory pathway. LC seems to target mainly structures in the low-level sensory system. SI doesn't appear to have a role in the regulation of activity in low-level structures, as no connections toward the trigeminal nuclei or VII could be confirmed. Notably, the neuromodulator-releasing nuclei display a high degree of interconnectedness, allowing for mutual modulation.

Top-down regulation is a prominent feature in the somatosensory system, occurring both between the barrel field cortex (bfd) and the thalamus and between the

thalamus and the trigeminal nuclei. Inhibitory projections, particularly originating in bfd and targeting VPM, RT (nRT), and PO, run in parallel to excitatory connections, allowing for effective top-down modulation of somatosensory thalamic activity. Additionally, a direct top-down connection from VPM to PSV highlights the regulatory influence of the lemniscal pathway.

## Shortcomings of the experimental approach

We used anatomical data collected through serial 2-photon tomography, made available by the Allen Brain Institute, to confirm targets and the source of the monosynaptic connection. This method allows visualization of the expressions of genetically encoded fluorescent proteins in anatomically targeted regions using cell-type-specific or non-specific promoters in various animal lines. However, it's important to note that the spatial resolution of this technique is not sufficient to resolve individual synapses, so it is not always possible to reliably distinguish en-passant projections from actual terminals. Additionally, the sensorimotor circuit outlined in our analysis is derived from anterograde tracing experiments. To further refine our understanding, trans-synaptic tracing of each discussed connection would be beneficial, enabling differentiation between en-passant fibers and terminals and providing cell-type information for the pre- and post-synaptic neurons.

Our results are based on the analysis of data from 732 different experiments. To anatomically confirm the presence of the connections mentioned in our results section and depicted in our summary map (Figure 7), we employed two-photon tomography imaging in brain slices. However, challenges arose during the alignment of the normalized brain atlas to each image due to variations in cut angles. Furthermore, tissue alterations caused by cuts, such as compression, and potential tissue shrinkage induced by the fixation solution injection added complexity to the alignment process. The inherent discretization of imaging data, in contrast to the continuous nature of data analysis, also presented challenges in achieving accurate alignment between the normalized brain and imaging data.

Finally, our analysis relies entirely on the Allen Brain database annotation and only integrates structures available in the database. For instance, a structure such as the nucleus basalis of Meynert is considered in this study as a subpart of SI, as it is not presented separately in the database. We are, therefore, limited to the granularity of analysis allowed by the Allen Brain database, thus, some of the structures presented in previous works (Bosman et al., 2011) were not included in this study.

## Are mice small rats?

In their prior study, Bosman et al. (2011) considered connections from various rodent species, encompassing both rats and mice, assuming uniformity across the whisker systems of different rodent subspecies. However, a review by Krubitzer et al. (Krubitzer et al., 2011) highlighted significant anatomical differences in rodents, particularly between rats and mice. Despite these differences, the two species are often treated interchangeably in anatomical structure, sizes, or positions, raising questions about the relevance of employing an average model for the broader category of rodents, where connections are constrained by brain anatomy.

The connections we demonstrate in this study are based on experiments conducted specifically on mice, avoiding the potential constraint imposed by assuming a uniform rodent model. Nevertheless, the original connections we built upon were not observed in studies that differentiated between rats and mice. To thoroughly assess the similarity between the rat and mouse connectomes, further translational anatomical studies will be necessary.

## Conclusions

Leveraging the Allen Brain database, we identified 42 new connections that were anatomically validated and 40 putative connections, categorizing their nature and enhancing our understanding of the subnetwork's connectome. Our analysis emphasizes the role of both low-level structures and neuromodulator-releasing nuclei, revealing the widespread occurrence of inhibition starting from the earliest stages of information processing. While this study provides

a clearer picture of how the sensorimotor pathway integrates whisker information as well as the contributions of the top-down and neuromodulatory circuits, further investigations, including functional studies and testing with additional transgenic lines, are necessary to elucidate the specific roles of each connection in sensorimotor integration. The road to a comprehensive understanding of the rodent whisker system's sensorimotor pathway requires more extensive circuit analysis, including trans-synaptic tracing experiments, particularly with higher granularity on low-level structures and neuromodulator-releasing nuclei, to pave the way for the development of a biologically inspired computational model of the entire network.

# References


[1] Ahissar, E., & Arieli, A. (2001). Figuring Space by Time. Neuron, 32(2), 185–201. https://doi.org/10.1016/s0896-6273(01)00466-4

[2] An, S., Li, X., Deng, L., Zhao, P., Ding, Z., Han, Y., ... & Gong, H. (2021). A whole-brain connectivity map of VTA and SNc glutamatergic and GABAergic neurons in mice. Frontiers in Neuroanatomy, 15, 818242.

[3] Aransay, A. M., Rodríıguez-López, C., García-Amado, M. A., Clascá, F., & Prensa, L. (2015). Long-range projection neurons of the mouse ventral tegmental area: a single-cell axon tracing analysis. Frontiers in Neuroanatomy, 9. https://doi.org/10.3389/fnana.2015.00059

[4] Ashwell KW. The adult mouse facial nerve nucleus: morphology and musculotopic organization. J Anat. 1982 Oct;135(Pt 3):531-8. PMID: 7153172; PMCID: PMC1169402.

[5] Azarfar, A., Calcini, N., Huang, C., Zeldenrust, F., & Celikel, T. (2018). Neural coding: A single neuron's perspective. Neuroscience & Biobehavioral Reviews, 94, 238-247.

[6] Bartho, P., Freund, T. F., & Acsády, L. (2002). Selective GABAergic innervation of thalamic nuclei from zona incerta. European Journal of Neuroscience, 16(6), 999-1014.

[7] Bellavance, M. A., Takatoh, J., Lu, J., Demers, M., Kleinfeld, D., Wang, F., & Deschˆenes, M. (2017). Parallel inhibitory and excitatory trigemino-facial feedback circuitry for reflexive vibrissa movement. Neuron, 95(3), 673-682.

[8] Benavidez, N. L., Bienkowski, M. S., Zhu, M., Garcia, L. H., Fayzullina, M., Gao, L., ... & Dong, H. W. (2021). Organization of the inputs and outputs of the mouse superior colliculus. Nature communications, 12(1), 4004.

[9] Bosman, L. W. J., Houweling, A. R., Owens, C. B., Tanke, N., Shevchouk, O. T., Rahmati, N., Teunissen, W. H. T., Ju, C., Gong, W., Koekkoek, S. K. E., & de Zeeuw, C. I. (2011). Anatomical Pathways Involved in Generating and Sensing Rhythmic Whisker Movements. Frontiers in Integrative Neuroscience, 5. https://doi.org/10.3389/fnint.2011.00053

[10] Cheng L, Arata A, Mizuguchi R, Qian Y, Karunaratne A, Gray PA, Arata S, Shirasawa S, Bouchard M, Luo P, Chen CL, Busslinger M, Gould- ing M, Onimaru H, Ma Q. Tlx3 and Tlx1 are post-mitotic selector genes determining glutamatergic over GABAergic cell fates. Nat Neurosci. 2004 May;7(5):510-7. doi: 10.1038/nn1221. Epub 2004 Apr 4. PMID: 15064766.

[11] Chiaia, N.L., Rhoades, R.W., Bennett-Clarke, C.A., Fish, S.E. and Killackey, H.P. (1991), Thalamic processing of vibrissal information in the rat. I. Afferent input to the medial ventral posterior and posterior nuclei. J. Comp. Neurol., 314: 201-216. https://doi.org/10.1002/cne.903140202

[12] Daigle TL, Madisen L, Hage TA, Valley MT, Knoblich U, Larsen RS, Takeno MM, Huang L, Gu H, Larsen R, Mills M, Bosma-Moody A, Siverts LA, Walker M, Graybuck LT, Yao Z, Fong O, Nguyen TN, Garren E, Lenz GH, Chavarha M, Pendergraft J, Harrington J, Hirokawa KE, Harris JA, Nicovich PR, McGraw MJ, Ollerenshaw DR, Smith KA, Baker CA, Ting JT, Sunkin SM, Lecoq J, Lin MZ, Boyden ES, Murphy GJ, da Costa NM, Waters J, Li L, Tasic B, Zeng H. A Suite of Transgenic Driver and Reporter Mouse Lines with Enhanced Brain-Cell-Type Targeting and Functionality. Cell. 2018 Jul 12;174(2):465-480.e22. doi: 10.1016/j.cell.2018.06.035. PMID: 30007418; PMCID: PMC6086366.

[13] Daigle, T. L., Madisen, L., Hage, T. A., Valley, M. T., Knoblich, U., Larsen, R. S., ... & Zeng, H. (2018). A suite of transgenic driver and reporter mouse lines with enhanced brain-cell-type targeting and functionality. Cell, 174(2), 465-480.

[14] Dorocic, I. P., F¨urth, D., Xuan, Y., Johansson, Y., Pozzi, L., Silberberg, G., ... & Meletis, K. (2014). A whole-brain atlas of inputs to serotonergic neurons of the dorsal and median raphe nuclei. Neuron, 83(3), 663-678.

[15] Dunigan, A. I., Swanson, A. G., Olson, D. L., & Roseberry, A. G. (2021). Whole-brain efferent and afferent connectivity of mouse ventral tegmental area melanocortin-3 receptor neurons. Journal of Comparative Neurology, 529(6), 1157–1183. https://doi.org/10.1002/cne.25013

[16] Esmaeili, V., Tamura, K., Foustoukos, G., Oryshchuk, A., Crochet, S., & Petersen, C. C. (2020). Cortical circuits for transforming whisker sensation into goal-directed licking. Current Opinion in Neurobiology, 65, 38-48.

[17] Ficalora, A. S., & Mize, R. R. (1989). The neurons of the substantia nigra and zona incerta which project to the cat superior colliculus are GABA immunoreactive: a double-label study using GABA immunocytochemistry and lectin retrograde transport. Neuroscience, 29(3), 567-581.

[18] Furuta, T., Timofeeva, E., Nakamura, K., Okamoto-Furuta, K., Togo, M., Kaneko, T., & Deschenes, M. (2008). Inhibitory Gating of Vibrissal Inputs in the Brainstem. Journal of Neuroscience, 28(8), 1789–1797. https://doi.org/10.1523/jneurosci.4627-07.2008

[19] Harris JA, Hirokawa KE, Sorensen SA, Gu H, Mills M, Ng LL, Bohn P, Mortrud M, Ouellette B, Kidney J, Smith KA, Dang C, Sunkin S, Bernard A, Oh SW, Madisen L, Zeng H. Anatomical characterization of Cre driver mice for neural circuit mapping and manipulation. Front Neural Circuits. 2014 Jul 10;8:76. doi: 10.3389/fncir.2014.00076. PMID: 25071457; PMCID:PMC4091307.

[20] Hattox, A., Li, Y., & Keller, A. (2003). Serotonin Regulates Rhythmic Whisking. Neuron, 39(2), 343–352. https://doi.org/10.1016/s0896-6273(03)00391-x

[21] Hayashi, H. (1980). Distributions of vibrissae afferent fiber collaterals in the trigeminal nuclei as revealed by intra-axonal injection of horseradish peroxidase. Brain Research, 183 (2), 442–446. https://doi.org/10.1016/0006-8993(80)90478-3

[22] Hemelt, M. E., & Keller, A. (2008). Superior Colliculus Control of Vibrissa Movements. Journal of Neurophysiology, 100(3), 1245–1254. https://doi.org/10.1152/jn.90478.2008

[23] Hooks, B. M., Mao, T., Gutnisky, D. A., Yamawaki, N., Svoboda, K., & Shepherd, G. M. (2013). Organization of cortical and thalamic input to pyramidal neurons in mouse motor cortex. Journal of Neuroscience, 33(2), 748-760.

[24] Hosp, J. A., Pekanovic, A., Rioult-Pedotti, M. S., & Luft, A. R. (2011). Dopaminergic Projections from Midbrain to Primary Motor Cortex Mediate Motor Skill Learning. The Journal of Neuroscience, 31(7), 2481–2487. https://doi.org/10.1523/jneurosci.5411-10.2011

[25] Hughes, S., & Celikel, T. (2019). Prominent Inhibitory Projections Guide Sensorimotor Computation: an invertebrate perspective. BioEssays, 41 (10). https://doi.org/10.1002/bies.201900088

[26] Isa, T., Marquez-Legorreta, E., Grillner, S., & Scott, E. K. (2021). The tectum/superior colliculus is the vertebrate solution for spatial sensory integration and action. Current Biology, 31(11), R741–R762. https://doi.org/10.1016/j.cub.2021.04.001

[27] Jacquin, M. F., Chiaia, N. L., Haring, J. H., & Rhoades, R. W. (1990). Intersubnuclear connections within the rat trigeminal brainstem complex. Somatosensory & motor research, 7(4), 399-420.

[28] Jeong, M., Kim, Y., Kim, J., Ferrante, D. D., Mitra, P. P., Osten, P., & Kim, D. (2016). Comparative three-dimensional connectome map of motor cortical projections in the mouse brain. Scientific reports, 6(1), 1-14.

[29] Kleinfield, D., W. Berg, R. & M. Connor, S. (1999). Invited Review Anatomical loops and their electrical dynamics in relation to whisking by rat, Somatosensory & Motor Research, 16(2), 69-88, DOI:10.1080/08990229970528

[30] Krubitzer, L., Campi, K. L., & Cooke, D. F. (2011). All rodents are not the same: a modern synthesis of cortical organization. Brain Behavior and Evolution, 78 (1), 51–93. https://doi.org/10.1159/000327320

[31] Lam, Y. W., & Sherman, S. M. (2007). Different topography of the reticulothalmic inputs to first- and higher-order somatosensory thalamic relays revealed using photostimulation. Journal of Neurophysiology, 98(5), 2903-2909.

[32] Leão RN, Mikulovic S, Le¨ao KE, Munguba H, Gezelius H, Enjin A, Patra K, Eriksson A, Loew LM, Tort AB, Kullander K. OLM interneurons differentially modulate CA3 and entorhinal inputs to hippocampal CA1 neurons. Nat Neurosci. 2012 Nov;15(11):1524-30. doi: 10.1038/nn.3235. Epub 2012 Oct 7. PMID: 23042082; PMCID: PMC3483451.

[33] Lee, S., Carvell, G. E., & Simons, D. J. (2008). Motor modulation of afferent somatosensory circuits. Nature Neuroscience, 11(12), 1430–1438. https://doi.org/10.1038/nn.2227

[34] Lee, S. H., & Dan, Y. (2012). Neuromodulation of Brain States. Neuron, 76(1), 209–222. https://doi.org/10.1016/j.neuron.2012.09.012

[35] Liu, X., Huang, H., Snutch, T.P. et al. The Superior Colliculus: Cell Types, Connectivity, and Behavior. Neurosci. Bull. 38, 1519–1540 (2022). https://doi.org/10.1007/s12264-022-00858-1

[36] Ma, P. M. (1991). The barrelettes—architectonic vibrissal representations in the brainstem trigeminal complex of the mouse. Normal structural organization. Journal of Comparative Neurology, 309(2), 161-199.

[37] Madisen L, Zwingman TA, Sunkin SM, Oh SW, Zariwala HA, Gu H, Ng LL, Palmiter RD, Hawrylycz MJ, Jones AR, Lein ES, Zeng H. A robust and high-throughput Cre reporting and characterization system for the whole mouse brain. Nat Neurosci. 2010 Jan;13(1):133-40. doi: 10.1038/nn.2467. Epub 2009 Dec 20. PMID: 20023653; PMCID: PMC2840225.

[38] McElvain, L. E., Friedman, B., Karten, H. J., Svoboda, K., Wang, F., Deschênes, M., & Kleinfeld, D. (2018). Circuits in the Rodent Brainstem that Control Whisking in Concert with Other Orofacial Motor Actions. Neuroscience, 368, 152–170. https://doi.org/10.1016/j.neuroscience.2017.08.034

[39] Morrow JA, Collie IT, Dunbar DR, Walker GB, Shahid M, Hill DR. Molecular cloning and functional expression of the human glycine transporter GlyT2 and chromosomal localisation of the gene in the human genome. FEBS Lett. 1998 Nov 20;439(3):334-40. doi: 10.1016/s0014-5793(98)01390-8. PMID: 9845349.

[40] Muñoz-Castañeda, R., Zingg, B., Matho, K.S. et al. Cellular anatomy of the mouse primary motor cortex. Nature 598, 159–166 (2021). https://doi.org/10.1038/s41586-021-03970-w

[41] Nicolelis, M. A., Chapin, J. K., & Lin, R. C. (1992). Somatotopic maps within the zona incerta relay parallel GABAergic somatosensory pathways to the neocortex, superior colliculus, and brainstem. Brain research, 577(1), 134-141.

[42] Nicolelis, M., & Chapin, J. (1994). Spatiotemporal structure of somatosensory responses of many-neuron ensembles in the rat ventral posterior medial nucleus of the thalamus. The Journal of Neuroscience, 14(6), 3511–3532.https://doi.org/10.1523/jneurosci.14-06-03511.1994

[43] Oh, S. W., Harris, J. A., Ng, L., Winslow, B., Cain, N., Mihalas, S., … & Zeng, H. (2014). A mesoscale connectome of the mouse brain. Nature, 508(7495), 207-214.

[44] Parolari, L. (2020). Dissection of Neurons and Circuits Involved in Regulating Innate Behaviors, Movement and Higher Cognitive Functions in Mice.

[45] Pinault, D., Bourassa, J., & Deschênes, M. (1995). The axonal arborization of single thalamic reticular neurons in the somatosensory thalamus of the rat. European Journal of Neuroscience, 7 (1), 31–40. https://doi.org/10.1111/j.1460-9568.1995.tb01017.x

[46] Plummer, N. W., Chandler, D. J., Powell, J. A., Scappini, E., Waterhouse, B. D., & Jensen, P. (2020). An intersectional Viral-Genetic method for fluorescent tracing of axon collaterals reveals details of noradrenergic locus coeruleus structure. ENeuro, 7(3), ENEURO.0010-20.2020.https://doi.org/10.1523/eneuro.0010-20.2020

[47] Rang, H. P., Dale, M. M., Ritter, J. M., Flower, R. J., & Henderson, G. (2015). Rang and Dale's Pharmacology.

[48] Ruhl DA, Bomba-Warczak E, Watson ET, Bradberry MM, Peterson TA, Basu T, Frelka A, Evans CS, Briguglio JS, Basta T, Stowell MHB, Savas JN, Roopra A, Pearce RA, Piper RC, Chapman ER. Synaptotagmin 17 controls neurite outgrowth and synaptic physiology via distinct cellular pathways. Nat Commun. 2019 Aug 6;10(1):3532. doi: 10.1038/s41467-019-11459-4. PMID: 31387992; PMCID: PMC6684635.

[49] Safran M, Dalah I, Alexander J, Rosen N, Iny Stein T, Shmoish M, Nativ N, Bahir I, Doniger T, Krug H, Sirota-Madi A, Olender T, Golan Y, Stelzer G, Harel A, Lancet D. GeneCards Version 3: the human gene integrator. Database (Oxford). 2010 Aug 5;2010:baq020. Doi: 10.1093/database/baq020. PMID: 20689021; PMCID: PMC2938269.

[50] Lee, E. Y., Hwang, Y. G., & Lee, H. S. (2017). Hypothalamic neuronal origin of neuropeptide Y (NPY) or cocaine- and amphetamine-regulated transcript (CART) fibers projecting to the tuberomammillary nucleus of the rat. Brain Research, 1657, 16-28. https://doi.org/10.1016/j.brainres.2016.11.025

[51] Shao-Ming Lu & Rick C.-S. Lin (1993) Thalamic Afferents of the Rat Barrel Cortex: A Light-and Electron-Microscopic Study Using Phaseolus vulgaris Leucoagglutinin as an Anterograde Tracer, Somatosensory & Motor Research, 10:1, 1-16, DOI: 10.3109/08990229309028819

[52] Smith, J. B., Watson, G. D., Alloway, K. D., Schwarz, C., & Chakrabarti, S. (2015). Corticofugal projection patterns of whisker sensorimotor cortex to the sensory trigeminal nuclei. Frontiers in Neural Circuits, 9, 160040.https://doi.org/10.3389/fncir.2015.00053

[53] Sokhadze, G., Campbell, P. W., & Guido, W. (2019). Postnatal development of cholinergic input to the thalamic reticular nucleus of the mouse. European Journal of Neuroscience, 49(8), 978-989.

[54] Stacey D, Bilbao A, Maroteaux M, Jia T, Easton AC, Longueville S, Nymberg C, Banaschewski T, Barker GJ, B¨uchel C, Carvalho F, Conrod PJ, Desrivi`eres S, Fauth-B¨uhler M, Fernandez-Medarde A, Flor H, Gallinat J, Garavan H, Bokde AL, Heinz A, Ittermann B, Lathrop M, Lawrence C, Loth E, Lourdusamy A, Mann KF, Martinot JL, Nees F, Palkovits M, Paus T, Pausova Z, Rietschel M, Ruggeri B, Santos E, Smolka MN, Staehlin O, Jarvelin MR, Elliott P, Sommer WH, Mameli M, Müller CP, Spanagel R, Girault JA, Schumann G; IMAGEN Consortium. RAS-GRF2 regulates alcohol-induced reinforcement by influencing mesolimbic dopamine neuron activity and dopamine release. Proc Natl Acad Sci U S A. 2012 Dec 18;109(51):21128-33. doi: 10.1073/pnas.1211844110. Epub 2012 Dec 5. PMID: 23223532; PMCID: PMC3529066.

[55] Sumser, A., Mease, R. A., Sakmann, B., & Groh, A. (2017). Organization and somatotopy of corticothalamic projections from L5B in mouse barrel cortex. Proceedings of the National Academy of Sciences, 114(33), 8853-8858. https://doi.org/10.1073/pnas.1704302114

[56] Sun, P., Wang, J., Zhang, M., Duan, X., Wei, Y., Xu, F., ... & Zhang, Y. H. (2020). Sex-related differential whole-brain input atlas of locus coeruleus noradrenaline neurons. Frontiers in Neural Circuits, 14, 53.

[57] Takatoh, J., Park, J. H., Lu, J., Li, S., Thompson, P. M., Han, B. X., ... & Wang, F. (2021). Constructing an adult orofacial premotor atlas in Allen mouse CCF. Elife, 10.

[58] Taniguchi H, He M, Wu P, Kim S, Paik R, Sugino K, Kvitsiani D, Fu Y, Lu J, Lin Y, Miyoshi G, Shima Y, Fishell G, Nelson SB, Huang ZJ. A resource of Cre driver lines for genetic targeting of GABAergic neurons in cerebral cortex. Neuron. 2011 Sep 22;71(6):995-1013. Doi: 10.1016/j.

neuron.2011.07.026. Epub 2011 Sep 21. Erratum in: Neuron. 2011 Dec 22;72(6):1091. Kvitsani, Duda [corrected to Kvitsiani, Duda]. PMID: 21943598; PMCID: PMC3779648.

[59] Tasic B, Menon V, Nguyen TN, Kim TK, Jarsky T, Yao Z, Levi B, Gray LT, Sorensen SA, Dolbeare T, Bertagnolli D, Goldy J, Shapovalova N, Parry S, Lee C, Smith K, Bernard A, Madisen L, Sunkin SM, Hawrylycz M, Koch C, Zeng H. Adult mouse cortical cell taxonomy revealed by single cell transcriptomics. Nat Neurosci. 2016 Feb;19(2):335-46. doi: 10.1038/nn.4216. Epub 2016 Jan 4. PMID: 26727548; PMCID: PMC4985242.

[60] Tritsch NX, Oh WJ, Gu C, Sabatini BL. Midbrain dopamine neurons sustain inhibitory transmission using plasma membrane uptake of GABA, not synthesis. Elife. 2014 Apr 24;3:e01936. doi: 10.7554/eLife.01936. PMID: 24843012; PMCID: PMC4001323.

[61] Uhlén M, Fagerberg L, Hallstr¨om BM, Lindskog C, Oksvold P, Mardinoglu A, Sivertsson ˚A, Kampf C, Sj¨ostedt E, Asplund A, Olsson I, Edlund K, Lundberg E, Navani S, Szigyarto CA, Odeberg J, Djureinovic D, Takanen JO, Hober S, Alm T, Edqvist PH, Berling H, Tegel H, Mulder J, Rockberg J, Nilsson P, Schwenk JM, Hamsten M, von Feilitzen K, Forsberg M, Persson L, Johansson F, Zwahlen M, von Heijne G, Nielsen J, Pont´en F. Proteomics. Tissue-based map of the human proteome. Science. 2015 Jan 23;347(6220):1260419. doi: 10.1126/science.1260419. PMID: 25613900.

[62] Urbain, N., & Deschênes, M. (2007). Motor cortex gates vibrissal responses in a thalamocortical projection pathway. Neuron, 56 (4), 714–725. https://doi.org/10.1016/j.neuron.2007.10.023

[63] Venkataraman, A., Hunter, S. C., Dhinojwala, M., Ghebrezadik, D., Guo, J., Inoue, K., Young, L. J., & Dias, B. G. (2021). Incerto-thalamic modulation of fear via GABA and dopamine. Neuropsychopharmacology, 46(9), 1658-1668. https://doi.org/10.1038/s41386-021-01006-5

[64] Voigts, J., Sakmann, B., & Celikel, T. (2008). Unsupervised Whisker Tracking in Unrestrained Behaving Animals. Journal of Neurophysiology, 100(1), 504–515. https://doi.org/10.1152/jn.00012.2008

[65] Voigts, J., Herman, D., & Celikel, T. (2015). Tactile object localization by anticipatory whisker motion. Journal of Neurophysiology, 113(2), 620–632. https://doi.org/10.1152/jn.00241.2014

[66] Volta M, Viaro R, Trapella C, Marti M, Morari M. Dopamine-nociceptin/orphanin FQ interactions in the substantia nigra reticulata of hemiparkinsonian rats: involvement of D2/D3 receptors and impact on nigro-thalamic neurons and motor activity. Exp Neurol. 2011 Mar;228(1):126-37. doi: 10.1016/j.expneurol.2010.12.024. Epub 2011 Jan 6. PMID: 21215744.

[67] Vitrac, C., & Benoˆıt-Marand, M. (2017). Monoaminergic modulation of motor cortex function. Frontiers in Neural Circuits, 11. https://doi.org/10.3389/fncir.2017.00072

[68] Wang, J., Wang, X., Xia, M., Liao, X., Evans, A., & He, Y. (2015). GRETNA: a graph theoretical network analysis toolbox for imaging connectomics. Frontiers in human neuroscience, 9, 386.

[69] Wang, Q., Ding, S. L., Li, Y., Royall, J., Feng, D., Lesnar, P., Graddis, N., Naeemi, M., Facer, B., Ho, A., Dolbeare, T., Blanchard, B., Dee, N., Wakeman, W., Hirokawa, K. E., Szafer, A., Sunkin, S. M., Oh, S. W., Bernard, A., . . . Ng, L. (2020). The Allen Mouse Brain Common Coordinate Framework: A 3D Reference Atlas. Cell, 181(4), 936–953.e20. https://doi.org/10.1016/j.cell.2020.04.007

[70] Watts, D. J., & Strogatz, S. H. (1998). Collective dynamics of 'small-world' networks. nature, 393(6684), 440-442.

[71] Woolsey, T. A., & Van der Loos, H. (1970). The structural organization of layer IV in the somatosensory region (SI) of mouse cerebral cortex: the description of a cortical field composed of discrete cytoarchitectonic units. Brain research, 17(2), 205-242.

[72] Yang, Y., Jiang, T., Jia, X., Yuan, J., Li, X., & Gong, H. (2022). Whole-Brain Connectome of GABAergic Neurons in the Mouse Zona Incerta. Neuroscience Bulletin, 1-15.

[73] Zakiewicz, I. M., Bjaalie, J. G., & Leergaard, T. B. (2014). Brain-wide map of efferent projections from rat barrel cortex. Frontiers in Neuroinformatics, 8. https://doi.org/10.3389/fninf.2014.00005

[74] Zeisel A, Hochgerner H, Lönnerberg P, Johnsson A, Memic F, van der Zwan J, Häring M, Braun E, Borm LE, La Manno G, Codeluppi S, Furlan A, Lee K, Skene N, Harris KD, Hjerling-Leffler J, Arenas E, Ernfors P, Marklund U, Linnarsson S. Molecular Architecture of the Mouse Nervous System. Cell. 2018 Aug 9;174(4):999-1014.e22. Doi: 10.1016/j.cell.2018.06.021. PMID: 30096314; PMCID: PMC6086934.

[75] Zhou, M., Liu, Z., Melin, M.D. et al. A central amygdala to zona incerta projection is required for acquisition and remote recall of conditioned fear memory. Nat Neurosci 21, 1515–1519 (2018). https://doi.org/10.1038/s41593-018-0248-4

# Supplementary Materials

**Supplemental Table 1.** Type of neuron marked by each transgenic line

| TG line | Classification | Source |
|---|---|---|
| A930038C07Rik-Tg1-Cre | Excitatory | Harris et al., 2014 |
| Adycap1-2A-Cre | Uncategorized | Zeisel et al., 2018 |
| Calb2-IRES-Cre | Inhibitory | Taniguchi et al., 2011 |
| Calb1-T2A-dgCre | Inhibitory | Daigle et al., 2018 |
| Cart-IRES2-Cre | Uncategorized | Zeisel et al., 2018 |
| Cart-Tg1-Cre | Uncategorized | Zeisel et al., 2018 |
| Cck-IRES-Cre | Uncategorized | Taniguchi et al., 2011 |
| Chat-IRES-Cre-neo | Uncategorized | Zeisel et al., 2018 |
| Chrna2-Cre-OE25 | Inhibitory | Leão et al., 2012 |
| Cort-T2A-Cre | Inhibitory | Taniguchi et al., 2011 |
| ctgf-T2A-dgCr | Excitatory | Tasic et al., 2016 |
| Cux2-CreERT2 | Excitatory | Zeisel et al., 2018 |
| Drd3-Cre-KI196 | Inhibitory | Volta et al., 2011 |
| Efr3a-Cre-NO108 | Uncategorized | Zeisel et al., 2018 |
| Erbb4-T2A-CreERT2 | Inhibitory | Madisen et al., 2010 |
| Gabrr3-Cre-KC112 | Inhibitory | Parolari 2020 |
| Gad2-IRES-Cre | Inhibitory | Taniguchi et al., 2011 |
| Gal-Cre-KI87 | Excitatory | Zeisel et al., 2018 |
| Grik4-Cre | Uncategorized | Zeisel et al., 2018 |
| Htr2a-Cre-KM20 | Excitatory | Rang et al., 2015 |
| Lypd6-Cre-KL156 | Uncategorized | Zeisel et al., 2018 |
| Nos1-CreErt2 | Inhibitory | Taniguchi et al., 2011 |
| Npr3-IRES2-Cre | Excitatory | Daigle et al., 2018 |
| Ntrk1-IRES-Cre | Uncategorized | Zeisel et al., 2018 |
| Ntsr1-Cre-GN220 | Excitatory | Madisen et al., 2010 |
| Oxtr-Cre-ON66 | Uncategorized | Zeisel et al., 2018 |
| Oxtr-T2A-Cre | Uncategorized | |
| Pdzk1ip1-Cre-KD31 | Uncategorized | Van der Togt et al., 1991 |
| Plxnd-Cre-OG | Excitatory | Zeisel et al., 2018 |
| Ppp1r17-Cre-NL1 | Inhibitory | Zeisel et al., 2018 |
| Prkcd-GluCla-CFP-IRES | Uncategorized | Zeisel et al., 2018 |
| Pvalb-IRES-Cre | Inhibitory | Madisen et al., 2010 |
| Rasgrf2-T2A-dCre | Uncategorized | Stacey et al., 2012 |

**Supplemental Table 1.** Continued

| TG line | Classification | Source |
|---|---|---|
| Rbp4-Cre-KI100 | Excitatory | Zeisel et al., 2018 |
| Rorb-IRES-Cre | Uncategorized | Zeisel et al., 2018 |
| Scnn1a-Tg3-Cre | Excitatory | Madisen et al., 2010 |
| Sepw1-Cre-NP39 | Uncategorized | Zeisel et al., 2018 |
| Sim1-Cre-KJ18 | Excitatory | Zeisel et al., 2018 |
| Slc6a3-Cre | Uncategorized | Zeisel et al., 2018 |
| Slc6a4-Cre-ET33 | Uncategorized | Zeisel et al., 2018 |
| Slc6a4-CreERT2-EZ13 | Uncategorized | Zeisel et al., 2018 |
| Slc6a5-Cre-KF10 | Inhibitory | Morrow et al., 1998 |
| Slc17a6-IRES-Cre | Excitatory | Harris et al., 2014 |
| Slc17a8-IRES2-Cre | Excitatory | Tasic et al., 2018 |
| Slc18a2-Cre-OZ14 | Excitatory | Tritsch et al., 2014 |
| Slc32a1-IRES-Cre | Inhibitory | Harris et al., 2014 |
| Sst-IRES-Cre | Inhibitory | Taniguchi et al., 2011 |
| Syt6-Cre-KI148 | Uncategorized | Safran et al., 2010 |
| Syt17-Cre-NO14 | Excitatory | Ruhl et al., 2019 |
| Tlx3-Cre-PL56 | Excitatory | Cheng et al. 2004 |
| Th-Cre-FI172 | Uncategorized | Uhlèn et al., 2015 |

**Supplemental Table 2**. For each structure, this table presents the number of experiments ran (transgenic and wild), the number of transgenic lines tested, the number of transgenic lines showing marked neurons in the considered structures, and the number of transgenic lines showing a connection.

| structure | wild-type experiments | transgenic line experiments | transgenic lines | expressed in number of structures | transgenic line showing connections |
|---|---|---|---|---|---|
| MOp | 8 | 21 | 15 | 13 | 12 |
| ZI | 4 | 15 | 13 | 11 | 11 |
| PO | 3 | 6 | 3 | 3 | 3 |
| bfd | 6 | 40 | 29 | 21 | 16 |
| PSV | 2 | 1 | 2 | 1 | 1 |
| VTA | 2 | 12 | 12 | 9 | 8 |
| SI | 7 | 10 | 8 | 7 | 7 |
| SPVO | 1 | 0 | 0 | 0 | 0 |
| LC | 0 | 0 | 0 | 0 | 0 |
| SC | 7 | 14 | 9 | 7 | 7 |
| TM | 0 | 1 | 1 | 0 | 0 |
| VPM | 3 | 6 | 6 | 5 | 5 |
| VII | 2 | 5 | 4 | 3 | 3 |
| PPN | 0 | 3 | 3 | 2 | 2 |
| SPVC | 3 | 6 | 6 | 5 | 5 |
| SPVI | 2 | 2 | 1 | 1 | 1 |
| RT | 2 | 11 | 7 | 7 | 7 |
| DR | 0 | 9 | 5 | 4 | 4 |

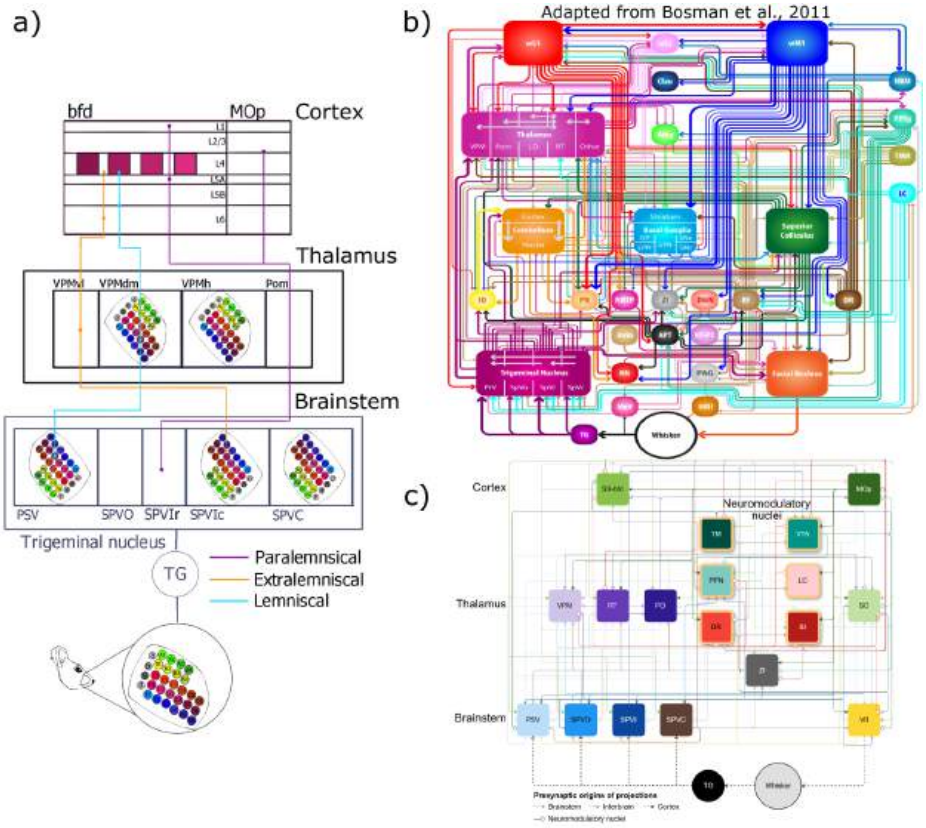


**Supplemental Fig. 1.** a) The whisker pad is organized in a grid-like structure. Each whisker is represented in SPVI, PSV, VPM, and bfd by an agglomerate of neurons organized in a barrel-like shape, respecting the coordinates of the whisker on the whisker pad with rotations. The information from the whisker enters the system through the trigeminal ganglion, projecting to the trigeminal nuclei. Here the information flow is divided into three major pathways: 1) the lemniscal pathway (blue), originating from the barrelettes of P SV, ascending to the barreloids of VPMdm and ending in the barrels of the layer 4 of the somatosensory pathway; 2) the extralemniscal pathway (orange), taking its origin in interbarrelette neurons of SPVI, connecting to VPMvl and targeting the primary somatosensory cortex; and 3) the paralemniscal pathway (purple), taking its source in SPVI, targeting PO, which then targets MOP and bfd. b) The connectivity map presented by Bosman et al. (2011). The 18 nuclei that we focus on in our study present 72 connections in the previous map. c) New connectome composed of 157 connections.

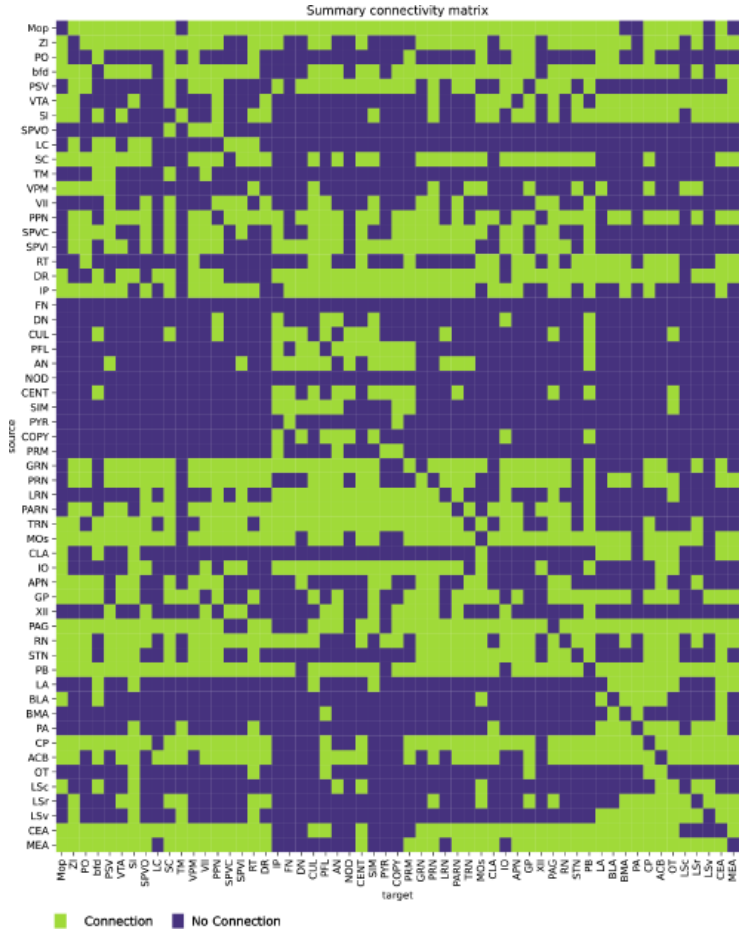


**Supplemental Fig. 2.** Summary of connection between 57 nuclei. MOp: Primary Motor Cortex, Zi: Zona Incerta, PO: Posterior complex of the thalamus, bfd: Barrel field of the primary somatosensory cortex, PSV: nucleus principalis of the trigeminal nucleus, VTA: Ventral tegmental area, SI: Substantia Innominata, SPVO: Spinal nucleus of the trigeminal nucleus oral part, LC: Locus coeruleus, SC: Superior Colliculus, TM: Tuberommaimillary Nucleus, VPM: Ventroposteromedial nucleus of the thalamus, VII: Facial motor nucleus, PPN: Pedunculopontine nucleus, SPVC: Spinal nucleus of the trigeminal nucleus caudal part, SPVI: Spinal nucleus of the trigeminal nucleus interoplaris part, RT: Reticular nucleus of the thalamus, DR: Dorsal Raphe nucleus, IP: Interposed nucleus, FN: Fastigial nucleus, DN: Dentate nucleus, CUL: Culmen, PFL: Paraflocculus, AN: Ansiform lobule, NOD: Nodulus(X), CENT: Central lobule, SIM: Simple lobule, PYR: Pyramus(VIII), COPY: Copula pyramidis, PRM: Paramedian lobule, GRN: Gigantocellular reticular nucleus, PRN: Pontine reticular nucleus, LRN: Lateral reticular nucleus, PARN: Parvicellular reticular nucleus, TRN: Tegmental reticular nucleus, MOs: Secondary motor area, CLA: Claustrum, IO: Inferior olivary complex, APN: Anterior pretectal nucleus, GP: Globus Pallidus, XII: Hypoglossal nucleus, PAG: Periaqueductal gray, RN: Red nucleus, STN: Subthalamic nucleus, PB: Parabrachial nucleus, LA: Lateral amygdalar nucleus, BLA: Basolateral amygdalar nucleus, BMA: Basomedial amygdalar nucleus, PA: Posterior amygdalar nucleus, CP: Caudoputamen, ACB: nucleus accumbens, OT: Olfactory tubercle, LSc: Lateral Septal nucleus caudal part, LSr: Lateral Septal nucleus rostral part, LSv: Lateral Septal nucleus

ventral part, CEA: Central amygdalar nucleus, MEA: Medial amygdalar nucleus.

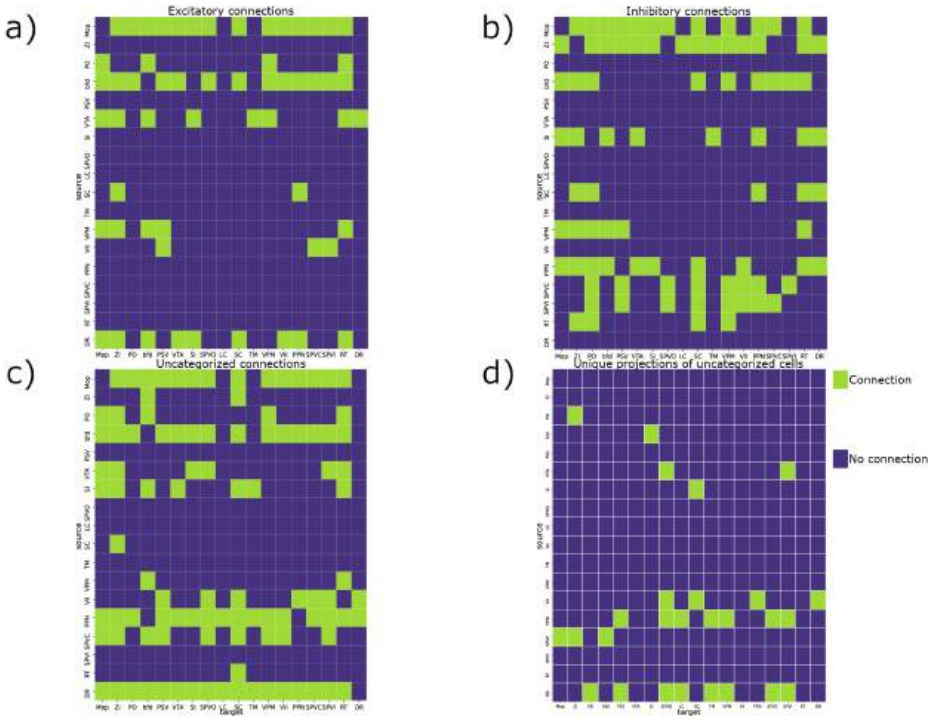


**Supplemental Fig. 3.** a) The excitatory connectivity matrix contains 58 connections. b) The inhibitory connectivity matrix contains 84 connections. c) 101 connections with uncategorized presynaptic cells were unveiled. d) 27 connections were shown only by uncategorized transgenic lines.

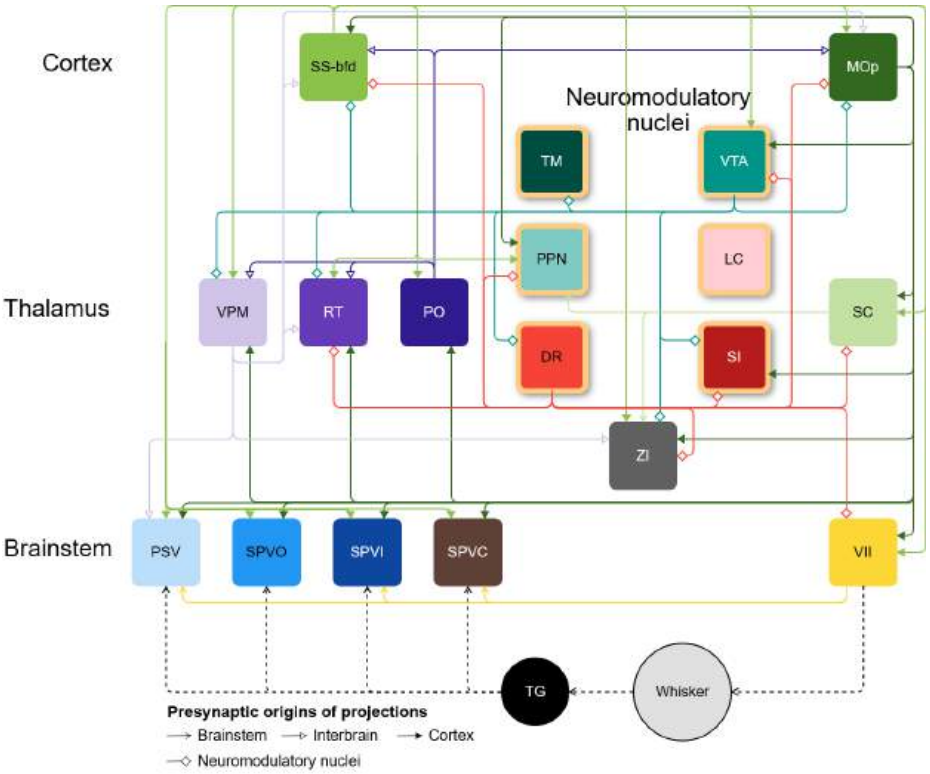


**Supplemental Fig. 4.** The excitatory connectivity map contains 58 connections. The dashed line represents the flow of information outside of the central nervous system. The neuromodulatory structures are represented with yellow borders.

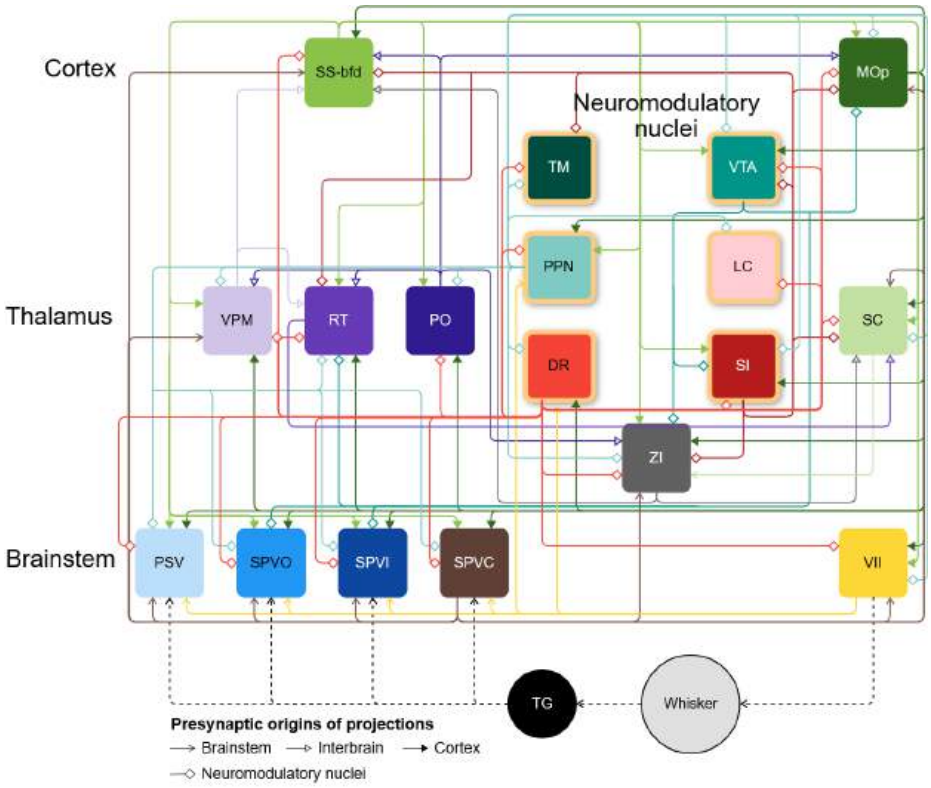


**Supplemental Fig. 5.** 101 connections were revealed by uncategorized transgenic lines. The dashed line represents the flow of information outside of the central nervous system. The neuromodulatory structures are represented with yellow borders.

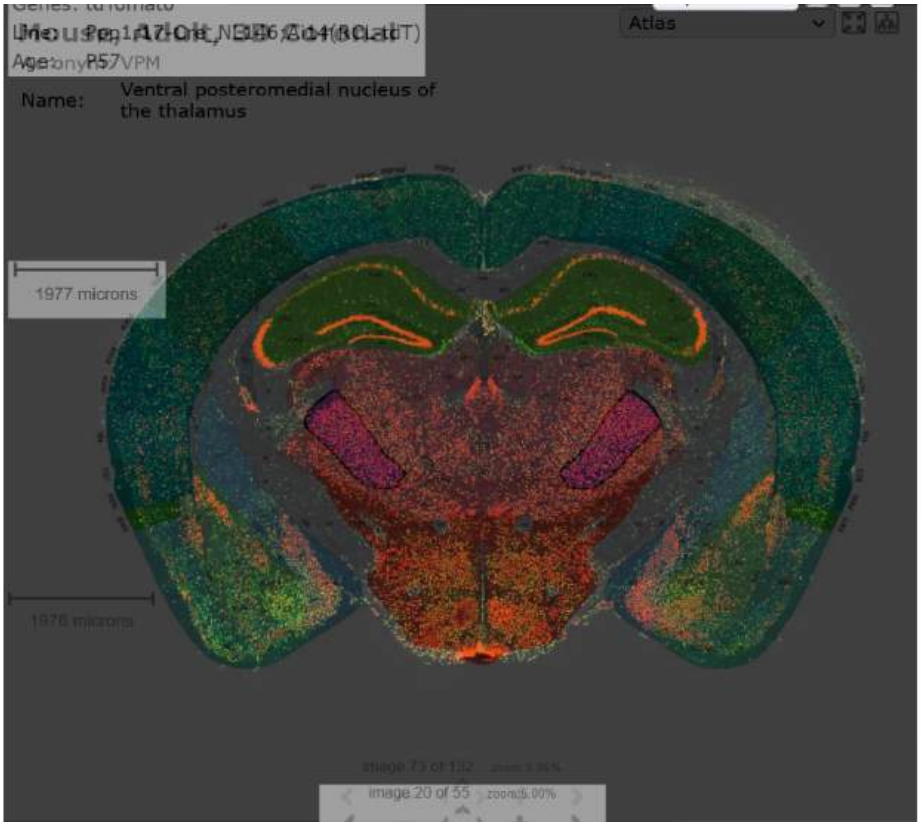


**Supplemental Fig. 6.** Expression in VPM of the transgenic lines PPP1r17 (inhibitory).

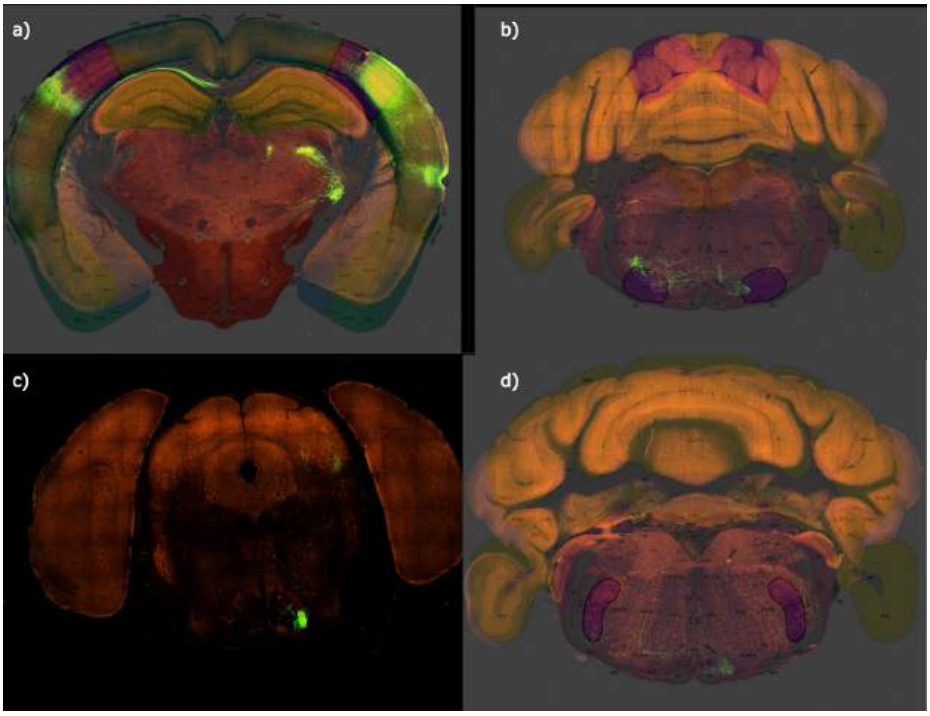


**Supplemental Fig. 7.** a) Injection structure bfd to b) VII, c) PPN, and d) SPVo. Experiment number 112951804, wild-type. The shortcomings of experimental procedures are addressed in the discussion.

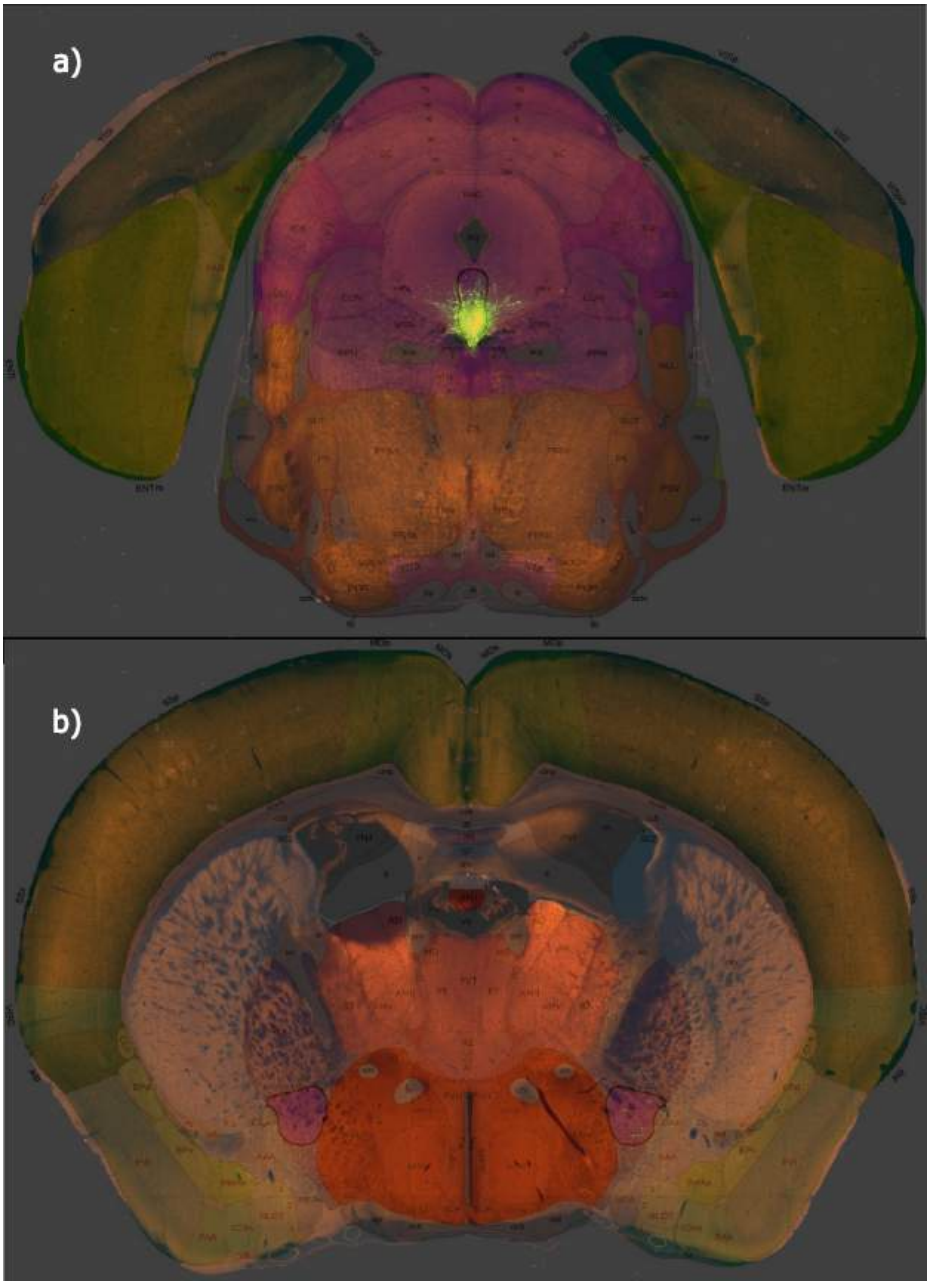


**Supplemental Fig. 8.** a) Injection structure DR to b) SI. Experiment number 582609848, line Esr2-IRES2-Cre. The shortcomings of experimental procedures are addressed in the discussion.

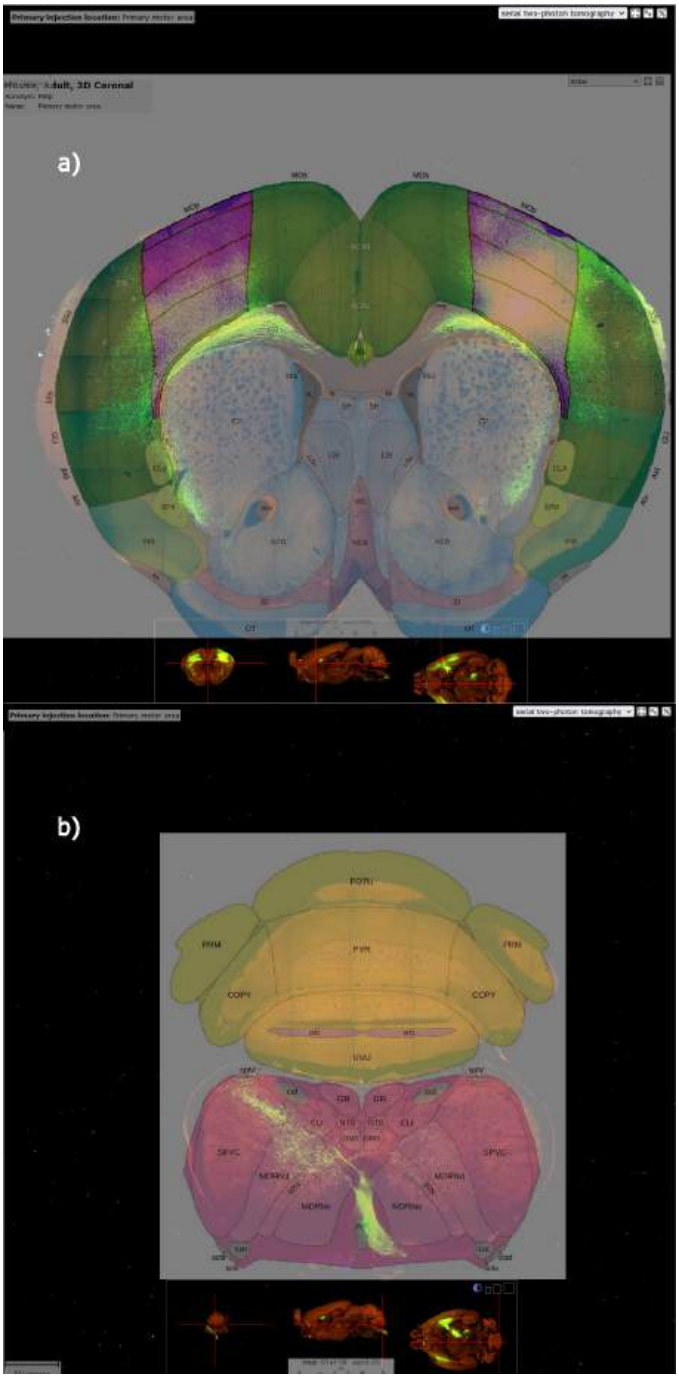


**Supplemental Fig. 9.** a) Injection structure MOp to b) SPVc. Experiment number 100141780, wild-type. The shortcomings of experimental procedures are addressed in the discussion.

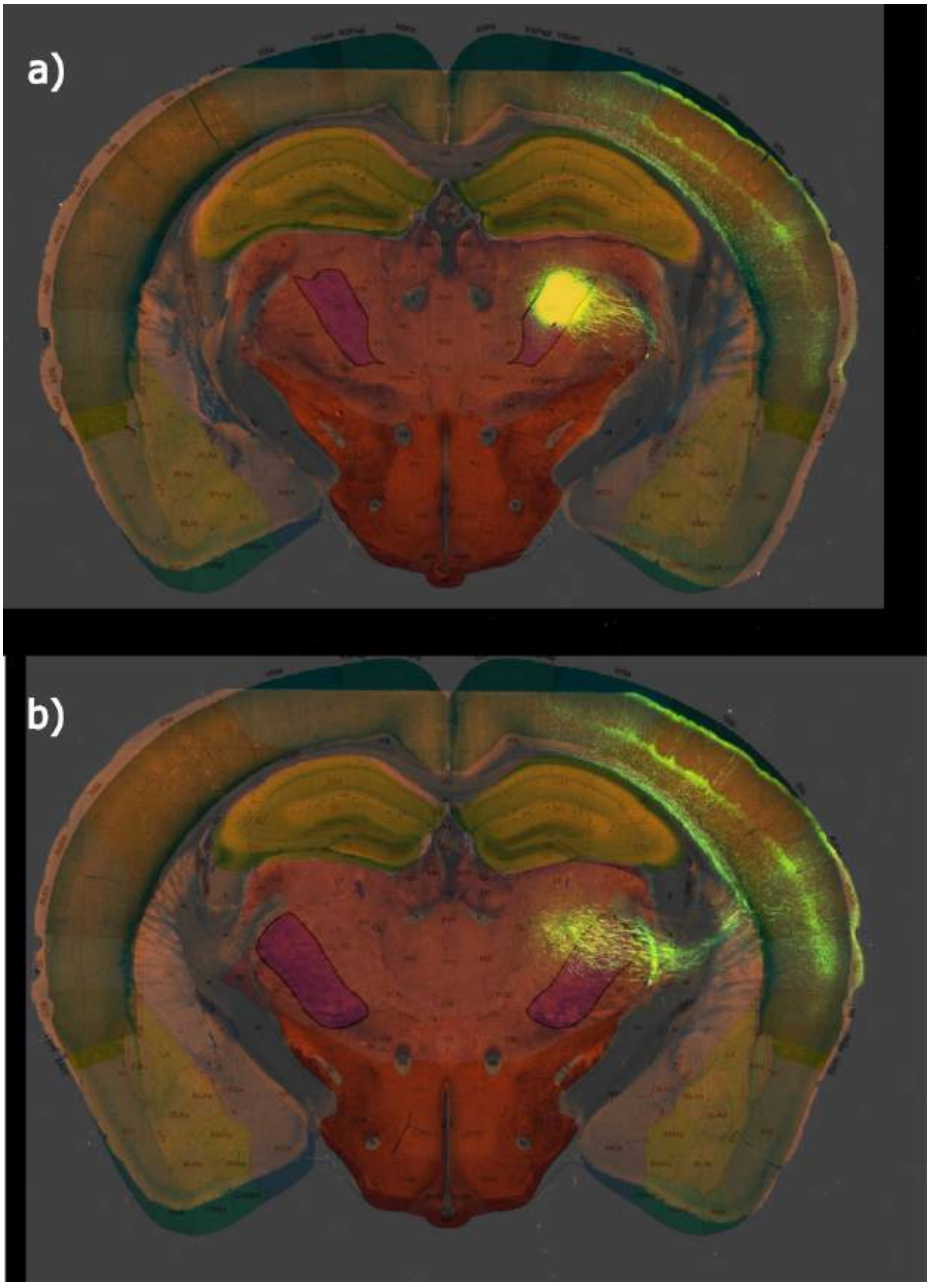


**Supplemental Fig. 10.** a) Injection structure PO to b) VPM. Experiment number 183011353, line Grik4-Cre. The shortcomings of experimental procedures are addressed in the discussion.

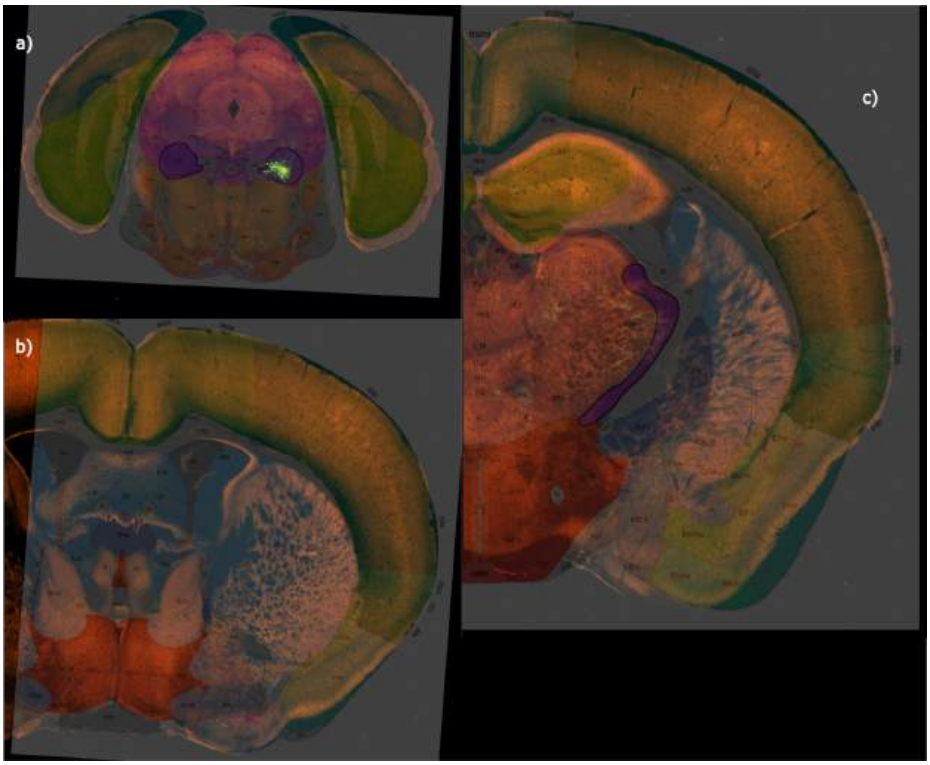


**Supplemental Fig. 11.** a) Injections structure PPN to b) SI and c) RT. Experiment number 264566672, line Chat-IRES-Cre-neo. The shortcomings of experimental procedures are addressed in the discussion.

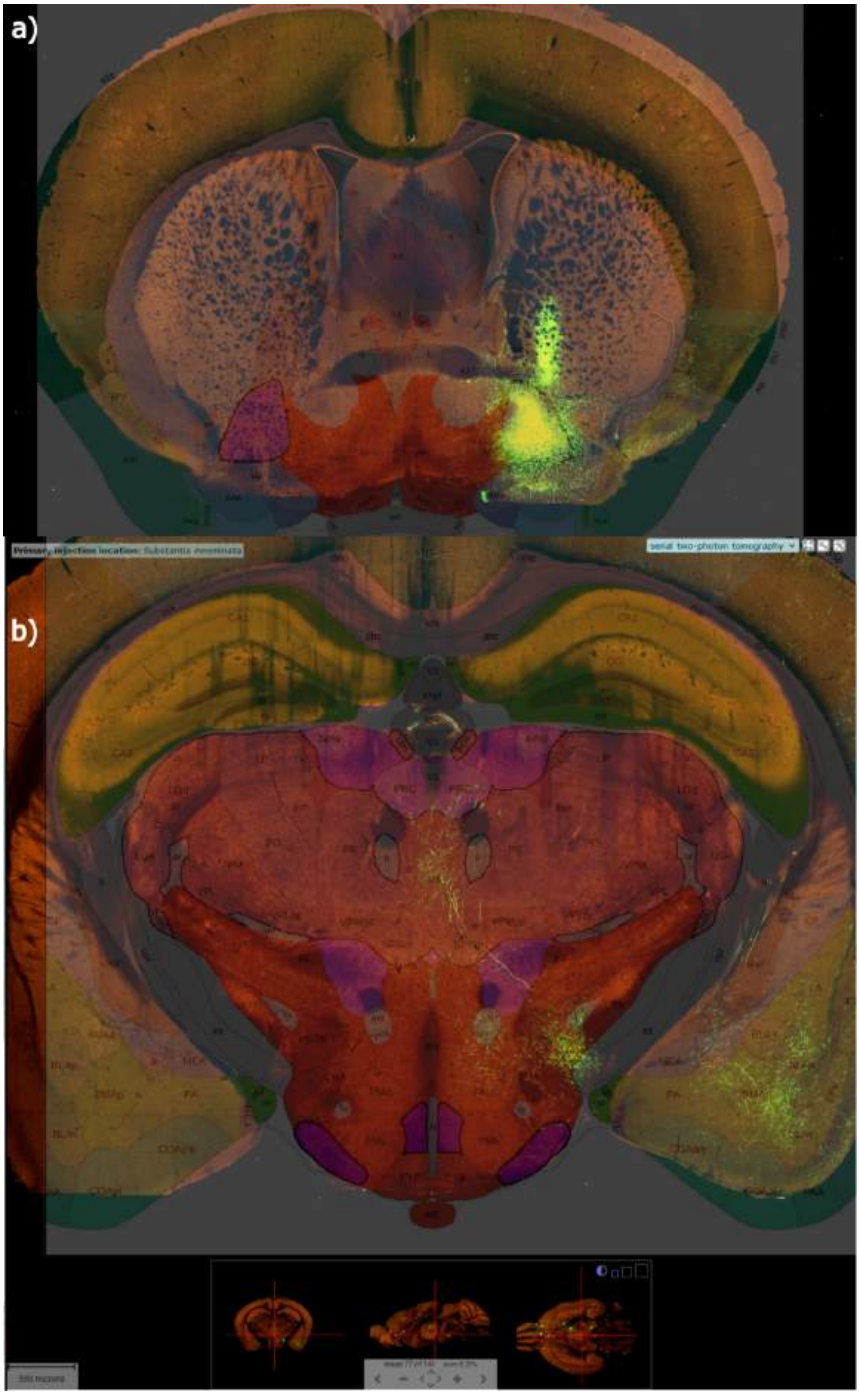


**Supplemental Fig. 12.** a) Injection structure SI to b) TM. Experiment number 305026861, line Drd3-Cre-KI196. The shortcomings of experimental procedures are addressed in the discussion.

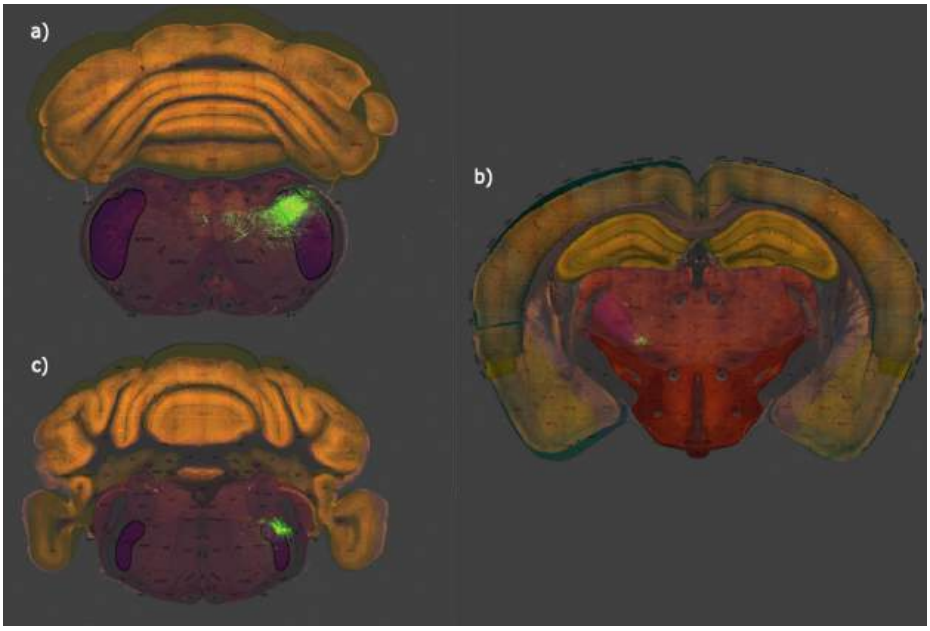


**Supplemental Fig. 13.** a) Injection structure SPVc to b) VPM and c) SPVo. Experiment number 114402050, wild-type. The shortcomings of experimental procedures are addressed in the discussion.

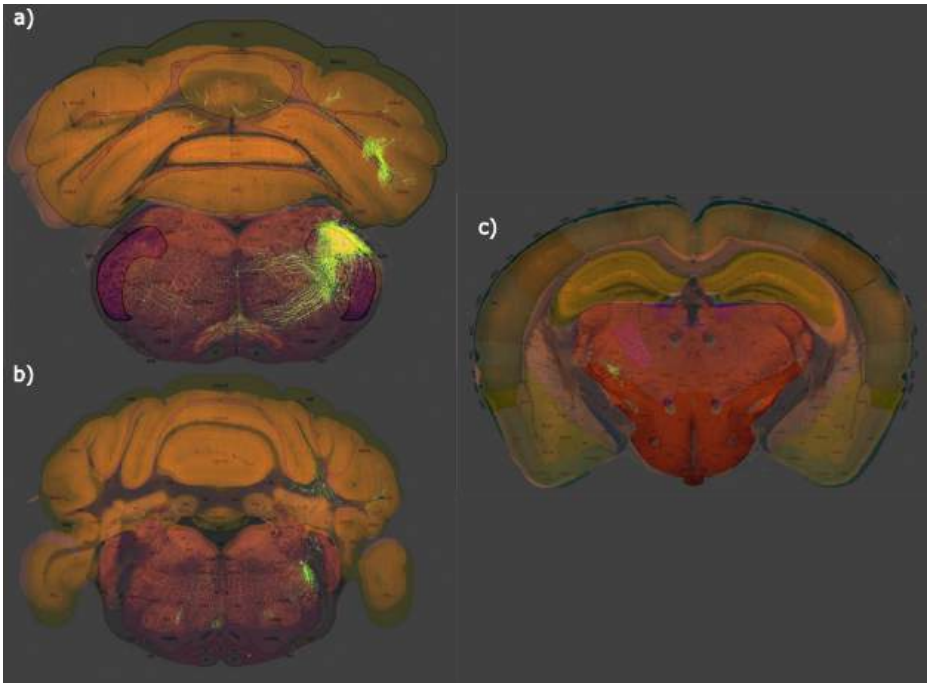


**Supplemental Fig. 14.** a) Injection structure SPVi to b) SPVo and c) PO. Experiment number 272738620, wild-type. The shortcomings of experimental procedures are addressed in the discussion.

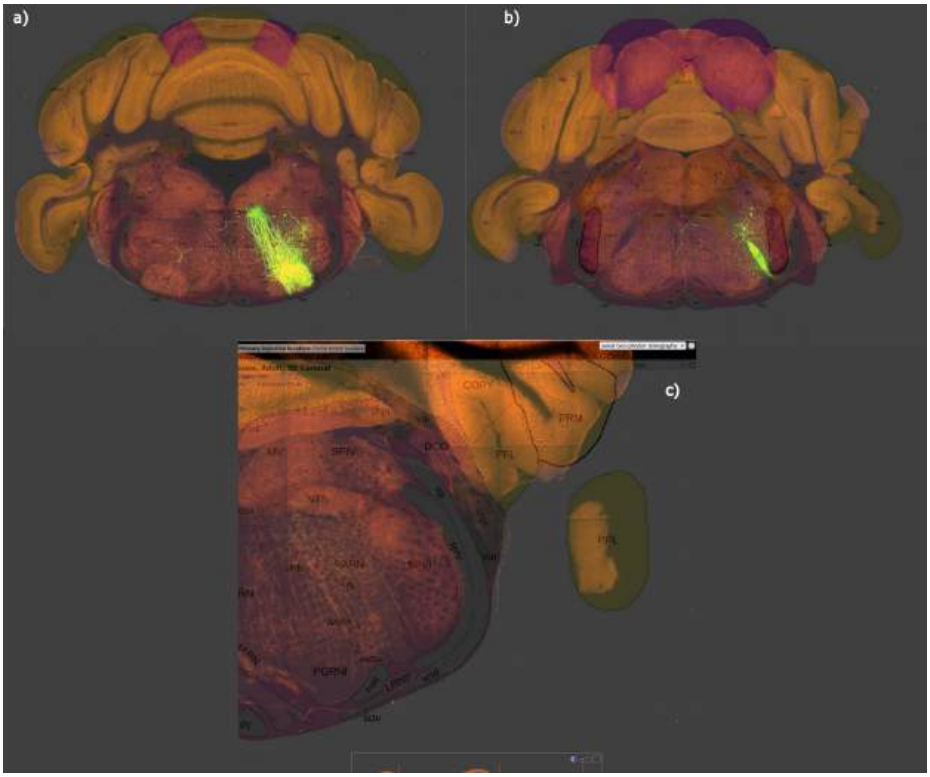


**Supplemental Fig. 15.** a) Injection structure VII to SPVo, b) PSV, and c) to SPVi. Experiment number 177905562, line Scnn1a-Tg2-Cre. The shortcomings of experimental procedures are addressed in the discussion.

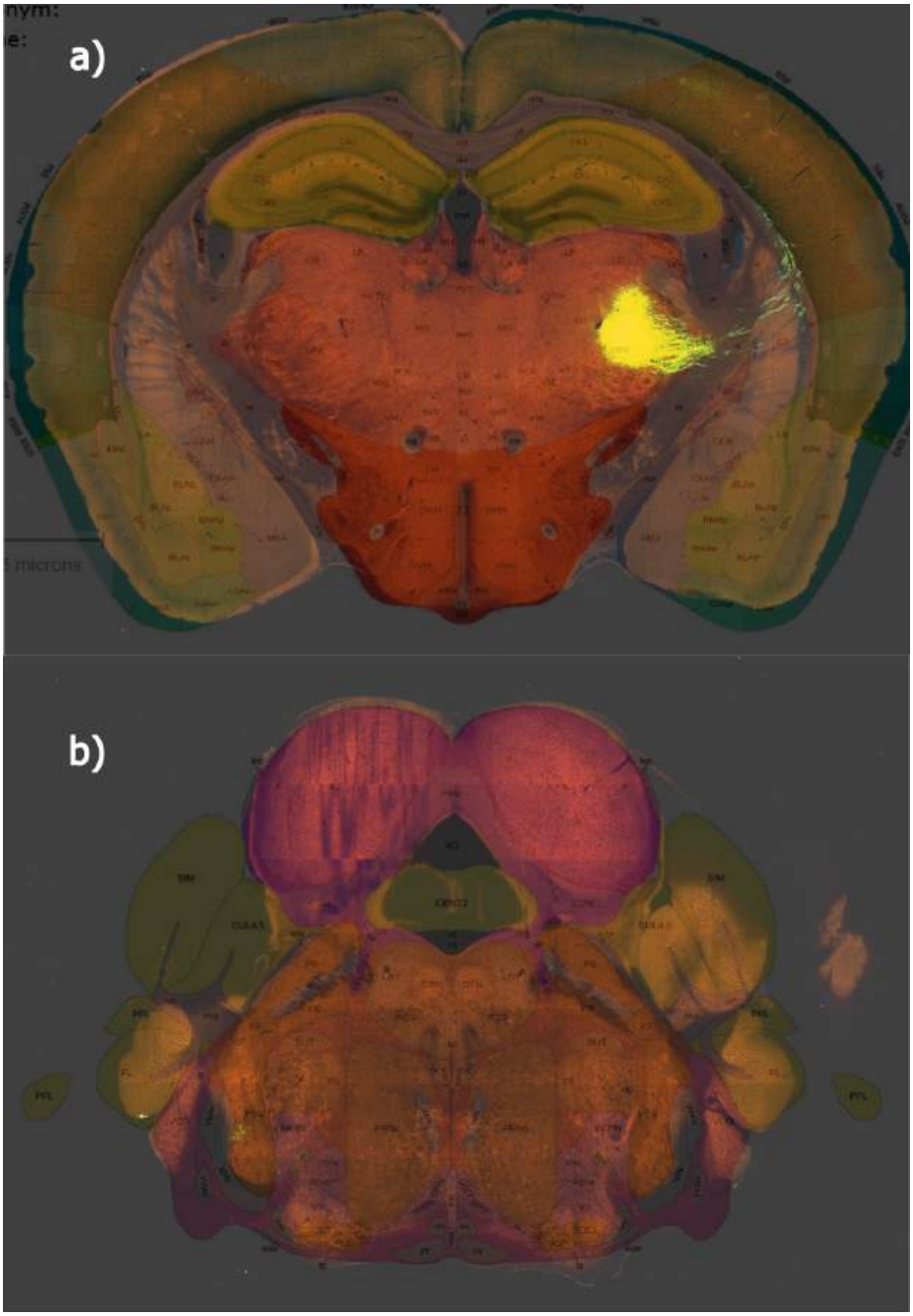


**Supplemental Fig. 16.** a) Injection structure VPM to b) PSV, experiment number 312240825, line Slc17a6-IRES-Cre. The shortcomings of experimental procedures are addressed in the discussion.

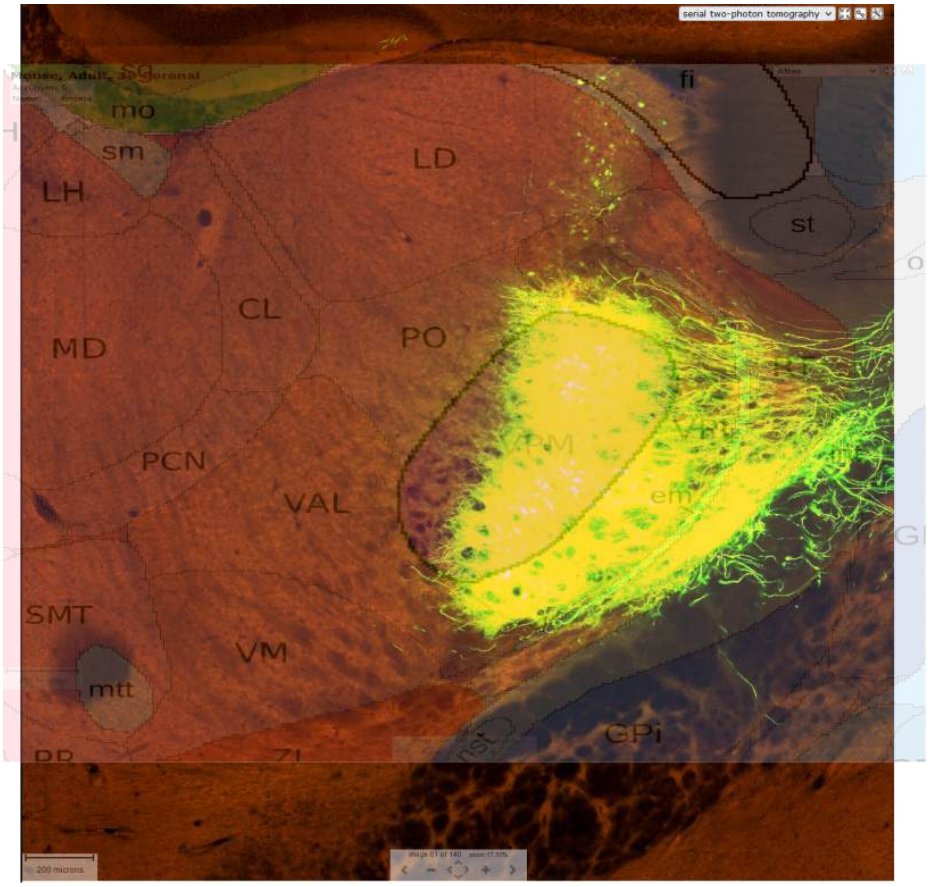


**Supplemental Fig. 17.** Inhibition target and source VPM to PO, experiment number 268206050, line Ppp1r17-Cre-NL146. The shortcomings of experimental procedures are addressed in the discussion.

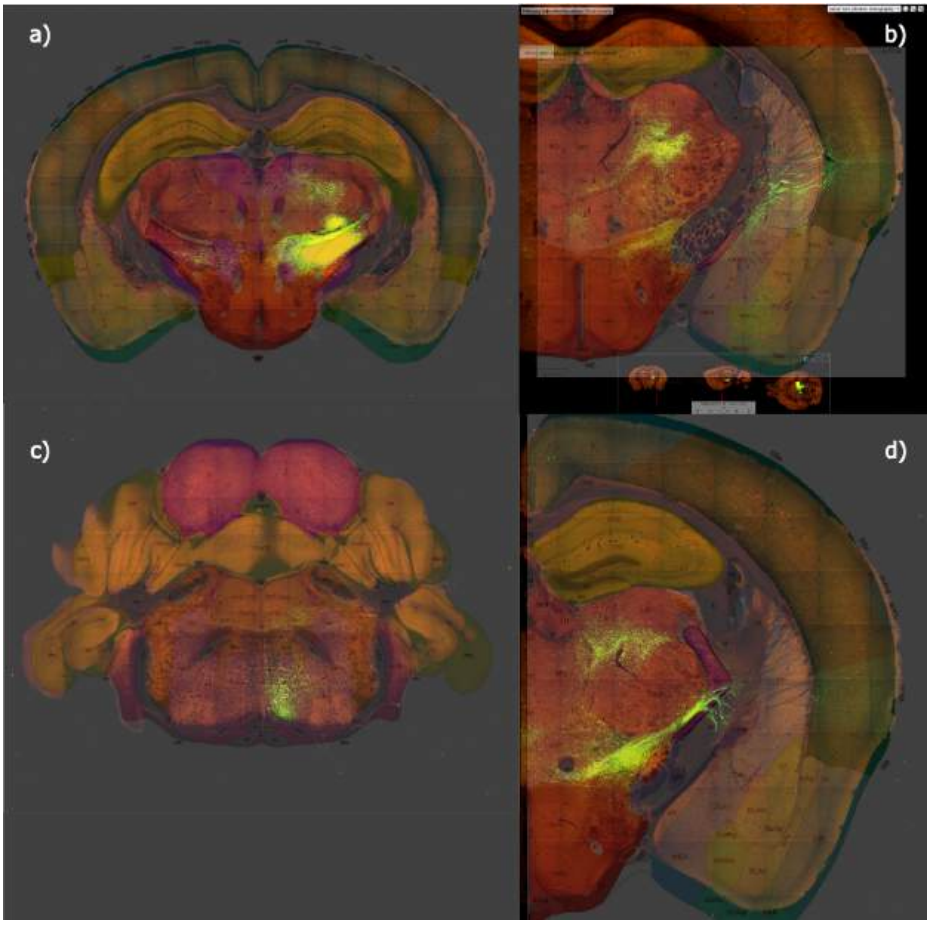


**Supplemental Fig. 18.** a) Injection structure ZI to b) SI, c) PSV, d) RT. Experiment number 113095845, wild-type. The shortcomings of experimental procedures are addressed in the discussion.

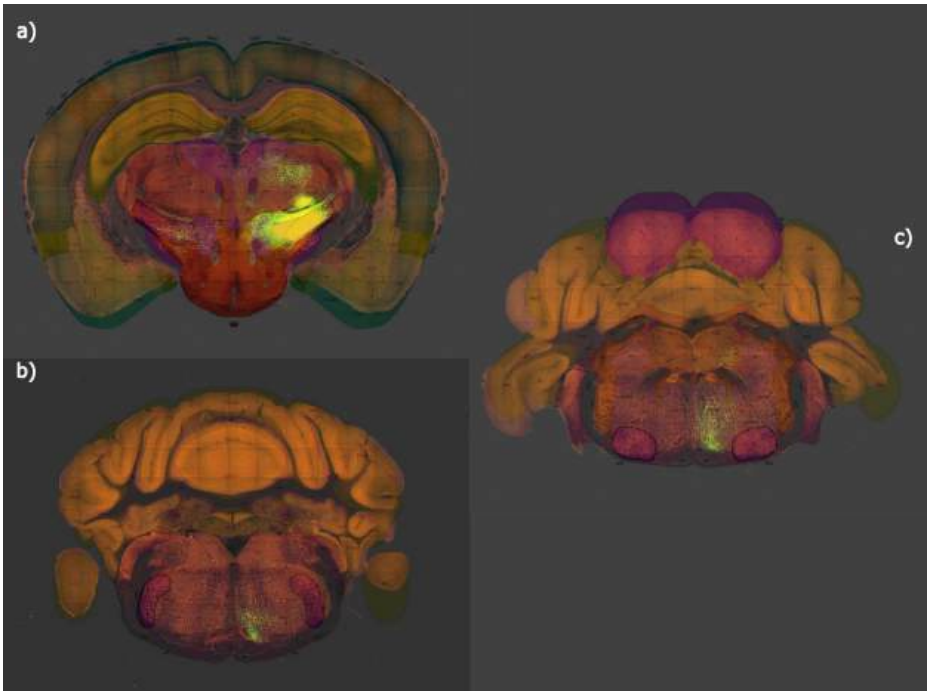


**Supplemental Fig. 19.** a) Injection structure ZI to b) SPVo, and c) VII. Experiment number 113095845, wild-type. The shortcomings of experimental procedures are addressed in the discussion.

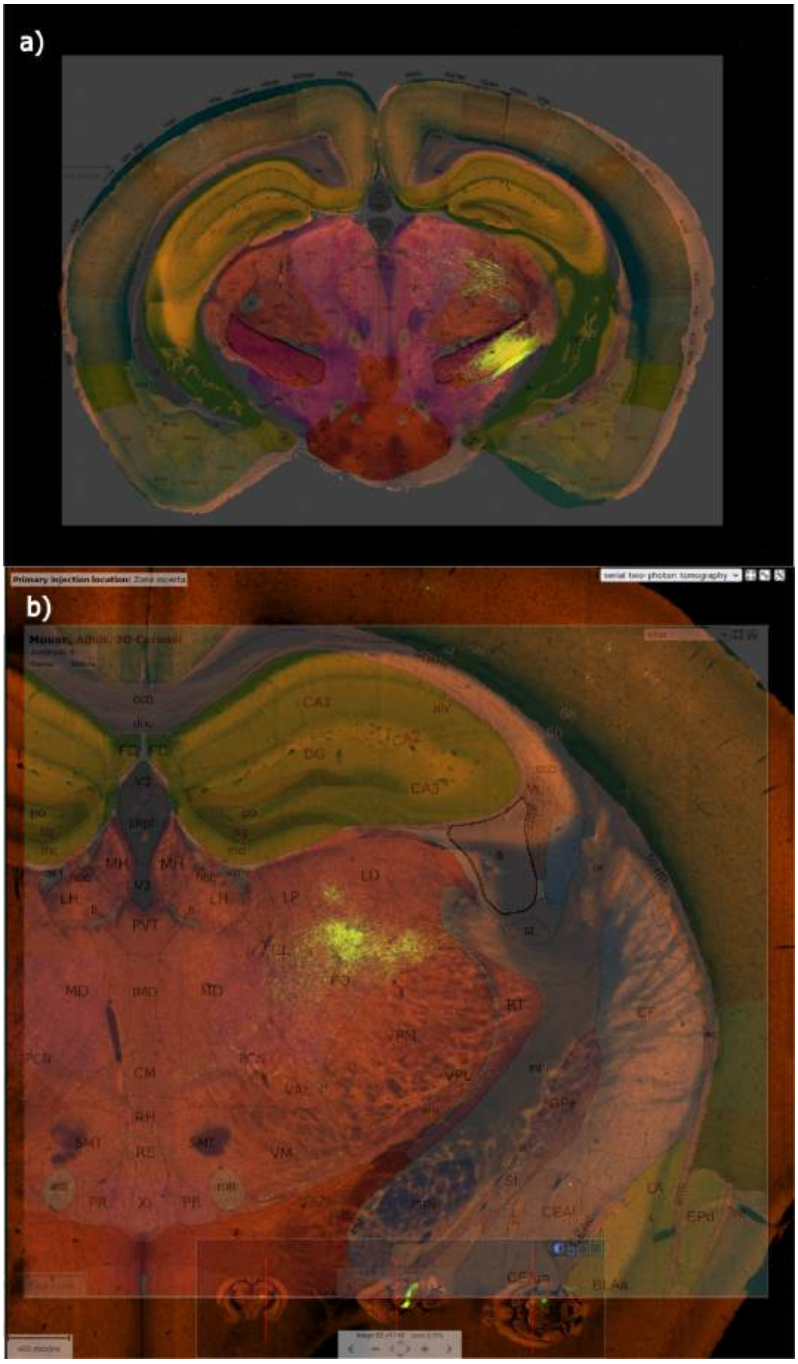


**Supplemental Fig. 20.** a) Injection structure ZI to b) VPM. Experiment number 301539438, line Pvalb-IRES-Cre. The shortcomings of experimental procedures are addressed in the discussion.

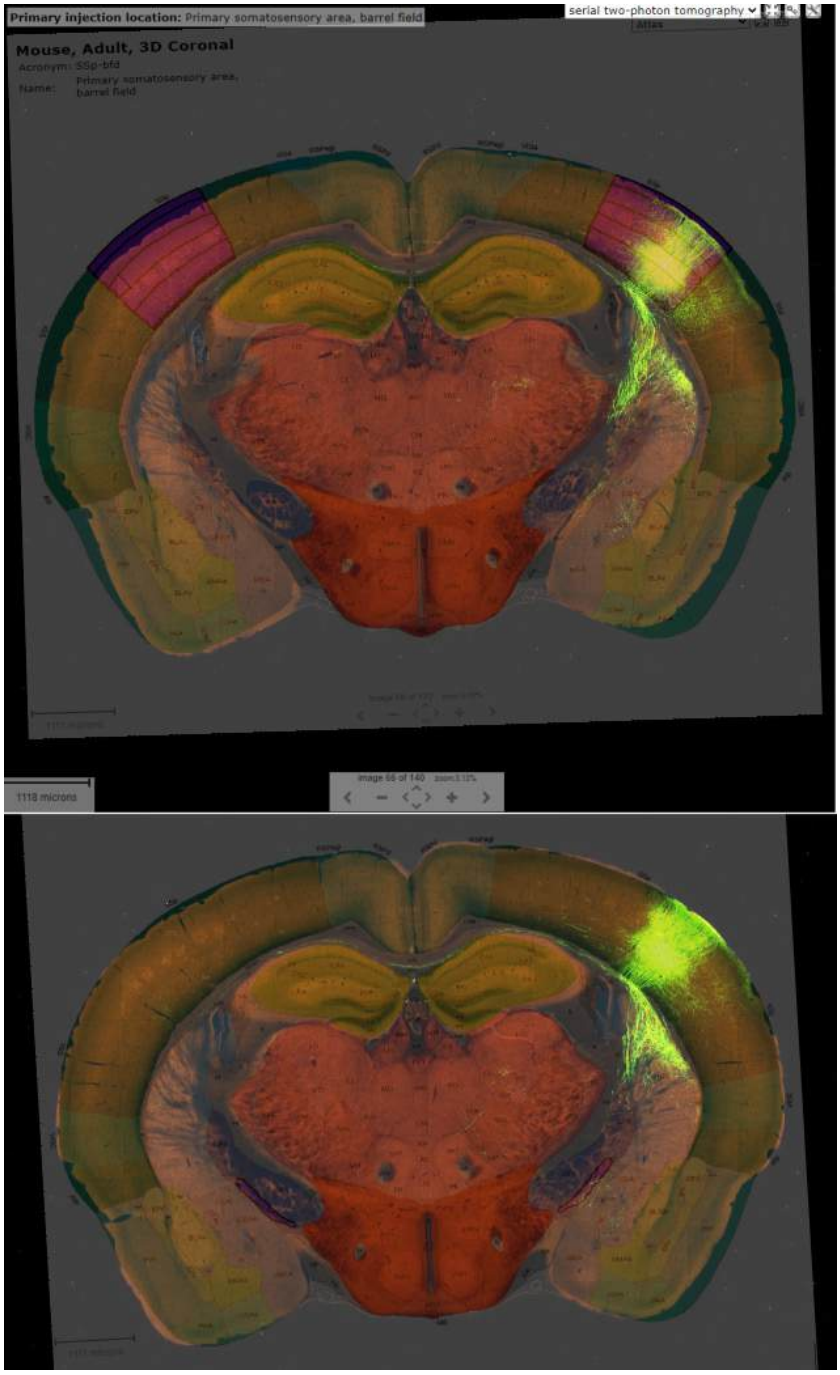


**Supplemental Fig. 21.** a) Injection structure bfd to b) SI. Experiment number 159602992, line Cart-Tg1-Cre. The shortcomings of experimental procedures are addressed in the discussion.

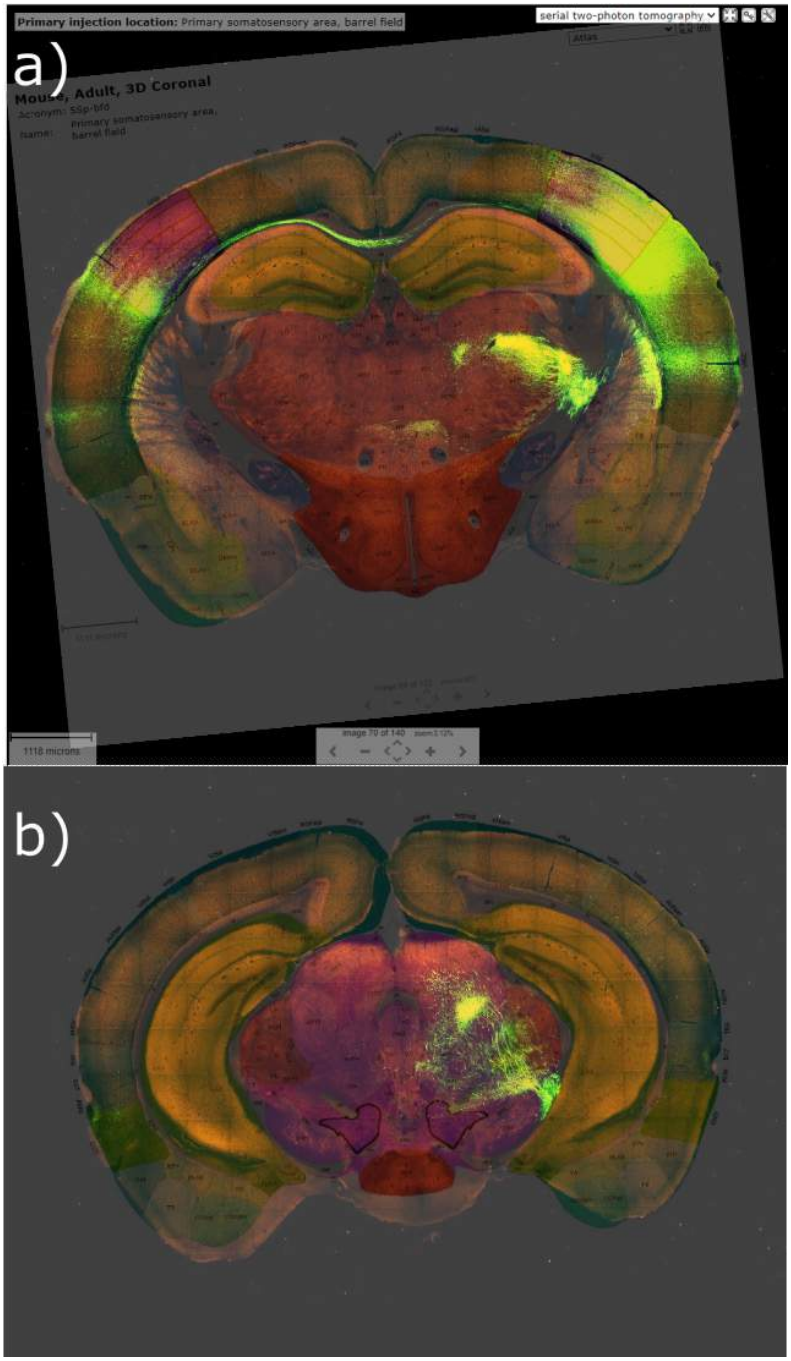


**Supplemental Fig. 22.** a) Injection structure bfd to b) VTA. Experiment number 112951804, wild-type. The shortcomings of experimental procedures are addressed in the discussion.

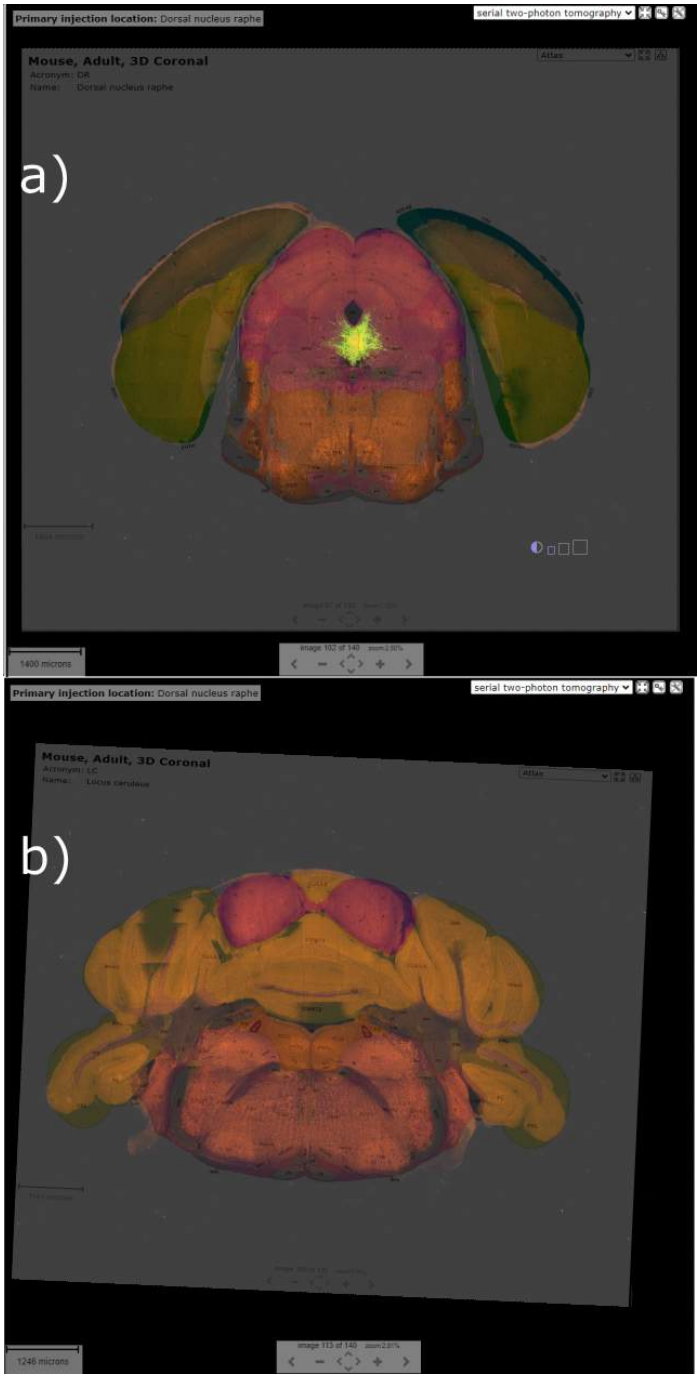


**Supplemental Fig. 23.** a) Injection structure DR to b) LC. Experiment number 547510030, S lc17a8-IRES2-Cre. The shortcomings of experimental procedures are addressed in the discussion.

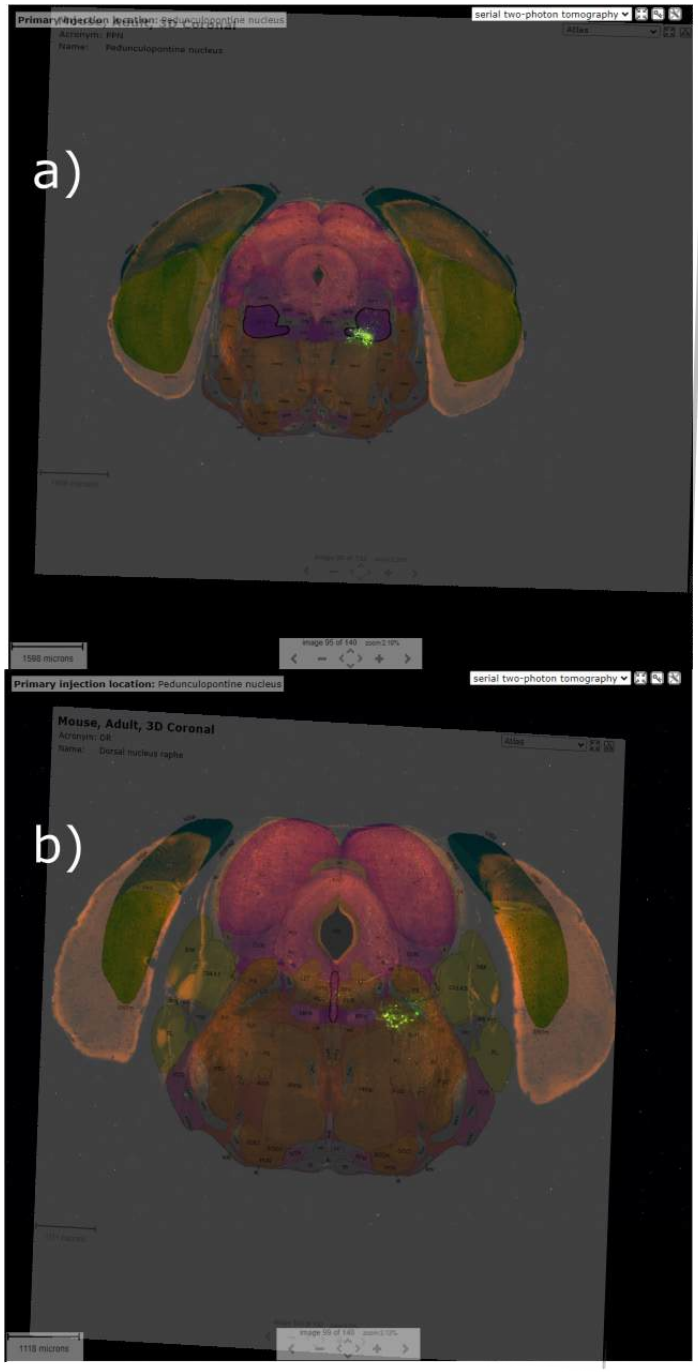


**Supplemental Fig. 24.** a) Injection structure PPN to b) DR. Experiment number 264566672, Chat-IRES-Cre-neo. The shortcomings of experimental procedures are addressed in the discussion.

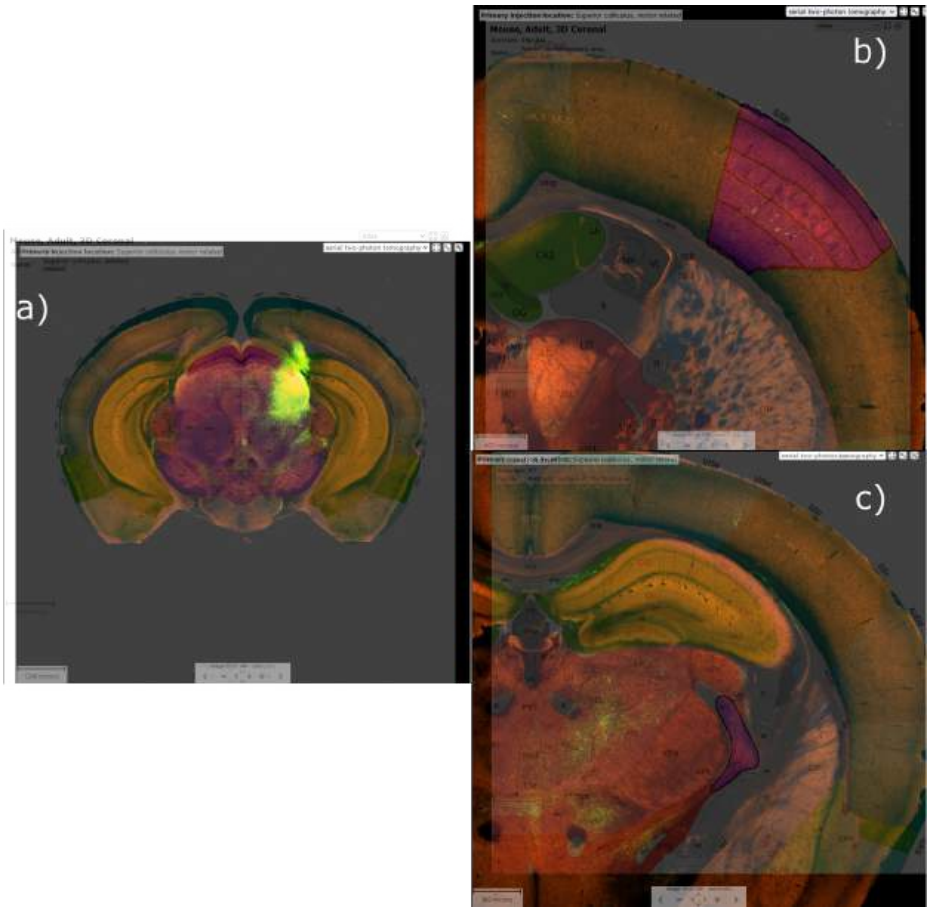


**Supplemental Fig. 25.** a) Injection structure SC to b) bfd and c) DR. Experiment number 146078721, wild-type. The shortcomings of experimental procedures are addressed in the discussion.

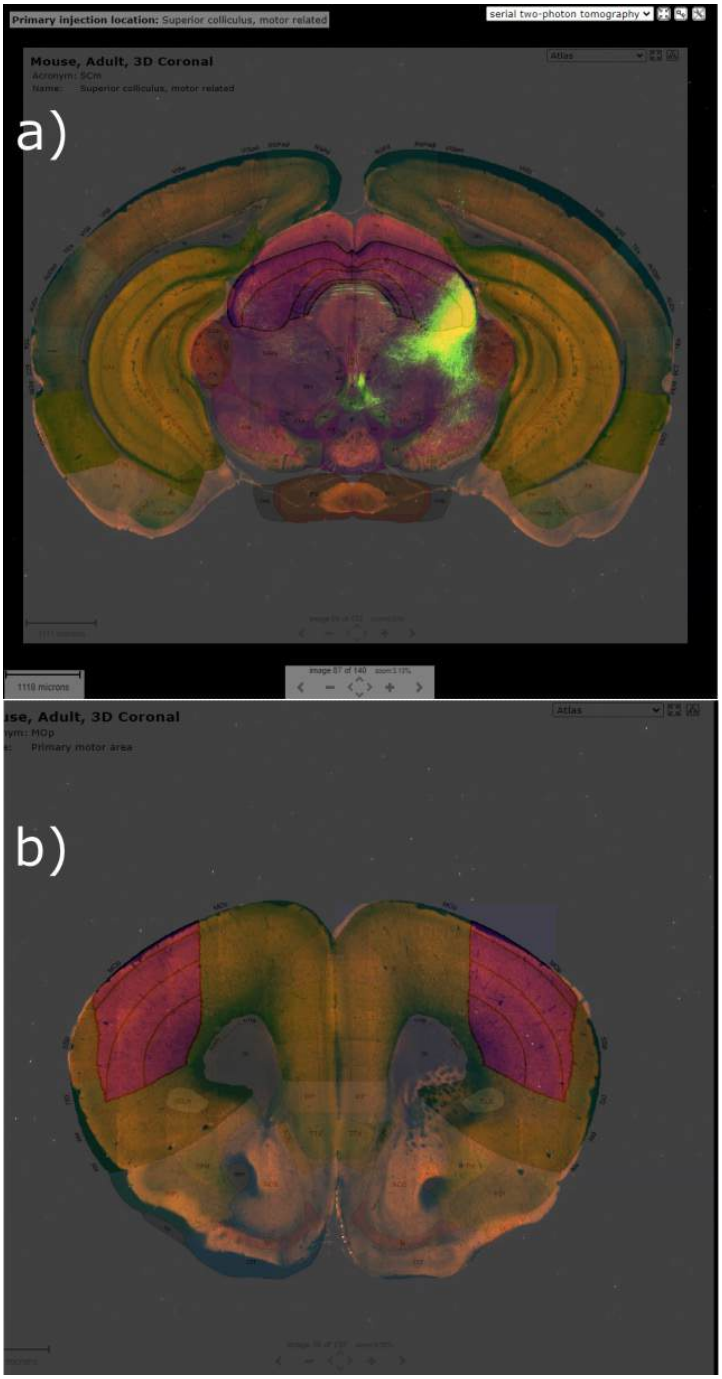


**Supplemental Fig. 26.** a) Injection structure SC to b) MOp. Experiment number 175158132, wild-type. The shortcomings of experimental procedures are addressed in the discussion.

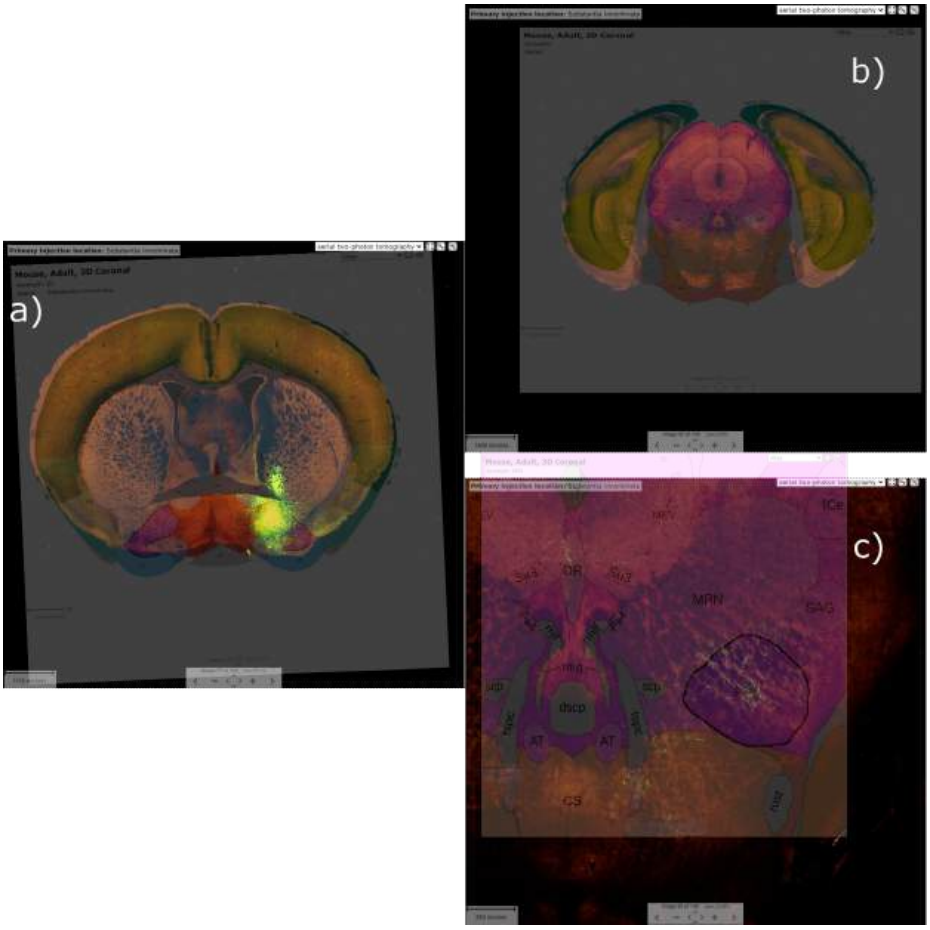


**Supplemental Fig. 27.** a) Injection structure SI to b) PPN. c) zoom on PPN. Experiment number 305026861, Drd3-Cre-KI196. The shortcomings of experimental procedures are addressed in the discussion.

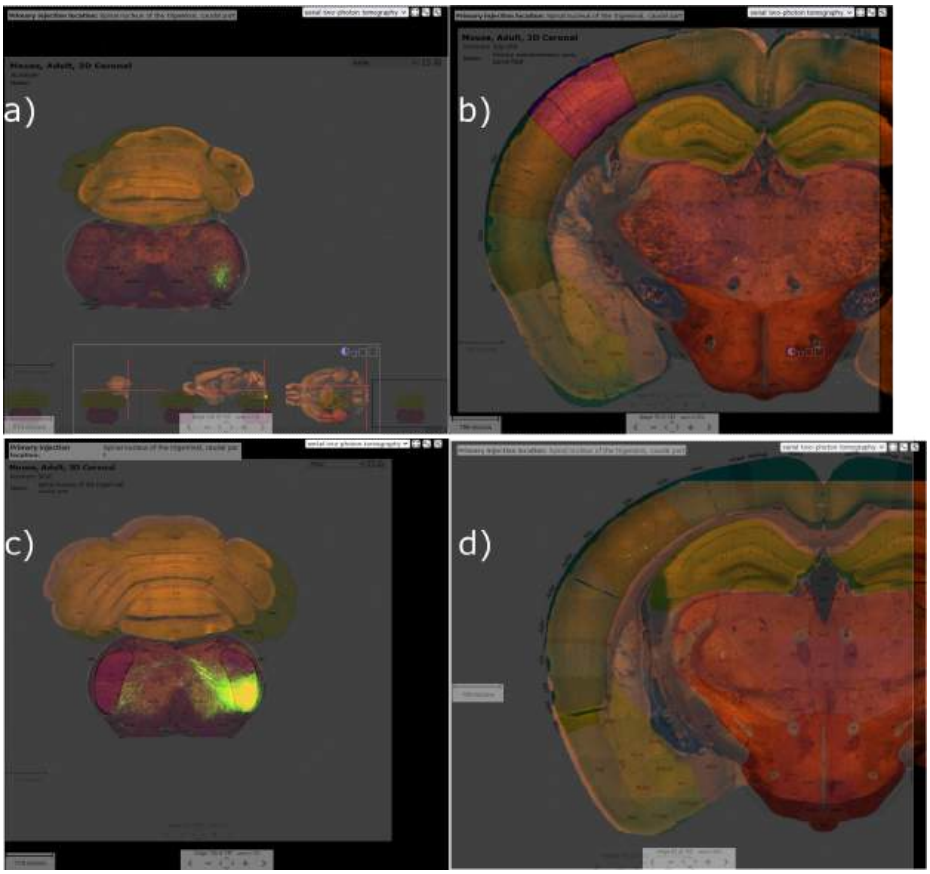


**Supplemental Fig. 28.** a) Injection structure SPVc to b) bfd. c) Injection structure SPVc to d) bfd. a) and b) experiment number 287460307, Cck-IRES-Cre. c) and d) experiment number 147215105, wild-type. The shortcomings of experimental procedures are addressed in the discussion.

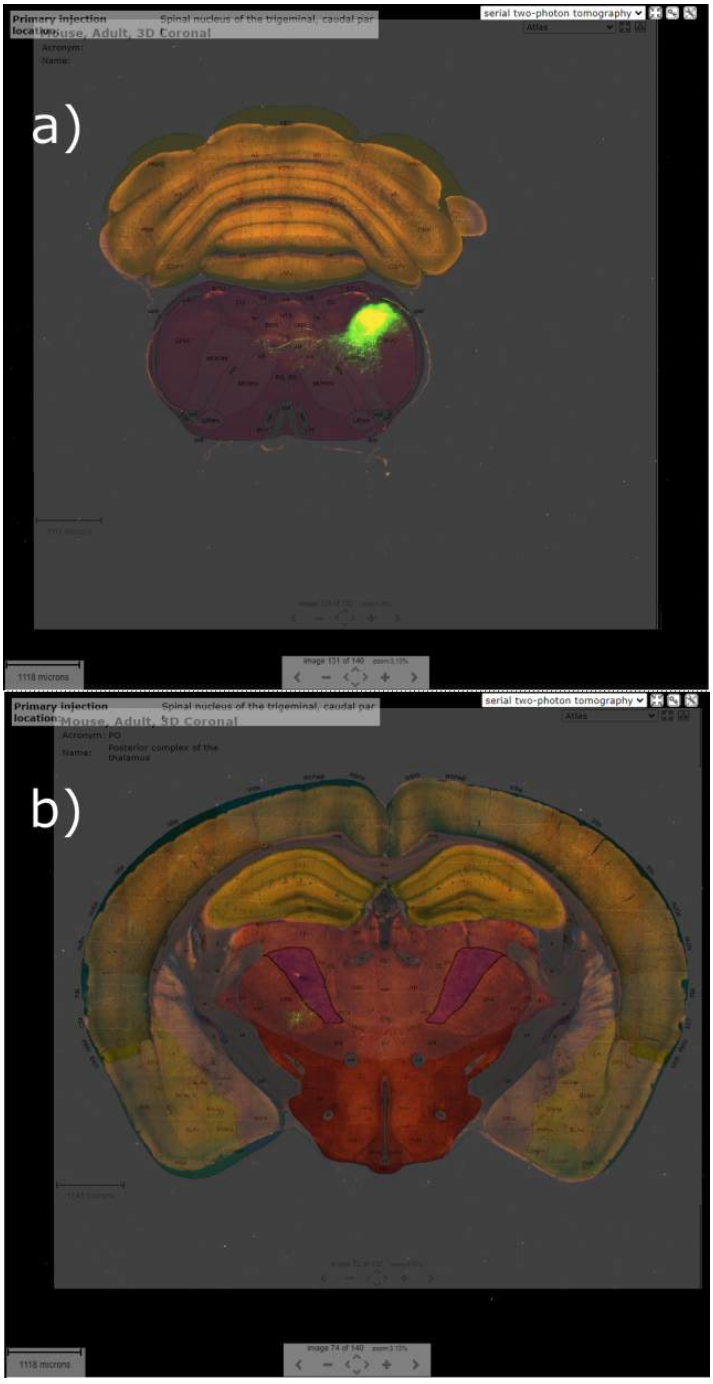


**Supplemental Fig. 29.** a) Injection structure SPVc to b) PO. Experiment number 114402050, wild-type. The shortcomings of experimental procedures are addressed in the discussion.

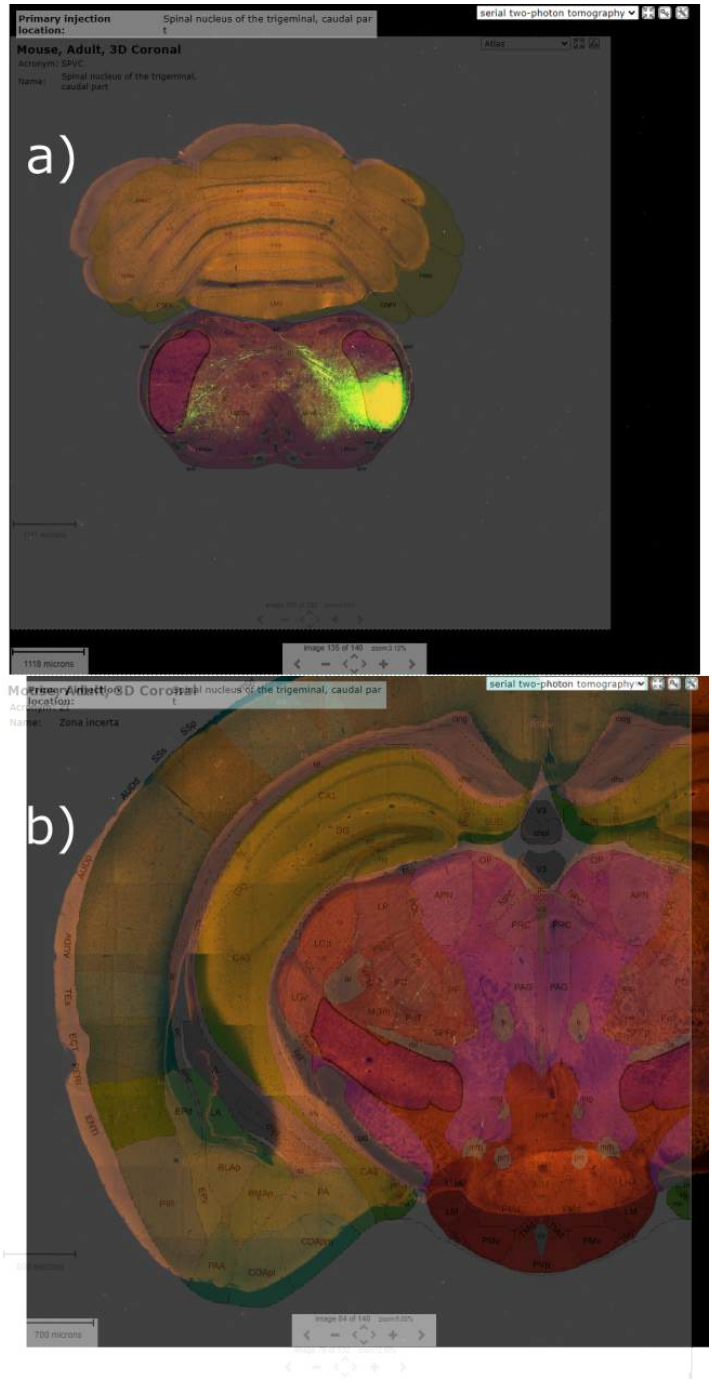


**Supplemental Fig. 30.** a) Injection structure SPVc to b) ZI. Experiment number 147215105, wild-type. The shortcomings of experimental procedures are addressed in the discussion.

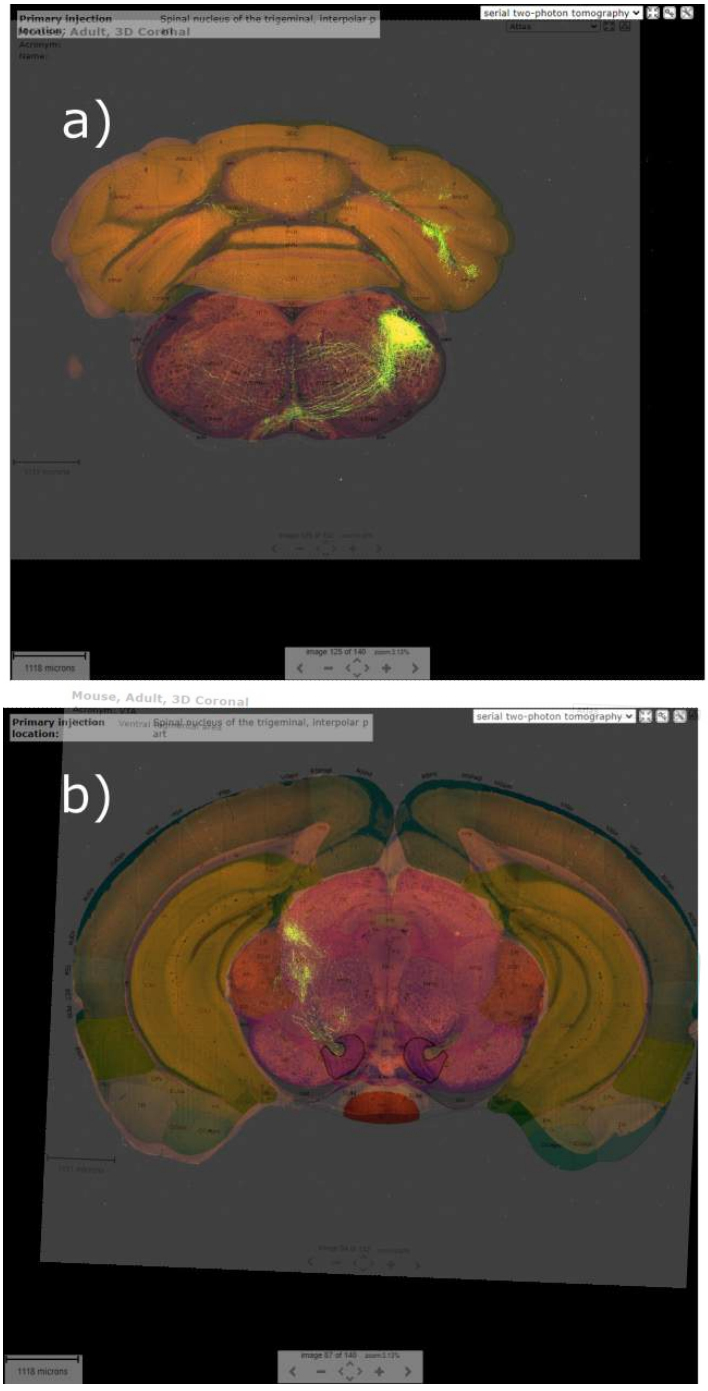


**Supplemental Fig. 31.** a) Injection structure SPVi to b) VTA. Experiment number 272738620, wild-type. The shortcomings of experimental procedures are addressed in the discussion.

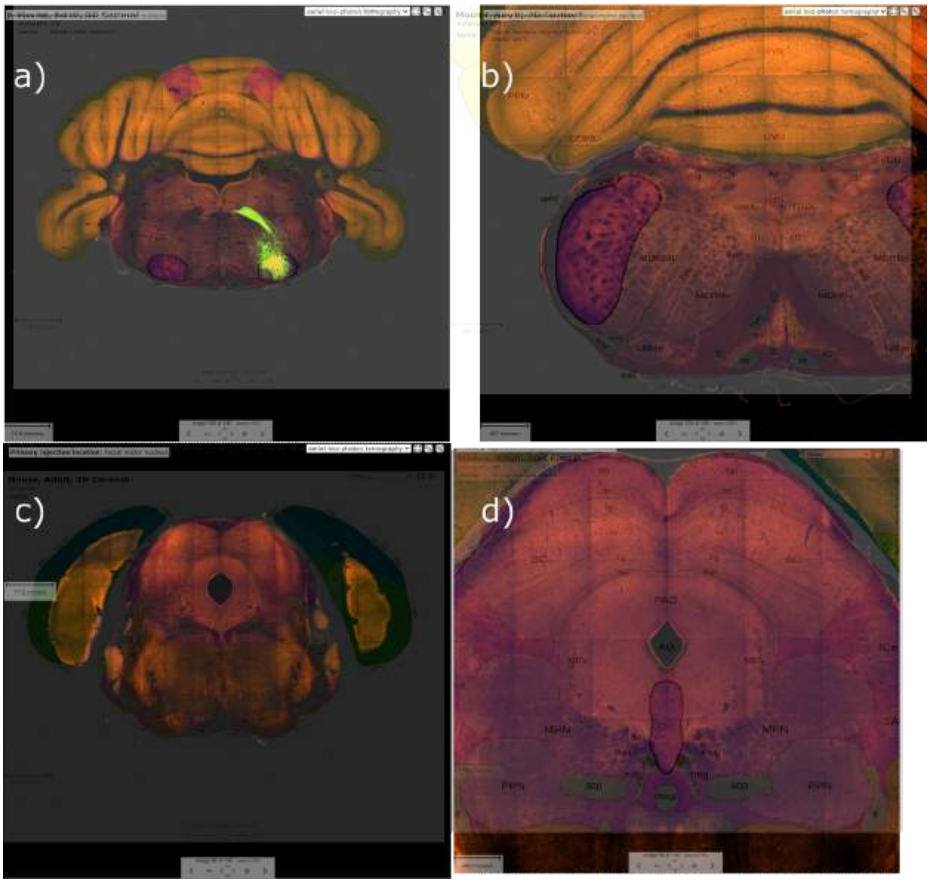


**Supplemental Fig. 32.** a) Injection structure VII to b) SPVc, c) SC and d) DR. Experiment number 113766744, Grik4-Cre. The shortcomings of experimental procedures are addressed in the discussion.

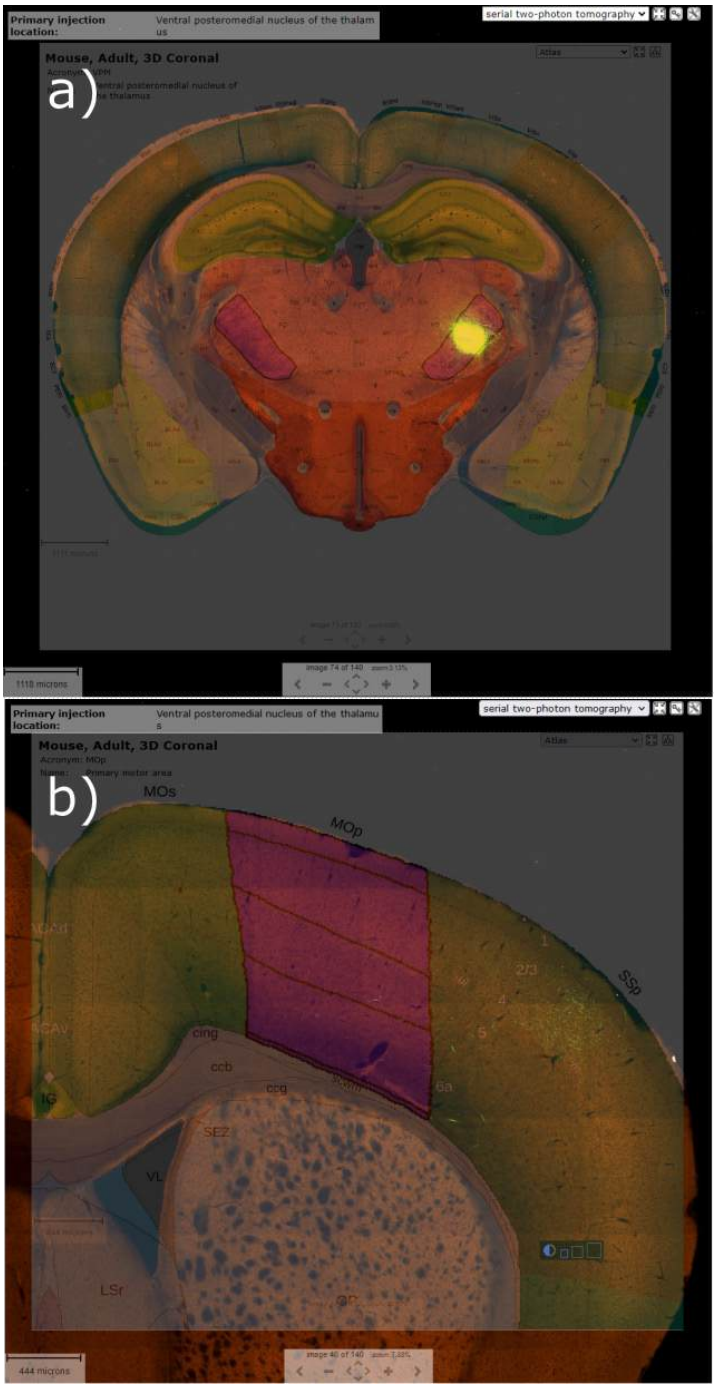


**Supplemental Fig. 33.** a) Injection structure VPM to b) MOp. Experiment number 312240825, Slc17a6-IRES-Cre. The shortcomings of experimental procedures are addressed in the discussion.

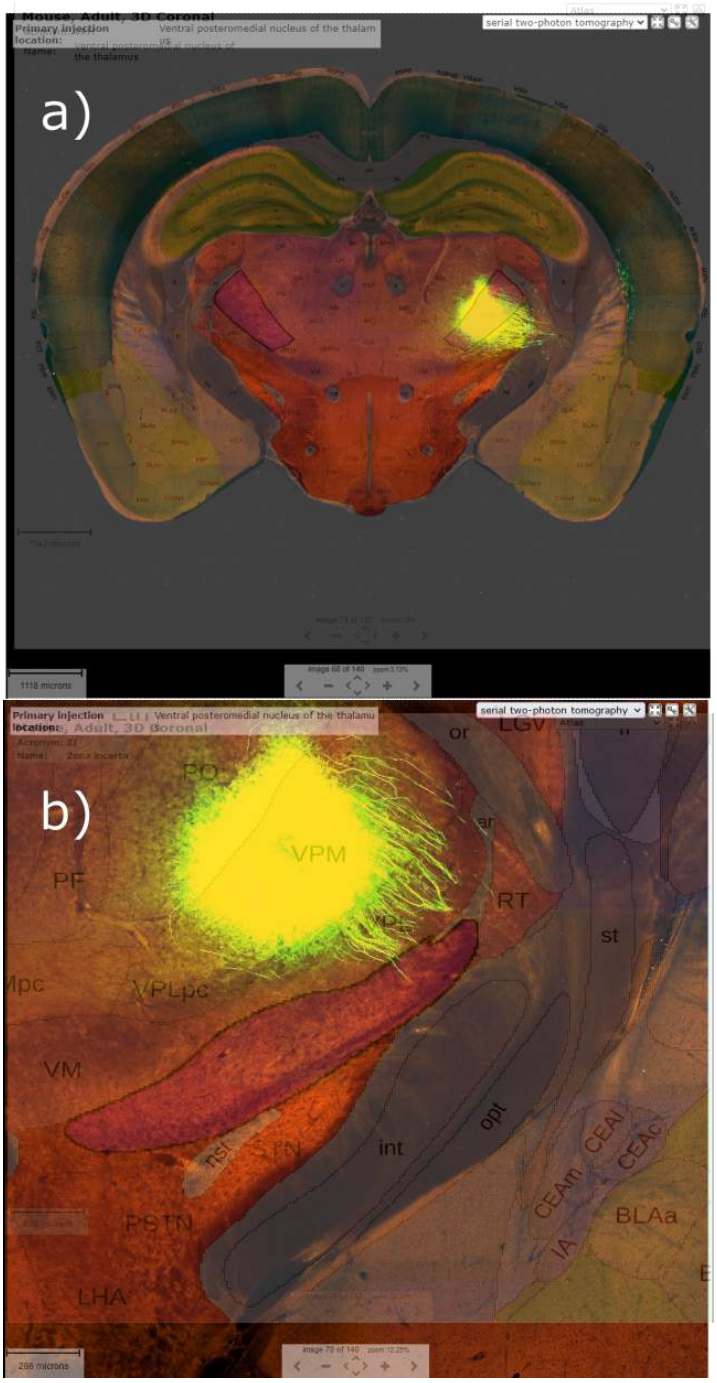


**Supplemental Fig. 34.** a) Injection structure VPM to b) ZI. Experiment number 268399868, Ppp1r17-Cre-NL146. The shortcomings of experimental procedures are addressed in the discussion.

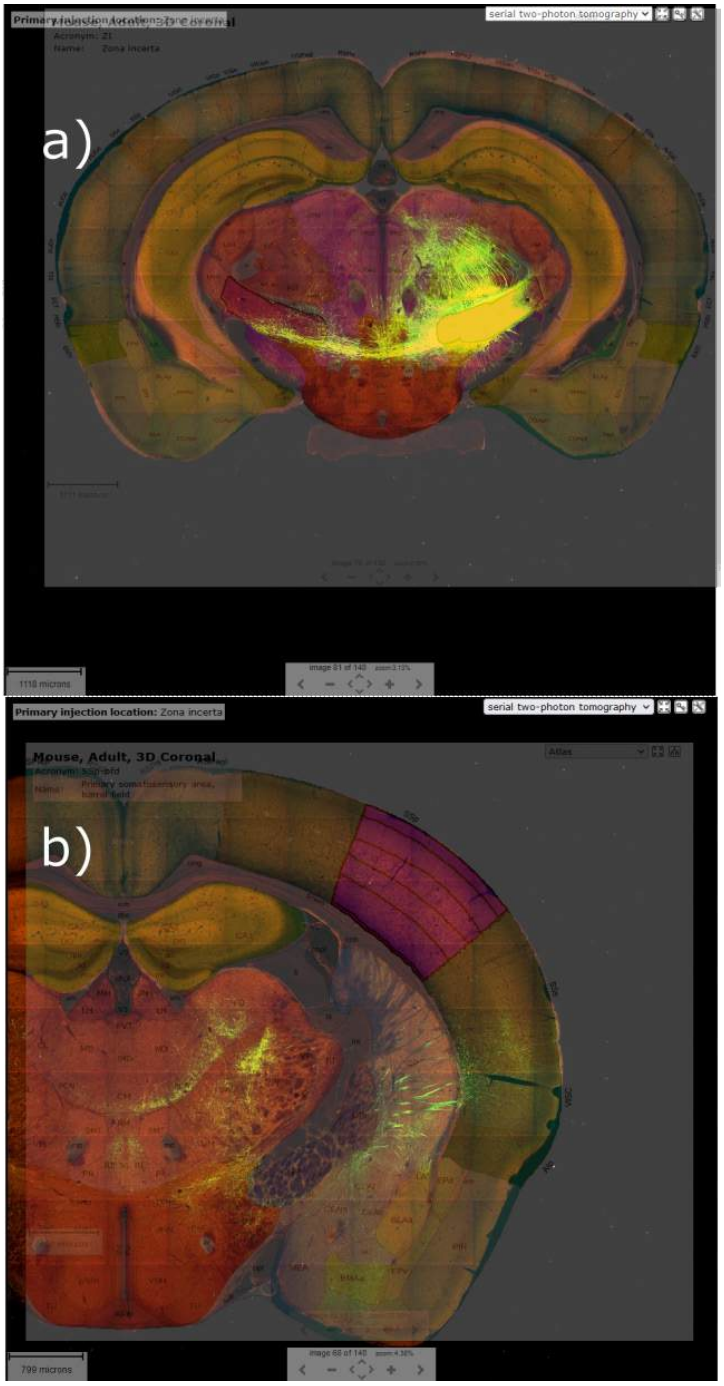


**Supplemental Fig. 35.** a) Injection structure ZI to b) bfd. Experiment number 113095845, wild-type. The shortcomings of experimental procedures are addressed in the discussion.

Chapter 3

# Artificial Human Touch: A Spiking Network Model of the Tactile Periphery

## Abstract

Touch is crucial in object manipulation, navigation, and social communication. Unlike vision or audition, which require line-of-sight access to stimuli, the tactile system provides direct feedback through mechanoreceptors. Despite extensive studies on mechanoreceptor function, how they collectively encode touch remains unclear. Here, we present the first spiking computational model of the somatosensory periphery integrating mechanoreceptor responses with trigeminal ganglion neuron dynamics. We show that the artificial neural network matches or exceeds human performance in psychophysical experiments. Using information-theoretic analyses, we demonstrate that the first action potential carries most stimulus-related information, with temporally neighboring spikes contributing largely redundant data. Finally, we introduce a novel sparse decoder network that accurately classifies tactile stimuli with minimal training, paving the way for neuromorphic applications in artificial touch sensing. These findings offer new insights into the neural coding of touch and provide a computational framework for studying the complex interplay of mechanoreceptors in somatosensory processing.

## Introduction

Touch is an essential sensory modality for perceiving and interacting with the environment, playing a critical role in object manipulation, navigation, and social interactions [1]. Unlike other sensory modalities, such as vision or audition, which often require line-of-sight access to stimuli, touch provides direct and immediate feedback from the physical world through mechanoreceptors embedded in the skin. The mechanoreceptive system encodes various tactile properties, including pressure, vibration, texture, and temperature [2], enabling fine motor control and haptic exploration.

The ability to precisely manipulate objects is a hallmark of human dexterity and relies heavily on tactile feedback. Mechanoreceptors in the glabrous skin of the hand—particularly Merkel cells, Meissner corpuscles, Ruffini corpuscles, and Pacinian corpuscles—encode critical information about object shape, texture, compliance, and surface friction [3]. Slowly adapting type 1 (SA1) fibers associated with Merkel [4] cells provide high-resolution spatial information necessary for fine form perception and grip control [3]. Ruffini corpuscles are classified as SA2 mechanoreceptors and are hypothesized to encode skin stretch and hand conformation [3], contributing to proprioception and kinesthetic awareness [5]. Among the rapidly adapting (RA) fibers innervating Meissner corpuscles respond to low-frequency vibrations and contribute to motion detection and slip prevention [3]. The Pacinian corpuscles, with their sensitivity to high-frequency vibrations, facilitate the perception of fine textures and tool-mediated touch [3]. Integrating these mechanoreceptive signals allows the somatosensory system to produce a neuronal representation of sensory information and regulate motor interaction with the object via sensorimotor loops in the brain [6].

The first step in touch processing occurs at the level of mechanoreceptors, which convert external mechanical forces into neural signals through mechanosensitive ion channels [7], before transmitting them to the trigeminal ganglion (TG) in the face or dorsal root ganglion (DRG) in the hand [8]. These afferents serve as the initial relay points in the somatosensory hierarchy, shaping early sensory representations that later influence cortical processing [5]. Despite significant experimental advancements in characterizing the neural responses of mechanoreceptors, a precise understanding of how these receptors collectively encode tactile stimuli remains elusive. Moreover, the mechanisms by which mechanoreceptors filter, encode, and transmit tactile information remain poorly understood, especially in terms of population coding, adaptation, and redundancy.

Given the complexity and heterogeneity of mechanoreceptor responses, a computational model is necessary to systematically explore how tactile information is represented at the periphery. Such a model would allow for the simulation of different mechanoreceptor types (SA1, SA2, RA) under various tactile stimuli, helping to clarify their individual and collective roles [9]. By analyzing the mutual information between tactile stimuli and neural responses, the model can reveal how efficiently different receptor populations encode object properties [10]. While electrophysiological studies provide insights into individual receptor responses, the computational model can integrate these findings into a cohesive framework, enabling predictions about how afferent populations collectively process stimuli [11]. Thus, in this study, we aimed to elucidate the fundamental principles underlying early tactile processing by developing a spiking computational model of mechanoreceptors and trigeminal ganglion neurons. By comparing the modeled mechanoreceptor responses to human psychophysical data, we show that haptic detection and stimulus duration discrimination are encoded by distinct classes of mechanoreceptors, suggesting that parallel processing of tactile information starts from the sensory periphery. Using information theoretic measures, we show that the first action potential (spikes) carries the most information about stimulus properties, tested herein, and information across temporally neighboring action potentials is largely redundant. Finally, we introduce a novel sparse decoder network to accurately classify stimuli in this spiking neural network with minimal training and sparse connectivity, enabling future applications to predict tactile perception from neural responses and for computationally efficient neuromorphic implementation of touch sensing.

## Methods

Here we detail the computational and experimental methods employed in this study. First, we present the adaptive exponential integrate-and-fire (AdEx) model used to simulate mechanoreceptor activity. Subsequently, we describe the focused ultrasound stimulation to acoustically deliver precise pressure on human skin to evoke tactile sensation, and finally, we outline the parameter optimization procedure used to fit the model to electrophysiological data. All code and documentation for the neural model, simulation procedures, and parameter fitting are publicly available on GitHub, ensuring reproducibility and facilitating further research (https://github.com/Nrault/Universal_model_of_touch).

## Neural model

To model the diverse adaptation properties of mechanoreceptors, the primary distinguishing characteristic [12] of mechanoreceptors, we implemented the Adaptive Exponential Integrate-and-Fire (AdEx) model [13]. The AdEx model offers a computationally efficient yet biologically plausible framework for simulating neuronal dynamics, particularly in scenarios where detailed biophysical data are limited. The core feature of the AdEx model is the incorporation of an adaptation current, which allows for the reproduction of key firing rate adaptation characteristics observed in mechanoreceptors, distinguishing between slowly adapting (SA) and rapidly adapting (RA) subtypes.

The AdEx model extends the exponential integrate-and-fire model by including an adaptive current (*W*) that introduces negative feedback, causing spike-frequency adaptation. This adaptive current increases following each spike and gradually converges logarithmically toward an upper bound. This allows the model to reproduce key adaptation properties observed in mechanoreceptors, such as slowly adapting (SA) and rapidly adapting (RA) responses. The model equations are as follows:

(1) $$dv/dt = (I_{leak} + g_{leak} * \Delta_{th} * e^{(v - v_{th})/\Delta_{th}} - W + I_{app})/C_m$$

(2) $$I_{leak} = g_{leak} * (E_{leak} - v)$$

(3) $$dW/dt = (a * (v - E_{leak}) - W)/\tau$$

Following each spike, the adaptation current *W* is instantaneously increased by a value *b*. The adaptation parameters a, b, and **τ**, which govern the adaptation dynamics, were fitted to experimental data from Sonekatsu and Gu (2019) [14], as detailed in the Parameter Optimization for Adaptation Current subsection. It is important to note that the negative sign of the adaptive current in this formulation leads to spike-frequency adaptation, consistent with mechanoreceptor physiology [12], whereas a positive adaptive current would induce bursting, a firing pattern not typical of primary mechanoreceptive afferents [15]. By adjusting the adaptation parameters, the AdEx model can effectively simulate the distinct firing patterns of different mechanoreceptor subtypes.

## Modeling mechanoreceptors

To simulate mechanoreceptor activation, we applied a continuous input current ($I_{app}$) of 900 pA, modulated by a function specific to each mechanoreceptor

subtype. This function, defined by equations (4), (5), and (6), governs how stimuli are presented to the receptors based on their receptive fields.

To ensure biologically accurate distribution of mechanoreceptors, we based our model on Johansson and Vallbo (1977) [16], which provides empirical data on the density and types of mechanoreceptors in human glabrous skin. From a total population of 200 simulated receptors, we assigned:

- 58 SA1 (Slowly Adapting Type 1) receptors
- 30 SA2 (Slowly Adapting Type 2) receptors
- 112 RA (Rapidly Adapting) receptors

Each receptor was individually connected to a corresponding neuron in a dummy layer composed of exponential leaky integrate-and-fire neurons. This one-to-one connectivity ensured that each mechanoreceptor's output was directly relayed to a neuron in the trigeminal ganglion (TG) layer, which acts as a central relay integrating tactile information.

The TG layer consisted of 200 neurons, each receiving input from a single mechanoreceptor. To maintain a direct and efficient encoding of mechanoreceptive activity, we designed the synaptic weight between mechanoreceptors and TG neurons such that each action potential in a receptor depolarized the corresponding TG neuron by 25 mV. This depolarization was sufficient to reach the threshold for action potential generation, ensuring that each spike in a mechanoreceptor resulted in a corresponding spike in the TG neuron (see Figure 1).

This approach allows the model to preserve the spatiotemporal fidelity of mechanoreceptive signals while simplifying the computational structure, making it suitable for large-scale simulations of tactile processing.

## SA1

SA1 receptors respond primarily to stimulus direction but poorly to amplitude [3, 17, 18]. Therefore, we assume an ON/OFF relationship to amplitude, that is, $I_{app}$ is multiplied by 1 if there is a stimulus, 0 otherwise :

(4) $I_{app} = (900\,pA * amplitudeOnOff(t))$ with t ∈ T the duration of the simulation.

### SA2

SA2 receptors are sensitive to direction and amplitude [3, 17, 18], we therefore assumed a linear relationship between the response intensity and the stimulus amplitude:

(5) $I_{app} = (900\,pA * amplitude(t)/maxAmplitude)$ with maxAmplitude empirically set to 90 a.u.

### RA

we assume that RA receptors are sensitive to direction and switch in amplitude [3, 17, 18] :

(6) $I_{app} = 900\,pA * log\,((amplitude(t) - amplitude(t-1))^2)$



## Parameter Optimization for Adaptation Current

To fine-tune the adaptation parameters in our neural model, we employed the Covariance Matrix Adaptation Evolution Strategy (CMA-ES) [19], an advanced evolutionary algorithm that iteratively adjusts parameters based on covariance relationships with an objective function. In our case, the objective function was the mean squared error (MSE) between the model's predicted firing rates and biological data. The parameters optimized included a, b, and $\boldsymbol{\tau}$ (introduced in the previous section), which define the adaptation dynamics of the mechanoreceptor model.

We implemented CMA-ES using the cmaes Python library, leveraging its robust global optimization capabilities. The algorithm estimated the best-fit parameters by minimizing the error between our model's predicted instantaneous firing rate and experimental data obtained from Sonekatsu and Gu (2019) [14], Supplemental Figure 1. The instantaneous firing rate was computed as the reciprocal of the interspike interval (ISI), also known as the instantaneous frequency. The fitting procedure was conducted as follows:

- SA1 mechanoreceptor models were optimized to match experimental data from Supplemental Figure 1.
- SA2 mechanoreceptor models were optimized to fit Supplemental Figure 1.
- RA mechanoreceptors lacked sufficient data points for a reliable automated fitting procedure. Instead, we manually hand-tuned the adaptation parameters to achieve the expected rapid adaptation behavior, ensuring a transient response to sustained stimuli.

The model was validated against responses to a ramp-and-hold stimulus (see Figure 1), which is commonly used to characterize mechanoreceptor adaptation dynamics.

The full implementation of our parameter optimization pipeline, including the CMA-ES code and data, is available on GitHub (https://github.com/Nrault/Neural_population_optimization_CMA).

## Simulating Behavioral Comparisons

To generate model outputs comparable to behavioral data, we simulated a stimulus duration discrimination task using pairs of direct current (DC) pulses (see Figure 3). Stimuli were presented in pairs and compared based on their duration. Trials were labeled as follows: '1' if the first stimulus duration exceeded the second, '0' if the second stimulus duration exceeded the first, and randomly assigned '0' or '1' if both stimuli were of equal duration.

To analyze neural responses, we calculated the firing rate of each neuron during two presentations of DC pulses. These firing rates were then concatenated into a feature vector of size twice the number of neurons, 2N (i.e., with N, the number of neurons), allowing for the separate encoding of responses to each stimulus within the input space. This feature vector of size 1x2N served as input for downstream classification models for each trial. For T, the number of trials, the complete input was of size Tx2N, the output was Tx1, i.e., one input was given for each trial.

We employed an ideal observer framework for stimulus duration classification, assuming access to the total spike count per neuron in each trial. This approach provides a biologically plausible proxy for perceptual decision-making by considering only the information potentially available to subsequent processing stages.

We implemented and evaluated four classification strategies using the Scikit-learn (Sklearn) library [20]:

- **Linear Classifier – Ridge Classifier**: A linear classifier assuming that stimulus labels can be predicted by a weighted sum of neural activity.
- **Multilayer Perceptron (MLP) – Neural Network Classifier**: An universal function approximator used as a non-linear classifier capable of learning more complex relationships between neural firing rates and stimulus duration.
- **Bayesian Classifier – Naïve Bayes**: A probabilistic classifier assuming neuronal independence and Gaussian-distributed spike counts for classification, which learns the distribution of the posterior (probability that stimulus 1 is longer than stimulus 2) based on the prior (distribution of the number of spikes per neurons).
- **MiPiNet** (Mutual Information based Pre Initialized Network) which is a novel multi-layer perceptron, introduced herein, with sparse connectivity inspired

by gene correlation networks in the rodent barrel cortex. MiPiNet addresses limitations of standard network pruning by incorporating a biologically-inspired pre-initialization strategy. Specifically, MiPiNet utilizes a connectivity matrix derived from mutual information analysis of gene expression data from 451 housekeeping genes common to male and female rodent somatosensory cortex, made available by Zeisel and colleagues [21]. This connectivity matrix, generated using the NETSCOPE toolbox [22], was used to initialize the weights of a sparse perceptron network in TensorFlow. The network consisted of an input layer, hidden layers with the same number of nodes as genes, and an output layer for classification. Weights between nodes in the hidden layers were initialized according to the gene connectivity matrix.



Classifiers were trained using the spike counts per neuron per trial as input and the stimulus duration label as the target variable. Decoder performance was evaluated using classification accuracy, calculated as: Accuracy = (Correctly classified trials) / (Total number of trials). Accuracy was averaged over 100 decoders to quantify the population encoding of stimulus duration and the impact of different classification strategies.

To compare classifier performance, we calculated the sum over the diagonal of the accuracy matrices and determined the difference between this matrix and a perfect accuracy matrix (all values equal to 1, e.i. 100% accuracy). The cumulative sum of this difference was then subjected to a Kolmogorov-Smirnov (KS) test to assess the statistical significance of performance differences across decoders. Structural Similarity Index Measure (SSIM) was also computed to account for the two-dimensional structure of the accuracy matrices.

To quantify the information encoded by individual spikes, we computed the mutual information between stimulus duration and the timing of the 1st to 5th spike independently using equation 7:

(7) $MI = \sum_{x \in X} \sum_{y \in Y} P(x,y) log(\frac{P(x,y)}{P(x)P(y)})$, with x, a stimulus, P(x) the probability to see stimulus x, y the neural response and P(y) the probability of seeing a neural response. P(x, y) is the joint probability of seeing a stimulus x and a response y

No bias correction was applied to the mutual information (MI) calculation. Although this might seem unexpected for biological data, our analysis concerns a deterministic model: for a given stimulus, the neural response is always identical. Consequently, subsampling bias cannot occur. The absence of noise ensures a

single possible output for each stimulus, though distinct stimuli can converge onto the same neural representation. In such cases, the conditional input entropy given the output, H(X|Y), may be smaller than the input entropy H(X), since two stimuli x and x′ can produce the same output y. Nevertheless, the mapping remains deterministic: whenever x or x′ is presented, the same response y will occur. For these reasons, bias correction was not required in our MI estimates.

Furthermore, to investigate the nature of information encoding (redundancy, synergy, or independence) across neurons, we computed coinformation [23], also known as interaction information, using equation 8:

(8) $coinformation\ =\ H(X)\ +\ H(Y)\ +\ H(Z)\ -\ H(X,Y)\ -\ H(X,Z)\ -\ H(Y,Z)\ +\ H(X,Y,Z)$, with H(x), the entropy of the stimulus, H(y) the entropy of the neural response y, H(z) the entropy of the neural response z. H(x, y) the joint entropy of x and y. H(x, z), the joint entropy of x and z. H(y, z) the joint entropy of y and z. H(x, y, z), the entropy of x, y and z.

Coinformation quantifies the dependence between multiple variables (spike times from different neurons in this context). Positive coinformation values indicate redundancy, as the individual entropy is higher than the joint entropy, suggesting overlapping information encoding; negative values indicate synergy, as the joint entropy contains more information than the sum of individual entropy, suggesting complementary information encoding; and values near zero indicate independence in information encoding.

## Psychophysical experiments

We used focused ultrasound stimulation (FUS) to probe human touch perception non-invasively. By harnessing the acoustic radiation force of 250 kHz ultrasound, FUS delivers contact-free, millimetre-scale focal vibrations with sub-millisecond timing, enabling precise excitation of cutaneous mechanoreceptors [24]. Participants consistently described the sensation as natural vibrotactile input localized to the fingertip.

All procedures were approved by the Georgia Institute of Technology Institutional Review Board (IRB protocols H23479, tactile detection; H24249, temporal discrimination). Healthy adults (18–34 yrs, male and female) gave written informed consent. Only data from individuals who achieved ≥75 % correct detection at two adjacent stimulus intensities were analysed.

Ultrasound pulses were produced with a TPO-105-17 power supply driving a CTX-250 single-element transducer (Sonic Concepts). Subjects rested the dominant-hand index finger on a custom designed 3-D-printed positioning jig aligned to the acoustic focus (21 mm above the transducer's geometrical center). Aquasonic 100 gel, centrifuged (2500 rpm, 30 min) to remove bubbles, coupled the transducer to the skin. A custom MATLAB script controlled pulse trains and randomised trial order. To eliminate extraneous cues, participants wore opaque eye masks and active noise-cancelling headphones (Soundcore Life Q20). Two behavioral tasks were administered in independent group of participants:

**Tactile-Detection Task:** We assessed whether FUS intensity and duty cycle modulate perceptual salience. Each participant completed 84 randomised trials comprising all pairings of seven intensities (10–30 W; 0.30–0.74 MPa) with three duty-cycle sets: Group 1, 0.25, 0.5, 0.75; Group 2, 0.25, 0.125, 0.0625, Group 3: 0.0625, 0.0312, 0.016. Other parameters were fixed: 25 ms period, 125 ms total train, 250 kHz carrier. Each condition was repeated four times. On every trial, subjects pressed Enter with the non-stimulated hand upon detecting a vibration. The experiment was double-blind.

**Temporal-Discrimination Task:** To probe temporal resolution, each trial presented two successive pulse trains (1 s inter-stimulus interval). Ultrasound power was held at 30 W while duty cycle varied independently for Stimulus 1 and Stimulus 2 across six values (0.0312–0.75). The $6 \times 6$ matrix (including identical pairs as controls) was repeated four times (144 trials). Participants indicated which stimulus felt stronger (left/right arrow) or reported no difference (down arrow). Accuracy and reaction time were logged.

Behavioural responses were time-stamped and processed with custom MATLAB routines. Detection probabilities and discrimination performance were computed per condition, and psychometric functions were fitted for each participant.

## Safety Evaluation

The highest spatial-peak pulse-average intensity ($I_{sppa}$) was 16.46 W $cm^{-2}$—well below the FDA diagnostic limit of 190 W $cm^{-2}$. The corresponding spatial-peak time-average intensity ($I_{spta}$) at the maximum 0.75 duty cycle was 12.35 W $cm^{-2}$, exceeding the diagnostic guideline (0.72 W $cm^{-2}$) but delivered for only 18.75 ms per train. Prior human and animal studies report no adverse heating under comparable exposures [25, 26]. We verified this by thermal imaging (≤0.1 °C resolution; FLIR camera): even 3 s of continuous 30 W sonication at 100 % duty raised gel-surface temperature by only 0.1 °C.

# Results

This study aimed to elucidate the neural encoding of tactile stimulus duration at the somatosensory periphery, focusing on the contributions of different mechanoreceptor subtypes and their integration at the trigeminal ganglion (TG). To achieve this, we developed a computational model of mechanoreceptor populations and TG neurons, and analyzed their responses to controlled tactile stimuli. The results, presented in the following sections, reveal a functional specialization among mechanoreceptor subtypes, differential encoding of stimulus duration, and insights into the efficiency of neural coding in the tactile periphery.

## Model Fitting

To investigate the contributions of individual mechanoreceptor (MR) subtypes to tactile stimulus encoding using a bottom-up approach, we first constructed a computational model comprising three distinct populations of Adaptive Exponential Integrate-and-Fire (AdEx) neurons. The adaptation dynamics of these model neurons were fitted to in vitro instantaneous firing rate data recorded directly from rat whisker follicle mechanoreceptors by Sonekatsu and Gu (2020) [14]. The relative sizes of these simulated populations were based on empirical data from Johansson and Vallbo (1977) [16] regarding human glabrous skin (see Methods for details). Consistent with anatomical findings suggesting segregated afferent pathways at the initial sensory ganglion [27], these MRs were connected with a one-to-one excitatory projection to a corresponding layer of 200 Trigeminal Ganglion (TG) neurons. This ensured that each TG neuron received input from only a single MR, allowing for an initial assessment of how individual mechanoreceptor signals are relayed. The overall skin organization and model connectivity are depicted in Figure 1A and 1B, respectively.

The distinct adaptation rates and receptive field properties inherent to each MR subtype, established through the fitting procedure, gave rise to characteristic temporal response profiles when subjected to a ramp-and-hold stimulus, as illustrated in Figure 1C.

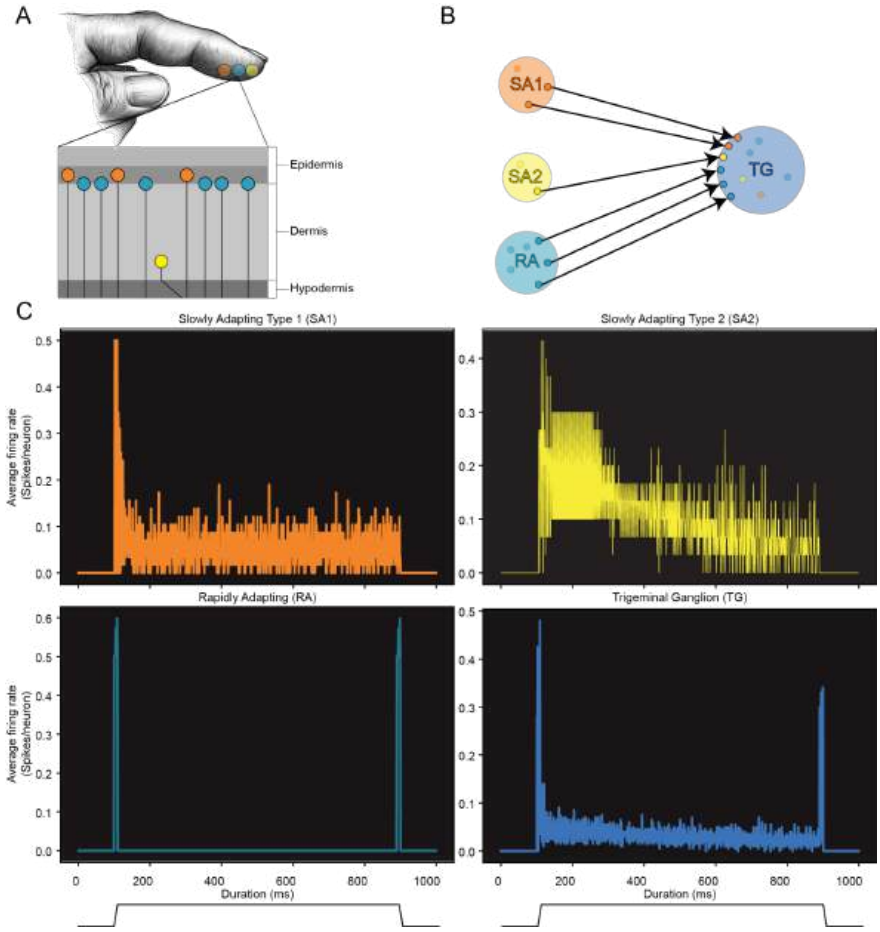


**Figure 1 - Model implementation and basic response properties.** A) Side view of the skin with the different mechanoreceptors represented at their position and with corresponding densities. B) Schematic of the model, each mechanoreceptor population is connected in a one-to-one fashion to TG so that each TG neuron receives input from only one mechanoreceptor. C) Bottom : Two ramp-and-hold stimulus starting at 100ms and finishing at 900ms. Top-left: SA1 activity in response to the stimulus. Top-right: SA2 response to the stimulus. Bottom-left: RA response to the stimulus. Bottom-right: TG response to the stimulus. The responses were computed as the number of spikes divided by the number of neurons in the considered population at each timestep (1ms).

The SA1 population exhibited a pronounced phasic response at the stimulus onset, characterized by a high-frequency burst of spikes, which then sharply declined to a lower, sustained firing rate (plateau phase) for the duration of the stimulus. No significant response was observed at stimulus offset. The SA2 population also demonstrated a slowly adapting profile, with an increase in activity around the stimulus onset followed by a gradual decrease to a stable plateau firing rate. Similar

to SA1, no distinct response was observed at stimulus offset for SA2 neurons. In contrast, the RA MRs responded exclusively to the transient phases of the stimulus. They produced robust bursts of spikes precisely at the stimulus onset (ramp-on) and offset (ramp-off) and remained virtually silent during the sustained plateau phase. The combined input from these three distinct MR populations to the TG neurons resulted in a composite response profile for the TG layer. As shown in Figure 1C, the TG activity reproduced key dynamics previously observed experimentally [28], featuring both onset and offset responses primarily driven by the RA inputs, superimposed on a lower level of sustained activity during the plateau phase, reflecting the contributions from the SA1 and SA2 populations. This faithful recapitulation of fundamental response properties validated our model's capacity to simulate early tactile processing.

Once the model fitted, we recorded the model's responses to different ramp-and-hold amplitude and duration.

## Differential Sensitivity and Receptive Fields across Mechanoreceptor Subtypes

Stimulus encoding properties of the mechanoreceptor (MR) populations revealed distinct sensitivities to stimulus amplitude and duration, giving rise to characteristic receptive fields and a sequential activation pattern across the subtypes in the model (Figure 2).

Figure 2A presents raster plots illustrating the spiking activity of individual SA1, SA2, RA, and Trigeminal Ganglion (TG) neurons in response to stimuli varying in duration and amplitude. These plots provide a qualitative overview of the neuronal responses. More quantitatively, Figure 2B displays the population-level receptive fields, visualized as heatmaps of normalized firing rate as a function of stimulus amplitude (x-axis) and duration (y-axis). These receptive fields highlight the differential tuning of each MR subtype. The SA1 MR response (Figure 2B, second panel) is primarily influenced by stimulus duration, showing an increase in firing rate as duration extends, particularly at lower to moderate amplitudes. This suggests a role for SA1 in integrating temporal information. In contrast, the RA MR response (Figure 2B, first panel) is predominantly governed by stimulus amplitude, exhibiting a sharp threshold; once this amplitude is surpassed, RA neurons fire robustly, largely independent of stimulus duration, consistent with their role in detecting the presence and onset/offset of a stimulus. The SA2 MRs (Figure 2B, third panel) demonstrate a clear sensitivity to both stimulus amplitude and duration, with their firing rate increasing systematically as either or both parameters increase.

This suggests that SA2 neurons encode a broader range of stimulus intensities and temporal extents. The TG population (Figure 2B, fourth panel), receiving convergent input, exhibits a receptive field that reflects a weighted combination of the three MR subtypes. It shows sensitivity to amplitude, influenced by RA, and to duration, influenced by SA1 and SA2.

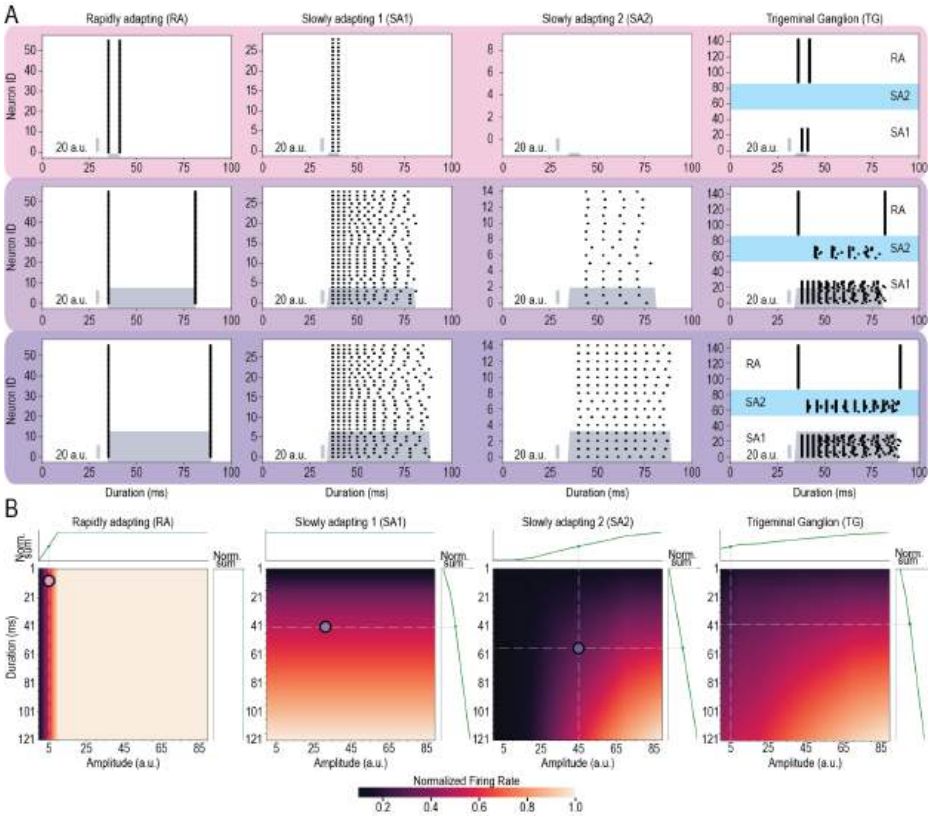


**Figure 2 - The relative sensitivity of each mechanoreceptors population create a sequence of activation with different functional roles.** A - Raster plots of SA1, SA2, RA and TG activity in response to stimuli with (Top to bottom) 7ms duration and amplitude of 5, 47 ms and amplitude of 30, and 55 ms and amplitude of 45. The amplitude corresponds to how much the whisker is pushed (a.u.) B - The heatmaps correspond to the normalized firing rate for the duration of the all stimulus (black : no activity, white : Maximum activity across all conditions is reached). X-axis represents the amplitude, y-axis the duration. For each heatmap, the green curve at the top is the normalized sum of the activity over the duration as a function of amplitude, the green curve on the side is the normalized sum of the activity over the amplitude as a function of duration.

Plotting the stimulus parameters at which each population reached 50% of its maximum response (contours in Figure 2B) further elucidates these differences. SA1 and RA populations show largely uni-dimensional thresholds: SA1 primarily

by duration and RA primarily by amplitude. In contrast, SA2 and TG exhibit bi-dimensional thresholds, requiring specific combinations of both amplitude and duration to reach half-maximal activation. The linear representation of the stimulus range by SA2 suggests it faithfully encodes graded stimulus features. The TG receptive field, while integrating these inputs, appears to somewhat "stretch" the stimulus representation, potentially enhancing resolution and discriminability for certain stimulus combinations.

This differential tuning leads to a sequence of activation depending on stimulus parameters. For stimuli of low amplitude and short duration, RA activity dominates, providing a rapid detection signal. As stimulus duration increases, even at low amplitudes, SA1 activity becomes more prominent, allowing for temporal integration and duration encoding. Finally, for stimuli of longer duration and higher amplitude, SA2 neurons are robustly activated, enabling the discrimination of both these variables. Consequently, as stimulus characteristics change, the TG activity dynamically reflects the underlying properties of the active MR populations, thereby conveying multifaceted information regarding stimulus amplitude and duration.

These results demonstrate that, at the periphery, distinct MR populations specialize in encoding different aspects of tactile stimuli. The observed dichotomy in encoding strategies – with RA focusing on detection and SA subtypes on detailed feature analysis (including duration and amplitude) – raises the question of how this segregated information is processed and whether this functional specialization is maintained or transformed at higher levels of the somatosensory system. This question was subsequently addressed by comparing model performance to behavioral data.

## Behavioral Characterization of Human Tactile Perception

To establish a behavioral benchmark for validating our computational model of mechanoreceptor encoding, we first characterized human tactile perception using precisely controlled stimuli delivered via focused ultrasound (Figure 3A). The stimuli were designed to allow independent manipulation of intensity (amplitude of 250 kHz ultrasound bursts) and perceived duration, achieved by varying the duty cycle (DC) of ultrasonic activation within a 125 ms stimulus envelope composed of five 25 ms sub-pulses (Figure 3B).

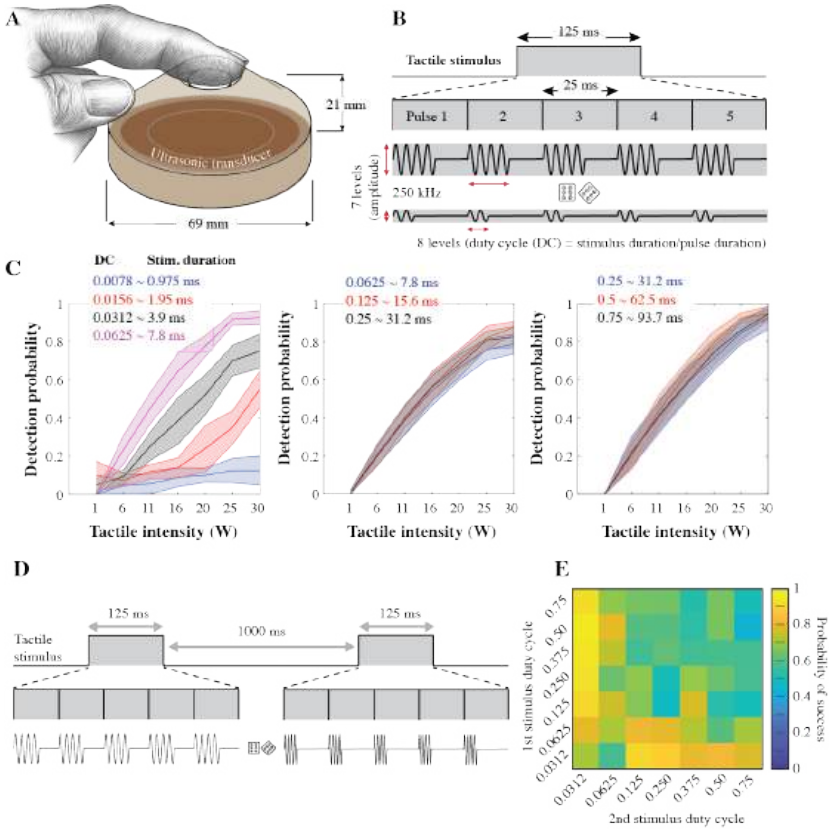


**Figure 3 - Characterization of Human Tactile Perception using Focused Ultrasound Stimulation.** A) Experimental setup depicting a participant's finger resting on the ultrasonic transducer (dimensions: 69 mm diameter, 21 mm height) used for delivering tactile stimuli. B) Schematic of the tactile stimulus structure. Each 125 ms overall stimulus envelope was composed of five 25 ms sub-pulses. Stimulus intensity was modulated across 7 amplitude levels of the 250 kHz ultrasound bursts. The perceived stimulus duration within each sub-pulse was varied across 8 levels of duty cycle (DC), defined as the ratio of active ultrasound burst duration to the sub-pulse duration (25 ms). C) Human psychometric performance in a tactile detection task. Detection probability is plotted against tactile intensity (W) for different stimulus durations, grouped into short (left panel: 0.0078 ms to 7.8 ms, corresponding to DC from 0.0078 to 0.0625 relative to the 125ms envelope, or 0.0312 to 0.312 relative to a 25ms sub-pulse), medium (middle panel: 0.0625 ms to 31.2 ms, corresponding to DC from 0.0625 to 0.25 relative to 125ms, or 0.25 to 1.0 relative to a 25ms sub-pulse assuming full activation of one or more sub-pulses), and long (right panel: 0.25 ms to 93.7 ms, corresponding to DC from 0.25 to 0.75 relative to 125ms) effective durations. Shaded areas represent ± SEM across participants. D) Stimulus paradigm for the temporal (DC) discrimination task. Two 125 ms tactile stimuli, each with a specific duty cycle defining its perceived duration, were presented sequentially, separated by a 1000 ms inter-stimulus interval. Participants were instructed to identify which of the two stimuli was longer. E) Human performance matrix for the duration discrimination task. The heatmap illustrates the probability of successfully identifying the longer stimulus as a function of the duty cycle (and thus effective duration) of the first stimulus (y-axis) and the second stimulus (x-axis). Warmer colors (yellow) indicate a higher probability of success, while cooler colors (blue/green) indicate performance closer to chance level (0.5).

### Stimulus Duration and Intensity Influence Tactile Detection Thresholds

We initially assessed the ability of human participants to detect these tactile stimuli (Figure 3C). As anticipated, detection probability increased monotonically with tactile intensity (measured in Watts, W) across all conditions. However, the effective stimulus duration, modulated by the duty cycle, also played a significant role. For stimuli with very short effective durations (e.g., ranging from 0.0078 ms to 7.8 ms, Figure 3C, left panel), distinct psychometric curves were observed. Longer durations within this short range generally resulted in higher detection probabilities for a given intensity, indicating that temporal summation contributes to detectability. This effect was less pronounced for stimuli with medium effective durations (0.0625 ms to 31.2 ms, Figure 3C, middle panel) and even more so for longer effective durations (0.25 ms to 93.7 ms, Figure 3C, right panel), where the psychometric curves for different specific durations within these ranges became more clustered. This suggests that while temporal summation is critical for the detection of brief stimuli, its impact on basic detection probability (for supra-threshold stimuli) diminishes as the overall duration increases, possibly due to saturation of neural responses or perceptual integration mechanisms. The distinct separation of curves at low durations implies a higher sensitivity to duration changes in this regime for basic detection.

### Duration Discrimination Performance Adheres to Weber's Law

Next, we investigated human ability to discriminate between the durations of two sequentially presented tactile stimuli in a temporal (DC) discrimination task (4 conditions: 1st stimulus is faster, 2nd is faster, they are the same, I felt a single stimulus. Figure 3D). The performance matrix (Figure 3E) shows the probability of successfully identifying the longer stimulus as a function of the duty cycle (proxy for effective duration) of the first and second stimuli. As depicted, discrimination accuracy was highest (approaching 1.0, yellow regions) when there was a large relative difference between the durations of the two stimuli (e.g., comparing a very short DC with a very long DC). Conversely, when the durations of the two stimuli were similar (i.e., along the diagonal of the matrix), performance approached chance level (0.5, greenish regions). This pattern, where the just-noticeable difference in stimulus duration is proportional to the reference duration, is characteristic of Weber's Law. This demonstrates that human tactile duration discrimination follows established psychophysical principles, providing a robust dataset for comparing the information processing capabilities of our neural model. The systematic variation in performance across the matrix provides a rich target for our model to replicate, reflecting the precision of temporal encoding in the human tactile system.

These behavioral experiments provide crucial quantitative data on how humans detect and discriminate tactile stimuli of varying intensities and durations. These psychophysical functions, particularly the duration discrimination matrix, serve as the primary "top-down" benchmark against which the "bottom-up" encoding capabilities of our mechanoreceptor model will be evaluated.

## Stimulus Duration Encoding in Firing Rate

The inherent adaptation rates of mechanoreceptor (MR) subtypes critically shape the relationship between stimulus duration and the resultant firing rate of their neural populations. Our simulations demonstrate that only the slowly adapting (SA) neurons exhibit firing rates that are systematically modulated by changes in stimulus duration.

To investigate this, we applied ramp-and-hold stimuli of varying durations to our modeled populations and quantified the number of spikes produced by each (Figure 4). Figure 4A presents raster plots illustrating the responses of SA1, SA2, RA, and Trigeminal Ganglion (TG) neurons to stimuli with increasing duty cycles (DC), which directly correspond to increasing durations of the stimulus "upstate" (the sustained portion of the stimulus). Visually, it is evident that RA MRs respond consistently with a burst of activity primarily at the onset of the stimulus upstate, irrespective of its total duration. If the stimulus was already in its upstate at the beginning of a simulation window (e.g., for longer DCs), RA neurons did not typically fire at that point, underscoring their sensitivity to *changes* in stimulation rather than sustained presence. In contrast, the density of spikes within the upstate period for both SA1 and SA2 populations clearly increases as the stimulus duration (DC) increases. The TG population, integrating these inputs, also shows an increased number of spikes with longer stimulus durations.

Quantifying this relationship, Figure 4B plots the population firing rate (spikes per trial) against the duration of the stimulus upstate. The RA population (bottom-left panel) exhibits a flat response curve, confirming that its firing rate is largely independent of the stimulus upstate duration. This reinforces the notion that RA receptors are specialized for signaling transient events (onset/offset) rather than encoding the duration of sustained stimuli. Conversely, both SA1 (top-left panel) and SA2 (top-right panel) populations demonstrate a clear and positive correlation between firing rate and stimulus duration. However, the nature of this relationship differs due to their distinct adaptation characteristics. The SA2 response increases approximately linearly with stimulus duration, indicating a relatively consistent encoding of duration over time. The SA1 response, on the other hand, increases

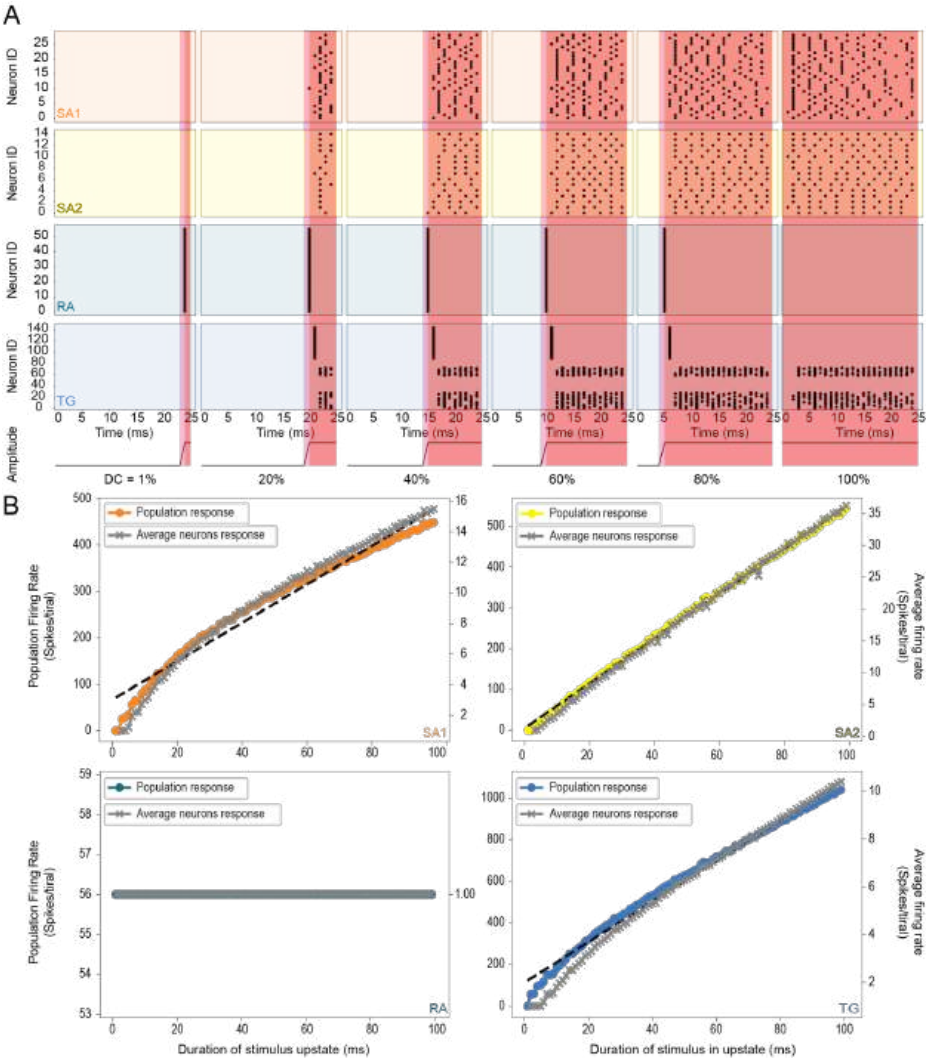


**Figure 4 - Only SA1 and SA2 mechanoreceptors bear information on the stimulus duration.** A) A raster plot of the different populations of the model in response to different durations of duty cycle. Y-axis is the ID of the neurons. Y-axis is the duration of the trial. The percentage corresponds to the fraction of the trial duration during which the stimulus is in an upstate status. Each dot on the raster plot represents a spike. B) Number of spikes produced by each population as a function of the upstate duration. X-axis (left) is the total number of spikes produced by the considered population. X-axis (right) is the average spike per neuron. Y-axis is the duration of the upstate, that is, the duration of the hold phase in the ramp-and-hold stimulus. The colored lines with dots are the population responses. The grey crossed line represents the average neuron's response.

more logarithmically (or sub-linearly initially, then becoming more linear). This pattern reflects its stronger initial adaptation; the firing rate is high at the onset but adapts, so the *total* number of spikes accumulates less rapidly than in the more linearly responding SA2 population. The TG population's response (bottom-right panel) appears to be a composite of these inputs. For shorter durations, its response profile more closely mirrors the SA1 profile, while for longer durations, it tends to follow the more linear increase characteristic of the SA2 input. This suggests a dynamic weighting or influence of the SA subtypes on the TG output depending on the stimulus duration.

Given these distinct response profiles, SA1, SA2, and consequently the TG, all possess firing rate characteristics that could, in principle, encode stimulus duration. To rigorously assess their respective capacities to represent this temporal dimension and to compare this encoding with human perceptual capabilities, we subsequently trained different classifiers on the firing rate outputs of these neural populations.

## Decoding Stimulus Duration from Mechanoreceptor and TG Activity

To evaluate the decodability of stimulus duration information encoded by each population, we trained and compared the performance of different classifiers on the firing rates of SA1, SA2, RA, and TG (Figure 5). The classification error plots (top row) and cumulative error plots (second row) consistently demonstrate that decoders trained on SA1, SA2, and TG activity achieve significantly better-than-chance performance in discriminating stimulus duration, with error rates decreasing as the difference in stimulus duration increases. In stark contrast, decoders trained on RA activity perform near chance level across all duration differences, confirming that RA firing rate is not informative for duration discrimination, consistent with Figure 5.

The accuracy matrices and SSIM heatmaps (bottom of Figure 5) provide a more nuanced comparison of decoder performance across populations and decoder types. For SA1 and SA2, all decoders – including the linear Ridge classifier, Bayesian Naïve Bayes, and non-linear MLP and MiPinet – achieve high and comparable accuracy, as indicated by the high SSIM values across decoder pairs. This suggests that duration information in SA1 and SA2 firing rates is relatively straightforward to extract, even with linear methods. However, for the TG, a notable divergence in decoder performance emerges. While MLP and MiPinet maintain high accuracy on TG data, comparable to their performance on SA1 and SA2, the simpler Linear and Bayes classifiers show a clear reduction in accuracy when decoding TG output. This is evidenced by the lower SSIM values when comparing MLP/MiPinet to Linear/Bayes for TG. This suggests that the integration of RA and SA inputs within

the TG, while potentially enriching the overall stimulus representation, creates a more complex and less linearly separable encoding of stimulus duration. The high performance of MLP and MiPinet, both capable of learning non-linear relationships, indicates that duration information is present in the TG output, but extracting it optimally may require more sophisticated, non-linear decoding strategies. This finding raises a critical question: if the TG integrates diverse mechanoreceptor signals, does this integration enhance or hinder the efficient decoding of specific stimulus features like duration? The reduced performance of simpler decoders on TG, despite the presence of duration information extractable by more complex methods, hints at a potential trade-off and suggests that segregated pathways might be more conducive to rapid and efficient downstream decoding, particularly by simpler neural circuits.

## Information Theoretic Analysis: First Spike Dominance and Redundancy

To further dissect the neural code for stimulus duration and assess the efficiency of information transfer, we employed information-theoretic measures, specifically Mutual Information (MI) and Coinformation (Figure 6). The MI analysis (Figure 6, left panels) reveals a striking and consistent pattern across all mechanoreceptor populations and the TG: the first spike carries the largest amount of information about stimulus duration, and the information content progressively decreases for subsequent spikes. This first-spike dominance is evident in the decreasing MI values from the 1st to the 5th spike rank for all populations. SA2 consistently exhibits the highest MI values across all spike ranks, indicating a more sustained and informative representation of duration in its spike train compared to SA1 and TG. RA shows the lowest MI, again confirming its limited role in duration encoding. The inset plot of average MI reinforces this trend, showing the overall ranking of information content across populations. This finding of first-spike dominance is significant, aligning with principles of efficient neural coding and suggesting that the somatosensory periphery prioritizes the rapid transmission of stimulus-relevant information in the initial neuronal response.

The Coinformation analysis (Figure 6, right panels) provides further insights into the redundancy or synergy in information encoding across spikes within each population. Crucially, all calculated coinformation values are negative, consistently indicating redundancy in information encoding between neighboring spikes across all populations and spike rank comparisons. This redundancy implies that subsequent spikes, beyond the first, largely convey overlapping information about stimulus duration, offering diminishing returns in terms of novel information. This

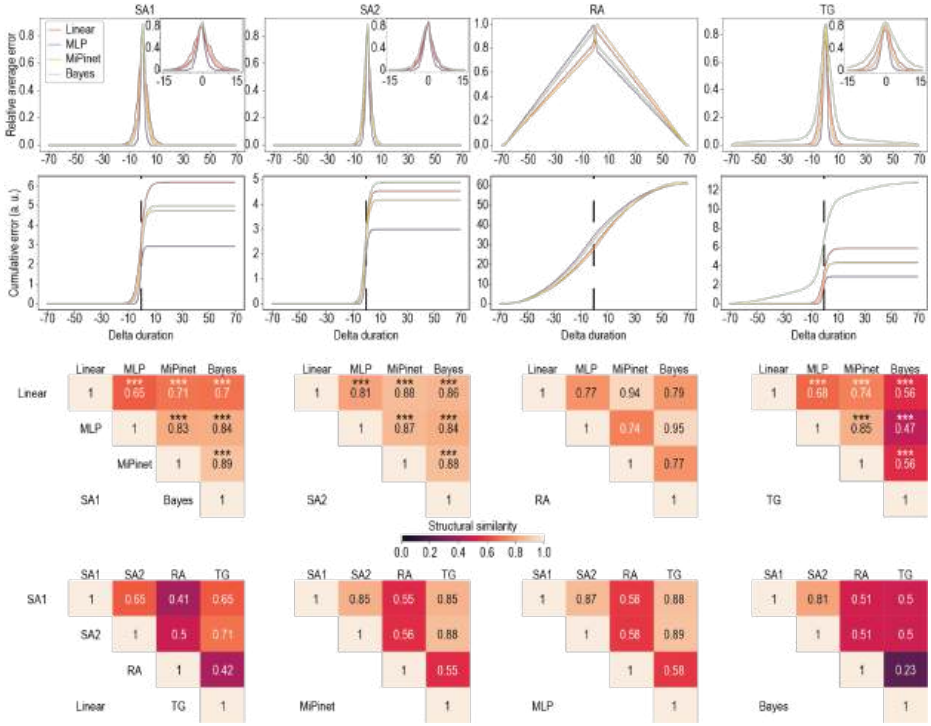


**Figure 5 - Classification Performance for Stimulus Duration Discrimination.** Relative average error (top row) and cumulative error (second row) for four different decoders (Linear - red, MLP - orange, MiPinet - yellow, Bayes - purple) as a function of the difference in duration (Delta duration) between two stimuli. Each column represents a different neural population (SA1, SA2, RA, TG) from which the decoder extracted firing rate information. Insets in the top row provide a magnified view around zero delta duration. Vertical black lines in the cumulative error plots roughly indicate the delta duration at which performance begins to saturate. The third row displays matrices of Structural Similarity (SSIM) comparing the overall accuracy patterns between pairs of decoders for each neural population. Higher SSIM values (warmer colors) indicate more similar performance patterns. Asterisks (***) denote statistically significant differences ($p < 0.001$) in decoder performance based on KS-tests on the cumulative error. The bottom row shows SSIM matrices comparing the performance of each individual decoder *across* the different neural populations (e.g., how similarly the Linear decoder performed on SA1 vs. SA2). These results collectively illustrate the decodability of duration information from each population and the relative efficacy of different decoding strategies.

redundancy, coupled with the first-spike dominance observed in the MI analysis, suggests a highly efficient coding strategy where the initial neuronal response is maximally informative, and subsequent spikes primarily serve to reinforce or refine the initial signal, rather than adding substantial new information about stimulus duration. The degree of information decay across spike ranks, as noted in the figure caption, correlates with the adaptation rates of the different populations. SA1, with faster adaptation, shows a more rapid decline in MI after the first spike compared to SA2, which exhibits slower adaptation and a more sustained information content across spike ranks. The TG, as a mixed population, falls in between. This link between adaptation rate and temporal information encoding further underscores the functional specialization of mechanoreceptor subtypes in shaping the temporal dynamics of tactile information processing.

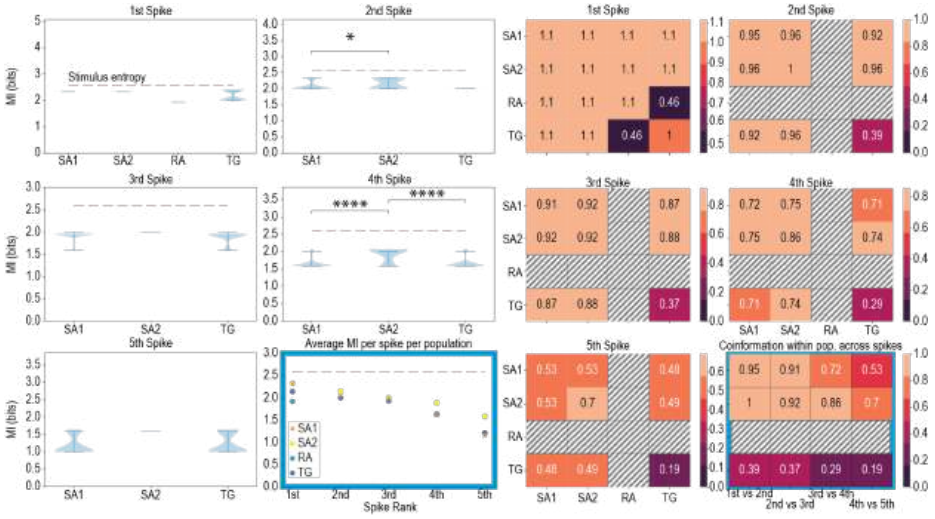


**Figure 6 - Mutual information and Co-information.** Left - Mutual information between the 1st spike timing of each neuron within a population and the duration of the stimulus. The timing of the 2nd spike of each neuron and the duration of the stimulus, ect. The y-axis is the Mutual information in bits. The x-axis is the population. The red dashed line represents the entropy of the stimulus (~= 2.6 bits). Each violin plot represents the distribution of the MI between the timing of the 1st, 2nd, 3rd, etc. spike of each neuron and the stimulus duration. The figure with the blue boundaries represents the average MI for the 1st spike, 2nd spike, etc. for the entire population. Right - Co-information between the timing of the 1st, 2nd, 3rd, etc. spike and the stimulus duration. Negative value represents synergy of information amongst the spikes across populations, positive values represent redundancy. The figure with the blue boundaries represents the co-information within the population across spikes, that is, a comparison between the information of the 1st and 2nd spike, 2nd and 3rd, etc.

In summary, the information-theoretic analyses in Figure 6 strongly support the notion of an efficient neural code in the somatosensory periphery for stimulus duration, characterized by first-spike dominance and redundancy in subsequent spikes. This efficient coding strategy may optimize rapid and reliable transmission of tactile information to higher processing centers, potentially enabling fast perceptual decisions and motor responses.



## Discussion

In this study, we addressed how the somatosensory periphery collectively encodes tactile information by developing the first spiking computational model integrating mechanoreceptor (MR) responses with trigeminal ganglion (TG) neuron dynamics. This bottom-up approach allowed us to investigate the neural encoding of touch starting from the initial sensory transduction at mechanoreceptors and compare our model's performance to behavioral data from human psychophysical experiments. Our findings reveal that the model accurately captures key aspects of tactile processing and matches or exceeds human performance. Through extensive information-theoretic analyses and the development of a novel sparse decoder network, we have gained critical insights into the neural coding of touch, explicitly highlighting the efficiency of early spike timing and parallel processing of touch in the somatosensory periphery.

### Model validity

We created a model relying on three types of MRs, fitted to electrophysiological data [14]. These three populations represent SA1, SA2, and RA MRs, found in mammals' tactile systems [16, 18, 14]. While the number of different mechanosensitive cell types in biology extends beyond this classification, their recordings are often limited to these three types of MRs [14], sometimes expanded with an RAII response [29]. In their work, Furuta et al. (2019) [30] developed different types of MRs along with their position within a whisker follicle. They showed that the placement of Merkel cells at different depths within the follicle had an impact on their activity: Merkel cells situated close to the surface of the skin exhibited an SA1 pattern of activity, that is, a strong response at the stimulus onset, followed by a lower baseline activity during the hold phase of a ramp-and-hold, while Merkel cells located deeper in the skin were exhibiting activity only at the onset. In their model, RA activity (activity at the onset and offset of the stimulus only) is produced by both lanceolate endings and club-like endings. In any case, none of the cells that they modelled demonstrated a SA2 pattern of activity (same as SA1 but with a slower decay toward a plateau phase during the hold

phase). The novelty of our network model comes from the joint reproduction of mechanosensitive cells and the TG. Our model of the TG receives input from the MRs in a one-to-one fashion, thus replicating the MRs' pattern of activation (Figure 2). Consequently, we can cluster TG cells into two categories: one population responding only at the onset/offset of the stimulus (RAs) and one firing at the onset/offset of the stimulus and throughout the hold period (SAs), as has been described before [31]. The inclusion of MR models allows us to replicate the precisely timed TG response to the transient part of the stimulus and regular spiking during stimulus presentation, as is witnessed in classical work led by Minnery and Simmons (2003) [28] or more recent work such as Bale et al., (2009) [32]. Moreover, this model preserves the ratio between a high ON response compared to a lower OFF response. The highly synchronized activity that we observed across the neurons in the periphery can be explained by the absence of noise in our model, inspired by the known low levels of noise in this system (Minnery and Simmons 2003) [28]. All these elements make our model a believable candidate to describe computations at the lower processing levels of the tactile system. While other models have focused on modelling the thalamus [33] or the barrel field [34, 33], the lower areas of the nervous system remain a blind spot to the modelling community. Our computational model aims at understanding the crucial stimulus transformation occurring at the very input of the tactile system. The low-level tactile systems of mammals are built from a shared set of mechanoreceptive cell types (Merkel cells, Ruffini endings, Meissner corpuscles, Pacinian corpuscles), which consistently give rise to SA1, SA2, RA, and, in some reports, RAII response patterns across species. Our model is deliberately grounded in these conserved building blocks. We replicate the stimulation conditions of the sonication experiments within the model and compare its output directly to the behavioral responses observed in humans.

## Duration Decoding and Neural Efficiency

The Multilayer Perceptron (MLP), known for its capacity as universal function approximators [35], and our novel and Mutual Information based Pre-Initialised Network (MiPinet) exhibited the highest decoding performance. Notably, these advanced classifiers achieved comparable accuracy regardless of whether they were trained on the activity of SA1, SA2, or TG populations, and they exceeded human performance in psychophysical tasks. However, simpler decoders, including the Bayesian and Linear classifiers, along with MiPinet, demonstrated a differential ability to leverage information from different neural populations. Specifically, these decoders did not fully exploit the information in the TG output, revealing that SA2 mechanoreceptors provided the most readily decodable representation of stimulus duration. Given the biologically implausible all-to-all connectivity structure of MLP, it is unlikely that biological systems achieve the same level of decoding capacity

as shown by our experimental data. This observation, coupled with the differential performance of simpler decoders, suggests that an optimal neural representation of tactile stimuli might necessitate a functional segregation of information related to stimulus duration and detection into distinct pathways within the TG. In biology, this separation has been witnessed amongst RAs and SAs responses [36] through electrophysiological recordings. We provide evidence that such a separation maximizes the decodability of the different dimensions of the stimulus, thus demonstrating the functional role of this differentiation. Our results suggest that the different SA responses should remain separated as well to maximize the decodability of a stimulus. We demonstrated that keeping the output of the MRs into three different pathways is necessary to preserve optimal decodability.

## First Spike Dominance and Redundancy: Implications for Efficient Coding

A key finding of our study, consistent with the efficient coding hypothesis in sensory systems, is the dominant role of the first action potential in encoding stimulus duration information [37]. The first spike consistently carried the largest proportion of stimulus-related information across all analyzed populations (SA1, SA2, RA, and TG). Furthermore, coinformation analysis revealed a high degree of redundancy among temporally neighboring spikes, implying that subsequent spikes contribute largely redundant information regarding stimulus duration. This observation aligns with the abstract's emphasis on the first spike carrying most information and highlights the efficiency of neural coding in the tactile periphery. While spike timing itself, as revealed by MI analysis, did not capture the entirety of duration variability, the temporal precision of the first spike is a crucial feature for efficient stimulus encoding. Interestingly, the rate of information decay across subsequent spike ranks was directly linked to the adaptation rate of each mechanoreceptor population. SA2 receptors, with their slower adaptation, exhibited a more sustained representation of duration across spike ranks compared to SA1 and RA subtypes, suggesting a differential contribution to temporal encoding. In this study, we demonstrated that within such a system, presented with such stimuli, the first spike is the most informative spike but also that all information not represented in this spike is lost to the system as every other spike is redundant. In summary, our results confirm the special role of the first spike in tactile encoding [37] and extend this principle by demonstrating that subsequent spikes contribute little beyond what is already conveyed in the initial response (Figure 6). This systematic redundancy—quantified through coinformation—reveals that the tactile periphery relies on a highly compressed representation in which virtually all stimulus-specific information is concentrated in the timing of the first spike. Thus, the novelty of our

finding lies not only in reaffirming the information dominance of the first spike, but in showing that later spiking activity fails to add new information, underscoring the efficiency and parsimony of peripheral neural coding.

The high values of the calculated MI might appear surprising when compared to previous work [32]. However, the found MI values depend on the stimulus entropy, which is unfortunately not given in [32]. In its absence, it is rather complicated to compare two MI values. Nevertheless, the information propagated in our system is a high proportion of the input entropy. This can be explained by the deterministic nature of the model and the lack of added noise to the neurons. In the absence of such components, for a given stimulus, the model's output will always remain the same. However, the same output can result from different stimuli, as explained in the methods section. Thus, the MI calculated here can be seen as an evaluation of the compression that the stimulus undergoes within the system, due to its architecture and basic components.

## Parallel Computation and Functional Specialization

Our results strongly support the concept of parallel computation in the somatosensory system, starting at the level of heterogeneous mechanoreceptor populations. As highlighted in the introduction, mechanoreceptors are not uniform sensors but are specialized to encode different aspects of tactile stimuli. Our model demonstrates a functional division of labor, with RA receptors primarily acting as detectors, signaling stimulus onset and offset, and SA1 and SA2 receptors encoding more detailed stimulus features, including duration. Classifier performance and information-theoretic measures consistently indicated that both SA1 and SA2 populations contribute to duration encoding, while RA responses were less informative about duration per se, but crucial for signaling stimulus presence. The observation that the TG, as a linear integrator of RA and SA inputs, paradoxically impaired the decodability of stimulus duration for simpler decoders, further reinforces the hypothesis that functional segregation of RA and SA pathways is beneficial for optimal tactile processing, potentially enabling parallel pathways for detection and discrimination from the periphery. This segregation might optimize the system for both rapid detection of tactile events (mediated by RA pathways) and detailed analysis of stimulus features like duration (mediated by SA pathways), as hypothesized in the introduction.

While our model mechanoreceptor populations exhibited near-perfect stimulus detection, spiking reliably in response to any stimulus, behavioral data still revealed a degree of uncertainty in stimulus detection, particularly at higher stimulus

intensities above 11 W. This apparent discrepancy does not necessarily invalidate our model's conclusions. The behavioral accuracy, although not perfect, remained significantly above chance level, suggesting that the necessary information for stimulus detection is indeed present within the neural system, potentially at the mechanoreceptor level. The observed behavioral uncertainty likely arises from information loss or degradation at subsequent processing stages beyond the mechanoreceptor and TG levels, including cortical processing and decision-making mechanisms.

Although the TG, as a central relay, receives and integrates inputs from both RA and SA pathways, our findings suggest that this integration, implemented in our model as a weighted sum, paradoxically impairs the decodability of stimulus duration compared to relying on SA populations alone. This counterintuitive result supports the hypothesis that to maximize the neural representation of stimulus duration, the information from RA and SA pathways should ideally be processed in functionally segregated channels within the TG or downstream targets.

While anatomical studies indicate a degree of segregation in TG projections from SA and RA afferents [36], it is important to acknowledge that TG neurons are likely to receive convergent input, potentially from multiple mechanoreceptors of the same or even different subtypes [38]. However, even in the presence of convergence, the relative balance of SA and RA inputs could still lead to TG neurons that are functionally dominated by either SA or RA signals. Furthermore, despite potential integration in the TG, downstream brainstem neurons, which receive convergent input from TG neurons, could still maintain a degree of functional specialization due to an imbalance in SA and RA-dominated TG inputs. Lateral inhibition, as demonstrated in previous studies of brainstem nuclei [6], could further enhance the ability of the system to accurately discriminate stimulus duration even with some degree of pathway convergence. In the absence of evidence for complex, non-linear processing within TG neurons from biophysical recordings, our model suggests that the TG primarily functions as a linear integrator.

In conclusion, by employing multiple decoders trained to discriminate between different stimulus durations, we demonstrated that segregating neural activity into RA, SA1, and SA2 populations optimizes the encoding of distinct stimulus dimensions. This finding underscores the functional significance of mechanoreceptor differentiation: RA populations provide a rapid and reliable detection of stimulus onset and offset, while SA1 and SA2 populations encode stimulus duration with a higher fidelity. Together, these results show that the

parallel anatomical organization of mechanoreceptor pathways has computational advantages in enabling the somatosensory system to simultaneously support both rapid detection and detailed discrimination of tactile events.

## Novel Sparse Decoder Network and Neuromorphic Applications

In addition to characterizing neural coding in the tactile periphery, we introduced a novel sparse decoder network, MiPinet, inspired by biological neural network architectures and gene regulatory networks. This network, with its sparse connectivity and biologically-informed initialization, demonstrated accurate classification of tactile stimuli with minimal training. The success of MiPinet paves the way for neuromorphic applications in artificial touch sensing. The efficient performance of this sparse decoder underscores the potential for developing computationally efficient and biologically plausible artificial tactile systems that mimic the encoding and decoding strategies employed by the somatosensory periphery.

## Limitations and Future Directions: Towards a Comprehensive Tactile Model

Our model, while providing valuable insights, incorporates several simplifications. First, we modeled a one-to-one connectivity between mechanoreceptors and TG neurons, although experimental evidence primarily supports this direct connectivity, the possibility of convergence from multiple mechanoreceptors of the same type onto a single TG neuron cannot be entirely excluded [27]. Second, our classification of mechanoreceptors into SA1, SA2, RA subtypes, while reflecting established categories, represents a simplification of the inherent heterogeneity within mechanosensitive cells in the skin. Mechanoreceptor properties and densities vary with location and depth within the skin, and cells classified under the same subtype umbrella may still encode different aspects of tactile stimuli. For instance, a cell exhibiting an SA1-like firing pattern in one skin region may respond to a different stimulus property than an SA1 cell in another region. The activity of Merkel cells at different depth within the whisker follicle is an example of this different responses as shown by Furuta et al. [30]

Third, our mechanoreceptor dynamics were parameterized based on experimental data from rats and validated against ramp-and-hold recording [28]. While the fundamental biophysical properties and spiking activity patterns of mechanoreceptors are broadly conserved across mammals [18, 14], including humans, direct validation of model parameters with human data would be beneficial. Across mammalian species, the same types of specialized mechanoreceptor structures (Merkel cells, Ruffini corpuscles, Meissner corpuscles, etc.) are responsible for tactile encoding, and

the SA1, SA2, and RA functional categories consistently emerge [18, 14]. However, the distribution and density of these subtypes can vary across body parts and species, reflecting adaptations to different tactile environments. While the appendices used for tactile perception may vary (vibrissae in rodents, trunks in elephants, fingertips in humans), the underlying architecture of the tactile system, based on these fundamental mechanoreceptor types, remains conserved.

Fourth, our model omits pre-neuronal filtering of tactile stimuli by the skin and surrounding tissues. In reality, the mechanical properties of the skin itself [39] and structures like whiskers in rodents [40] play a significant role in shaping the stimulus reaching mechanoreceptors. These pre-neuronal filtering mechanisms can modify stimulus intensity, detection thresholds, and frequency sensitivity. While these factors could shift the population response characteristics, the fundamental relationship between the stimulus and mechanoreceptor firing patterns, particularly in terms of adaptation dynamics and relative encoding of different stimulus features, is likely to remain qualitatively similar.

Finally, our study focused primarily on encoding stimulus duration, representing a limited dimensionality of the rich tactile world. Tactile perception encompasses multiple stimulus dimensions, including frequency, amplitude, direction, and spatial location, and these variables are often integrated and interact in complex ways. For instance, the firing rate of SA2 receptors is influenced by both stimulus amplitude and duration, such that an increase in either variable can result in increased firing, potentially confounding decoders trained solely on duration discrimination. Therefore, this study should be viewed as a foundational step towards a more comprehensive model that incorporates the multi-dimensional nature of tactile information and the interactions between different stimulus features in shaping mechanoreceptor responses and perceptual outcomes. Future research should extend this model to encompass these additional stimulus dimensions and explore their integration within the tactile pathway to provide a complete understanding of tactile processing.

# References


[1] L. L. Orefice, A. L. Zimmerman, A. M. Chirila, S. J. Sleboda, J. P. Head, D. D. Ginty, Peripheral mechanosensory neuron dysfunction underlies tactile and behavioral deficits in mouse models of ASDs. Cell 166, 299–313 (2016).

[2] J.M. Loomis, S.J. Lederman Tactual perception K.R. Boff, L. Kaufman, J.P. Thomas (Eds.), Cognitive processes and performance, Handbook of perception and human performance, Vol. 2, John Wiley & Sons, New York (1986), pp. 31.1-31.41 (chap. 31)

[3] Johnson, K. O., Yoshioka, T., & Vega–Bermudez, F. (2000). Tactile Functions of Mechanoreceptive Afferents Innervating the Hand. *Journal Of Clinical Neurophysiology*, *17*(6), 539–558. https://doi.org/10.1097/00004691-200011000-00002

[4] Maksimovic, S., Nakatani, M., Baba, Y., Nelson, A. M., Marshall, K. L., Wellnitz, S. A., Firozi, P., Woo, S., Ranade, S., Patapoutian, A., & Lumpkin, E. A. (2014). Epidermal Merkel cells are mechanosensory cells that tune mammalian touch receptors. *Nature*, *509*(7502), 617–621. https://doi.org/10.1038/nature13250

[5] De Haan, E. H., & Dijkerman, H. C. (2020). Somatosensation in the Brain: A Theoretical Re-evaluation and a New Model. *Trends in Cognitive Sciences*, *24*(7), 529–541. https://doi.org/10.1016/j.tics.2020.04.003

[6] Rault, N., Bergmans, T., Delfstra, N., Kleijnen, B. J., Zeldenrust, F., & Celikel, T. (2024b). Where Top-Down Meets Bottom-Up: Cell-Type Specific Connectivity Map of the Whisker System. Neuroinformatics, 22(3), 251–268. https://doi.org/10.1007/s12021-024-09658-6

[7] Jin, P., Jan, L. Y., & Jan, Y. (2020). Mechanosensitive Ion Channels: Structural Features Relevant to Mechanotransduction Mechanisms. *Annual Review Of Neuroscience*, *43*(1), 207–229. https://doi.org/10.1146/annurev-neuro-070918-050509

[8] Shao, Y., Hayward, V., & Visell, Y. (2020). Compression of dynamic tactile information in the human hand. *Science Advances*, *6*(16). https://doi.org/10.1126/sciadv.aaz1158

[9] Ouyang, Q., Wu, J., Shao, Z., Chen, D., & Bisley, J. W. (2020). A Simplified Model for Simulating Population Responses of Tactile Afferents and Receptors in the Skin. *IEEE Transactions On Biomedical Engineering*, *68*(2), 556–567. https://doi.org/10.1109/tbme.2020.3007397

[10] Gerling, G. J., Rivest, I. I., Lesniak, D. R., Scanlon, J. R., & Wan, L. (2013). Validating a Population Model of Tactile Mechanotransduction of Slowly Adapting Type I Afferents at Levels of Skin Mechanics, Single-Unit Response and Psychophysics. *IEEE Transactions On Haptics*, *7*(2), 216–228. https://doi.org/10.1109/toh.2013.36

[11] Deflorio, D., Di Luca, M., & Wing, A. M. (2022). Skin and Mechanoreceptor Contribution to Tactile Input for Perception: A Review of Simulation Models. *Frontiers in Human Neuroscience*, *16*. https://doi.org/10.3389/fnhum.2022.862344

[12] Abraira, V. E., & Ginty, D. D. (2013). The sensory neurons of touch. *Neuron*, *79*(4), 618–639. https://doi.org/10.1016/j.neuron.2013.07.051

[13] Brette, R., & Gerstner, W. (2005b). Adaptive Exponential Integrate-and-Fire Model as an Effective Description of Neuronal Activity. *Journal Of Neurophysiology*, *94*(5), 3637–3642. https://doi.org/10.1152/jn.00686.2005

[14] Sonekatsu, M., & Gu, J. G. (2019b). Functional properties of mechanoreceptors in mouse whisker hair follicles determined by the pressure-clamped single-fiber recording technique. *Neuroscience Letters*, *707*, 134321. https://doi.org/10.1016/j.neulet.2019.134321

[15] Johansson, R. S., & Vallbo, Å. B. (1983). Tactile sensory coding in the glabrous skin of the human hand. *Trends in Neurosciences*, *6*, 27–32. https://doi.org/10.1016/0166-2236(83)90011-5

[16] Johansson, R. S., & Vallbo, A. B. (1979). Tactile sensibility in the human hand: relative and absolute densities of four types of mechanoreceptive units in glabrous skin. *The Journal Of Physiology*, *286*(1), 283–300. https://doi.org/10.1113/jphysiol.1979.sp012619

[17] Bensmaia, S. (2008). Tactile intensity and population codes. *Behavioural Brain Research*, *190*(2), 165–173. https://doi.org/10.1016/j.bbr.2008.02.044

[18] Saal, H. P., & Bensmaia, S. J. (2014). Touch is a team effort: interplay of submodalities in cutaneous sensibility. *Trends in Neurosciences*, *37*(12), 689–697. https://doi.org/10.1016/j.tins.2014.08.012

[19] Hansen, N. (2007). The CMA Evolution Strategy: A Comparing review. *Studies in Fuzziness And Soft Computing*, 75–102. https://doi.org/10.1007/3-540-32494-1_4

[20] Pedregosa F., Varoquaux G., Gramfort A., Michel V., Thirion B., Grisel O., Blondel M., Prettenhofer P., Weiss R., Dubourg V., Vanderplas J., Passos A., Cournapeau D., Brucher M., Perrot M., & Duchesnay É. (2011b). SciKit-Learn: Machine Learning in Python. *Journal Of Machine Learning Research*. https://doi.org/10.5555/1953048.2078195

[21] Zeisel, A., Muñoz-Manchado, A. B., Codeluppi, S., Lönnerberg, P., La Manno, G., Juréus, A., Marques, S., Munguba, H., He, L., Betsholtz, C., Rolny, C., Castelo-Branco, G., Hjerling-Leffler, J., & Linnarsson, S. (2015). Brain structure. Cell types in the mouse cortex and hippocampus revealed by single-cell RNA-seq. *Science (New York, N.Y.)*, *347*(6226), 1138–1142. https://doi.org/10.1126/science.aaa1934

[22] Bergmans, T., Jamal, T., & Celikel, T. (2022). NETSCOPE: Information-Theory based Network Discovery and Analysis. *bioRxiv (Cold Spring Harbor Laboratory)*. https://doi.org/10.1101/2022.04.18.488630

[23] Bell, A. J. (2003, April). The co-information lattice. In Proceedings of the fifth international workshop on independent component analysis and blind signal separation: ICA (Vol. 2003).

[24] Bao, S. C., Li, F., Xiao, Y., Niu, L., & Zheng, H. (2023). Peripheral focused ultrasound stimulation and its applications: From therapeutics to human-computer interaction. *Frontiers in neuroscience*, *17*, 1115946. https://doi.org/10.3389/fnins.2023.1115946

[25] Verhagen, L., Gallea, C., Folloni, D., Constans, C., Jensen, D. E., Ahnine, H., Roumazeilles, L., Santin, M., Ahmed, B., Lehericy, S., Klein-Flügge, M. C., Krug, K., Mars, R. B., Rushworth, M. F., Pouget, P., Aubry, J. F., & Sallet, J. (2019). Offline impact of transcranial focused ultrasound on cortical activation in primates. *eLife*, *8*, e40541. https://doi.org/10.7554/eLife.40541

[26] Legon, W., Sato, T. F., Opitz, A., Mueller, J., Barbour, A., Williams, A., & Tyler, W. J. (2014). Transcranial focused ultrasound modulates the activity of primary somatosensory cortex in humans. *Nature neuroscience*, *17*(2), 322–329. https://doi.org/10.1038/nn.3620

[27] Sakurai, K., Akiyama, M., Cai, B., Scott, A., Han, B., Takatoh, J., Sigrist, M., Arber, S., & Wang, F. (2013). The Organization of Submodality-Specific Touch Afferent Inputs in the Vibrissa Column. *Cell Reports*, *5*(1), 87–98. https://doi.org/10.1016/j.celrep.2013.08.051

[28] Minnery, B. S., Bruno, R. M., & Simons, D. J. (2003). Response Transformation and Receptive-Field Synthesis in the Lemniscal Trigeminothalamic Circuit. *Journal Of Neurophysiology*, *90*(3), 1556–1570. https://doi.org/10.1152/jn.00111.2003

[29] Lewin, G. R., & Moshourab, R. (2004). Mechanosensation and pain. Journal of neurobiology, 61(1), 30-44.

[30] Furuta, T., Bush, N. E., Yang, A. E., Ebara, S., Miyazaki, N., Murata, K., Hirai, D., Shibata, K. I., & Hartmann, M. J. Z. (2020). The Cellular and Mechanical Basis for Response Characteristics of Identified Primary Afferents in the Rat Vibrissal System. *Current biology : CB*, *30*(5), 815–826.e5. https://doi.org/10.1016/j.cub.2019.12.068

[31] Lichtenstein, S. H., Carvell, G. E., & Simons, D. J. (1990). Responses of rat trigeminal ganglion neurons to movements of vibrissae in different directions. Somatosensory & motor research, 7(1), 47-65.

[32] Bale, M. R., & Petersen, R. S. (2009). Transformation in the neural code for whisker deflection direction along the lemniscal pathway. *Journal of neurophysiology*, *102*(5), 2771-2780.

[33] Huang, C., Zeldenrust, F., & Celikel, T. (2022). Cortical Representation of Touch in Silico. *Neuroinformatics*, *20*(4), 1013–1039. https://doi.org/10.1007/s12021-022-09576-5

[34] Sharp T, Petersen R and Furber S (2014) Real-time million-synapse simulation of rat barrel cortex. Front. Neurosci. 8:131. doi: https://doi.org/10.3389/fnins.2014.00131

[35] Cybenko, G. (1989). Approximation by superpositions of a sigmoidal function. *Mathematics of control, signals and systems*, *2*(4), 303-314.

[36] Kwegyir-Afful, E. E., Marella, S., & Simons, D. J. (2008). Response properties of mouse trigeminal ganglion neurons. *Somatosensory & motor research*, *25*(4), 209–221. https://doi.org/10.1080/08990220802467612

[37] Panzeri, S., Petersen, R. S., Schultz, S. R., Lebedev, M., & Diamond, M. E. (2001). The role of spike timing in the coding of stimulus location in rat somatosensory cortex. *Neuron*, *29*(3), 769–777. https://doi.org/10.1016/s0896-6273(01)00251-3

[38] Jones, L. M., Lee, S., Trageser, J. C., Simons, D. J., & Keller, A. (2004). Precise temporal responses in whisker trigeminal neurons. *Journal of neurophysiology*, *92*(1), 665–668. https://doi.org/10.1152/jn.00031.2004

[39] Scheibert, J., Leurent, S., Prevost, A., & Debrégeas, G. (2009). The role of fingerprints in the coding of tactile information probed with a biomimetic sensor. *Science (New York, N.Y.)*, *323*(5920), 1503–1506. https://doi.org/10.1126/science.1166467

[40] Hartmann, M. J., Johnson, N. J., Towal, R. B., & Assad, C. (2003). Mechanical Characteristics of Rat Vibrissae: Resonant Frequencies and Damping in Isolated Whiskers and in the Awake Behaving Animal. *Journal Of Neuroscience*, *23*(16), 6510–6519. https://doi.org/10.1523/jneurosci.23-16-06510.2003

# Supplemental Materials

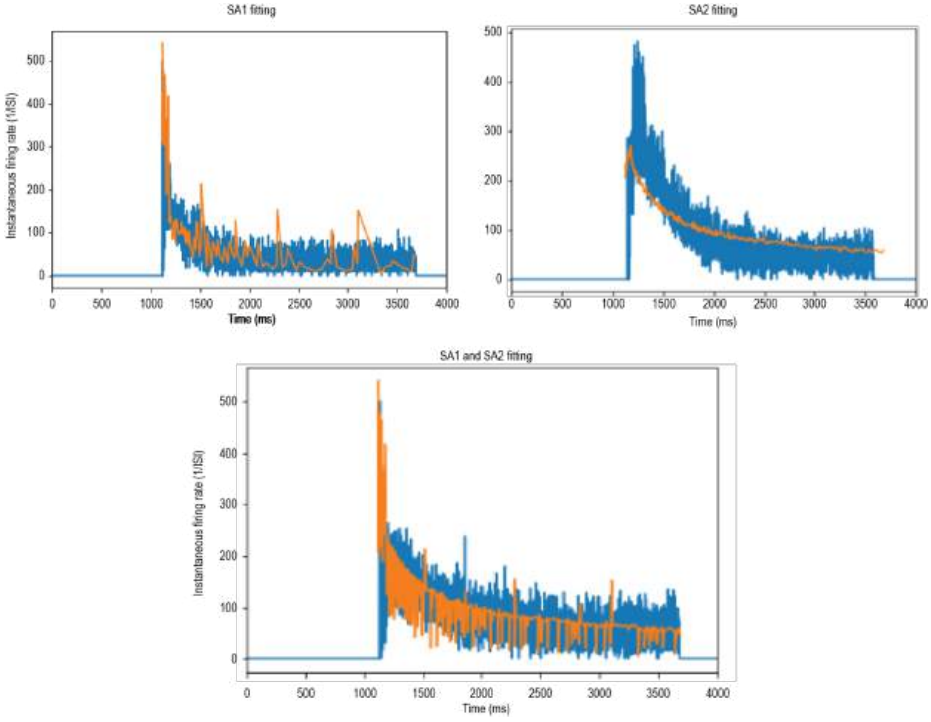


**Supplemental figure 1 -** We fitted the adaptive parameters of Adex neurons to the instantaneous firing rate from SA1 and SA2 MCs population.

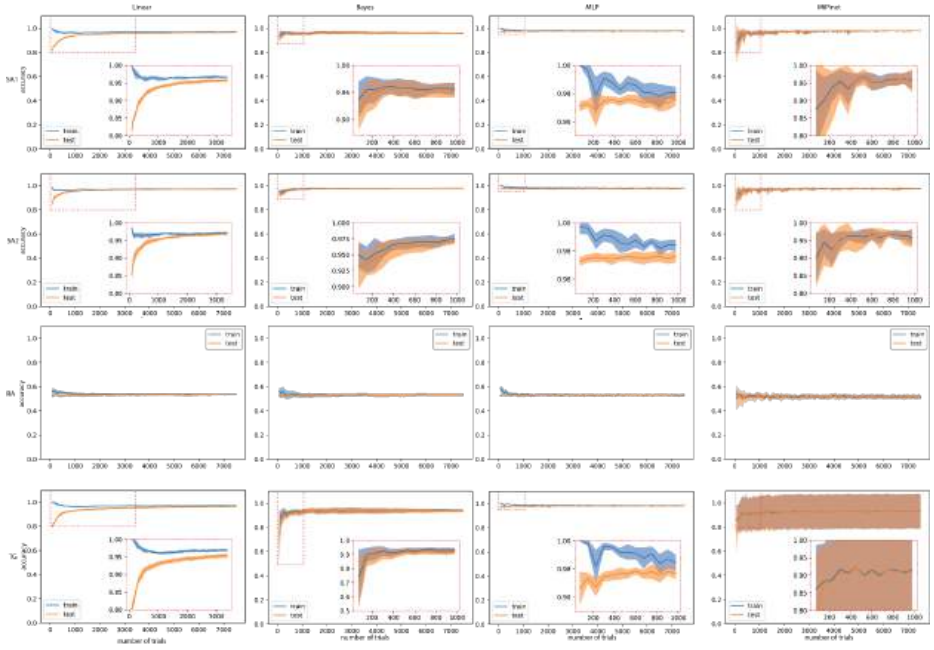

**Supplemental figure 2 -** We trained the different decoders on the firing rate per neuron per population on 10 000 data point. Over 10 epochs, 7500 datapoints were used for training, 2500 were used for testing.

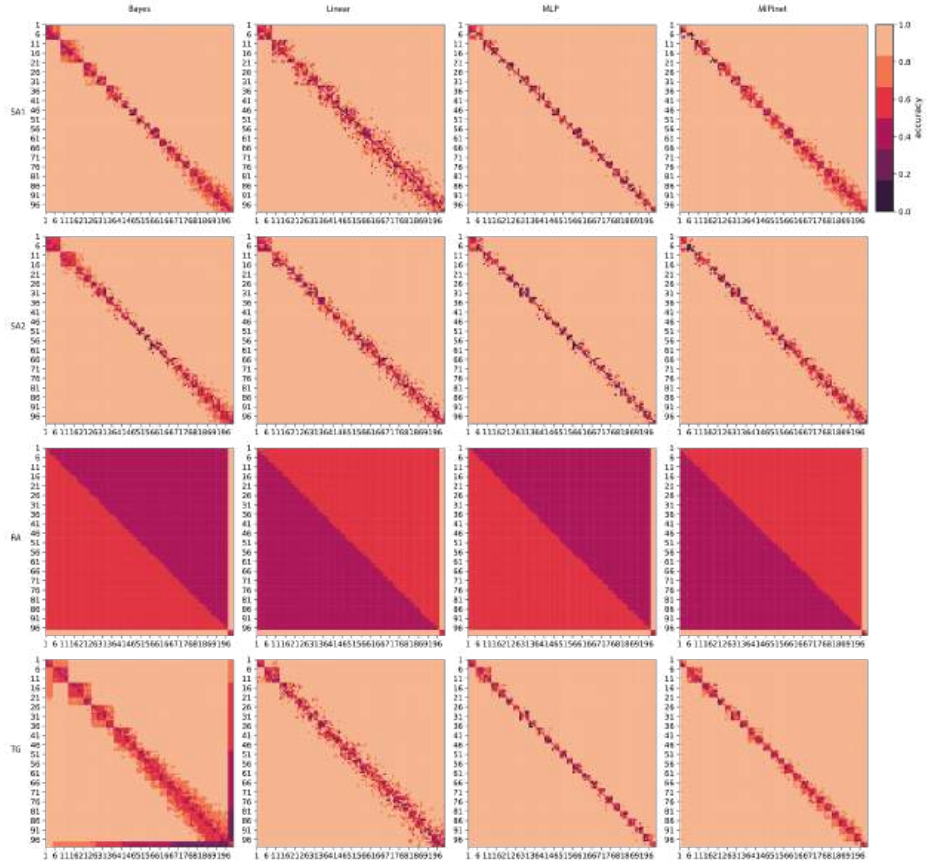


**Supplemental Figure 3 -** Once trained, we iterated through each stimulus condition and assessed the accuracy of 100 decoders.

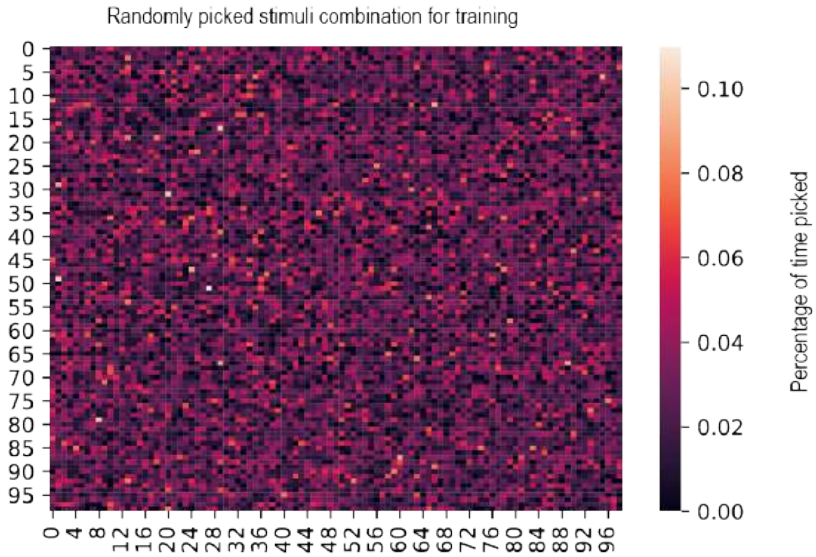


**Supplemental Figure 4 -** Heatmap representing for each pixel, the percentage time it was selected for training for a dataset of 10000 points.

**Table 1 -** Parameters of the adaptive current for SA1 and SA2 population fitted to the instantaneous firing rate from Sonekatsu and Gu 2019.

| | **SA1** | **SA2** |
|---|---|---|
| a | 20.23 nS | 46.11 nS |
| b | 69.65 pA | 3.21 pA |
| **τ** | 44.09 ms | 1882.05 ms |

**Table 2 -** KS-test score across decoders' accuracy within a neural population.

| | **KS test p-values on cumulative distributions** | | | | | | | | | | | | | | | |
|---|---|---|---|---|---|---|---|---|---|---|---|---|---|---|---|---|
| | **SA1** | | | | **SA2** | | | | **RA** | | | | **TG** | | | |
| | **Linear** | **MiPInet** | **MLP** | **Bayes** | **Linear** | **MiPInet** | **MLP** | **Bayes** | **Linear** | **MiPInet** | **MLP** | **Bayes** | **Linear** | **MiPInet** | **MLP** | **Bayes** |
| Linear | 1 | 2.5e-15 | 9.5e-17 | 7e-15 | 1 | 7e-15 | 8.5e-16 | 2e-14 | 1 | 0.49 | 1 | 1 | 1 | 2.5e-15 | 2.9e-16 | 9.5e-17 |
| MiPinet | | 1 | 2.9e-16 | 5.4e-14 | | 1 | 8.5e-16 | 2.5e-15 | | 1 | 0.49 | 0.49 | | 1 | 8.5e-16 | 9.9e-18 |
| MLP | | | 1 | 2.0e-16 | | | 1 | 2.0e-16 | | | 1 | 1 | | | 1 | 2.9e-19 |
| Bayes | | | | 1 | | | | 1 | | | | 1 | | | | 1 |

Chapter 4

# From Physical Contact to Neural Spiking: Modeling Tactile Perception in the early stages of sensory processing

## Abstract

The sense of touch allows us to navigate and manipulate objects while interacting with our environment. Through mechanotransduction, mechanoreceptors can transform pressure into neural signals. This pressure can encode the shape, direction, frequency, speed, or force of an object. Despite efforts to understand sensory processing, the process through which the tactile system dissects a stimulus to extract information about the environment remains elusive. We provide a model of the early stages of the ascending somatosensory pathway connected to a 3D model of a whisker (WhiskIt). The model of the ascending somatosensory pathway consists of three populations of mechanoreceptors responding to the forces applied to the whisker, which sends feed-forward connections to the Trigeminal Ganglion (TG), which is in turn connected to the brainstem (BS). We deflect the virtual whisker and record the forces and torques at its base. Varying one parameter at a time, we change the direction, amplitude of deflection, speed, and the point on the whisker at which we deflect. Additionally, we positioned a pole at the tip of the whisker and made it vibrate at different frequencies. Inputting the forces and torques to the mechanoreceptors, we train different decoders on the neural activity of each population to retrieve the stimulus identity and assess the quantity and type of information transferred by each population on the different dimensions of a touch stimulus. Through this approach, we demonstrate that while the neural populations in the periphery carry information on all aspects of the stimuli, each population is more informative on specific aspects of the stimulus and thus appears to be specialized, allowing the sensory system to build upon the heterogeneity of the mechanoreceptors to accurately represent all the ranges of tactile stimuli. This discrepancy in the encoding of the different aspects of a touch stimulus is abolished in the central nervous system as the connection from the touch cells converges to a single structure, which leverages the information gathered by the receptors.

## Introduction

Tactile integration is necessary for navigation, object manipulation, and social interactions [1]. Of all senses, tactile perception is at a peculiar place, as it matches with the boundaries of our body, determining what belongs to us and what is foreign, for the touch cells are embedded in our skin. Mechanoreceptors inform the system on vibration, texture, pressure, or temperature [2], allowing the body to interact with the environment



For rodents, the acquisition of accurate tactile information is a matter of life and death as they live in dark and narrow spaces, leaving little to interpret for vision. To resolve the nature of their environment, they rely on their vibrissae, attached to their snout, which they can sweep around to gather information [3]. These sensitive appendages take their root in a whisker follicle, paved with a variety of mechanosensitive cells that transform tactile stimuli into neural information [4]. These mechanoreceptor cells can be divided into several subtypes: Merkel cells exhibit an irregular firing pattern and account for Slowly Adapting Type 1 (SA1) behavior [5], characterized by a sharp increase of activity upon a stimulus onset and sharp decrease toward an irregular spiking pattern when the stimulus is sustained. Ruffini corpuscles are associated with Slowly Adapting Type 2 (SA2) behaviour, in which a sharp increase of activity is witnessed upon stimulus onset and a slow decrease toward a plateau activity when the stimulus is sustained. They are also sensitive to stretch [6]. Rapidly Adapting (RA) cells, cells that show activity only during the transient part of a stimulus (onset and offset), are divided between Meissner Corpuscles, sensitive to low-frequencies [6], and Pacinian Corpuscles, which respond to high-frequencies and are therefore sensitive to textures [6]. Relying on the information gathered by the touch-sensitive cells, the sensorimotor pathway can identify tactile stimuli and react accordingly through highly interconnected somatosensory and motor pathways [7].

Despite lots of efforts to investigate the neural code behind touch perception, little is known about the role of the diverse mechanosensitive cells and structures that send input to the cortex, mostly due to the difficulty of accessing and recording such areas. To bridge this gap, we build upon a 3D whisker model [8], allowing the manipulation of whiskers and accurate kinematics extraction at the basis of the vibrissae, and connect it to a spiking neural network [9] composed of three populations of mechanoreceptors (MCs): SA1, SA2, and RA. This network transmits activity to a model of the trigeminal ganglion, which itself sends activity to a model of the brainstem (nucleus principalis). These 4 nuclei form a complete model of the early stages of the lemniscal pathway [10].

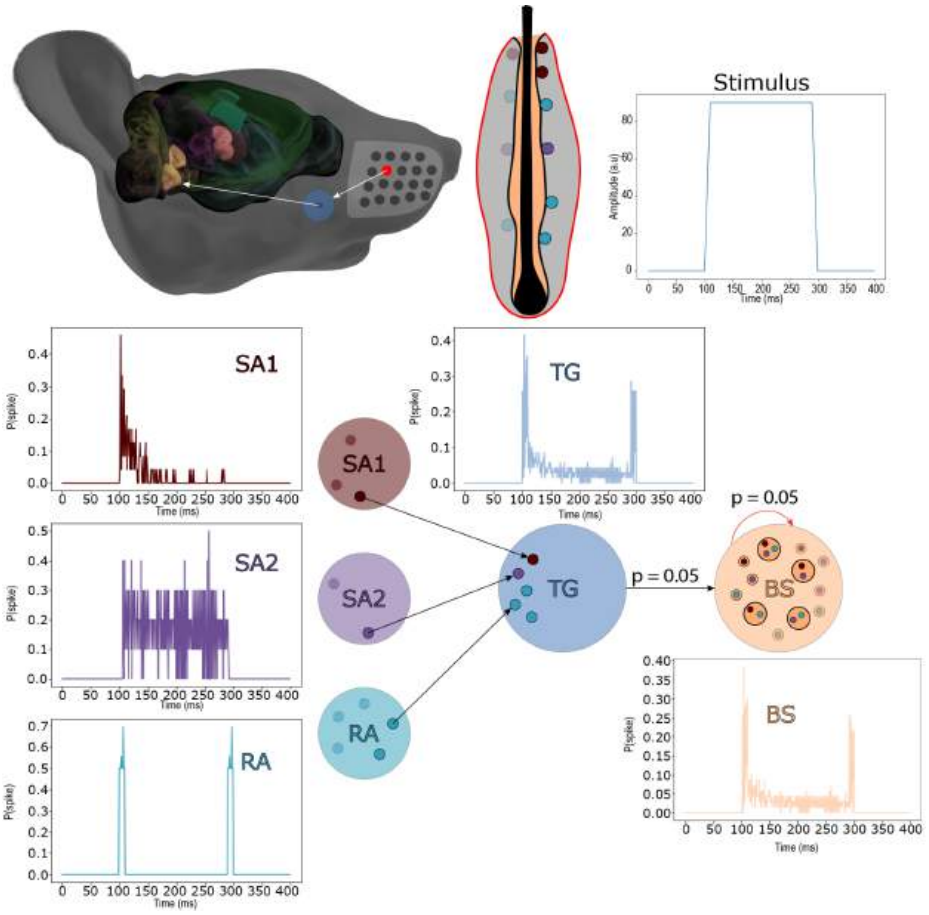


**Figure 1 - Schematic representation of the whisker-to-brainstem pathway and the response of each population to a ramp-and-hold stimulus. Top-left -** The modeled pathway going from the whisker (red), to the TG (blue), to the brainstem (orange). **Top-middle -** A representation of the whisker follicle with the mechanoreceptors (brown: SA1, purple: SA2, blue: RA) distributed within. **Top-left -** Amplitude of whisker deflection in time (x-axis is time in ms and y-axis is amplitude (a.u.)). **Bottom -** The plots represent the probability of each population to spike as a function of time, in response to the plotted amplitude (Top-left). The y-axis is the probability to spike, the x-axis is the time in ms. The three mechanoreceptor populations send a one-to-one connection to TG. Each neuron in TG has a probability of 0.05 to send an excitatory connection to any neuron in BS. Each neuron in BS has a probability of 0.05 to send an inhibitory connection to any other neuron in BS.

To investigate the roles of the different MCs in the encoding of tactile stimuli, we move a virtual pole against a 3D whisker model. This movement of the pole varies in its amplitude, speed, direction, and distance from the whisker basis. In addition, we place the pole at the tip of the whisker and change the frequency at which it vibrates. Next, we record the resulting neural activity from each population.

Through such extensive manipulation and recording of simulated tactile stimuli, we increase our insight into the neural code of touch perception, and we provide a whisker-to-brainstem model that relies on the accurate modeling of whisker kinematics and their conversion into neural codes. By training decoders on the neural activity of the different populations, we quantify the information transfer from whisker to cortex and assess the role taken by each population in the early stages of tactile information. Through correlation calculations between the firing rate of each neuron within each population, we show that the further the information travels along the ascending pathway, the more decorrelated single neuron activity becomes amongst the same population. Building on this finding, we demonstrate that single-neuron activity is sufficient to train a Bayesian decoder. Taken together, these results provide insight into the coding strategies of tactile stimuli along the ascending sensory pathway.



## Methods

In order to provide a full account of the somatosensory input the cortex receives from the periphery, we connected an existing whisker model [8] to a neural network model of the ascending pathway and recorded the resulting neural activity resulting from different stimuli. We then trained different classifiers to identify stimulus identities based on individual neuron firing rates and, in parallel, quantified the information transferred through spike timing and firing rate. Finally, we identified the neuron that transferred the most information for each stimulus in each population and retrained the decoders on the activity of this neuron only, to assess the portion of information carried by single neurons in the different layers of the early somatosensory system.

### Whisker stimulation

Virtual whiskers were stimulated with a virtual pole, using a `ramp and hold' protocol. In such a protocol, a pole is pushed toward a whisker during a ramp-on phase, held in position during a hold phase, and pulled back during a ramp-off phase (Figure 1). Different parameters of such ramp and hold protocols were varied: the maximum amplitude, direction, distance to whisker base, slope, and frequency (Figure 2). For each set of stimuli, the same set of initial parameters was used: for the first stimulus: The pole was positioned at 10 mm of the targeted whisker and moved at a speed of 0.3 m/s, with an angle of 0° around the x-axis (along the whisker). The amplitude of the stimulus was 1 mm, and it was held against the whisker for 100 ms.

For sets of stimuli where the maximum amplitude was varied, the maximum amplitude was varied from 1 mm to 20 mm with a step of 1 mm (Figure 2). For sets of stimuli where the direction was varied, the pole was oriented from 0° to 350° with steps of 10° (Figure 2). For sets of stimuli where the distance to the whisker basis was varied, we targeted each of the 20 links that compose the whisker once (see –ref Whiskit paragraph and Figure 2). For sets of stimuli where the slope speed was varied, the pole moved from 0.25 to 0.35 m/s with steps of 0.01 m/s (Figure 2). Finally, for sets of stimuli where the frequency was varied, the pole was placed against the last link of the whisker and vibrated with a frequency of 2 to 32 Hz with steps of 2 Hz (Figure 2).

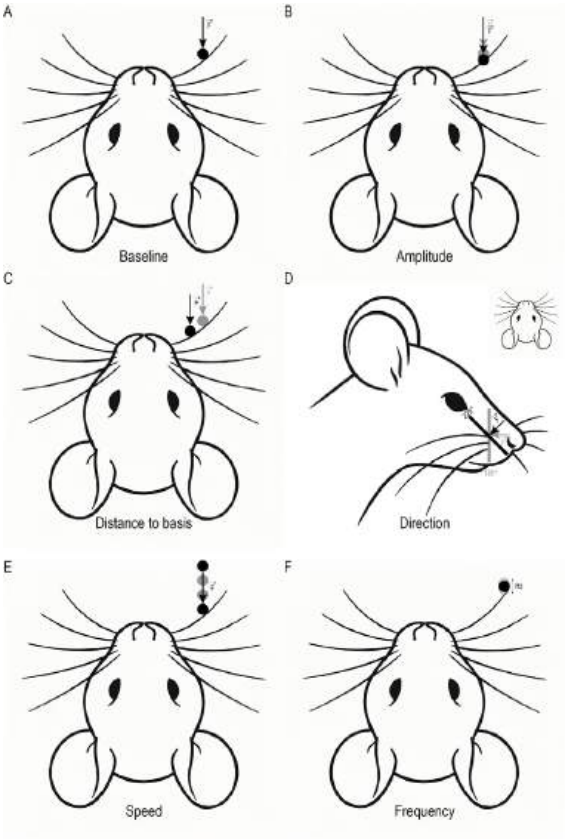


**Figure 2 - Stimulus paradigm for whisker deflection. A -** Baseline setup for whisker deflection: A pole is pushed toward the whisker of the mouse, held in position, and moved back (ramp-and-hold). **B -** From the baseline, we varied the amplitude of deflection. **C -** From the baseline, we varied the distance between the pole and the whisker base. **D -** From the baseline, we varied the direction of the pole around the whisker. **E -** From the baseline, we varied the speed of movement of the pole toward the whisker. **F -** Frequency paradigm: The pole was held against the whisker and vibrated at a constant frequency for one trial. Across trials, this frequency was changed

## WhiskIt to neuron connection

The whisker was modelled using WhiskIt, a whisker model publicly available on GitHub.

WhiskIt [8] is a physical model of whiskers relying on the Bullet3D physics engine. It represents the head of a rat with whisker pads containing whiskers. Each whisker is a beam discretized as 20 cylindrical elements connected by springs with different elasticity and damping constants, fitted to reproduce real whisker dynamics. The whiskers can thus be used to deduce the forces and torques applied to the mechanoreceptors within the whisker follicle. We applied different sets of stimuli to the whisker (varying in speed, force, frequency, direction, and distance to base as described above) and communicated the bending moment to a Python script through a socket (an endpoint allowing bidirectional communication within a network) to extract the amplitude of the movement at the base of the whisker through equation (1).



(1) $amplitude(t) = \sqrt{M_y^2(t) + M_z^2(t)}$ , equation from Yang et al., (2016) [11]

Where My denotes the bending moment at the whisker basis around the y-axis, and Mz denotes the bending moment at the whisker basis around the z-axis. We define, in the equation above, the y-axis as oriented toward the top of the head of the mouse, the z-axis toward its snout, and the x-axis toward the tip of the whisker. Here, we assume that the moment along the x-axis has a negligible effect on the base deflection and thus only consider the YZ moments. The resulting amplitude was then converted to neural activity by our mechanoreceptor models.

## Neuron model

We developed models of different mechanoreceptors that can be distinguished by their adaptation rate, shaping their responses to stimuli. To accurately represent these differences in adaptation rate, we relied on the Adaptive Exponential Integrate-and-Fire (AdEx) model [12], which explicitly implements an adaptation term, while offering a trade-off between computational efficiency and biological realism. Moreover, extensive model fitting is not possible due to the scarcity of recordings from mechanoreceptors.

AdEx neurons implement a negative feedback current *W* that increases after each spike and converges logarithmically towards an upper bound. This increases the time between each subsequent two spikes, thus allowing the model to reproduce the adaptation profile observed in the different mechanoreceptors. By tuning the

parameters of this adaptive current, the model can replicate the firing pattern of RA and SA mechanoreceptors. The model is described by the following equations:

(2) $dv/dt = (I_{leak} + g_{leak} * \Delta_{th} * e^{(v - v_{th})/\Delta_{th}} - W + I_{app})/C_m$

(3) $I_{leak} = g_{leak} * (E_{leak} - v)$

(4) $dW/dt = (a * (v - E_{leak}) - W)/\tau.$

Once the membrane potential $v$ reaches a threshold $v_{th}$, a spike occurs, the membrane potential is reset to its resting value $v_{reset}$, and the adaptive current increases by a value $b$. In the absence of activity, the adaptive current decays to 0 with time constant $\boldsymbol{\tau}$. We fitted the adaptation parameters (a, b, $\boldsymbol{\tau}$) to biological data from Sonekatsu and Gu, (2020) [13] as explained in the section Parameter optimization for adaptation current.

## Modeling mechanoreceptors

To simulate mechanoreceptor activation, we stimulated the AdEx models with a continuous input current ($I_{app}$) of 900 pA, modulated by a function specific to each mechanoreceptor subtype. These functions, defined by equations (5), (6), and (7), govern how stimuli are presented to the receptors based on their receptive fields.

To ensure a biologically accurate distribution of mechanoreceptors, we based our model on the study of Johansson and Vallbo (1977) [14], which provides empirical data on the density and types of mechanoreceptors in human glabrous skin. As both the fingertip and whisker are used for fine discrimination of tactile stimuli, we respected the same ratio of receptors. From a total population of 200 simulated receptors, we assigned:

- 58 SA1 (Slowly Adapting Type 1) receptors
- 30 SA2 (Slowly Adapting Type 2) receptors
- 112 RA (Rapidly Adapting) receptors

Each receptor was individually connected to a corresponding neuron in TG, which is a dummy layer composed of exponential integrate-and-fire neurons. This one-to-one connectivity ensured that each mechanoreceptor's output was directly relayed to a neuron in the trigeminal ganglion (TG) layer, which acts as a central relay integrating tactile information.

The TG layer consisted of 200 neurons, each receiving input from a single mechanoreceptor. To maintain a direct and efficient encoding of the activity of the mechanoreceptors, we assigned a synaptic weight between each mechanoreceptor and TG neuron, such that each action potential in a receptor depolarized the corresponding TG neuron by 25 mV. This depolarization was sufficient to reach the threshold for action potential generation, ensuring that each spike in a mechanoreceptor resulted in a spike in the corresponding TG neuron (see Figure 1). This approach allows the model to preserve the spatiotemporal fidelity of mechanoreceptive signals while simplifying the computational structure, making it suitable for large-scale simulations of tactile processing.



To ensure that the receptive fields of the mechanoreceptors cover the entire space surrounding each whisker in the follicle, the receptive field of each mechanoreceptor was modelled as a cosine-shaped bump:

(5) $\Gamma_{ti} = (cos(d_t - p_i)$, with t ∈ T, the duration of the simulation.

where $d_t$ is direction of whisker deflection at time t, is the position of mechanoreceptor i, and $\Gamma_{ti} \in [0; 1]$ is the direction selectivity of mechanoreceptor i at time t. The parameter that gives each receptor's maximum response, $\Gamma_{ti}$ *was* unique for each receptor and was drawn from a Gaussian distribution centered around 0 degrees (toward the snout of the mouse) and 180 degrees (toward the tail of the mouse) with a standard deviation of 90 degrees.

## SA1

SA1 receptors respond primarily to stimulus direction and are poorly modulated by the amplitude of whisker deflection [15, 6, 4, 16]. Therefore, for SA1 receptors, we assume an ON/OFF relationship to differences in amplitude, described by the Heaviside function *H* (*t*), that is, the stimulus current $I_{app}$ is multiplied by 1 if there is a stimulus and 0 otherwise. The activation threshold was hand-tuned and set to 0.01 :

(5) $I_{app_i} = (900\,pA * H(t)) * \Gamma_{ti}$ with t ∈ T, the duration of the simulation, and i is the id of the mechanoreceptor.

(6) $H(t) := \{0, amplitude(t) \geq 0.01;\ 1, amplitude(t) < 0.01\}$

### SA2

SA2 receptors are sensitive to direction and amplitude of whisker deflection [15, 6, 4, 16], We therefore assumed a logarithmic relationship between the response intensity and the stimulus amplitude:

(7) $I_{app_i} = (900\,pA * log(1 + 2 * amplitude(t))) * \Gamma_{ti}$ with t ∈ T, the duration of the simulation, and i is the id of the mechanoreceptor.

### RA

We assume that RA receptors are sensitive to a switch in amplitude [15, 6, 4, 16]:

(8) $I_{app_i} = (900\,pA * log\,(amplitude(t) / amplitude(t-1)) * \Gamma_{ti}$ with t ∈ T, the duration of the simulation, and i is the id of the mechanoreceptor.

### Parameter Optimization for Adaptation Current

To fine-tune the adaptation parameters for each receptor model, we used a Covariance Matrix Adaptation Evolution Strategy (CMA-ES) [17], an advanced evolutionary algorithm that iteratively adjusts parameters based on covariance relationships with an objective function. In our case, the objective function was the mean squared error (MSE) between the model's predicted firing rates (number of spikes per timestep of 1 ms) and biological data. The parameters optimized included a, b, and $\tau$ (equations (2-4)), which define the adaptation dynamics of the mechanoreceptor model.

We implemented CMA-ES using the cmaes Python library, leveraging its robust global optimization capabilities. The algorithm estimated the best-fit parameters by minimizing the error between our model's predicted instantaneous firing rate and experimental data obtained from Sonekatsu and Gu (2019) [13], as a response to a ramp-and-hold stimulus, with a duration of 2000 ms, and both ramp-on and ramp-off lasting 100 ms. The instantaneous firing rate was computed as the reciprocal of the interspike interval (ISI), also known as the instantaneous frequency. The fitting procedure was conducted as follows:

- SA1 mechanoreceptor models were optimized to match experimental data from Supplemental Figure 1.
- SA2 mechanoreceptor models were optimized to fit Supplemental Figure 1.
- RA mechanoreceptors lacked sufficient data points for a reliable automated fitting procedure. Instead, we manually hand-tuned the adaptation parameters

to achieve the expected rapid adaptation behavior, ensuring a transient response to sustained stimuli.

The model was validated against responses to a ramp-and-hold stimulus (see Figure 1), which is commonly used to characterize mechanoreceptor adaptation dynamics.

The full implementation of our parameter optimization pipeline, including the CMA-ES code and data, is available on GitHub: Neural Population Optimization with CMA-ES.



## Trigeminal Ganglion and Brainstem

The three populations of mechanoreceptors (SA1, SA2, and RA) were connected in a one-to-one fashion to a model of Trigeminal Ganglions (TG) composed of 200 neurons, which in turn sends feed-forward connections to the brainstem (BS) with a probability of p=0.005 for a connection between neurons to exist. BS sent lateral random inhibitory connections with a probability of p = 0.005 for a connection to exist. Each BS neuron was modeled as an exponential integrate and fire (EIF) neuron described by the following equations:

(9) $dv/dt = (I_{leak} + g_{leak} * \Delta_{th} * e^{(v - v_{th})/\Delta_{th}})/C_m$

(10) $I_{leak} = g_{leak} * (E_{leak} - v)$,

Each spike from a presynaptic BS neuron triggers an increase of 25 mV for the following dt=1*ms in the post-synaptic BS neuron in case of an excitatory connection or a decrease of 25 mV in case of an inhibitory one. The parameters can be found in supplementary table 1.

## Decoding

We extracted the number of spikes per neuron per stimulus for each population and trained decoders to identify the stimulus within a given set, e.i. the value of the applied amplitude, direction, frequency, etc… We implemented three different classifiers using the Scikit-learn (Sklearn) library [18] and evaluated the different decoding strategies:

1. Linear Classifier – *Ridge Classifier* (linear_model.RidgeClassifier()):
   - A linear classifier that assumes a simple weighted sum of neural activity can predict stimulus labels.

2. MultilayerPerceptron(MLP)–*NeuralNetworkClassifier*(neural_network.MLPClassifier()):
   - A more flexible, universal approximator, non-linear classifier that can learn complex relationships between neural firing rates and stimulus duration.
3. Bayesian Classifier – *Naïve Bayes* (naive_bayes.GaussianNB()):
   - A probabilistic approach that assumes independence between neurons and classifies based on Gaussian-distributed spike counts.

We also trained each decoder on the firing rate per stimulus of a single most informative neuron for each population.

To assess whether a single neuron could encode the stimulus or if the encoding relied on population synergy in each layer of the network, we computed the Pearson correlation across single neurons' firing rate within each population in response to each varied parameter of the tactile stimulus.

## Information quantification

Next, we wanted to assess the information transferred by each neuron and each population about the stimulus. For each component of the tactile stimulus (amplitude, direction, slope speed, frequency, and distance to basis, Figure 2), we computed the mutual information between the stimulus and neural activity based on the Shannon entropy:

$$MI(X,Y) = H(X) - H(X|Y),$$

With $H$ being the Shannon entropy, X the distribution of the number of spikes for a given population or a given neuron (number of times a specific number of spikes has been seen), and Y the distribution of the stimulus (number of times a specific stimulus has been seen). No bias correction was applied to the mutual information (MI) calculation. Although this might seem unexpected for biological data, our analysis concerns a deterministic model: for a given stimulus, the neural response is always identical. Consequently, subsampling bias cannot occur. The absence of noise ensures a single possible output for each stimulus, though distinct stimuli can converge onto the same neural representation. In such cases, the conditional input entropy given the output, H(X|Y), may be smaller than the input entropy H(X), since two stimuli x and $x'$ can produce the same output y. Nevertheless, the mapping remains deterministic: whenever x or $x'$ is presented, the same response y will occur. For these reasons, bias correction was not required in our MI estimates.

This was performed between the stimulus and the firing rate of every neuron, the stimulus and the firing rate of each population, as well as between the stimulus and the firing rate of the brainstem activity with and without inhibition. We identified the most informative neuron within each population as the neuron for which MI is closest to the entropy of the stimulus.

### Correlation

To analyze redundancy within the network, we computed the Pearson correlation between the firing rate of each neuron within a population across the entire stimulus duration. This was done through the following equation:



$$(11)\quad r(x,y) = \frac{\sum_i^N (x_i - m_x) * (y_i - m_y)}{\sqrt{\sum_i^N (x_i - m_x)^2 * \sum_i^N (y_i - m_y)^2}},$$

With $m_x$ the mean of vector $x_i$ and $m_y$ the mean of vector $y_i$, with $x_i$, the firing rate of neuron x in response to stimulus *i*, and $y_i$, the firing rate of neuron y in response to stimulus *i*. N is the number of stimuli presented to the network for a given parameter, modified from the baseline.

## Results

To analyze the information flow in the early stages of the whisker system, we built a three-layer network with three input populations consisting of different types of mechanoreceptors. We verified the ability of each population to transmit information through the usage of decoders. We then unveiled the coding strategies of the various populations by computing the mutual information between the firing rate of each neuron within a population and a stimulus, as well as the correlation across the activity of each neuron Here we describe the results of this procedure.

### Model fitting of mechanoreceptors to a ramp-and-hold stimulus

To develop models of different types of mechanoreceptors (SA1, SA2, and RA), we fitted the adaptation parameters of the Adaptive Exponential Integrate-and-Fire (AdEx) model [12] to the activity of these receptor types recorded by Sonekatsu and Gu (2021) [13] (see section Parameter optimization for adaptation current in the Methods for details on the procedure). These mechanoreceptor populations are the input layer of the network. Therefore, we made them sensitive to the amplitude and direction of whisker deflection, as every parameter that comprises a tactile stimulus results ultimately in different directions and amplitudes of whisker deflection. The remaining layers of the network were modelled as simple Exponential Integrate-

and-fire (EIF) neurons, without adaptation. Through the application of a ramp and hold whisker deflection, we see the population activity increasing in SA1, and SA2 during the entire stimulus and RA during the transient phase. This activity propagates to TG and BS. The dynamics of this activity compared to the recordings by Minnery and Simons in 2003 [19]. After developing the model by fitting population responses to recordings of neural population responses to a simple stimulus, we connected the network to a virtual whisker model (WhiskIt model [8]). While the movement of the pole against the virtual whisker was made to perform a ramp and hold stimulus as well, the resulting bending moment of the whisker at its basis was far noisier than the ideal amplitude applied in Figure 1, as the elastic nature of the vibrissa makes the tip oscillate during the entire simulation (Figure 2). Nonetheless, the movement of the whisker could still produce activity within the network. In the next section, we will discuss how the spiking activity spreads from the mechanoreceptors to the brainstem and how it varies depending on the properties of the stimulus.

## The model's response to deflection of the virtual whisker

The responses of the different modelled neural populations fluctuate depending on the stimulus properties. Here, we will assess how different parameters of the stimulus impact the population activity of the network. To do that, we applied a ramp-and-hold stimulus to a virtual whisker, and modified one parameter at a time such as amplitude of deflection, distance of the pole to the whisker base, direction of deflection, speed of deflection, and frequency of vibration at the tip of the whisker (Figure 2).

We first assessed if changes in the amplitude of whisker deflection change the responses of all neurons: a stronger amplitude increases the activity of all populations of neurons. Particularly, the activity of the SA2 population shows a striking increase as its response goes from silence for a small amplitude stimulus to the most active type of mechanoreceptor for a high amplitude stimulus (Figure 3). By design, the TG response is a weighted sum of the afferent population, and its one-to-one connectivity to the different mechanoreceptors is visible in the raster plot, as we can identify three distinct population activity within TG. In the BS, the spike pattern appears noisy, it is not easy to distinguish which mechanoreceptor population is responsible for the activation of a given neuron (Figure 3).

A second stimulus property we varied was the distance of the pole to the basis of the whisker (Figure 2). The variation of this distance to the base also highly impacts the firing rate of the SA2 population and its upstream populations (TG and BS).

The closer to the whisker basis the pole is, the less dampening happens and thus the stronger the amplitude appears, as shown in the bottom plot (Supplemental figure 2). In other words, decreasing the whisker basis to pole distance increases the population activities of SA2, TG, and BS. For this particular stimulus, we see an impact of inhibition, as it appears that for an amplitude further from the whisker basis, without inhibition, BS would keep spiking. For a stimulus at the whisker basis, the activity of the BS is reduced after stimulus presentation compared to BS without inhibition, which keeps firing even after the ramp-off. The firing rates of SA1 and RA seem to be rather unimpacted by this parameter, although the timing of the activity changes.



The frequency of vibration has an impact on the activity of SA1 and RA, as well as that of TG and BS. At first glance, it seems that the SA1 population is the population that tracks the frequency the best and transmits this information to the following layers.

The fourth stimulus property that was varied was the direction of the pole movement (Figure 2). The variation of the pole direction doesn't seem to impact the firing rate of the different populations, but does change the raster plot.

Finally, the speed of whisker deflection highly impacts RA neurons' firing patterns, while the other population seems rather unchanged.

From the raster plots and the population activities, we can already see that some populations preferentially respond to different properties of the stimulus. This interaction between the stimulus properties and the population responses promises that at least some information regarding these properties will be present within the system, as each of them produced a shift in the neural activity. To unveil the specificity of these preferences within the network, one would need to assess the decoding capacity of the readout provided by the populations.

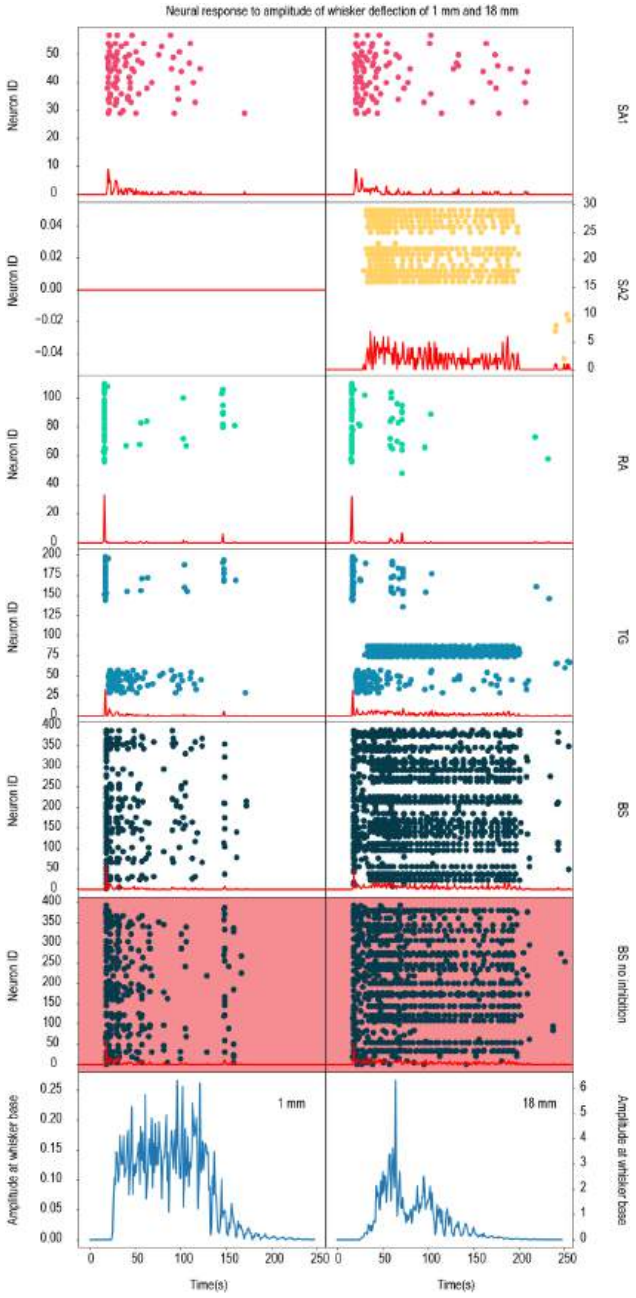


**Figure 3 - Population response to two amplitudes.** Top to bottom: Raster plot of neural activity from SA1, SA2, RA, TG, BS with inhibition, and BS without inhibition, as a response to the stimulus plotted at the bottom. For each raster plot, the y-axis is the neuron ID, and the x-axis is the time in ms. The red line is the number of spikes as a function of time, in which case the y-axis is the number of spikes. Bottom plot - The amplitude extracted from the whisker basis resulting from a whisker deflection of 1 (left) and 18 (right).

## The stimulus identity can be decoded from neural activity in each population

The population responses are informative about the stimulus and can be grasped by all decoders.

In Figure 3, we show the decoding performance of decoders trained on the firing rate per neuron within a population to distinguish the values of amplitude, direction, distance to basis, frequency, and slope speed. By reaching 1.0 (i.e., perfect accuracy), the decoders demonstrate that not only are they capable of training on each population activity, but also that most of the populations, with the exception that we will discuss later, are informative about all aspects of the stimulus. The exception is SA2, while it seems to be informative about amplitude, direction, and distance to the basis of the whisker, slope speed, and frequency seem to have little to no effect on the population activity. Furthermore, even when SA2 is informative, the maximum accuracy isn't reached by all decoders, thus, it seems that the relationship between single neuron firing rate within SA2 and stimulus parameters is the hardest to grasp for the decoders.



After showing that the firing rate per neuron could be used to decode the stimulus properties, we aimed to find the encoding strategy within the different populations, asking whether the whole population bears information about the stimulus or if it is diffused in the "happy few" neurons. To answer this question, we assessed information transfer through MI calculation and quantified the overlap of neural activity with the Pearson coefficient.

## A single mechanoreceptor bears more information about the stimulus than a single neuron in the brainstem

Discrepancy in information transfer amongst single neurons within a population reduces the further we look into the ascending somatosensory pathway.

In Figure 4, we plotted the mutual information computed from the rate of single neurons per population along the entire duration of the stimulus. We see that a single neuron from SA1 and TG encodes amplitude and distance to basis, and almost reaches the entropy of the stimulus for both these properties. Direction, frequency, and slope speed seem to be spread more evenly amongst the populations. The MI calculation also demonstrates that the population rate is always more informative than individual neurons, and increases to reach its maximum value in the brainstem.

The decrease in information transfer by a single neuron within a population and the increase in MI at the level of population rate tend to show a shift from single neuron coding to population coding, as the information appears to be more evenly distributed amongst the different neurons, as the variance of the MI decreases in BS.

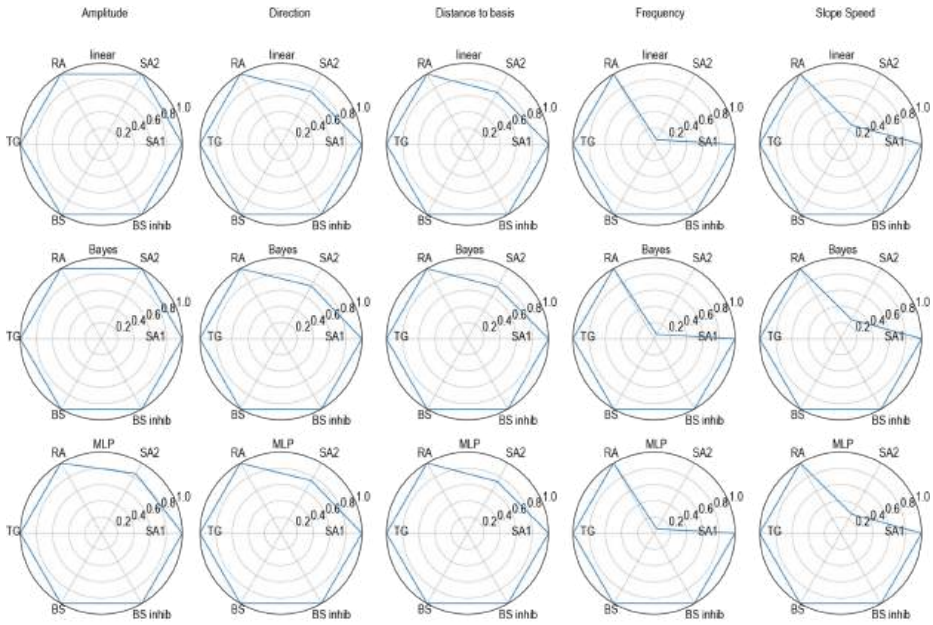


**Figure 4 - Decoding accuracy per population per stimulus property.** Each row corresponds to a different decoder (top to bottom: linear, Bayesian, and MLP). Each column represents the parameters that we changed and asked the decoder to identify. Each radar plot represents the decoder accuracy when trained on the different population activity (SA1, SA2, RA, TG, BS, BS inhib). The accuracy goes from 0 (none of the applied stimuli were correctly labeled by the decoders) to 1.0 (all applied stimuli were correctly labeled). The blue line represents the accuracy of each decoder trained on each population.

## Correlation across neurons' firing rate decreases between the periphery and the brainstem

To analyze the shift of the coding strategy discussed above, we computed the Pearson correlation coefficient between the firing rate of a single neuron within a population with the idea that decorrelation of neural activity meant less overlap in their response to a given stimulus, thus maximizing the coverage of the stimulus range.

The results shown in Figure 5 demonstrate that while the minimal correlation is not always at the brainstem level, the maximum value is always reached in the periphery.

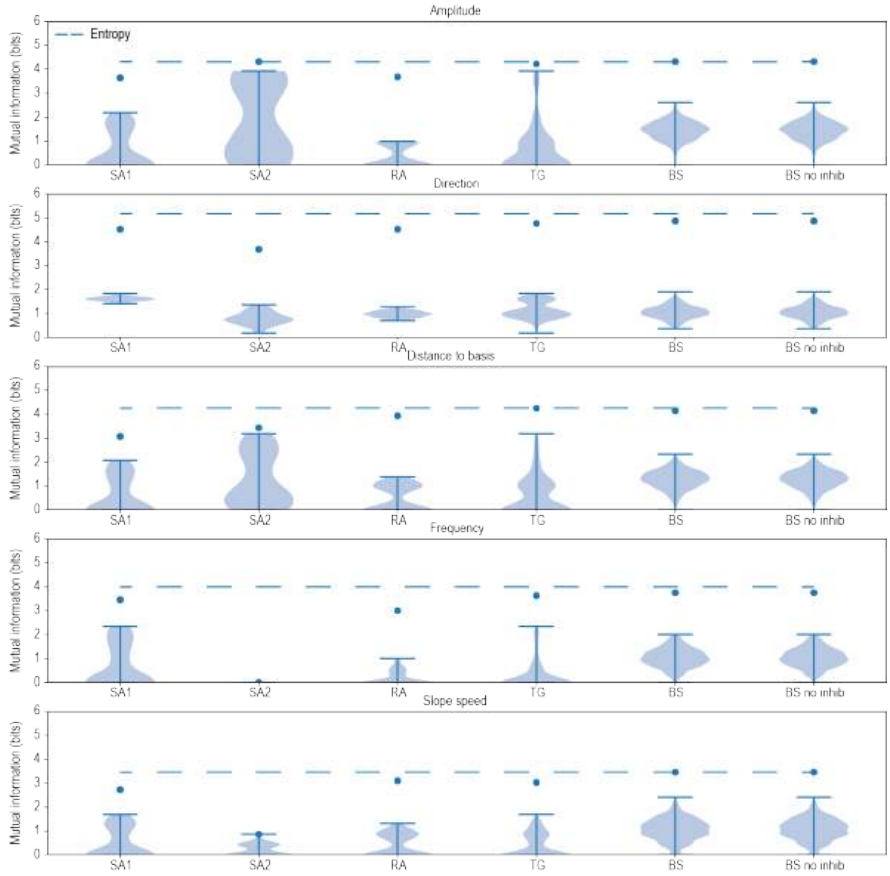


**Figure 5 - Mutual information between firing rate at the single neuron within a population (violin plot), population level (scatter), and the stimulus.** Each row corresponds to one parameter of the whisker simulation that was changed (top to bottom: Amplitude of deflection, direction of deflection, distance between the pole and the whisker basis, frequency of vibration for the pole at the tip of the whisker, and speed of the pole toward the whisker). The x-axis represents the different populations of neurons, the y-axis represents the information in bits. The blue dashed lines represent the entropy of the stimulus (calculated based on the different values applied). The dots correspond to the MI between the distribution of the stimulus and the distribution of the firing rate for an entire population. The violin plot represents the MI calculated between the distribution of the stimulus and the distribution of the firing of each neuron within a population.

The low correlation can be linked to a low encoding of the studied parameter. For instance, the correlation in SA1 for the distance to the basis is low, but together with the result presented in Figure 4, we see that this population poorly encodes the position of the stimulus along the whisker. With this consideration in mind, we see that BS always offers the best readout in terms of MI with the lowest correlation amongst its neurons. Again, when considering the distance to the basis of the whisker,

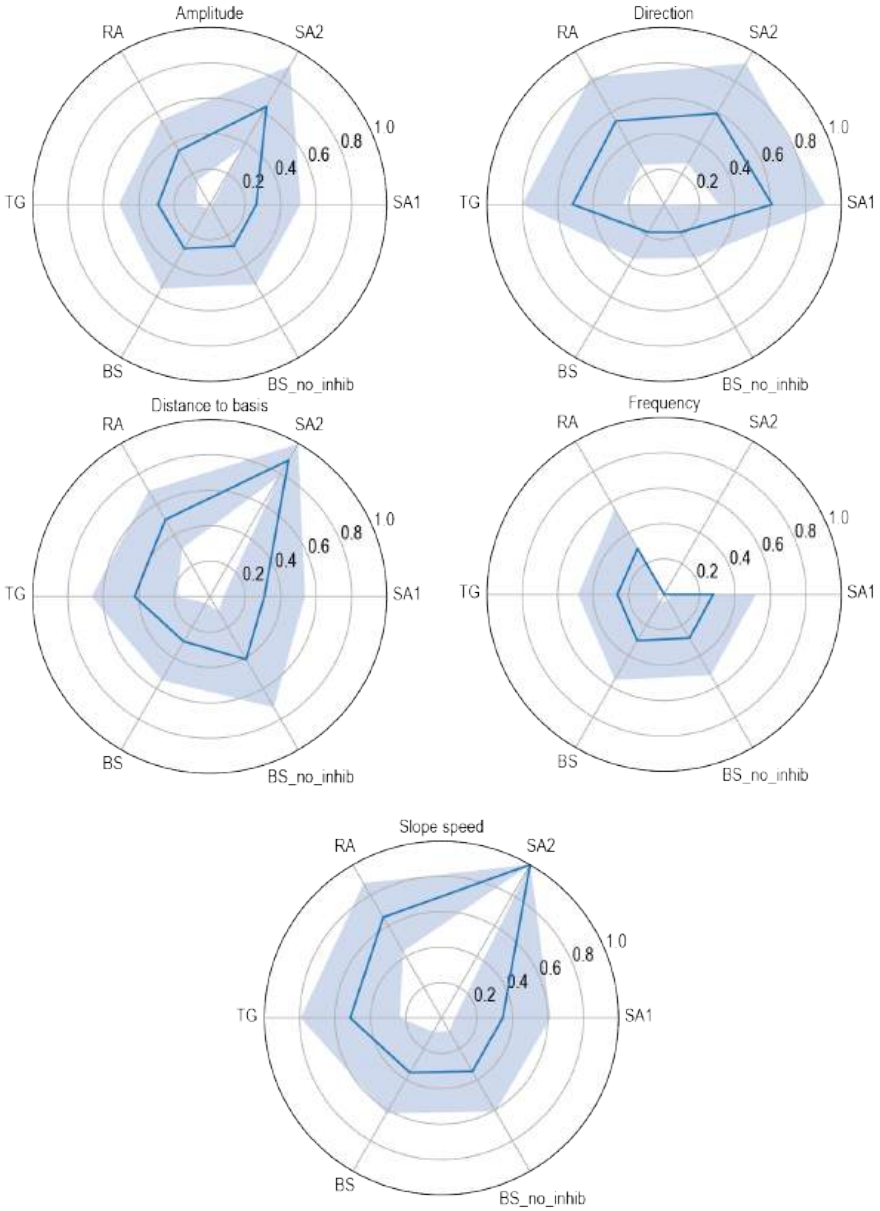


**Figure 6 - The correlation across neuron firing rate within a population decorrelates in the brainstem.** The radar plot represents the correlation between the firing rate of each neuron within the population. The populations are represented around the circle, while the axis represents the Pearson correlation. The solid blue line is the average correlation amongst neurons' firing rate within a population. The faded blue areas represent the standard deviation of the correlation amongst neurons' firing rate within a population. Each radar plot corresponds to a different property of the whisker simulation.

we can also notice that inhibition seems to decrease the correlation within the population. The lack of effect of inhibition for the other parameters can be due to the small inhibition probability that we used (Figure 1, p=0.05) or to the huge difference between the tested stimuli.

Taken together, these results and the information transfer calculation seem to show that the encoding strategy within the network goes from a single neuron in the periphery encoding to population encoding in the central nervous system through the decorrelation of neural activity. Here we show that decorrelation occurs at the very entrance of the nervous system.



## A single neuron is sufficient for a Bayesian decoder to retrieve the stimulus identity

A single neuron can accurately represent the stimulus, and its response is sufficient to decode its identity.

After analyzing the MI within each population, we selected the most informative neuron about the stimulus (e.i, highest MI). We then used its responses (firing rate) to the different stimuli to train the decoders (Figure 6). While the results of the training are poor for linear decoders and MLP, we see that the naive Bayesian decoders are capable of grasping the relationship between the activity of the neuron and the identity of the stimulus. In particular, we see that the decoder could learn the amplitude from TG and SA2 activity, Direction from all populations except SA2, Distance to basis from all populations except SA1, Frequency from RA and BS, with and without inhibition, and finally slope speed from every population except SA2 and SA1. These results demonstrate that a single neuron can be used to decode the stimulus properties.

Despite a decrease in correlation between the neuron's firing rate within a population and MI in a single neuron within the brainstem, it seems that the amount of information retained at the single unit level is still sufficient to decode the stimulus properly to the extent that BS contains, for most of the properties discussed in this paper, the most reliable neuron within the network to decode from (Figure 7).

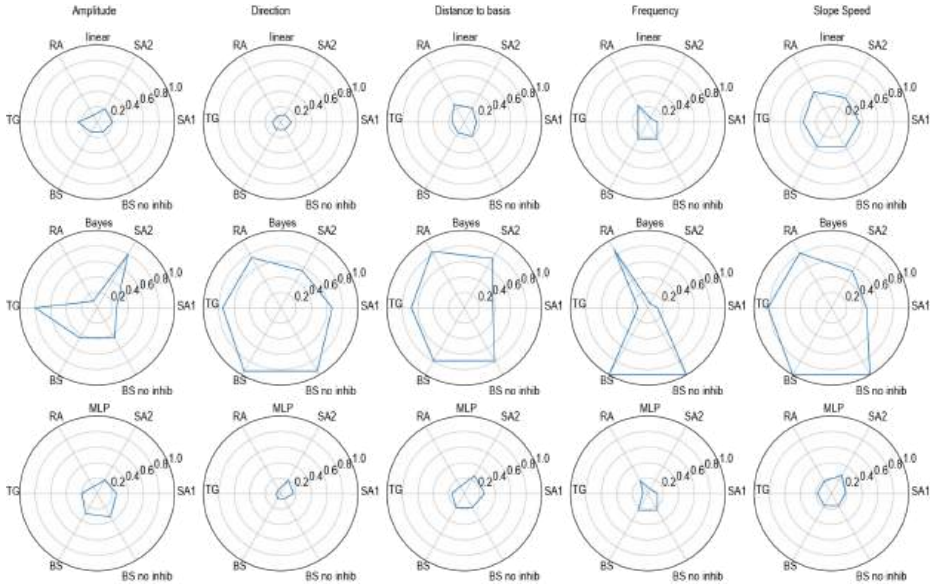


**Figure 7 - Accuracy of decoders trained on the firing rate of the most informative neuron per population.** Each row corresponds to a decoder (top to bottom: Linear, Bayes, MLP). Each column corresponds to a parameter that is varied from the baseline. Each radar plot represents the accuracy of a decoder relying on a single most informative neuron. The axis represents the accuracy, ranging from 0 (no stimuli were correctly identified) to 1 (all stimuli were correctly identified). Around the radar plot are the populations from which the most informative neuron is drawn.

# Discussion

We created a model of early tactile integration stages composed of a whisker model [8], 3 types of mechanoreceptors, the first-order sensory neurons (TG), and the brainstem, building upon the neural network introduced previously [Rault et al., in prep]. This model could reliably respond to different shifts in tactile stimuli that were applied to the modeled whisker, despite being fitted on a simplified version of a ramp-and-hold stimulus. The classification demonstrated that each population bears information about the stimuli even at the single-neuron level. However, the information sent by a single neuron decreased in the latest stage of the network due to the decorrelation of activity across the single unit. This shows a switch of the encoding strategy from single neuron coding to population coding.

## Validity of the model

We developed the first model of the early whisker pathway comprising a whisker model [8], three mechanoreceptor classes (SA1, SA2, RA), first-order trigeminal ganglion (TG) neurons, and brainstem neurons, building on a previously introduced

neural network [9]. In response to a ramp-and-hold whisker deflection, the model reproduces the stereotyped TG and brainstem response profiles reported in vivo: brief, high-amplitude bursts at stimulus onset and offset with a lower-amplitude sustained response during the hold period [19] and reproduced in previous models [20]. In the model, these onset/offset transients arise from near-synchronous activation within the receptor populations, which is relayed to TG and preserved in brainstem outputs. Although our simulations terminate at the brainstem, the resulting temporally synchronized bursts are expected to drive correspondingly synchronous thalamic volleys. Prior work has shown that such thalamic synchrony is a key precondition for cortical damping in barrel cortex—i.e., a net suppressive transformation produced by the timing-dependent interplay of strong feedforward/recurrent inhibition and excitatory drive—yielding reduced cortical activity relative to thalamus and sharpened spatiotemporal selectivity [21, 22]. Thus, the lower-stage synchrony emerging in our network provides a mechanistic substrate that could, in downstream stages, evoke the timing-gated cortical damping described by these studies. Our model reliably responds to different changes in tactile stimuli (Figure 2) that were applied to the modeled whisker, although the properties of the neural population were not fitted to responses to such tactile stimuli, but to the recorded response to a simple version of a ramp-and-hold stimulus. The resulting activity is consistent with experimental observations in early stages of the pathway, including mechanoreceptors, trigeminal ganglion, and brainstem neurons [19]. Thus, the model provides a biologically grounded output that can be used as input to the subsequent thalamic stage, setting the conditions under which classically described thalamocortical transformations—such as the cortical damping effect—can emerge.



### Presence of oscillations in the stimulus (preneuronal filtering)

The model was fitted to a simple ramp-and-hold stimulus, not taking into account the oscillations presented by the whisker model. This changes the dynamics of adaptation of the different receptors and might produce a different encoding strategy within the periphery. However, the whisker is not constrained by the elastic properties of the follicles as it is in biology, which can dampen the oscillations and act as pre-neuronal filtering as it occurs to certain frequencies in the human hand [23], thus, we have no guarantees that in real animals, the oscillations remain that strong. In this case, the sensitivity of the MCs to the oscillations may be overestimated by the current model. The model of the whisker follicle proposed by [24], considering the variable elasticity within the follicle, showed that the whisker shape changes within the follicle. This results in the MCs receiving different pressures along the depth of the whisker. To improve the model, one could implement the follicle resistance as well as the spatial distribution in the depth of the whisker.

## Oscillation effect on RA activity

Among mechanoreceptors, RA units are particularly affected by whisker oscillations: their transient responses can appear not only during the ramp phase but also during the hold phase, depending on oscillation strength. As a result, RA activity can resemble either Rapidly Adapting type I (RAI) or type II (RAII) patterns, making the two response types indistinguishable in the absence of oscillatory stimulation. In their study, Sonekatsu and Gu [13] directly recorded from isolated follicles; this preparation may have altered tissue elasticity, dampening oscillations and thereby masking differences between RA responses—potentially explaining why they did not observe RAII mechanoreceptors. This interpretation suggests that the apparent distinction between RAI and RAII is not an intrinsic receptor property, but rather emerges from follicle position and the mechanical filtering imposed by follicular tissue.

## From single neuron coding to population coding

Despite these changes in the dynamics of the stimulus between the ideal ramp-and-hold and the modeled one, the neural population was able to respond to the different variations within the stimulus parameter, to the extent that, besides SAII, the stimulus identity could be recovered by every population. SAII inaccuracy is mainly due to its sensitivity to amplitude, as its threshold of activation is higher than the other receptors [9]. Thus, for the various frequencies and slope speeds, SAII didn't produce any spike, hence the inability of the decoders to identify the stimulus correctly, although its activity was the most informative about amplitude.

When looking at the details of how the information is transmitted within the network, we notice that the population rate is always more informative than the single unit rate. This remains true for every stimulus tested in this experiment. Nevertheless, the MI calculation shows that a single neuron's activity is highly variable in the periphery and is closest to the entropy of the stimulus, showing that a single unit is capable of grasping most of the information contained within the stimulus. This does not hold in the brainstem, as the information transferred by each neuron is less variable and globally smaller than in the periphery. An explanation for this would be an increase in the complexification of the response of a single unit in the central nervous [25] system, similar to what has been witnessed in the visual pathway, going from center-surround responses [26] to edge orientation [27]. This shall result in a decorrelation of the neural activity [28]. In conclusion, our analyses reveal a previously unreported shift in coding strategy along the tactile pathway: in the periphery, the activity of individual mechanoreceptors shows a nearly saturated amount of information about the stimulus, whereas in the brainstem, single-unit responses lose informativeness and decoding instead relies on population-level

activity. This transition from single-neuron to population coding, demonstrated here for the first time at the brainstem level in the whisker system, underscores the role of this structure as the stage where tactile information becomes decorrelated and redistributed across neurons to support higher-level processing.

### Further decorrelation in the ascending pathway

The correlation calculation performed here has shown that the most correlated populations within the periphery were, unsurprisingly, the most reliable for the decoders to learn from, and the most informative from an MI perspective. Thus, SAII is highly informative and highly correlated when considering amplitude and slope speed. The relationship between MI, correlation, and the stimulus properties is less clear when studying other parameters such as direction (encoded by all receptors), and frequency and distance to basis that most likely have a non-linear relationship to the firing rate. Nevertheless, the decrease in correlation within the central nervous system remains consistent across the different parameters [28]. When considered together, the correlation and MI calculation seem to show a shift in the coding strategies, moving from single neuron coding to population coding as early as within the brainstem, the very input of the CNS.



### On the importance of the periphery

If the previous observation holds, tracking the stimulus in the nervous system becomes more and more complicated the deeper we go along the ascending somatosensory pathway as the neural response becomes more and more specific. Thus, to encode a stimulus, the deeper the structure, the more neurons need to be recruited to encode a percept. This brings complexity in several ways. First, the neurons representing the stimulus are not guaranteed to be spatially clustered together nor to receive the same input. Second, the decorrelation and lateral inhibition sharpen the receptive field and make the neuron more specific, thus, the percept relies on the activity of more neurons the deeper you go within the network. Third, these neurons receive pre-processed information on the stimulus as each neuron and synapses act at least as a low-pass filter; hence, more assumption needs to be made on the nature of the computation within the lower structure of the brain. These observations stress the importance of understanding the periphery as the closer to the periphery the stimulation is, the more reliable the percept will be. Thus, the primary afferent sensory neuron should be considered the primary target for sensory neuroprosthetics.

# References


[1] L. L. Orefice, A. L. Zimmerman, A. M. Chirila, S. J. Sleboda, J. P. Head, D. D. Ginty, Peripheral mechanosensory neuron dysfunction underlies tactile and behavioral deficits in mouse models of ASDs. Cell 166, 299–313 (2016).

[2] J.M. Loomis, S.J. Lederman Tactual perception K.R. Boff, L. Kaufman, J.P. Thomas (Eds.), Cognitive processes and performance, Handbook of perception and human performance, Vol. 2, John Wiley & Sons, New York (1986), pp. 31.1-31.41 (chap. 31)

[3] Wallach, A., Deutsch, D., Oram, T. B., & Ahissar, E. (2020). Predictive whisker kinematics reveal context-dependent sensorimotor strategies. *PLoS Biology*, *18*(5), e3000571. https://doi.org/10.1371/journal.pbio.3000571

[4] Furuta, T., Bush, N. E., Yang, A. E., Ebara, S., Miyazaki, N., Murata, K., Hirai, D., Shibata, K., & Hartmann, M. J. (2020). The Cellular and Mechanical Basis for Response Characteristics of Identified Primary Afferents in the Rat Vibrissal System. *Current Biology*, *30*(5), 815-826.e5. https://doi.org/10.1016/j.cub.2019.12.068

[5] Maksimovic, S., Nakatani, M., Baba, Y., Nelson, A. M., Marshall, K. L., Wellnitz, S. A., Firozi, P., Woo, S., Ranade, S., Patapoutian, A., & Lumpkin, E. A. (2014). Epidermal Merkel cells are mechanosensory cells that tune mammalian touch receptors. *Nature*, *509*(7502), 617–621. https://doi.org/10.1038/nature13250

[6] Johnson, K. O., Yoshioka, T., & Vega–Bermudez, F. (2000). Tactile Functions of Mechanoreceptive Afferents Innervating the Hand. *Journal Of Clinical Neurophysiology*, *17*(6), 539–558. https://doi.org/10.1097/00004691-200011000-00002

[7] Rault, N., Bergmans, T., Delfstra, N., Kleijnen, B. J., Zeldenrust, F., & Celikel, T. (2024b). Where Top-Down Meets Bottom-Up: Cell-Type Specific Connectivity Map of the Whisker System. Neuroinformatics, 22(3), 251–268. https://doi.org/10.1007/s12021-024-09658-6

[8] Zweifel, N. O., Bush, N. E., Abraham, I., Murphey, T. D., & Hartmann, M. J. Z. (2021). A dynamical model for generating synthetic data to quantify active tactile sensing behavior in the rat. *Proceedings Of The National Academy Of Sciences*, *118*(27). https://doi.org/10.1073/pnas.2011905118

[9] Rault, N., Doğan D., Marx, F. E., Jamal, T., Emoghene, A. E., Chandler, F. V., Pridgon, S., Sathani, A., Zeldenrust, F., Celikel, T. (2025). Artificial Human Touch: A Spiking Network Model of the Tactile Periphery. *In prep.*

[10] Van Der Loos, H. (1976). Barreloids in mouse somatosensory thalamus. *Neuroscience Letters*, *2*(1), 1–6. https://doi.org/10.1016/0304-3940(76)90036-7

[11] Yang, A. E. T., & Hartmann, M. J. Z. (2016). Whisking Kinematics Enables Object Localization in Head-Centered Coordinates Based on Tactile Information from a Single Vibrissa. *Frontiers in Behavioral Neuroscience*, *10*. https://doi.org/10.3389/fnbeh.2016.00145

[12] Brette, R., & Gerstner, W. (2005b). Adaptive Exponential Integrate-and-Fire Model as an Effective Description of Neuronal Activity. *Journal Of Neurophysiology*, *94*(5), 3637–3642. https://doi.org/10.1152/jn.00686.2005

[13] Sonekatsu, M., & Gu, J. G. (2019b). Functional properties of mechanoreceptors in mouse whisker hair follicles determined by the pressure-clamped single-fiber recording technique. *Neuroscience Letters*, *707*, 134321. https://doi.org/10.1016/j.neulet.2019.134321

[14] Johansson, R. S., & Vallbo, A. B. (1979). Tactile sensibility in the human hand: relative and absolute densities of four types of mechanoreceptive units in glabrous skin. *The Journal Of Physiology*, *286*(1), 283–300. https://doi.org/10.1113/jphysiol.1979.sp012619

[15] Saal, H. P., & Bensmaia, S. J. (2014). Touch is a team effort: interplay of submodalities in cutaneous sensibility. *Trends in Neurosciences*, *37*(12), 689–697. https://doi.org/10.1016/j.tins.2014.08.012

[16] Yamada, A., Furue, H., & Gu, J. G. (2022). Angular Tuning Properties of Low Threshold Mechanoreceptors in Isolated Rat Whisker Hair Follicles. *eNeuro*, *9*(6), ENEURO.0175-22.2022. https://doi.org/10.1523/ENEURO.0175-22.2022

[17] Hansen, N. (2007). The CMA Evolution Strategy: A Comparing review. *Studies in Fuzziness And Soft Computing*, 75–102. https://doi.org/10.1007/3-540-32494-1_4

[18] Pedregosa F., Varoquaux G., Gramfort A., Michel V., Thirion B., Grisel O., Blondel M., Prettenhofer P., Weiss R., Dubourg V., Vanderplas J., Passos A., Cournapeau D., Brucher M., Perrot M., & Duchesnay É. (2011b). SciKit-Learn: Machine Learning in Python. *Journal Of Machine Learning Research*. https://doi.org/10.5555/1953048.2078195

[19] Minnery, B. S., Bruno, R. M., & Simons, D. J. (2003). Response Transformation and Receptive-Field Synthesis in the Lemniscal Trigeminothalamic Circuit. *Journal Of Neurophysiology*, *90*(3), 1556–1570. https://doi.org/10.1152/jn.00111.2003

[20] Bale, M. R., & Petersen, R. S. (2009). Transformation in the neural code for whisker deflection direction along the lemniscal pathway. *Journal of neurophysiology*, *102*(5), 2771-2780.

[21] Kyriazi, H. T., & Simons, D. J. (1993). Thalamocortical response transformations in simulated whisker barrels. *Journal of Neuroscience*, *13*(4), 1601-1615.

[22] Pinto, D. J., Brumberg, J. C., Simons, D. J., Ermentrout, G. B., & Traub, R. (1996). A quantitative population model of whisker barrels: re-examining the Wilson-Cowan equations. *Journal of computational neuroscience*, *3*(3), 247-264.

[23] Wiertlewski, M., & Hayward, V. (2012). Mechanical behavior of the fingertip in the range of frequencies and displacements relevant to touch. Journal Of Biomechanics, 45(11), 1869–1874. https://doi.org/10.1016/j.jbiomech.2012.05.045

[24] Luo, Y., Bresee, C. S., Rudnicki, J. W., & Hartmann, M. J. Z. (2021). Constraints on the deformation of the vibrissa within the follicle. *PLoS Computational Biology*, *17*(4), e1007887. https://doi.org/10.1371/journal.pcbi.1007887

[25] Parvizi-Fard, A., Amiri, M., Kumar, D., Iskarous, M. M., & Thakor, N. V. (2021). A functional spiking neuronal network for tactile sensing pathway to process edge orientation. *Scientific Reports*, *11*(1). https://doi.org/10.1038/s41598-020-80132-4

[26] Kuffler, S. W. (1953). DISCHARGE PATTERNS AND FUNCTIONAL ORGANIZATION OF MAMMALIAN RETINA. *Journal Of Neurophysiology*, *16*(1), 37–68. https://doi.org/10.1152/jn.1953.16.1.37

[27] Hubel, D. H., & Wiesel, T. N. (1959). Receptive fields of single neurons in the cat's striate cortex. *The Journal Of Physiology*, *148*(3), 574–591. https://doi.org/10.1113/jphysiol.1959.sp006308

[28] Kohn, A., Coen-Cagli, R., Kanitscheider, I., & Pouget, A. (2016). Correlations and Neuronal Population Information. *Annual Review Of Neuroscience*, *39*(1), 237–256. https://doi.org/10.1146/annurev-neuro-070815-013851

# Supplemental materials

**Supplemental Table 1 -** Parameter values of the Adex model [11] for SA1, SA2, and RA receptors as well as parameters for the elif neurons model for TG and BS.

| Parameters | SA1 | SA2 | RA | TG and BS |
|---|---|---|---|---|
| a | 20.24 $nS$ | 46.11 $nS$ | 59.1 $nS$ | |
| b | 69.65 $pA$ | 3.21 $pA$ | 86.53 $pA$ | |
| $\tau$ | 44.09 $ms$ | 1882.05 $ms$ | 1890.10 $ms$ | |
| $E_{leak}$ | | $-50$ $mV$ | | |
| $V_{th}$ | | $-30$ $mV$ | | |
| $V_{reset}$ | | $-45$ $mV$ | | |
| $C_m$ | | $-0.1$ $nF$ | | |
| $g_{leak}$ | | 10 $nS$ | | |
| $\Delta_{th}$ | | 5 $mV$ | | |

**Supplemental Table 2 -** Set of parameters used for whisker deflection simulation. For each set of stimuli, the same set of initial parameters was used: The pole was positioned at 10 mm from the targeted whisker and moved at a speed of 0.3 m/s, with an angle of 0° around the x-axis (along the whisker). The amplitude of the stimulus was 1 mm, and it was held against the whisker for 100 ms at the 10th link of the whisker (middle). Then, only one of these parameters was changed, as shown in the table above.

| | Amplitude of deflection | Direction of deflection | Position of deflection along the whisker | Velocity of deflection | Frequency of vibration at the tip |
|---|---|---|---|---|---|
| Range of simulation: min to max (step) | 1mm to 22 mm (1mm) | 0° to 350° (10°) | 1st link -20th link (1) | 0.25 m/s to 0.35 m/s (0.01m/s) | 2 Hz to 32Hz (2Hz) |

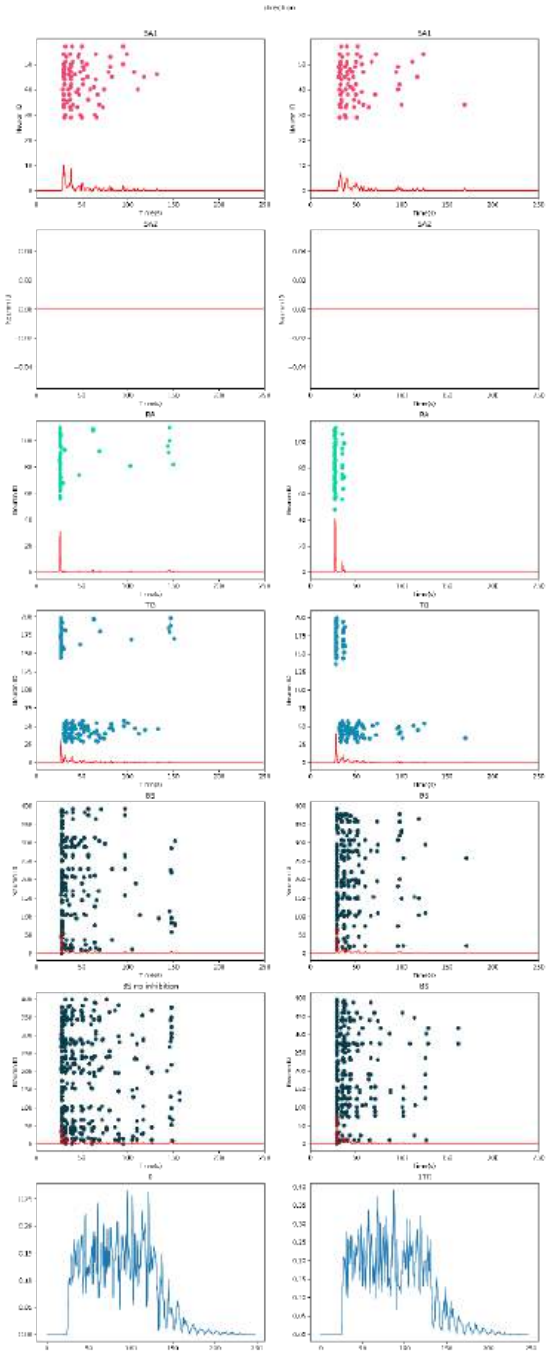

**Supplemental Figure 1 -** Population responses and raster plot to a direction of 0 degrees and 170 degrees.

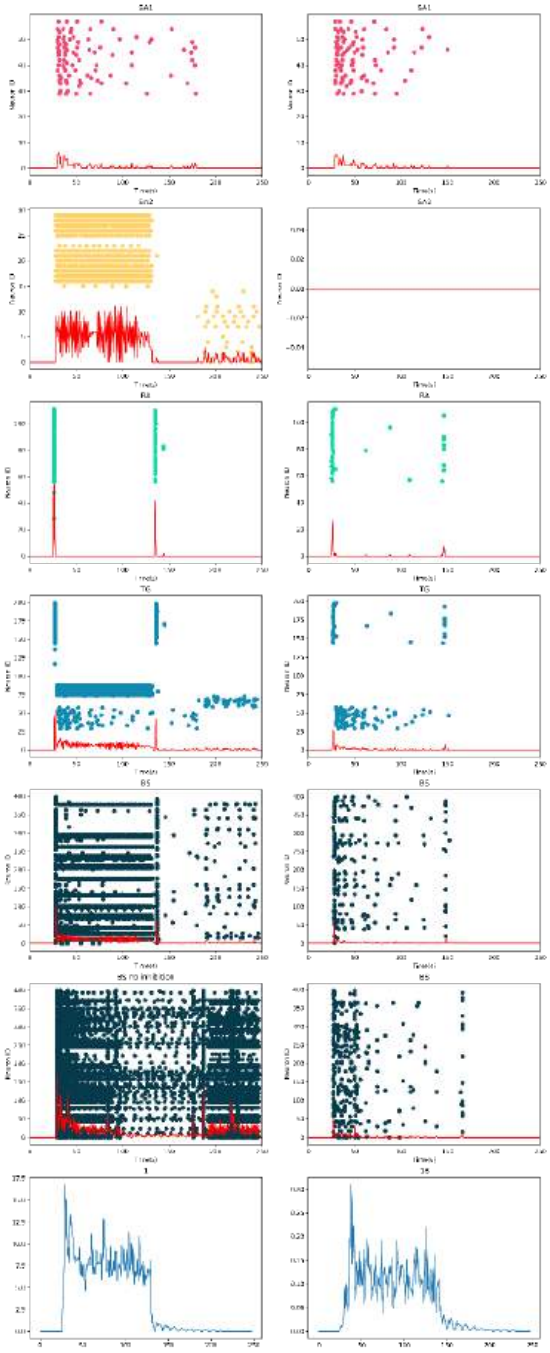

**Supplemental figure 2 -** Population response and raster plot for the pole applied to the 1st link (close to the snout) of the whisker and the 18th (close to the tip) link of the whisker.

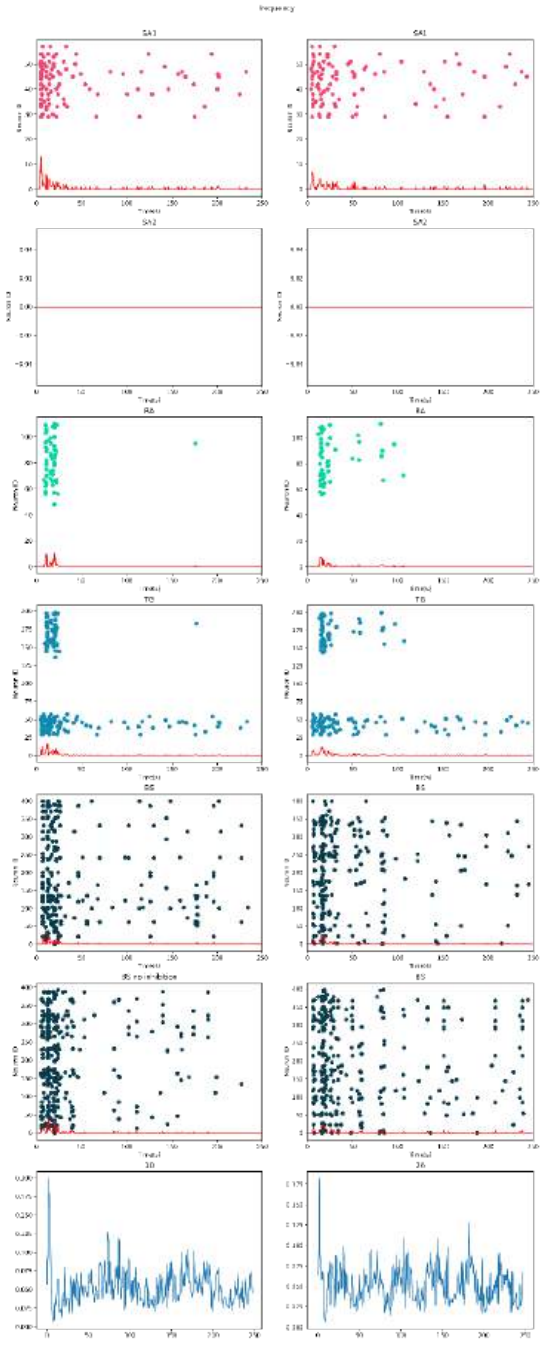

**Supplemental figure 3 -** Population response and raster plot to a frequency of 10 Hz and 26 Hz.

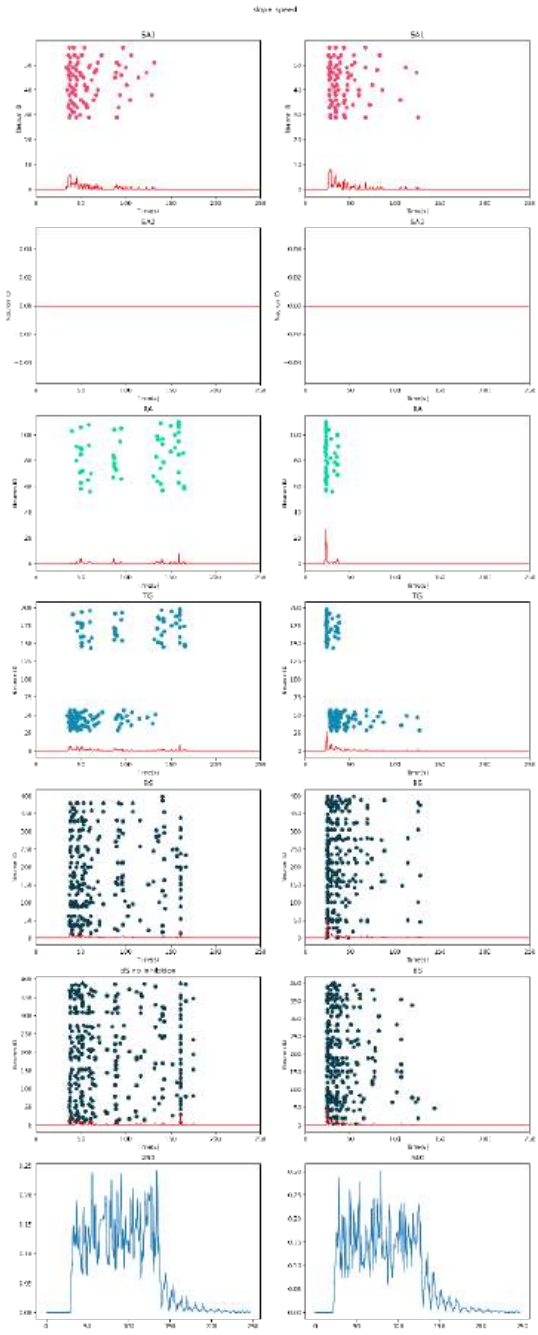

**Supplemental figure 4 -** Population response and raster plot to a pole movement against the whisker of 0.25m/s and 0.34 m/s.

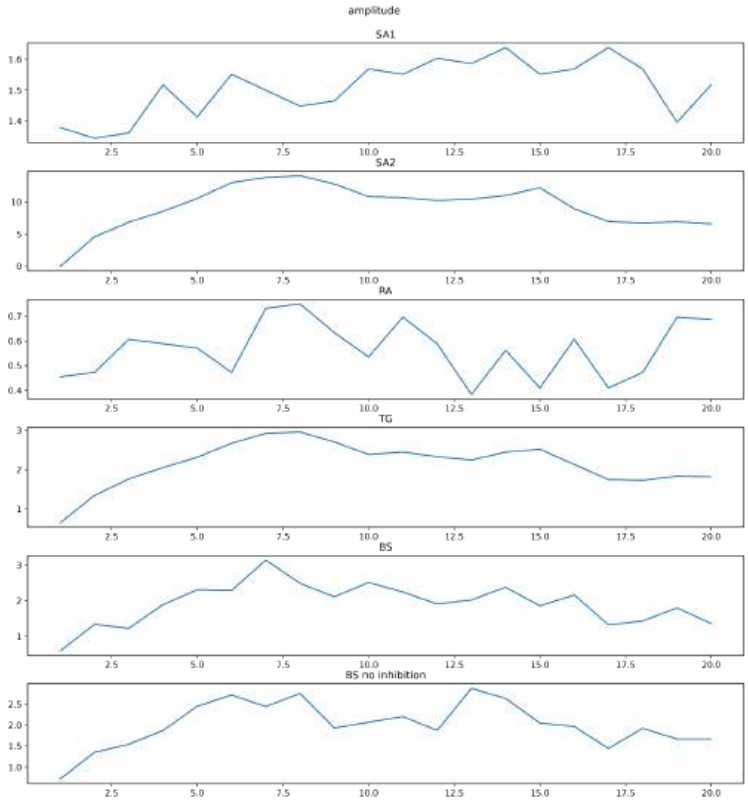


**Supplemental figure 5 -** Average number of spike per neuron as a response to different amplitudes.

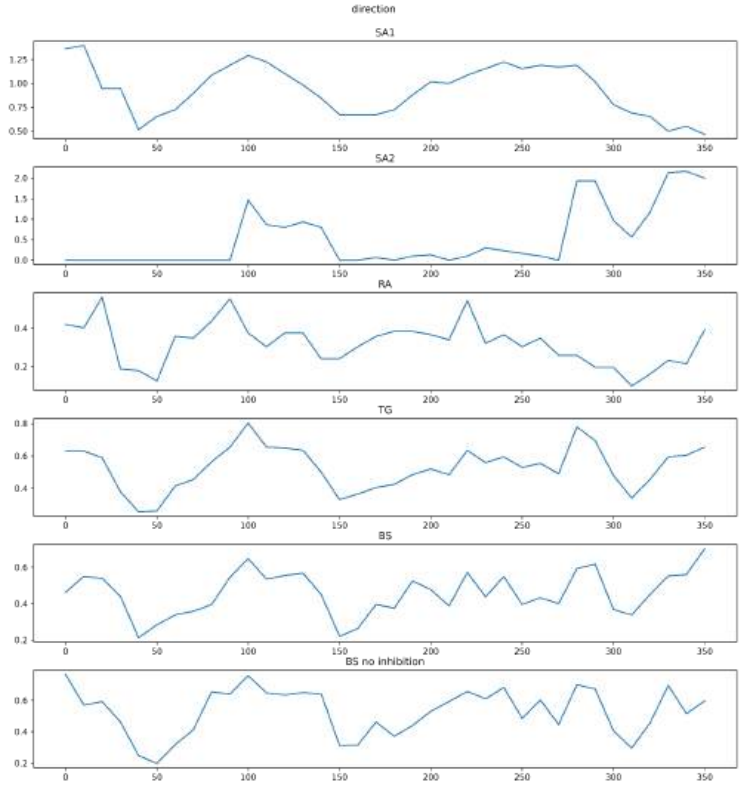


**Supplemental figure 6 -** Average number of spikes per neurons as a response to direction.

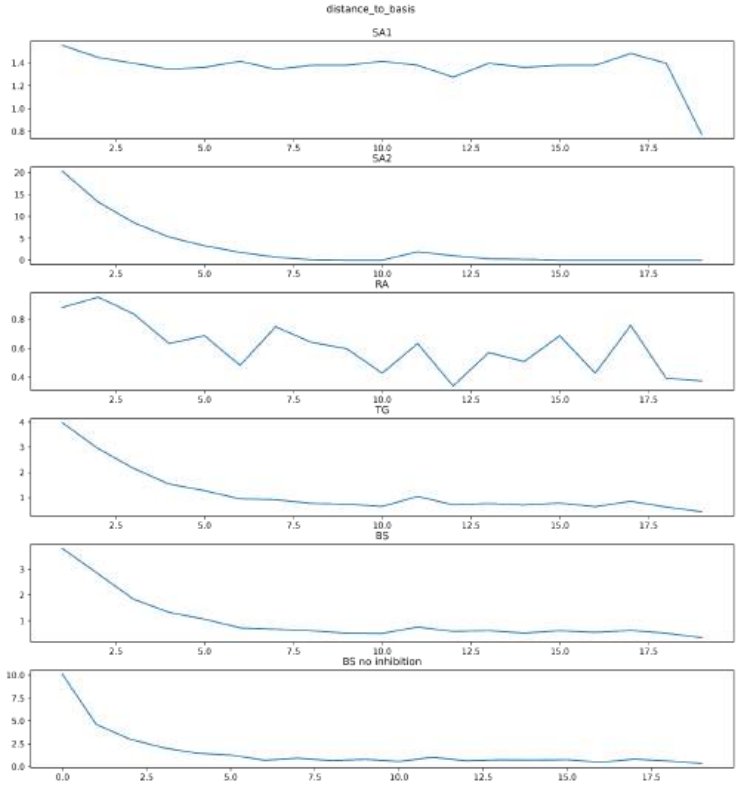


**Supplemental figure 7 -** Average number of spike per neuron as a response to distance to basis.

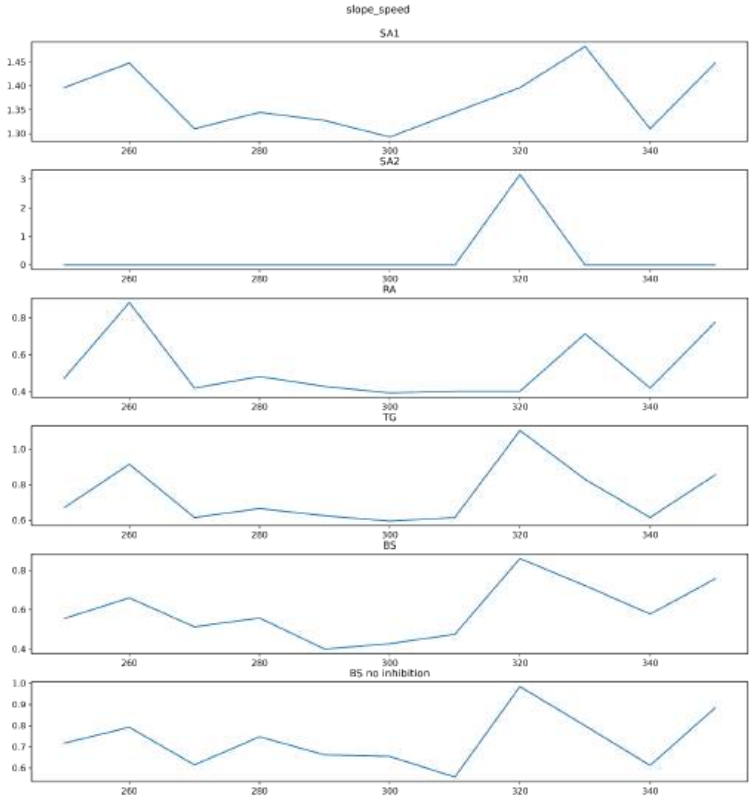


**Supplemental Figure 8 -** Average number of spikes per neuron as a response to slope speed.

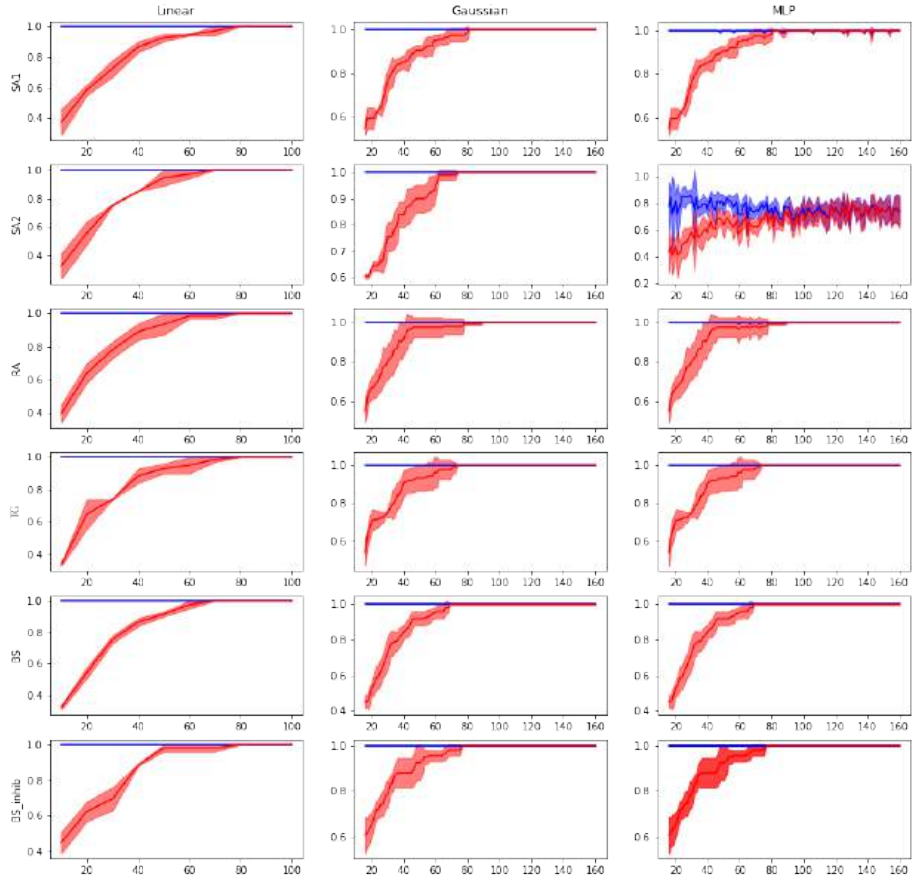


**Supplemental Figure 9 -** Learning curve for whole population on amplitude decoding.

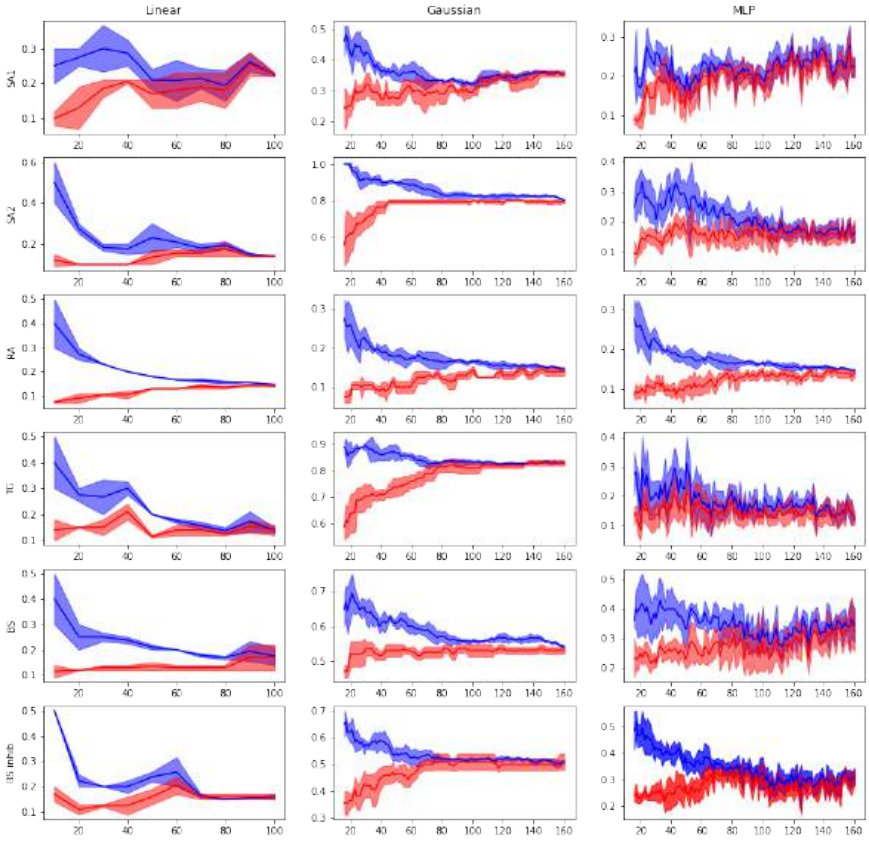


**Supplemental Figure 10 -** Learning curve for most informative neuron on amplitude decoding.

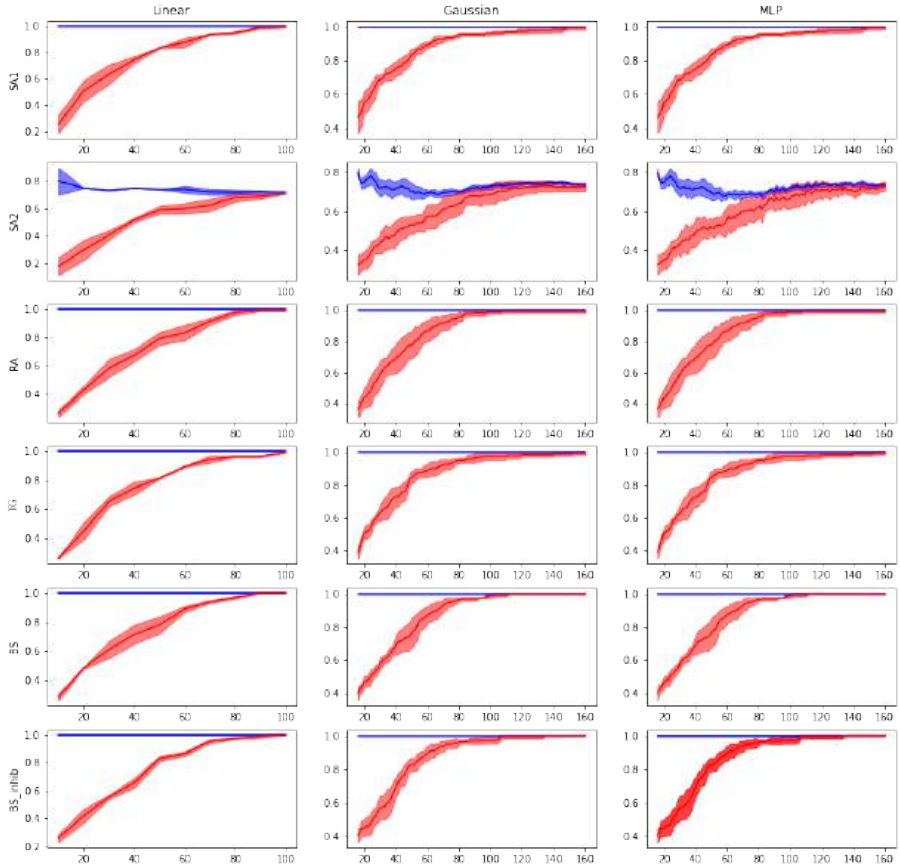


**Supplemental Figure 11 -** Learning curve for whole population on direction decoding.

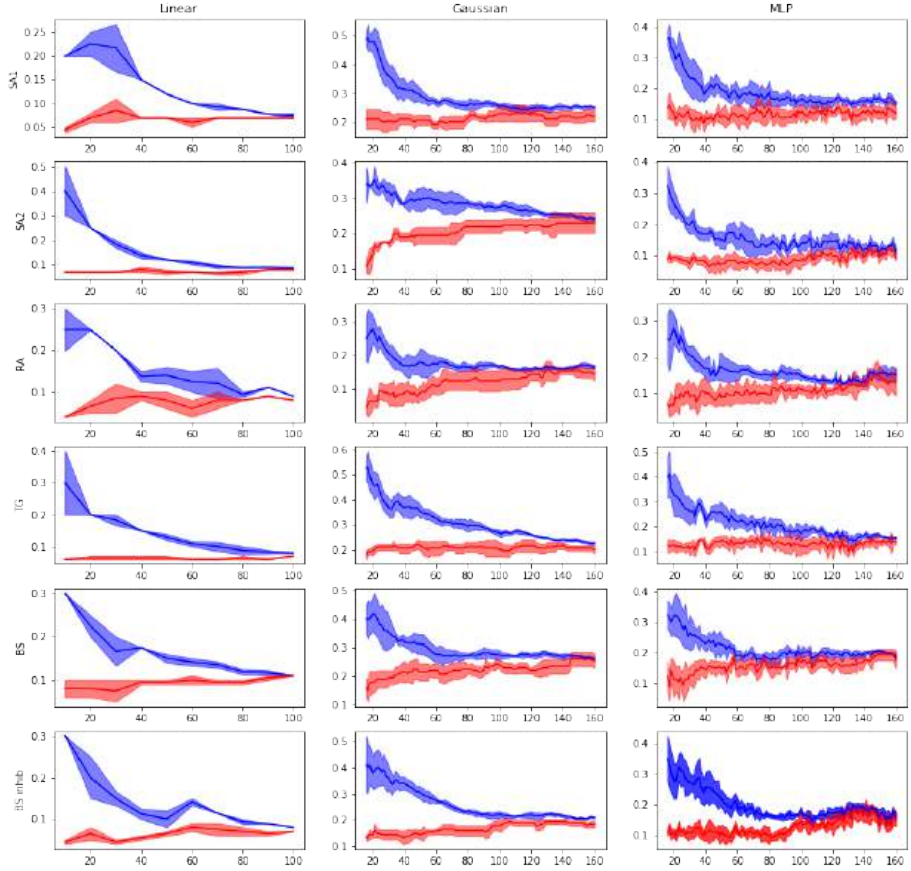


**Supplemental Figure 12 -** Learning curve for the most informative neuron on direction decoding.

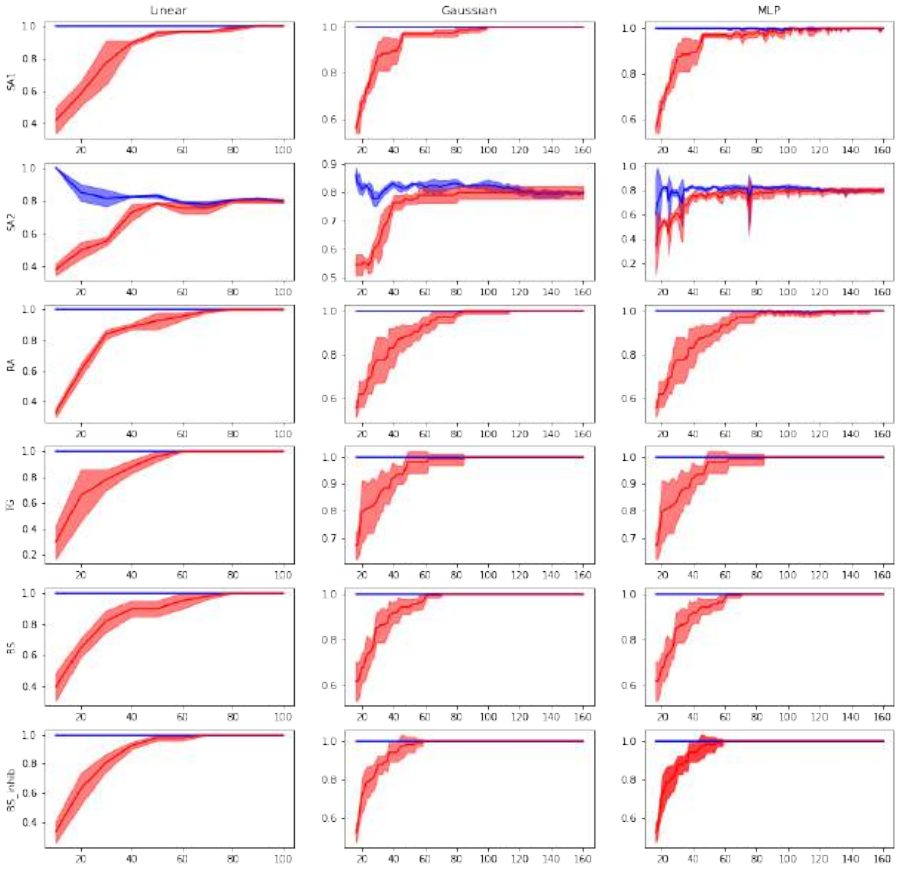


**Supplemental Figure 13 -** Learning curve for whole population on distance to basis decoding.

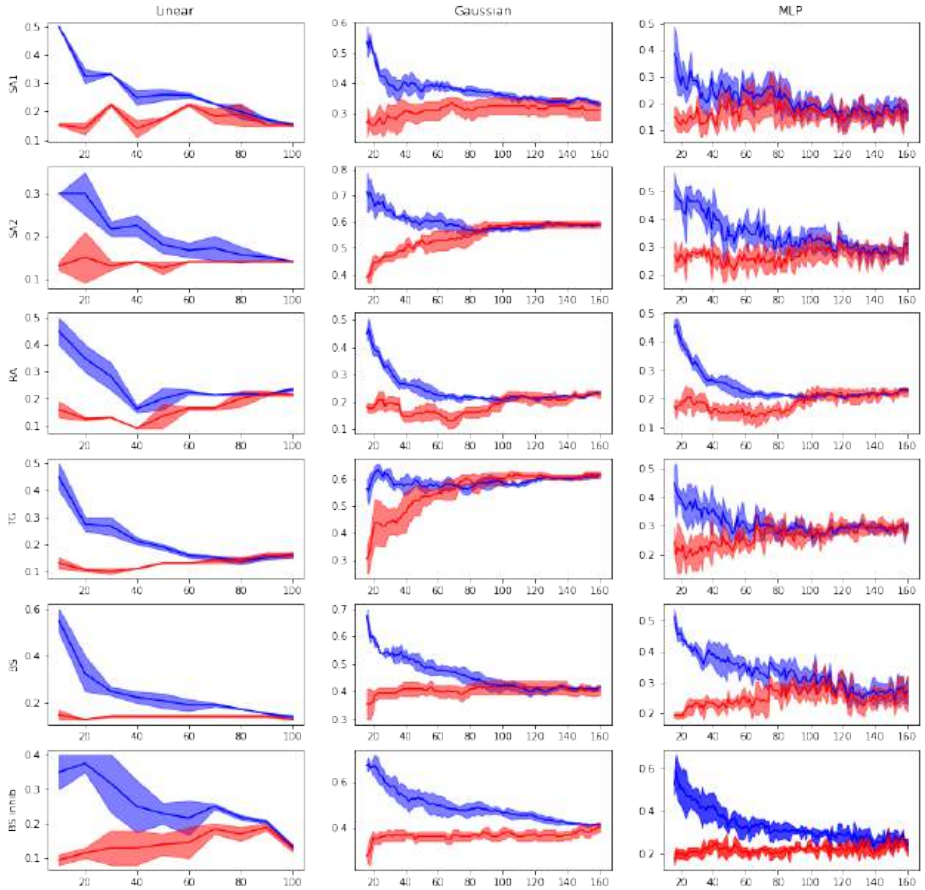


**Supplemental Figure 14 -** Learning curve for most informative neuron on distance to basis decoding.

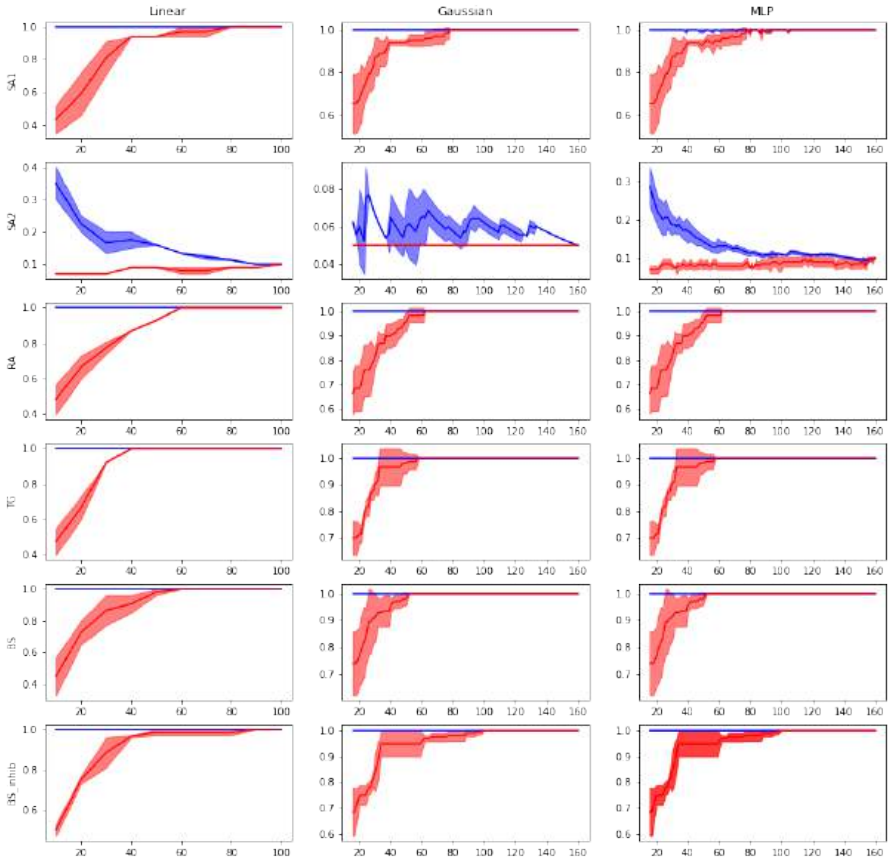


**Supplemental Figure 15 -** Learning curve for whole population on frequency decoding.

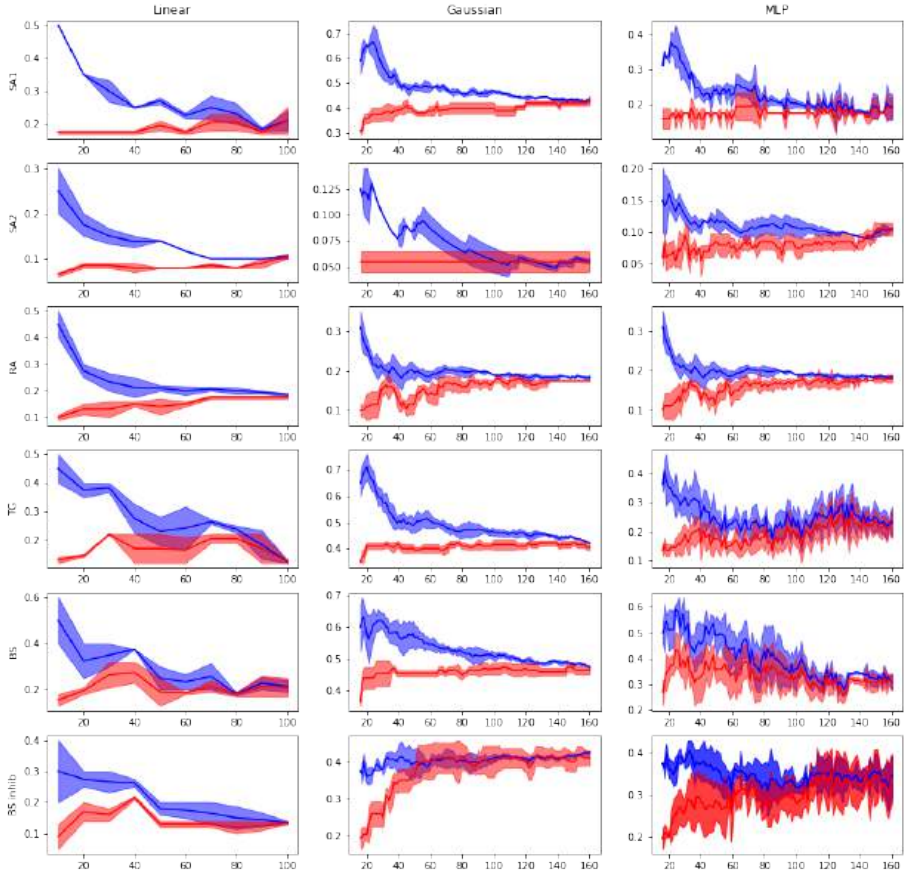


**Supplemental Figure 16 -** Learning curve for the most informative neuron on frequency decoding.

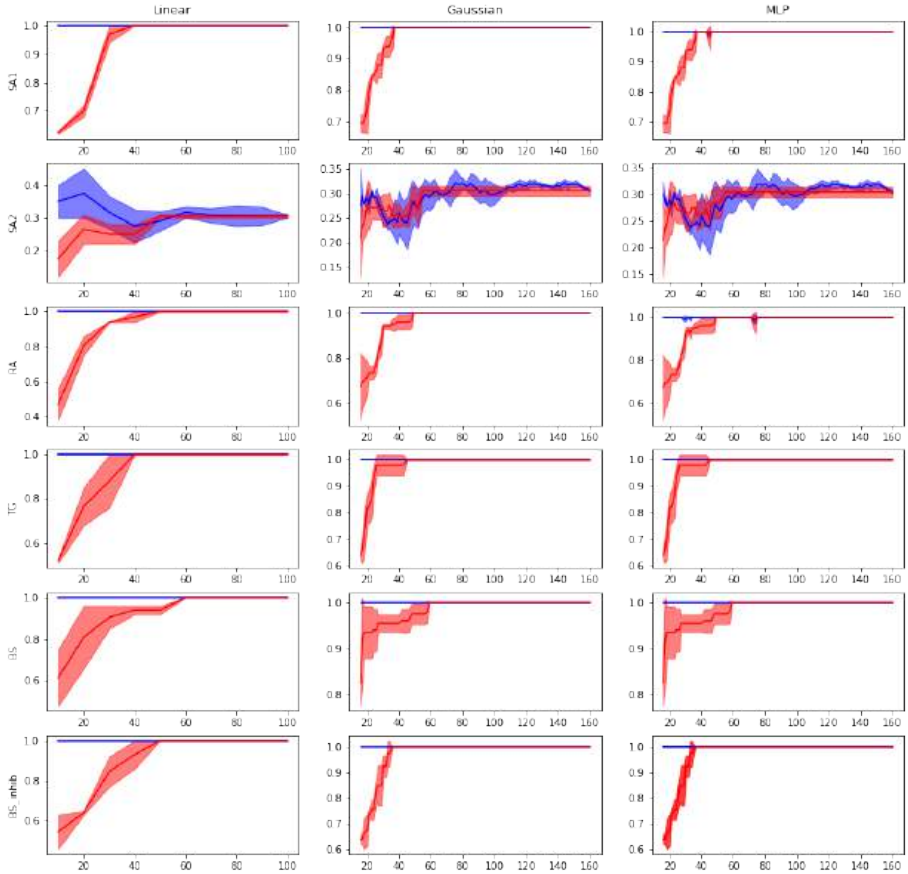


**Supplemental Figure 17 -** Learning curve for whole population on slope speed decoding.

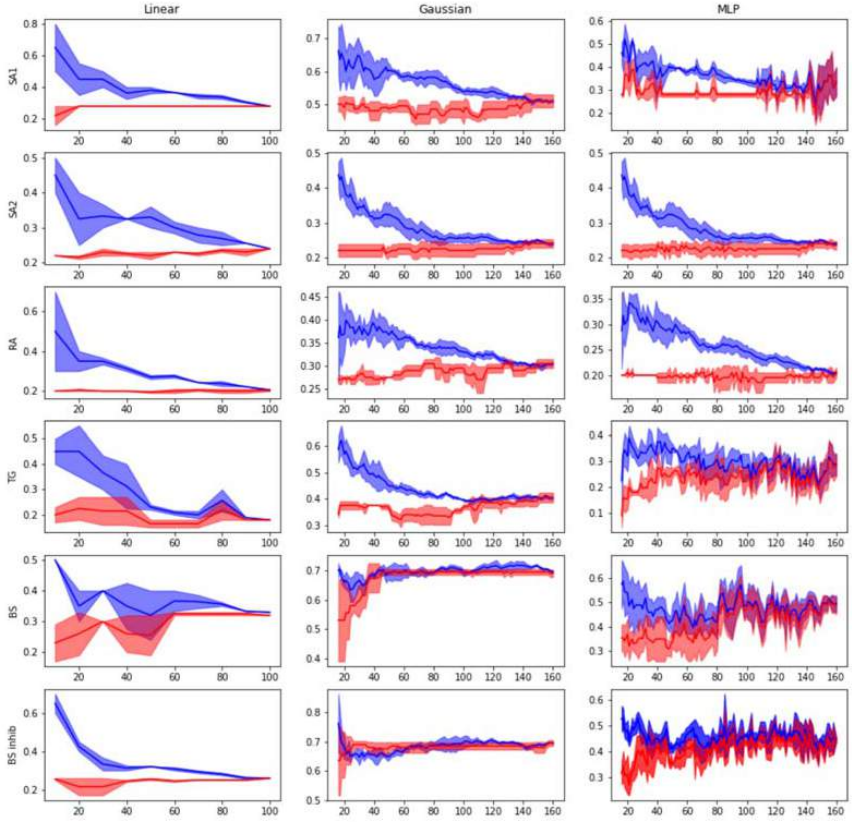


**Supplemental Figure 17 -** Learning curve for most informative neuron on slope speed decoding.

Chapter 5

# From Vibrissae to Cortex: A Computational Model of Whisker-Based Sensory Signal Integration in the Ascending Somatosensory Pathway

## Abstract

Extracting and integrating sensory information is crucial for interacting with our environment. While cortical processing of touch is heavily studied, the contributions of subcortical structures in the ascending somatosensory pathway are often underestimated. We developed a computational model of the rodent whisker pathway, simulating signal transmission from a virtual whisker (WhiskIt) driving distinct mechanoreceptor populations (SA1, SA2, RA), through the trigeminal ganglion, brainstem, thalamus, and into interconnected excitatory and inhibitory populations within cortical layers (L4-L2). By applying a wide range of whisker stimuli (varying deflection direction, force, speed, location, and vibration frequency) and employing decoders alongside information-theoretic measures, we quantitatively assessed stimulus representation and information flow at each stage. Our results reveal significant subcortical processing. Information transfer, measured at both single-neuron and population levels, peaks sharply in the thalamus, coinciding with signal decorrelation, before declining notably in subsequent cortical layers. Similarly, decoding accuracy diminishes progressively through the cortical hierarchy compared to the thalamus. This strongly suggests the ascending pathway, particularly the thalamus, performs substantial integration and optimization, actively transforming signals rather than acting as simple relays. Consequently, the cortex may not aim solely for the highest fidelity stimulus representation but rather for features extracted through this subcortical refinement.

## Introduction

The tactile system allows us to navigate our environment, manipulate objects, and engage in social interactions [1] through responses to pressure, vibration, and heat. The importance of the sense of touch is illustrated by the abandonment of a prosthesis resulting from the lack of tactile feedback for upper-limb amputees [2], making the movement of the prosthesis imprecise, object manipulation tedious, and the prosthetics requiring the whole attention of the patients at all times. Tackling the lack of sensory feedback is a logical step forward in the improvement of artificial limbs. While some solutions have been proposed, they do not rely on biologically plausible feedback, rather, they make use of different vibration patterns applied on the skin, correlated with a stimulus [3]. This approach, while improving the ease to use a prosthetic, still requires learning. To alleviate this shortcoming, taking a bio-inspired approach to sensory stimulation through the study of the somatosensory system is required.



The tactile system has been extensively studied anatomically [4] and functionally [5], particularly the whisker system of the rodent, as the information from a single whisker is easily tracked through the entire ascending pathway because of its topographical organisation [6]. On top of that, the easy manipulation of vibrissae allows for a fine control of different properties of the incoming input (i.e. whisker deflections). Together, these properties of the whisker system make coverage of the stimulus dimensions (whisker deflections) easy to link with neural representations. While the focus has been on cortical representations and modelization [7], the earlier structures along the ascending somatosensory pathway are often overlooked and considered simple relay stations. However, the complex connectivity of the ascending somatosensory pathway [8] and the heterogeneous population of touch cells [9] suggest that complex information processing already occurs at the earlier stages of this system. Therefore, a more in-depth study of the entire pathway from touch cells to the cortex is needed. Here, we propose such a study. We develop a model of the ascending lemniscal somatosensory pathway, of the whisker system [10, 11, 12], in order to quantify the information processing of the early tactile system.

A tactile stimulus enters the central nervous system by activating touch cells, which can be functionally separated into three populations, based on the adaptive properties of a response to a sustained stimulus [13]: Slowly Adaptive Type 1 (SA1) receptors, with a sharp increase of their activity at the onset of a stimulus and a sharp activity decrease towards a low plateau and irregular activity during a sustained stimulus; Slowly Adaptive Type 2 (SA2) receptors, that show an increase of

activity before slowly decaying toward an activity plateau which is higher than that of SA1 receptors during a sustained stimulus; and Rapidly Adapting (RA) receptors, which exhibit activity only during the onset and offset of a stimulus. Therefore, our network's input layer consists of three neural populations mimicking these adaptive properties of the mechanoreceptors. Next, the stimulus information propagates to the Trigeminal Ganglion (TG), before entering the lemniscal pathway. From the TG, the activity propagates to the brainstem (BS), in particular the PrV (nucleus principalis). From PrV, it propagates to the thalamus (TC), in particular to the lemniscal pathway VPM (ventral posteromedial nucleus). From VPM, the activity reaches layer 4 (L4) of the somatosensory cortex, first the barrel field of the somatosensory cortex (bfd), then layer 3 (L3), and it ends its course in layer 2 (L2) in our model. Our network reproduces the architecture of the lemniscal pathway [10, 11, 12] together with the periphery of the whisker system.

Using the 3D whisker model of Zweifel and colleagues (2021) [14], which allows a fine control of whisker movements, we model the forces exerted at the base of a whisker and use these as input to our mechanoreceptor populations. This allows us to record neural activity as a response to various types of whisker deflections, where we manipulate the direction, amplitude, speed and application position along the whisker of the deflection. Additionally, we position a pole at the tip of the virtual whisker and make it vibrate at different frequencies. Through the manipulation of these 5 parameters and the recording of the resulting neural responses for each population, we assess the encoding capacity of tactile stimulus for each structure in the lemniscal pathway. To do so, we decode the different stimulus identities (i.e, we decode the amplitude of deflection amongst other applied amplitude, direction of deflection amongst other direction of deflection, etc.) based on the neural activity of each population, compute the mutual information between the stimulus and either single neurons' or population firing rates, analyze the correlations between pairs of single neuron firing rates amongst each population, and train decoders on the single most informative neuron of each population. We find that the neural activity from each layers of the network allows the different decoders to identify a stimulus, that the transferred information and decorrelation peaks in the thalamus, and that single-neurons' activity in the central nervous system but not in the periphery is sufficient to train a decoder to identify a stimulus.

With this approach, we provide a whisker to cortex model allowing a fine movement of the whisker integrated with a biophysically realistic spiking neural network that responds to these whisker movements. We provide an in-depth quantification of information transfer along the entire lemniscal pathway, and provide insight into

the encoding strategies of each layer to accurately represent the stimulus through the use of different decoding algorithms and calculations of correlations. With this model we improve our understanding of tactile integration in the nervous system by demonstrating that the ascending somatosensory pathway decorrelates and maximizes information transfer up to the thalamus, while the cortex, which stays decorrelated, shows a decrease in the amount of transferred information. Based on these results, we can hypothesize that the cortex reads from the optimal stimulus representation offered by the thalamus to extract features from tactile information, rather than representing the stimulus per se.

## Methods



To analyze the information transfer, the coding strategies, and stimulus representation in the whisker system, we connected a 3D model of a whisker [14] to a neural network mimicking the architecture of the ascending somatosensory pathway. It comprises three input layers, representing the aforementioned three populations of touch cells receiving the force applied at the basis of the whisker as input. The output of these input layers is sent to the trigeminal ganglion, which agglomerates the responses from these three populations. Next, the information propagates to the brainstem (BS), which is the first layer to contain lateral inhibition. The thalamus (TC) then receives the output from BS and connects to the layer 4 excitatory and inhibitory populations, themselves connected to layer 3 excitatory and inhibitory neurons. Finally, the information ends its course in the layer 2 excitatory and inhibitory neurons. We record the firing rate of each neuron upon the application of different sets of stimuli to the whisker and compute the mutual information (MI) between the population activity of each processing layer and the stimuli. We train decoders on this recorded activity to retrieve the stimulus identity. We also compute the Pearson correlation across neurons' firing rates within a population. We conclude by training decoders on the single most informative neuron of each population to assess the evolution of stimulus representation carried by a single neuron along the ascending somatosensory pathway. The model and analysis carried for this research are available on GitHub (https://github.com/Nrault/StimulusRepInAscendingPathway).

### Stimuli

The first component of the whisker-to-cortex model is the whisker itself. To accurately grasp the behavior of a whisker, we rely on the WhiskIt model [14]. In this model, each whisker is composed of 20 links held together by springs for which the elasticity and dampening coefficients were optimized to match the kinematics of

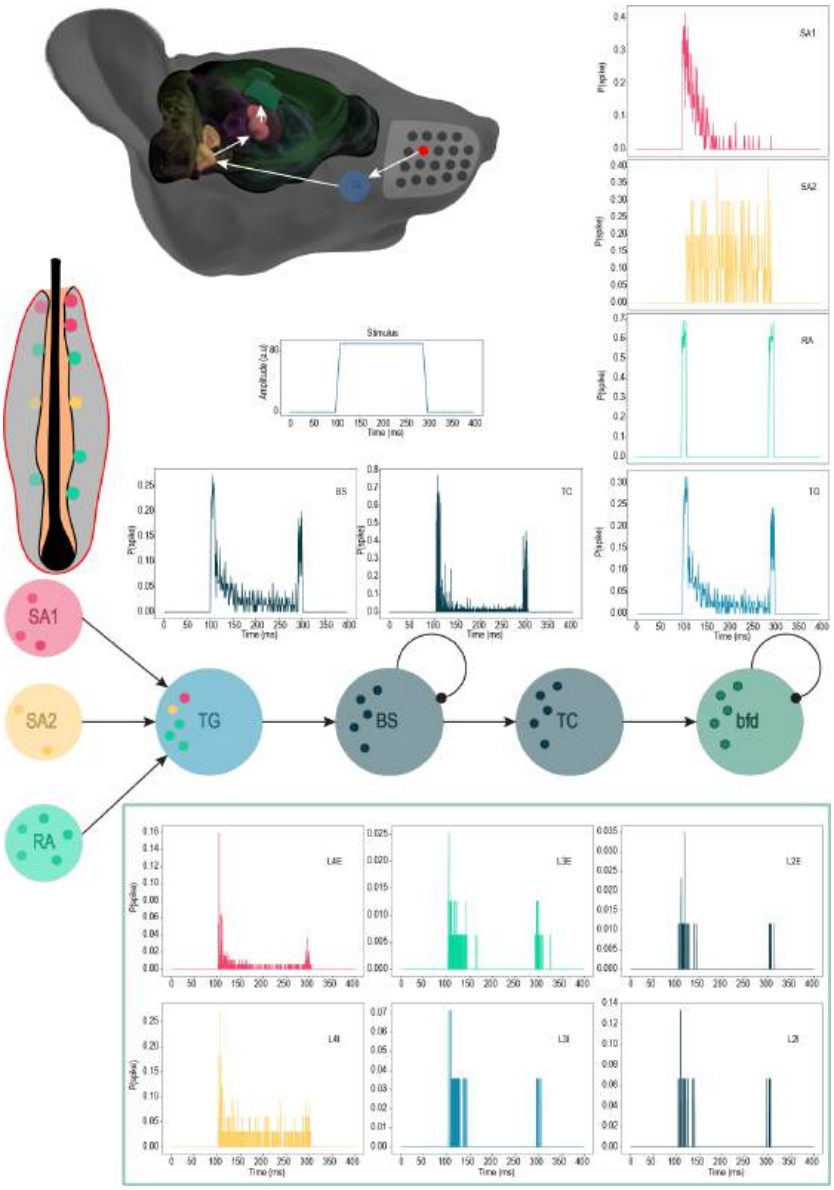


**Figure 1 - Neural response from mechanoreceptors (SA1, SA2, RA) to the layer 2 of the cortex to a ramp-and-hold stimulus. Top-Left** - Side view of a mouse head highlighting the pathway starting in the whisker follicle, going to the brainstem, the thalamus and finally the cortex. Side-view of a whisker follicle with the three types of mechanoreceptors. A plot representing the ramp-and-hold stimulus composed of a ramp-on, a plateau and a ramp-off phase. The x-axis represents the time in ms and the y-axis represents the amplitude of whisker deflection (a.u.). **Middle** - The architecture of the model of the ascending somatosensory pathway. Arrows represent excitation, lines with circle-ends represent inhibition. The plots represent the normalized number of spikes for a population as a response to the ramp-and-hold stimulus. The x-axis represents the time and the y-axis represents the normalized number of spikes.

recorded whisker trajectories during whisking behavior. For the current simulation, we focus on a single whisker in the ramp-and-hold paradigm. The ramp-and-hold paradigm is a passive perception paradigm where a pole is pushed toward a single whisker during a ramp-on phase, held into position during the hold phase, and released back to its initial position during a ramp-off phase (Figure 1). This paradigm allows the manipulation of the orientation of the pole around the whisker (direction) and along the whisker axis, the speed at which the pole moves, and how much pressure the pole applies to the whisker (amplitude) as shown in Figure 2. We also implemented a paradigm (frequency paradigm) where a pole is held against the tip of the whisker and vibrates at different frequencies. Thus, in this set of experiments, we manipulated direction, distance to the whisker basis, slope speed of the ramp-and-hold stimulus, amplitude of whisker deflection, and frequency of vibration. For the ramp-and hold stimuli, each whisker stimulation lasted for 250ms, of which the hold phase lasted 100ms. From these simulations, we extracted the amplitude of the deflection of the base of the whisker as follows:



(1) $amplitude(t) = \sqrt{M_y^2(t) + M_z^2(t)}$ , equation from Yang et al., (2016) [15]

Where My denotes the bending moment at the whisker basis on the y-axis, and Mz denotes the bending moment at the whisker basis on the z-axis. We define the y-axis as oriented toward the top of the head of the mouse, the z-axis toward its snout, and the x-axis toward the whisker tip. Here, we assume that the moment along the x-axis has a negligible effect on the base deflection and thus only consider the YZ moments.

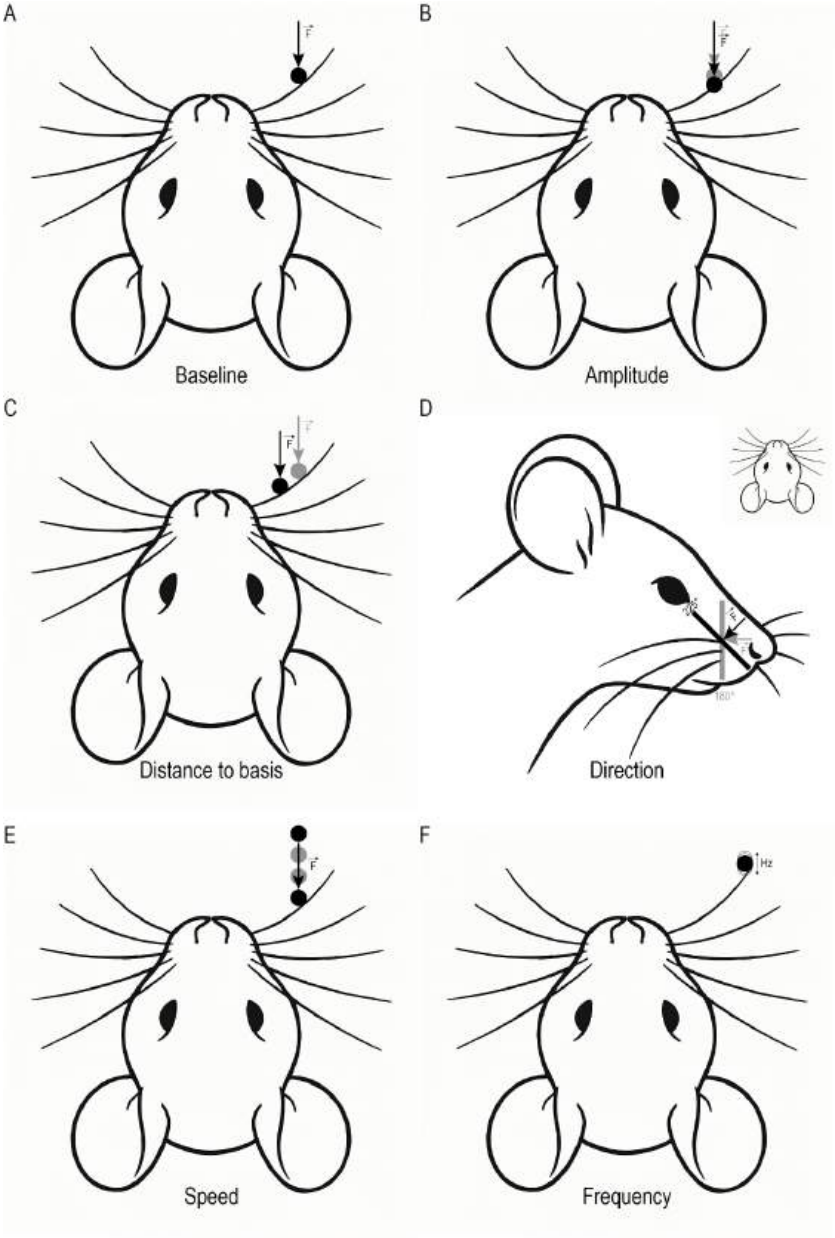


**Figure 2 - Stimulus paradigm for whisker deflection. A -** Baseline setup for whisker deflection: A pole is pushed toward the whisker of the mouse, held in position, and moved back (ramp-and-hold). **B -** From the baseline, we varied the amplitude of deflection. **C -** From the baseline, we varied the distance between the pole and the whisker base. **D -** From the baseline, we varied the direction of the pole around the whisker. **E -** From the baseline, we varied the speed of movement of the pole toward the whisker. **F -** Frequency paradigm: The pole was held against the whisker and vibrated at a constant frequency for one trial. Across trials, this frequency was changed

## Input Layer

The whisker deflection amplitude, as defined in the previous section, forms the input of the mechanoreceptors. This input layer is composed of three touch cell populations matching the Slowly Adapting type 1 (SA1), Slowly Adapting type 2 (SA2), and Rapidly Adapting (RA) mechanoreceptors as found in [13]. The SA1 cells respond with a sharp decrease in their activity slightly after the onset of a stimulus, toward a plateau phase activity with an irregular spiking pattern [16]. SA2 cells have a slower decay time than SA1 and a higher activity during the plateau phase [17]. RA cells respond to the transient part of the stimulus (ramp on and off) [17]. These cells mainly differ in their adaptation rate. To model these input cells, we rely on the Adaptive exponential integrate and fire (AdEx) neuron model [18], which explicitly implements an adaptive current. The basis of the model is described in the equations below (2, 3, and 4):



(2) $dv/dt = (I_{leak} + g_{leak} * \Delta_{th} * e^{(v - v_{th})/\Delta_{th}} - W + I_{app})/C_m$

(3) $I_{leak} = g_{leak} * (E_{leak} - v)$

(4) $dW/dt = (a * (v - E_{leak}) - W)/\tau.$

Where $I_{leak}$ represent the leak current, $g_{leak}$ the leak conductance, $\Delta_{th}$ the slope factor, $v$ is the membrane potential, $v_{th}$ the threshold, $W$ the adaptive current, $I_{app}$ the applied current, $C_m$ the capacitance, $E_{leak}$ the leak reverse potential, $a$ is the strength of adaptation and $\tau$ is the adaptation time constant. The values of each parameter are described in supplemental table 1.

Upon application of a current *Iapp* to the cell, the membrane potential *v* will increase; if it reaches a spike threshold *vth* (-30mV), it is reset to its resting potential vr (-45mV), and the adaptive current *W* is increased by a value *b*. If the threshold is not reached, then the membrane potential and the adaptive current both follow an exponential decay toward their resting values. In the case of several spikes, the adaptive current increases logarithmically before reaching an asymptote where the adaptation saturates (4). We used this model for our receptors and modified the applied current for each cell type according to the descriptions in the following sections.

To ensure that the receptive fields of the mechanoreceptors cover the entire space surrounding a whisker (i.e. a deflection of the whisker in any direction results in activation of a mechanoreceptor), the receptive field of each mechanoreceptor

was modelled as a cosine-shaped bump set to a position that modulated their responses according to the following equation:

(5), $\Gamma_{ti} = (cos(d_t - p_i)$, with t ∈ T, the duration of the simulation.

Where $d_t$ is direction of the whisker deflection at time t, $p_i$ is the position of mechanoreceptor i, and $\Gamma_{ti} \in [0; 1]$ is the direction selectivity of mechanoreceptor i at time t. The parameter that gives each receptor's maximum response, $\Gamma_{ti}$ *was* unique for each receptor and was drawn from a Gaussian distribution centered around 0 degrees (toward the snout of the mouse) and 180 degrees (toward the tail of the mouse) with a standard deviation of 90 degrees.

## SA1

SA1 receptors response is primarily modulated by direction of whisker deflection but poorly by amplitude [19, 17, 9, 20]. Therefore, for SA1 receptors, we assume an ON/OFF relationship to differences in amplitude of whisker deflection; that is, the stimulus current $I_{app}$ is multiplied by 1 if there is a stimulus and 0 otherwise (6, 7). The activation threshold to estimate whether a stimulus was present (sensitivity) was hand-tuned and set to 0.01:

(6) $I_{app} = (900\,pA * H(t)) * \Gamma_{ti}$, with t ∈ T, the duration of the simulation, and i is the id of the mechanoreceptor.

(7) $H(t) := \{0, amplitude(t) \geq 0.01;\ 1, amplitude(t) < 0.01\}$

with t ∈ T the duration of the simulation.

## SA2

SA2 receptors are sensitive to direction and amplitude [19, 17, 9, 20] of whisker deflection; we, therefore, assumed a logarithmic increase of their response as a function of the whisker deflection amplitude :

(7) $I_{app} = (900\,pA * log(1 + 2 * amplitude(t)))$

## RA

We assume that RA receptors are sensitive to a switch in amplitude [19, 17, 9, 20]:

(8) $I_{app} = (900\,pA * log\,(amplitude(t) / amplitude(t - dt))$, with t ∈ T the duration of the simulation and dt = 1 ms.

## Fitting of the mechanoreceptor model parameters

The parameters (*a, b,* and **τ**) used in the receptor models SA1, SA2, and RA were fitted to recordings performed by Sonekatsu and Gu [13] in 2019. They extracted a whisker follicle from a mouse and recorded directly the response of the receptor to a ramp-and-hold stimulus. From there, they computed the instantaneous firing rate (1/ISI, interspike interval). To fit the AdEx model parameters to the recordings, we used the CMAES algorithm from the CMA python toolbox, a covariance-matrix-based evolutionary algorithm that relies on the covariance between the parameters of the model and the error function (here a mean squared error, MSE between the instantaneous firing rate of the modeled receptors and the instantaneous firing rate of Sonekatsu and Gu's recordings [13]). With this, we optimized the adaptive parameters of the model (i.e., *a, b,* and **τ**, see supplemental Table 1), allowing us to replicate the adaptation rate of the different populations of receptors. The parameters of the RA receptors were hand-fitted, as the number of data points was too low to allow the model to train. We thus changed the value of the adaptation current (*a, b,* and **τ**) so that RA responds to the transient part of the stimulus.



## Network models for the early stages of the central nervous system

The trigeminal ganglion (TG) and brainstem (BS) neurons are both modeled using the adaptive exponential integrate and fire neurons (Adex with parameters *a* and *b* set to 0 to inactivate the adaptation). TG neurons receive one-to-one connections (see supplemental Table 2) from the receptor layer, with each presynaptic action potential resulting in an instantaneous increase in the postsynaptic membrane potential that was set so that a TG neuron responds to the activity of a single receptor (supplemental Table 3). BS neurons receive a probabilistic connection pattern. Each BS neuron has a probability of 0.01 to receive an input from a TG neuron. Similarly, each BS neuron has a probability of 0.01 to send an inhibitory connection to another BS neuron (supplemental Table 3). Excitatory synapses are modelled as instantaneous synapses that increase the membrane potential of the afferent neuron by 25mV, while inhibitory connections decrease it by 25mV (supplemental Table 3). The thalamocortical part of the model is adapted from [21] and is defined below.

## Conductance based Model for cortical neurons

Excitatory and inhibitory (E and I) cortical neurons were modeled as conductance-based neurons. The membrane potential of the neuron *i* at time *t* is described by the following equation:

$$(9)\quad \dot{V}_i = \left(-\sum_k I_k(t) + I_i(t)\right)/C_m + \sum_{syn} V_{syn},$$

where  denotes the membrane capacitance, and  is the sum of ionic currents that pass through ion channel *k*. Unlike the receptors, TG and BS neurons, for the thalamic and cortical neurons the full action potential is modelled. Synapses are modelled as instantaneous synapses: when a presynaptic neuron spikes, the postsynaptic membrane potential is increased by an amount of , whose value is described in supplemental Table 3. $I_i(t)$ corresponds to an intrinsic noise current of neuron *i* behaving as described in the equation (10):

(10) $I_i(t) = \sqrt{dt}\sigma\xi_i(t)$,

where the timestep of the simulation for cortical neurons is dt = 0.01ms, $\xi_i$ is a random value drawn at every step for each neuron independently from a normal distribution centered around $\mu = 0$ and standard deviation 1, which is then multiplied by the amplitude $\sigma = 100pA/\sqrt{ms}$.

The ionic currents  used in equation (9) for excitatory (E) and inhibitory (I) neurons are adapted from the work by Pospischil and colleagues from 2008 [22]:

(11) $\sum_k I_k = I_{Na} + I_{KDR} + I_M + I_L$.

The membrane potential is depolarized by a sodium current (Na) and repolarized by a delayed corrected potassium current (KDR). Hyperpolarisation is achieved through a slow non-inactivating potassium current (M) and leak current (L) maintains the neuron's membrane potential at its baseline in the absence of input.

The sodium channel is described by (12):

(12) $I_{Na} = g_{Na}m^3h(v - E_{Na})$,

where $g_{Na}$ is the maximum channel conductance, $E_{Na}$ is the reversal potential of the sodium channel (supplemental Table 2), $m$ and $n$ are, respectively, the activation and inactivation variables of the channel such that

(13) $\dot{m} = \alpha_m(V)(1 - m) - \beta_m(V)m$,

(14) $\dot{h} = \alpha_h(V)(1 - h) - \beta_h(V)h$,

Here, α is the transition rate from open to closed and β is the transition from closed to open. Both α and β depend on a fixed threshold $V_T$ (supplemental table 2) as described below:

(15) $\alpha_m = \frac{-0.32(V-V_T-13)}{exp[\frac{-(V-V_T-13)}{4}]-1}$

(16) $\beta_m = \frac{-0.28(V-V_T-40)}{exp[\frac{-(V-V_T-40)}{5}]-1}$

(17) $\alpha_h = 0.128\, exp[\frac{-(V-V_T-17)}{18}]$

(18) $\beta_h = \frac{4}{1+exp[\frac{-(V-V_T-40}{5}]}$.

The delayer-rectified potassium channel's behaviour is described as

(19) $I_{KDR} = g_{KDR} n^4 (V - E_{KDR})$,

where $g_{KDR}$ is the maximum channel conductance, $E_{KDR}$ is the reversal potential (supplemental Table 2), and  is the activation is the channel described by

(20) $\dot{n} = \alpha_n(V)(1-n) - \beta_n(V)n$,

with the transition rates  and given by:

(21) $\alpha_n = \frac{-0.032(V-V_T-15)}{exp[\frac{-(V-V_T-15)}{5}]-1}$

(22) $\beta_n = 0.5 exp[\frac{-(V-V_T-10)}{40}]$,

The slow non-inactivation current is described by

(23) $I_M = g_M p(V - E_M)$,

where $g_M$ is the maximum channel conductance, $E_M$ is the reversal potential (supplemental Table 2), and $p$ is the activation variable of the channel described by

(24) $\dot{p} = \frac{p_\infty(V)-p}{\tau_p(V)}$.

Here, $p_\infty$ is the steady-state activation function defined as:

(25) $p_\infty = \frac{1}{1+exp[\frac{-(V+35)}{10}]}$

and $\tau_p$ is the channel time constant depending on $\tau_{max}$ (supplemental table 2) as:

(26) $\tau_p = \frac{\tau_{max}}{3.3exp[\frac{V+35}{20}] + exp[\frac{-(V+35)}{20}]}$

Finally, the leak channel current is described by

(27) $I_{leak} = g_{leak}(V - E_{leak})$,

with $g_{leak}$ the maximum channel conductance and $E_{leak}$ the reversal potential of the channel (supplemental Table 2).

## Parameter Fitting for Cortical Neurons

The distinction between E and I neurons in this model was made through channel-specific parameters to mimic known differences between their input-output characteristics [22]. E neurons emit action potentials at a lower frequency than I neurons in the barrel field of the primary somatosensory cortex when stimulated with injected current with similar amplitude [23]. The $g_{Na}$, $g_M$, $g_{leak}$, $V_T$ and $\tau_{max}$ from the neuron model described above were fitted to reproduce the current-frequency (I-f) curves from Zeldenrust et al. (2024) [23].

## Model of Thalamic Neurons

Thalamocortical relay (TCR) neurons are also modeled as single-compartment models.and are based on a model from Ching et al. (2010) [24]. For these neurons, the membrane potential of neuron over time is described as follows:

(28) $\dot{V}_i = - \sum_k I_k(t)/\mathrm{C}$

Following the description of the cortical neuron model, $\sum_k I_k$ is the sum of ionic currents passing through the voltage-gated channels $k$. For every spike originating from presynaptic neurons in the brainstem (BS), the postsynaptic TCR cell's membrane potential was increased by 10 mV. In this model, following the TCR model from Ching et al. (2010) [24], the ionic currents can be expressed as:

(29) $\sum_k I_k = I_{Na} + I_k + I_T + I_h + I_{K-L} + I_L$

The sodium channel (Na) dynamics are the same as for the cortical neurons, described in equations (12) to (18), with $g_{Na} = 90mS$, and $E_{Na} = 50mV$ (supplemental Table 2).

The potassium (K) current is described by

(30) $I_k = g_K m^4 (V - E_k)$,

with the maximum conductance $g_K = 10mS$, and the reversal potential $E_K = -100mV$ and the channel activation variable $m$ given by

(31) $\dot{m} = \alpha_m(V)(1 - m) - \beta_m(V)m$..

Here, transition rates α and β are given by

(32) $\alpha_m(V) = \frac{0.032(15 - V + V_T)}{exp[\frac{(15 - V + V_T)}{5}] - 1}$

(33) $\beta_m(V) = \frac{0.5(10 - V + V_T)}{exp[\frac{(10 - V + V_T)}{40}]}$, ,

with threshold $V_T = 25mV$.

In addition to the sodium and potassium currents, TCR neurons exhibit a T-type calcium current

(34) $I_T = g_{Ca} m_\infty^2 h(V - E_{Ca})$,

where $g_{Ca} = 2mS$ is the maximum channel conductance, $E_{Ca} = 120mV$ is the reversal potential and $m$ represent the channel activation based on the steady state given by

(35) $m_\infty = \frac{1}{(1+exp[\frac{-(V + V_T + 57)}{6.3}]}$. .

Similarly, $h$ represents the inactivation based on its steady state $h_\infty$

(36) $\dot{h} = (h_\infty - h)/\tau_h$

(37) $h_\infty = \frac{1}{(1 + exp[\frac{(V + V_T + 81)}{4}]}$.

The time constant $\tau_h$ is described as:

(38)

$$\tau_h = (30.8 + (211.4 + exp[(V + V_T + 113.2)/5])/(1 + exp[(V + V_T + 84)/3.2]))/3.72$$

5

Both $m$ and $h$ depend on a fixed threshold $V_T = 2mV$.

The TCR neurons also have an h-current, of which the dynamics are described by

(39) $I_h = g_h(o_1 + 2(1 - c_1 - o_1))(V - E_h)$,

where $g_h = 0.01\, mS/cm^2$ is the maximum conductance of the channel, $E_h = -40mV$ the reversal potential and $o_1$ and $c_1$, respectively, the channel activation and inactivation variables described by:

(40) $\dot{o}_1 = 0.001(1 - c_1 - o_1) - 0.001(\frac{(1-p_0)}{0.01})$

(41) $\dot{p}_0 = 0.0004(1 - p_0) - 0.0004([Ca]_i/0.002)^4$

(42) $[\dot{Ca}]_i = \frac{-10I_T}{2*96489} + \frac{0.00024-[Ca]_i}{5}$.

Here, $p_0$ modulates the h-current according (equation(41)), based on the calcium concentration in the cell (equation (42)).

The inactivation $c_1$ is given by

(43) $\dot{c}_1 = \beta(V)o_1 - \alpha(V)c_1$,

with transition rates α and β given by

(44) $\alpha(V) = \frac{h_\infty(V)}{\tau_s(V)}$

(45) $\beta(V) = \frac{(1 - h_\infty(V))}{\tau_s(V)}$.

Here, $h_\infty$ is the steady state value and $\tau_s$ the time constant such that:

(46) $h_\infty(V) = \frac{1}{1+exp[\frac{(V+75)}{5.5}]}$

(47) $\tau_s(V) = 20 + 1000/((1 + exp[(V + 71.5)/14.2]) + (1 + exp[-(V + 89)/11.6]))$

TCR neurons contain two leak channels (potassium: $I_{K-L}$, and general $I_L$) described by

(48) $I_{K-L} = 0.0172(V + 100)$

(49) $I_L = 0.01(V + 70)$.

## Parameter fitting for Thalamic Neurons

The initial TCR neurons model from Ching et al. (2010) [24] modeled the thalamic neurons during anaesthesia. This state makes the TCR neurons burst upon stimulation. To reproduce thalamic activity in an awake state, we depolarized the membrane potentials of the TCR neurons by increasing the maximal conductance of the hyperpolarization-activated h-current (supplemental table 3).

## Network Architecture

The network was composed of 12 populations, among which, three input populations:



- SA1 population was composed of 24 neurons
- SA2 population was composed of 10 neurons
- RA population was composed of 36 neurons
- TG, BS, and TC populations were composed of 70 neurons
- L4E population was composed of 188 neurons
- L4I population was composed of 33 neurons
- L3E population was composed of 158 neurons
- L3I population was composed of 28 neurons
- L2E population was composed of 86 neurons
- L2I population was composed of 15 neurons

The connectivity between the neuron populations is described in supplemental table 3. Simply, all populations up to BS (excluded) are connected with a one-to-one connectivity pattern following the scheme in Figure 1. Once within BS the connections become probabilistic. For instance, BS as 1% probability to send a lateral inhibitory connection to BS, which means that amongst $(70^2 - 70)$ possible connections amongst all BS neurons, 1% of it will exist. BS neurons are both excitatory (feedforward connections to VPM) and inhibitory (lateral connection to BS), VPM contains only excitatory neurons. Starting from the L4, each structure contains excitatory and inhibitory populations which have their own connectivity pattern as described in supplemental table 4.

## Decoders

Virtual whiskers were stimulated with a virtual pole, using a `ramp and hold' protocol. In such a protocol, a pole is pushed toward a whisker during a ramp-on phase, held in position during a hold phase, and pulled back during a ramp-off

phase (Figure 1). Different parameters of such ramp and hold protocols were varied: the maximum amplitude, direction, distance to whisker base, slope, and frequency (Figure 2). For each set of stimuli, the same set of initial parameters was used: for the first stimulus: The pole was positioned at 10 mm of the targeted whisker and moved at a speed of 0.3 m/s, with an angle of 0° around the x-axis (along the whisker). The amplitude of the stimulus was 1 mm, and it was held against the whisker for 100 ms.

For sets of stimuli where the maximum amplitude was varied, the maximum amplitude was varied from 1 mm to 20 mm with a step of 1 mm (Figure 2). For sets of stimuli where the direction was varied, the pole was oriented from 0° to 350° with steps of 10° (Figure 2). For sets of stimuli where the distance to the whisker basis was varied, we targeted each of the 20 links that compose the whisker once (see –ref Whiskit paragraph and Figure 2). For sets of stimuli where the slope speed was varied, the pole moved from 0.25 to 0.35 m/s with steps of 0.01 m/s (Figure 2). Finally, for sets of stimuli where the frequency was varied, the pole was placed against the last link of the whisker and vibrated with a frequency of 2 to 32 Hz with steps of 2 Hz (Figure 2).

For each stimulus, we trained different decoders to identify the value of the applied stimulus. The recorded neural activity was then split across populations so that a decoder was trained on the activity of neurons from a single population and not the entire pathway.

The firing rate of each neuron was given as input to a linear decoder, a Bayesian decoder, and a multilayer perceptron (from scikit-learn [25]: RidgeClassifier, NaiveBayes, and MLPClassifier). In a final calculation, the firing rate from only the most informative neuron based on Mutual information calculation (see below) was selected to train the decoders. The decoders were tasked to retrieve the stimulus parameters, for instance if the amplitude of whisker deflection was varied, we asked the decoder to identify the applied amplitude amongst all 19 applied amplitudes that were simulated. To do so, the decoders relied on a vector containing the number of spikes for each neuron of a population as an input (in the case of the most informative neuron, the input was of size 1x1). The accuracy of each decoder was then calculated as the number of correct responses over the total number of responses.

## Information Quantification

We quantified the information transferred across layers within the pathway by computing the mutual information between the stimulus and the firing rate of a whole population or of a single neuron for each stimulus. This MI was computed as follows:

$$(50)\ MI(X, Y) = H(X) - H(X|Y),$$

with $H$ being the Shannon entropy, X the distribution of spikes for a given population or a given neuron, and Y the distribution of the stimulus conditions. No bias correction was applied to the mutual information (MI) calculation. Although this might seem unexpected for biological data, our analysis concerns a deterministic model: for a given stimulus, the neural response is always identical. Consequently, subsampling bias cannot occur. The absence of noise ensures a single possible output for each stimulus, though distinct stimuli can converge onto the same neural representation. In such cases, the conditional input entropy given the output, H(X|Y), may be smaller than the input entropy H(X), since two stimuli x and x′ can produce the same output y. Nevertheless, the mapping remains deterministic: whenever x or x′ is presented, the same response y will occur. For these reasons, bias correction was not required in our MI estimates.

The resulting MI was plotted against the entropy of the stimulus computed as:

$$(51)\ H(Z) = -\sum_{x \in Z} p(x)\, log\, p(x),$$

where Z is the distribution of t either the stimulus values, the firing rate of a single neuron or the firing rate of a whole population.

Based on the MI values computed for each neuron, we identified the most informative neuron for each population for each condition as the neuron that had the maximum MI and used its firing rate as input for decoders (see Decoders).

## Pearson correlation

We computed the Pearson correlation coefficient within each population across pairs of neurons' firing rates to determine the redundancy of each structure. It is given by

$$(52)\ r(x, y) = \frac{\sum_{i}^{N}(x_i - m_x) * (y_i - m_y)}{\sqrt{\sum_{i}^{N}(x_i - m_x)^2 * \sum_{i}^{N}(y_i - m_y)^2}},$$

With $m_x$ the mean of vector $x_i$ and $m_y$ the mean of vector $y_{i'}$ with $x_i$, the firing rate of neuron x in response to stimulus *i*, and $y_{i'}$ the firing rate of neuron y in response to stimulus *i.* N is the number of stimuli presented to the network for a given parameter, modified from the baseline.

# Results

To determine the coding strategies of the different structures along the ascending somatosensory pathway, we built a neural network composed of 7 layers and 12 populations (3 receptor populations, TG, BS, Thalamus, 3 excitatory cortical populations and 3 inhibitory), 3 of which are input layers consisting of the different types of mechanoreceptors found in the whisker follicle. We assessed the capacity of each population to carry information about a whisker stimulus through decoding the neural activity. Through mutual information calculation between each neuron's firing rate and a stimulus, we assessed how information is distributed within each population. We determined the degree of redundancy in each layer by computing the Pearson correlation coefficient between the firing rate of pairs of neurons within a population. Here, we describe the results.

## Model Description

We fitted the parameters of an AdeX neuron [18] to the instantaneous firing rate recorded by Sonekatsu and Gu in 2019 [13] (see Methods and supplemental table 1). Through this procedure, we obtained three input populations that responded like the recorded mechanoreceptors in the whisker follicle to ramp-and-hold stimuli. The TG and BS neurons were tuned to spike whenever they received synaptic input. The cortical excitatory neurons were tuned to have a regular spiking pattern, while the inhibitory neurons were tuned to have a fast spiking pattern [21].

Based on the optimizations described above, we now have a neural network model that describes the propagation of neural activity from the touch cells up to the cortex upon whisker stimulation (Figure 1). The activity profile remains the same from TG to the layer 2 of the somatosensory cortex: It shows a sharp surge of activity at the onset of a stimulus, a decrease toward a plateau phase during the hold part of a ramp-and-hold and another increase of activity when the force is released. Upon the application of force on the 3D virtual whisker, activity appears in the receptor population and propagates across each structure up to layer 2 of the somatosensory cortex (Figure 3). A shift in the stimulus, either in amplitude of deflection, direction, frequency, speed, or the pole position along the whisker

resulted in a shift in the neural response for every population, easily noticeable in the periphery (Figure 3 and supplemental Figures 1 to 4) except for in SA1, which appears unaffected by speed or frequency of the stimulus or in SA2, which was not triggered during the frequency paradigm as the force applied to the whisker was not sufficient to trigger activity in these receptors.



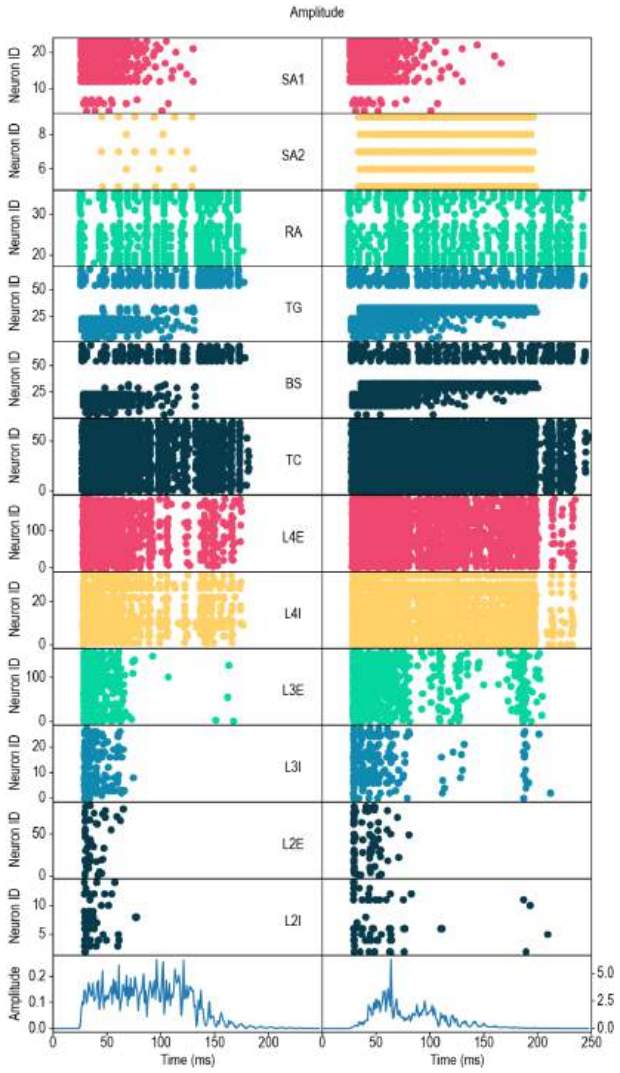


**Figure 3 - Example model response.** Model response to two different stimuli varying in the applied amplitudes. Each row is a raster plot of the spike responses of a population when the network receives stimuli with a different amplitude (say which and refer to stimulus explanations) under two different applied amplitudes of deflection, as represented in the last row. We thus see the propagation of the spiking activity from the touch cells (SA1, SA2, RA) to the cortex (L4, L3, L2). The x-axis represents the time in ms, and the y-axis the neuron ID or the applied amplitude for the last row.

Overall, our network exhibits responses mimicking biological responses to a ramp-and-hold stimulus and responds to deflections of the virtual whisker from WhiskIt [14].

## Decoding Population Activity

We trained decoders on each population's output to assess each structure's ability to represent the stimulus. To do so, we used the firing rate of each neuron (so a population firing rate vector) as an input to different decoders (see Methods) and trained them to provide the value of the stimulus parameter that was varied in sets (amplitude of deflection, angle of deflection (for direction), speed of deflection, frequency of deflection, and position along the whisker). In summary, a decoder needs to identify one applied amplitude amongst other amplitudes, one direction amongst other directions of deflection, etc… at a time.

The decoders were able to determine the value of each applied stimulus regardless of the feature that was modified (i.e. the accuracy was the same if the amplitude, direction, etc…, was modified) (Figure 4). While the maximum accuracy of the decoders remained constant across the different applied stimuli, not all populations' outputs were providing the same decoding capacity, as SA2, and particularly, SA1, since the decoders trained on the activity of these 2 populations demonstrated poorer performance compared to others. The SA1 population seems to be specialized for direction encoding, as the accuracy of the decoders trained on SA1 are approaching 0 for all dimensions except direction. SA2 seems to be informative about every component of the tactile stimuli except for frequency, in agreement with previous results showing no activity in SA2 for the frequency paradigm (Supplemental Figure 3). Of all decoders, it appears that the naive Bayesian decoder performs best in determining different stimulus features from the recorded neural activity.

In conclusion, it appears that decoders can distinguish different stimulus features from the firing rate vector of an entire population. While in the periphery some receptors appear to be specialized for specific stimulus features, this does not propagate to higher layers of the CNS; each further structure in the lemniscal pathway contains enough stimulus information to achieve a 100% decoding accuracy.

## Information transfer is maximized in the thalamus

To determine the encoding strategies in each structure of the ascending somatosensory pathway, we compute the MI between each single neuron firing rate and the stimulus, as well as the MI between the population firing rate and the stimulus.

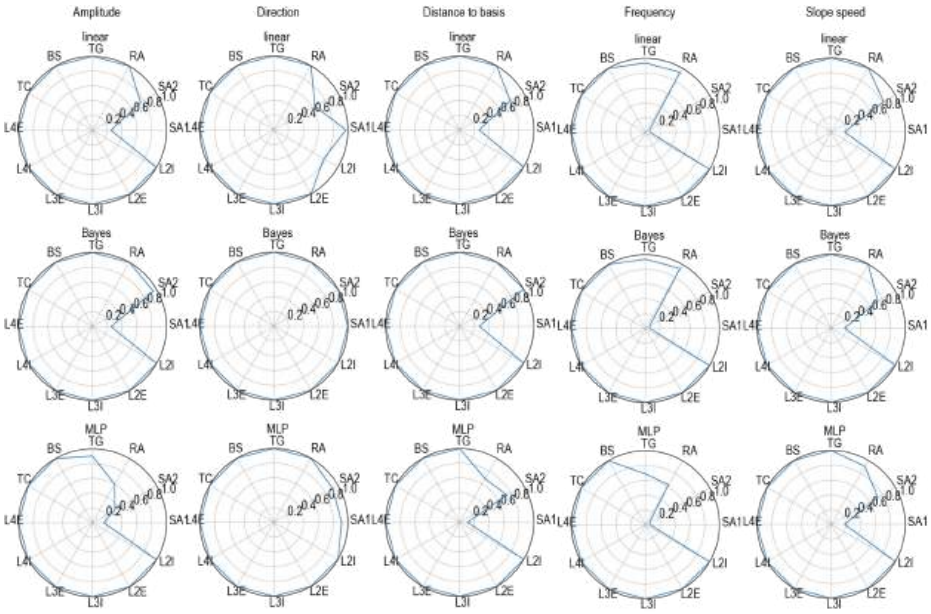


**Figure 4 - Decoding accuracy of the different populations.** The decoding accuracy was calculated based on the population firing rate vector (i.e. the firing rate of each per neuron) for sets of stimuli where different features were varied, each different stimulus applied to the whisker. Each radar plot represents the decoding accuracy per stimulus, ranging from 0 to 1 (perfect decoding of the applied stimulus). Each row corresponds to one of the three decoder types (linear, Bayesian, and MLP).

This analysis revealed that while the activity of some neurons in the periphery provide no information about the stimulus, from the Thalamus on, the activity of each neuron carries stimulus information (Figure 5). Except for the direction, half of the receptors' population do not respond to the stimuli (Figure 3 and supplemental figures 1-4), this is propagated to TG and BS. SA1 is the least informative type of touch cell, as it carries information only about one feature: the direction, the MI between a stimulus feature and a single cell activity for other dimensions of the stimulus is minimal. SA2's lack of response makes the MI null for the frequency paradigm, as expected. At the single-neuron level, information transfer drops consistently past layer 3 of the cortex and even layer 4 in the case of direction, distance to basis, and slope speed (Figure 5, violin plots). The same can be seen at the population level (Figure 5, dots).

To summarize, we see that in the periphery, single neurons carry a wide distribution of stimulus information, that goes from close to entropy to zero. As soon as information reaches the Thalamus, we see that the distribution of MI values decreases in width, showing that every neuron in this structure contains a similar

amount of information about the stimulus. While the shape of the distribution remains narrow after TC, the maximum and minimum MI for single-neurons starts to fall in Layer 3 and drops quickly in Layer 2. When considering the population MI (Figure 5, dots), we see that while it is more informative (closer to entropy) than that of single-neurons, it follows the same trend, dropping from Layer 3, and sharply decreasing in Layer 2.

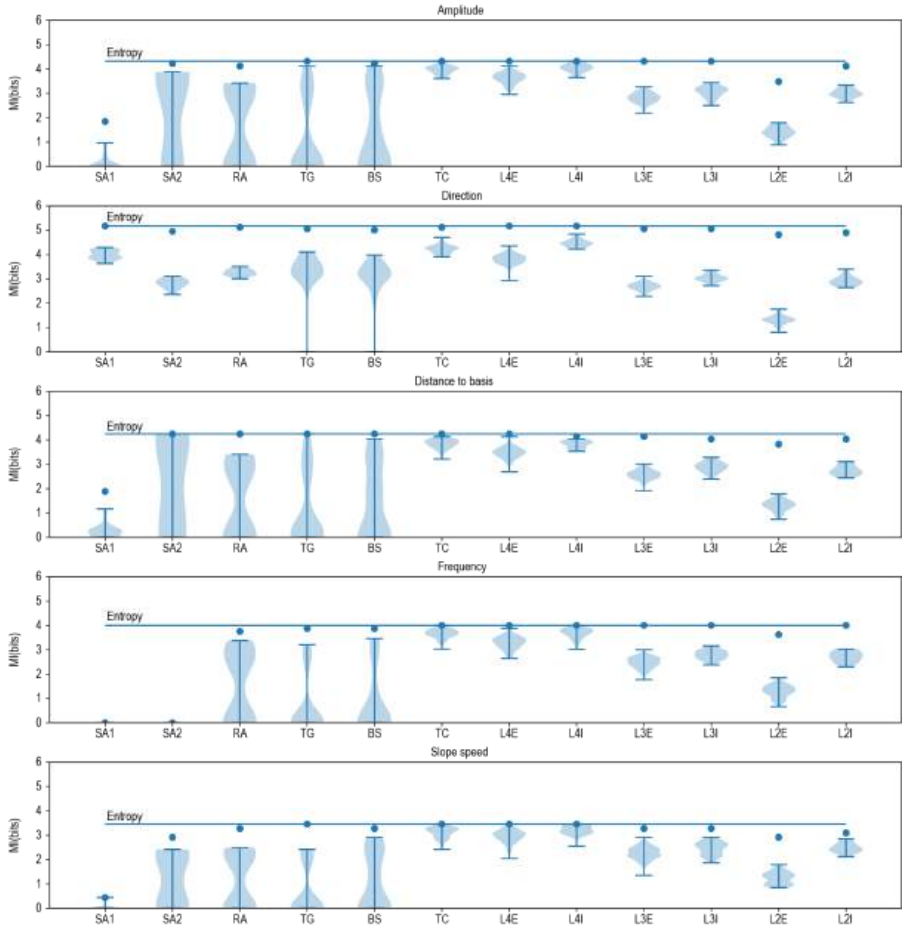


**Figure 5 - Mutual information distribution over the populations.** The mutual information calculation for between the firing rate of each neuron within a population and the stimulus (violinplot), population information rate (dot), and the entropy of the stimulus (line) is shown for each population (horizontal axis) and for different stimulus features (rows). The mutual information is computed between the stimulus and the firing rate of each neuron within the population. Each row corresponds to a different dimension of the stimulus, the y-axis is the mutual information (MI) in bits, the x-axis contains the different populations and the blue line corresponds to the entropy of the dimension of the specific stimulus set that is considered (amplitude, duration, etc…).

## Neural activity is decorrelated in the central nervous system compared to the periphery

While in Figure 5 we see, at both single-neuron and population level, an increase in stimulus information and a narrowing of the distribution of MI within TC, the information within single neurons may be highly redundant at the population level, making single-neuron activity certainly informative but overlapping with the information that other neurons within the same population transfer. To assess the overlap between single neurons' activity, we computed the Pearson correlation coefficient, which was performed between the firing rate of each neuron within a population and a stimulus set in which a single feature was varied.

The Pearson correlation calculation reveals that the peripheral layers present a high degree of redundancy, as single neurons' activities overlap, the correlation being maximal within the layers up to TG (Figure 6). In BS already, we see a drop of correlation across neurons, which remain the same along the entire ascending pathway. This profile holds for every tested stimulus feature set.



We can conclude that while information transfer at the single neuron level is maximized in the thalamus, the Pearson correlation coefficient within this structure demonstrates that single thalamic neurons's responses are rather decorrelated, thus not redundant. This makes each neuron within the thalamus carry a unique representation of the features of a tactile stimulus.

## The activity of a single neuron in the Thalamus or Layer 4 of the cortex is sufficient for a decoder to identify a stimulus

Given the high information content of a single neuron within the central nervous system and the lack of overlap in activity between pairs within a population, we want to know if a single neuron's activity is sufficient to represent a tactile stimulus. Therefore, we trained a decoder on the activity of the most informative neuron (based on MI).

Amongst the decoders, this procedure reveals that only the Naive Bayesian decoder was able to decode the stimulus given the activity of a single neuron from some of the populations (Figure 7). The populations for which stimulus feature values could be decoded remain the same across all stimulus dimensions we explored. Indeed, the most informative neurons from the thalamus, Layer 4, and Layer 3 are the most reliable neurons for the decoders to determine the feature value of the applied stimulus, while Layer 2's most informative neuron could be used only to decode direction. The peripheral neurons' activity was not able to provide the decoders any information about the stimulus; the same was true for the inhibitory populations.

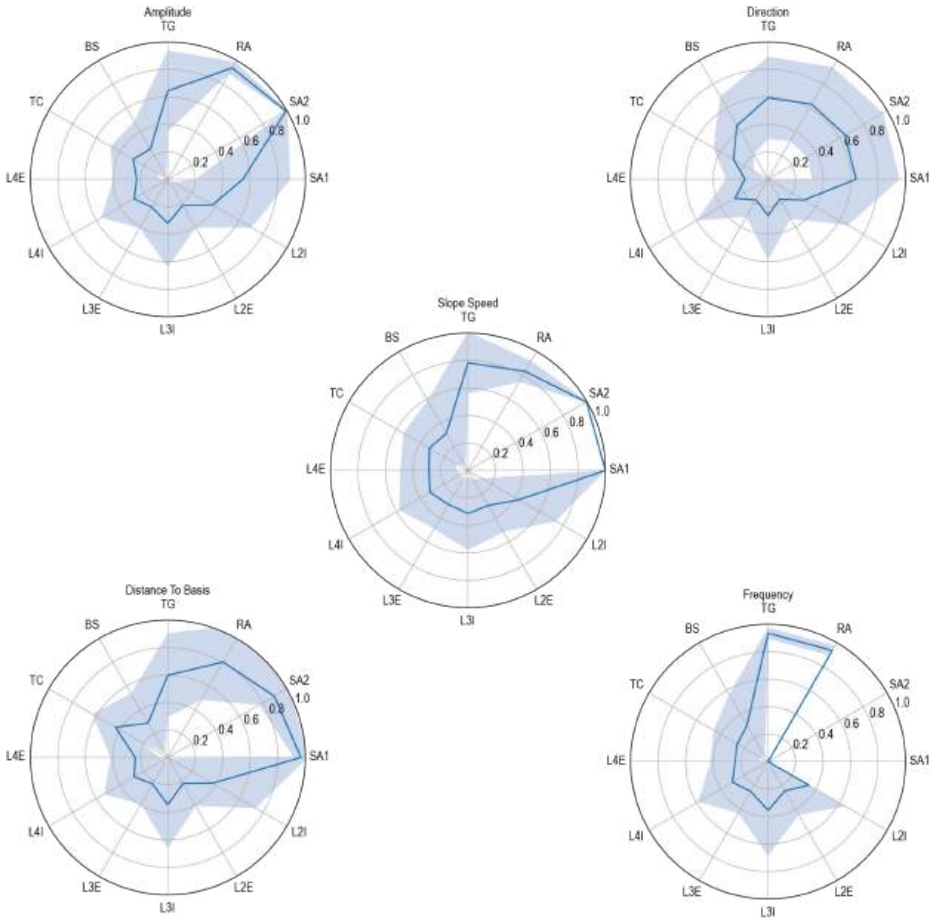


**Figure 6 - Correlations between neuron's activities.** Pairwise Pearson correlation between the firing rates of each neuron within a population in response to a shift in deflection amplitude, direction, speed of deflection, distance to basis, and frequency. Each radar plot corresponds to the correlation across neurons' firing rates within a population in response to shifts in one of the considered dimensions of the tactile stimulus (amplitude, direction, etc)

To summarize, while we see that in the periphery, single neurons are more specialized, making it impossible for the decoders to use a single neuron to determine the stimulus, individual neurons in the CNS appear to have more broadly tuned activities (e.i. Their responses change for every feature of a tactile stimulus), thus allowing a decoder to read a stimulus feature value from the activity of a single neuron. Put together with the MI and correlation calculations of the previous sections, we see that single neurons in the periphery show widely distributed stimulus MI values and a high pairwise correlation. When entering the central nervous system, the overlap in activity decreases (Figure 6), and information

transferred by a single neuron is maximized (Figure 5), thus allowing an overarching view of the stimulus range.

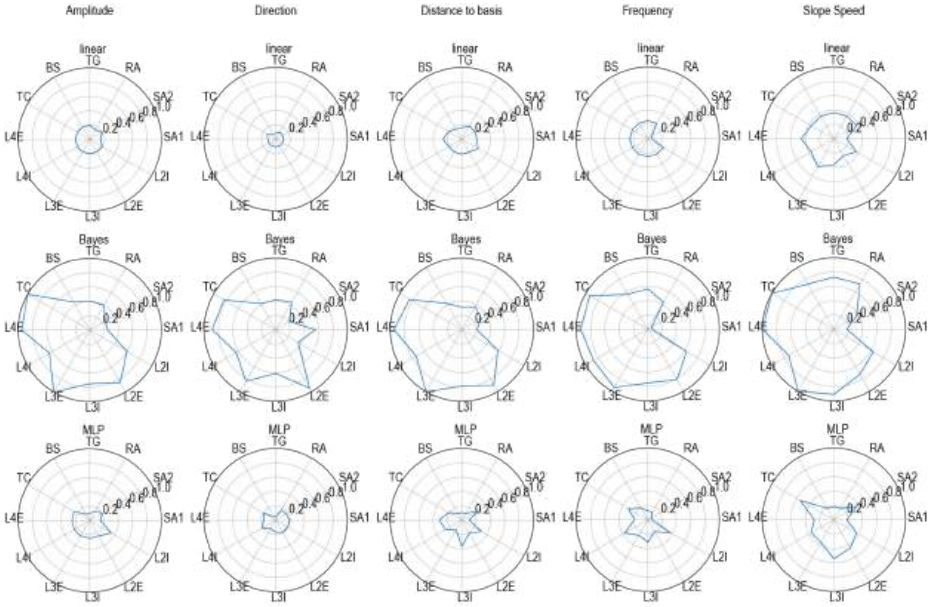


**Figure 7 - Decoding performances of decoders on the firing rate of the single most informative neuron within a population in response to a shift in deflection amplitude, direction, speed of deflection, distance to basis, and frequency.** Similar to figure 4, but the decoders were trained on the activity of a single neuron, activity as opposed to the firing rate vector per neuron of the entire population. Each radar plot represents the decoding accuracy per population, ranging from 0 to 1 (perfect accuracy). Each row corresponds to one of three types of decoders trained (linear, Bayesian, and MLP). Each column corresponds to one dimension of the tactile stimulus (amplitude, direction, etc).

## Discussion

In this paper, we presented a model of the lemniscal pathway receiving input from 3 populations of mechanoreceptors triggered by the forces at the base of a virtual whisker pushed by a pole. We modelled different paradigms, where the speed of the pole, the amplitude of the pole movement, the direction of the pole movement, the position on the whisker against which the pole was pressed and the frequency of vibration of the pole against the whisker tip were changed (Figure 2). This allowed us to cover the parameter space of a tactile stimuli and assess their respective representations or effects on the activities of the different neural populations. We applied decoders, quantified the information transfer and the Pearson correlation to assess the coding strategies used by the layers paving the

ascending somatosensory pathway. In this section, we will put the results together and conclude.

## The model responds to whisker deflection

Our model builds upon communication between the WhiskIt model [14] and a neural network. A deflection of the virtual whisker results in activity in the input populations and propagates up to the cortex, showing that the model of the ascending somatosensory pathway encodes whisker information. Contrary to previous studies focusing on specific nodes of the whisker system [26, 27], our model replicates the entire lemniscal pathway from the periphery to the cortex. Additionally, the neurons used in the thalamocortical layer are conductance based models (Hudgkin-Huxley), allowing for bursting behaviour and a more accurate description of cortical neuron behaviour than the reduced approach of Pinto et al., (1996) [28]. Similarly, Sharp et al., (2014) [27] decided to focus on the cortex using a larger number of neurons that we did, but described as leaky integrate-and-fire neurons. Here, we chose to focus on the entire pathway, using fewer neurons, but relying on a more accurate model. This allows us to study the stimulus propagation from the periphery to the cortex. The model relies on the same structure as in Rault et al., [29]. As a result the same pattern of activity as shown in Furuta et al., [9] can be witnessed in the mechanoreceptors and the SA1, SA2 and RA populations. The SAs and RAs TG subunits show a precisely timed activation at the onset of a stimulus. The RAs systematically spike at the offset, however not as precisely as in the previous work [29] due to the oscillation of the modelled whisker. A different pattern of activity appears from SAs (responding for the entire stimulus duration) and RAs (which respond only to the transient part of the stimulus [30]). The overall population demonstrates the distinct response of TG and the brainstem to a ramp-and-hold stimulus in the whisker system with a surge of activity at the onset, a lower response at the offset of the stimulus and a plateau of activity during the hold phase [31, 32]. This pattern of activity is preserved throughout the thalamus and the cortex, where the response of the inhibitory neurons appears to be more sensitive to the transient part of the stimulus than their excitatory counterpart, as was also observed in Pinto et al., (2003) [26]. Importantly, the cortical damping effect [32, 26] is reproduced: inhibitory neurons in layer 4 exhibit a stronger responsiveness than excitatory neurons, resulting in an overall attenuation of cortical firing relative to thalamic input. This transformation results from the high synchrony of thalamic activity during the transient phase of stimulation (Figures 1 and 3), which briefly drives excitatory neurons but rapidly recruits inhibition that suppresses sustained responses. We thus provide a model that can be used to study the effect of whisker deflections on neural activity. While in this study, we focus on passive perception

relying on ramp-and-hold stimuli, WhiskIt is capable of producing whisking behavior, and the expansion of the neural network to include nodes from the motor pathway would allow to communicate protraction and retraction instructions to the virtual whisker. We also focus here on a model of one whisker, while WhiskIt implements the whole whisker array on both sides of the snout. As an extension of this work, several whiskers can be included, thus implementing the inter-whisker communication within the neural network that is known to exist [33, 34].

### Every population is informative, given they are active

As stated previously, the activity resulting from the virtual whisker deflection is able to propagate through the entire network and a change in a stimulus feature results in a change of the activity of the neurons in the different populations, except for the SA1 receptors whose responses are not affected by change in the speed of deflection, and the SA2 receptors, which don't spike at all during the frequency paradigm. This shows that every structure along the ascending somatosensory pathway is capable of providing information about the stimulus and encoding it to the extent that the trained decoders were able to reach almost 100% accuracy for every tested tactile stimulus. This framework thus provides a solid basis to explore more naturalistic tactile stimuli that could be used to compare modelled neural responses to neural recordings during tasks (for instance, gap crossing experiments).



Notably, our analyses reveal a new finding: among all structures in the ascending pathway, the thalamus and layer 4 of the cortex yield the highest decoding accuracy, allowing decoders to reach near-perfect performance. This identifies these two stages as key bottlenecks for optimal tactile representation, highlighting their unique role in transforming peripheral inputs into maximally decodable neural codes at the single whisker level.

### Mutual information peaks in the thalamus

The calculated MI might appear surprisingly high as compared to previous work [30]. This is due to the deterministic nature of the model and the lack of intrinsic noise within the neurons. In the absence of such components, for a given stimulus, the model's output will always remain the same. However, the same output can result from different stimuli as explained in the method section. Thus, the MI calculated here can be seen as an evaluation of the compression that the stimulus undergoes within the system, due to its architecture and basic components.

When considering the decoding accuracy, it is unsurprising that the mutual information at the population level is close to the stimulus entropy, showing that

the population firing rate transmits almost as much information as there is available in the stimulus. Yet, when taking a closer look, we see not only that the periphery is specialized, as SA1 and SA2 do not respond to all features of tactile stimulus as the following layers, but also that the stimulus information drops in the cortex when it reaches layer 3. When diving into the details and considering the information provided by single neurons within a population, we see that the variation in information distribution over neurons in the periphery up to the brainstem is huge, showing some neurons carrying a lot of information while some do not carry any. When the activity reaches the thalamus, we see a consistent shift toward a narrower distribution, with all neurons carrying a similar amount of stimulus information which is almost equal to the entropy, showing that each neuron in TC is informative. This high information content is kept in layer 4 of our model before dropping in layer 3, similar to the information carried by the population firing rate. We demonstrate that, when considering a single whisker, information about the stimulus peaks in the thalamus and layer 4, then slightly decays in the more superficial layers. At a first glance, this might appear to contradict the findings of Simons and Carvell (1989) [35], who reported higher information content in cortical neurons relative to their thalamic inputs. However, this difference may be explained by their focus on multiwhisker integration in the barrel cortex, where our analysis is restricted to a single whisker. In the cortex, a strong center–surround inhibition suppresses responses to adjacent whiskers more than in the thalamus, thereby reducing redundancy across barrels and improving spatial contrast. In other words, while the thalamus conveys detailed information about the *stimulus applied to a specific whisker*, the cortex emphasizes the *identity of the whisker being stimulated* by integrating across multiple inputs and suppressing neighboring activity. Such a transformation enhances discrimination at the level of the vibrissal array, allowing the animal to localize which whisker was deflected—a computation not accessible in our single-whisker model. Extending the model to include multiple vibrissae will therefore be a necessary next step to capture this integrative function of the barrel cortex.

## Neural activity is decorrelated in the CNS

To check whether the increase in the information carried by single neurons in TC did not result in an increase in redundancy, we computed the Pearson correlation coefficient between the firing rates of single neurons within a population. This revealed a high degree of correlation in the periphery up to the trigeminal ganglion, which drops consistently across stimulus features as soon as it enters the brainstem. This reveals that while the MI increases in single neurons, especially in the thalamus, the neural activity does not become redundant. While this doesn't

prove that the information carried by a neuron is not repeated, it shows that the overlap of activity between neurons is lower in the thalamocortical areas compared to the periphery. Nonetheless, it remains possible that several neurons encode the same information, but at least it is guaranteed that it is not encoded in the same way. This form of coding could increase the certainty about the stimulus, providing different points of view on the same information, or increase robustness, as the loss of an encoding pathway can be compensated by other pathways.

## Single-neuron activity in L4 and the thalamus is sufficient to decode a stimulus

Given the changes in the MI and Pearson correlation profiles across layers, it appears that a single neuron is to give enough information to a decoder to determine the applied stimulus, given its activity. We thus trained the decoders not on the activity of all the neurons within a population but only on the activity of the most informative neuron from a structure, i.e,. the neurons with the highest stimulus information. The decoders' performance showed that the stimulus could be retrieved consistently from a single neuron in the thalamus, Layer 4 and 3 of the somatosensory cortex, whereas the activity of the single most informative neuron in other layers did not provide enough information for the decoders to estimate the stimulus feature values. From this observation, we can conclude that there exist neurons in these structures (L4 and L3) that react differently to all changes of the stimulus, thus providing an overarching/global view of the tactile stimulus. While there is no guarantee that the stimulus can be reconstructed based on these single most informative neurons, their activity is sufficient to determine the stimulus that has been applied to the system.



## Limitations

### *Downscale of periphery offers poor coverage*

To model the entire pathway and keep it computationally efficient, we downscaled the size of the thalamocortical layers compared to biology, as they are composed of the most complex neuron models within our network. As a result, we needed to downscale the size of the periphery as well so that the size of the brainstem matched the size of the thalamus. This had repercussions on the size of TG and the receptor population. As a result, while respecting the proportions of types of receptors from [36], the model relies on a really small population of SA1 (24) and SA2 (10) neurons. Thus, the entire shaft of the virtual whisker was not populated equally by these populations. As a result, the populations' activities and their

significance for stimulus decoding and information transfer were most probably reduced due to the scaling of the whole neural population.

***Different types of neuron models were used***

We relied on different types of neurons along the pathway. While the thalamocortical neurons were based on a conductance-based model, the neuron models for the periphery relied on a more simple model with far fewer parameters, such as AdeX and Elif neurons. This is due principally to the lack of recent accurate recordings of peripheral neurons, leaving us without the possibility to fit the kinematics of the ion channels (in particular Piezo2) to develop a conductance-based model. On the other hand, models and recordings of cortical neurons in the whisker system are numerous, and thalamic neurons' behavior requires a more complex model to fit their activity. As a result, our model is a patchwork of different types of neuronal models explained by the heterogeneous availability of data, in which thalamocortical neurons have an internal dynamic while peripheral neurons react instantaneously to shifts in the input. This lack of internal dynamic, through the modeling of the ion channels' kinematics might lead to an over estimation of the information transferred in the periphery.

***Responsiveness of SA1 and SA2***

In this model, SA1 and SA2 receptors lack responsiveness. This is due partially to the size of the populations, as explained before, but also to the tuning of their response to whisker deflections. When looking at the traces of the forces at the basis of the whisker, we see a lot of oscillations (Figure 3 and supplemental Figure (1-4)). In the case of RA, which responds to differences in amplitude of deflection (Figure 1), it increases its activity. For SA2 receptors, which take more time to activate, the stimulus duration is not long enough to trigger activity, thus making SA2 receptors silent. Since SA2 receptors integrate deflection duration and amplitude [29], to produce activity, a short stimulus needs a high deflection amplitude, whereas a stimulus with a low amplitude needs a long duration. In the frequency paradigm, SA2 neurons are not receiving forces for a long enough duration high enough amplitude for activation. SA1 receptors are highly sensitive to the pole movement direction, and the sparsity of this population (24 SA1 receptors) around the whisker shaft make the receptive fields of these receptors very narrow, so that the activity of these touch cells remains very low unless the whisker is bent directly toward the receptor's favourite direction. As a consequence, the MI value and decoding capacity of SA1 and SA2 receptors might be underestimated, whereas that of RA receptors might be overestimated.

***No synaptic dynamics***

The different types of neuron models we rely on and the different timescales they operate at made us rely on non-dynamic synapses, in the sense that they only increase the value of a postsynaptic neuron by a fixed value upon a presynaptic spike. As a result, no EPSPs nor IPSPs were reproduced in our model. However, the exponential decay typically present in naturalistic synapses plays a big role in the timing of each spike, as it modifies the weight of each incoming spike depending on how close in time they are to one another. This bring another source of variability of the neural response into the picture, as the pattern of the input spike train will play a role in the excitability of the post-synaptic neuron. In our model, this dimension completely collapses due to the lack of synaptic dynamics, while it could be informative for a decoder or even the somatosensory system itself.



In summary, our comprehensive computational model of the whisker-to-cortex ascending somatosensory pathway reveals a significant transformation of tactile information prior to extensive cortical processing. We demonstrated that while peripheral receptors show specialization and high redundancy, the thalamus acts as a critical hub where single-neuron information about the stimulus peaks, accompanied by a notable decorrelation of activity. This efficient representation allows single neurons in the thalamus and cortical layer 4 to sufficiently inform decoders about stimulus identity, despite an overall decrease in information content and decoding capacity observed in subsequent cortical layers compared to the thalamus. The take-home message is that substantial signal integration and efficient, decorrelated encoding occur subcortically, culminating in the thalamus. This suggests the ascending pathway optimizes information for cortical entry, potentially prioritizing features relevant for further cortical computation rather than solely maximizing the fidelity of the raw sensory input.

# References


[1] L. L. Orefice, A. L. Zimmerman, A. M. Chirila, S. J. Sleboda, J. P. Head, D. D. Ginty, Peripheral mechanosensory neuron dysfunction underlies tactile and behavioral deficits in mouse models of ASDs. Cell 166, 299–313 (2016).

[2] Peerdeman, B., Boere, D., Witteveen, H., `tVeld, R. H. I., Hermens, H., Stramigioli, S., Rietman, H., Veltink, P., & Misra, S. (2011). Myoelectric forearm prostheses: State of the art from a user-centered perspective. *The Journal Of Rehabilitation Research And Development*, *48*(6), 719. https://doi.org/10.1682/jrrd.2010.08.0161

[3] Guémann, M., Halgand, C., Bastier, A., Lansade, C., Borrini, L., Lapeyre, É., Cattaert, D., & De Rugy, A. (2022). Sensory substitution of elbow proprioception to improve myoelectric control of upper limb prosthesis: experiment on healthy subjects and amputees. *Journal Of NeuroEngineering And Rehabilitation*, *19*(1). https://doi.org/10.1186/s12984-022-01038-y

[4] Wang, L., Ma, L., Yang, J., & Wu, J. (2021). Human Somatosensory Processing and Artificial Somatosensation. *Cyborg And Bionic Systems*, *2021*. https://doi.org/10.34133/2021/9843259

[5] Panchuelo, R. M. S., Besle, J., Schluppeck, D., Humberstone, M., & Francis, S. (2018). Somatotopy in the Human Somatosensory System. *Frontiers in Human Neuroscience*, *12*. https://doi.org/10.3389/fnhum.2018.00235

[6] Staiger, J. F., & Petersen, C. C. H. (2020). Neuronal Circuits in Barrel Cortex for Whisker Sensory Perception. *Physiological Reviews*, *101*(1), 353–415. https://doi.org/10.1152/physrev.00019.2019

[7] Huang, C., Zeldenrust, F., & Celikel, T. (2022). Cortical Representation of Touch in Silico. *Neuroinformatics*, *20*(4), 1013–1039. https://doi.org/10.1007/s12021-022-09576-5

[8] Rault, N., Bergmans, T., Delfstra, N., Kleijnen, B. J., Zeldenrust, F., & Celikel, T. (2024b). Where Top-Down Meets Bottom-Up: Cell-Type Specific Connectivity Map of the Whisker System. Neuroinformatics, 22(3), 251–268. https://doi.org/10.1007/s12021-024-09658-6

[9] Furuta, T., Bush, N. E., Yang, A. E., Ebara, S., Miyazaki, N., Murata, K., Hirai, D., Shibata, K., & Hartmann, M. J. (2020). The Cellular and Mechanical Basis for Response Characteristics of Identified Primary Afferents in the Rat Vibrissal System. *Current Biology*, *30*(5), 815-826.e5. https://doi.org/10.1016/j.cub.2019.12.068

[10] Erzurumlu, R. S., Bates, C. A., & Killackey, H. P. (1980). Differential organization of thalamic projection cells in the brain stem trigeminal complex of the rat. *Brain Research*, *198*(2), 427–433. https://doi.org/10.1016/0006-8993(80)90756-8

[11] Williams, M. N., Zahm, D. S., & Jacquin, M. F. (1994). Differential Foci and Synaptic Organization of the Principal and Spinal Trigeminal Projections to the Thalamus in the Rat. *European Journal Of Neuroscience*, *6*(3), 429–453. https://doi.org/10.1111/j.1460-9568.1994.tb00286.x

[12] Veinante, P., & Deschênes, M. (1999). Single- and Multi-Whisker Channels in the Ascending Projections from the Principal Trigeminal Nucleus in the Rat. *Journal Of Neuroscience*, *19*(12), 5085–5095. https://doi.org/10.1523/jneurosci.19-12-05085.1999

[13] Sonekatsu, M., & Gu, J. G. (2019b). Functional properties of mechanoreceptors in mouse whisker hair follicles determined by the pressure-clamped single-fiber recording technique. *Neuroscience Letters*, *707*, 134321. https://doi.org/10.1016/j.neulet.2019.134321

[14] Zweifel, N. O., Bush, N. E., Abraham, I., Murphey, T. D., & Hartmann, M. J. Z. (2021). A dynamical model for generating synthetic data to quantify active tactile sensing behavior in the rat. *Proceedings Of The National Academy Of Sciences*, *118*(27). https://doi.org/10.1073/pnas.2011905118

[15] Yang, A. E. T., & Hartmann, M. J. Z. (2016). Whisking Kinematics Enables Object Localization in Head-Centered Coordinates Based on Tactile Information from a Single Vibrissa. *Frontiers in Behavioral Neuroscience*, *10*. https://doi.org/10.3389/fnbeh.2016.00145

[16] Maksimovic, S., Nakatani, M., Baba, Y., Nelson, A. M., Marshall, K. L., Wellnitz, S. A., Firozi, P., Woo, S., Ranade, S., Patapoutian, A., & Lumpkin, E. A. (2014). Epidermal Merkel cells are mechanosensory cells that tune mammalian touch receptors. *Nature*, *509*(7502), 617–621. https://doi.org/10.1038/nature13250

[17] Johnson, K. O., Yoshioka, T., & Vega–Bermudez, F. (2000). Tactile Functions of Mechanoreceptive Afferents Innervating the Hand. *Journal Of Clinical Neurophysiology*, *17*(6), 539–558. https://doi.org/10.1097/00004691-200011000-00002

[18] Brette, R., & Gerstner, W. (2005b). Adaptive Exponential Integrate-and-Fire Model as an Effective Description of Neuronal Activity. *Journal Of Neurophysiology*, *94*(5), 3637–3642. https://doi.org/10.1152/jn.00686.2005

[19] Saal, H. P., & Bensmaia, S. J. (2014). Touch is a team effort: interplay of submodalities in cutaneous sensibility. *Trends in Neurosciences*, *37*(12), 689–697. https://doi.org/10.1016/j.tins.2014.08.012

[20] Yamada, A., Furue, H., & Gu, J. G. (2022). Angular Tuning Properties of Low Threshold Mechanoreceptors in Isolated Rat Whisker Hair Follicles. *eNeuro*, *9*(6), ENEURO.0175-22.2022. https://doi.org/10.1523/ENEURO.0175-22.2022

[21] Tompos, T., Zeldenrust, F., Celikel, T. (2025).Stability and Adaptability in Balance: A Dual Mechanism for Metaplasticity in Cortical Networks. bioRxiv. https://doi.org/10.1101/2025.04.02.646896

[22] Pospischil, M., Toledo-Rodriguez, M., Monier, C., Piwkowska, Z., Bal, T., Frégnac, Y., Markram, H., & Destexhe, A. (2008). Minimal Hodgkin–Huxley type models for different classes of cortical and thalamic neurons. *Biological Cybernetics*, *99*(4–5), 427–441. https://doi.org/10.1007/s00422-008-0263-8

[23] Zeldenrust, F., Calcini, N., Yan, X., Bijlsma, A., & Celikel, T. (2024). The tuning of tuning: How adaptation influences single cell information transfer. *PLoS Computational Biology*, *20*(5), e1012043. https://doi.org/10.1371/journal.pcbi.1012043

[24] Ching, S., Cimenser, A., Purdon, P. L., Brown, E. N., & Kopell, N. J. (2010). Thalamocortical model for a propofol-induced α-rhythm associated with loss of consciousness. *Proceedings Of The National Academy Of Sciences*, *107*(52), 22665–22670. https://doi.org/10.1073/pnas.1017069108

[25] Pedregosa F., Varoquaux G., Gramfort A., Michel V., Thirion B., Grisel O., Blondel M., Prettenhofer P., Weiss R., Dubourg V., Vanderplas J., Passos A., Cournapeau D., Brucher M., Perrot M., & Duchesnay É. (2011b). SciKit-Learn: Machine Learning in Python. *Journal Of Machine Learning Research*. https://doi.org/10.5555/1953048.2078195

[26] Pinto, D. J., Hartings, J. A., Brumberg, J. C., & Simons, D. J. (2002). Cortical Damping: Analysis of Thalamocortical Response Transformations in Rodent Barrel Cortex. *Cerebral Cortex*, *13*(1), 33–44. https://doi.org/10.1093/cercor/13.1.33

[27] Sharp T, Petersen R and Furber S (2014) Real-time million-synapse simulation of rat barrel cortex. Front. Neurosci. 8:131. doi: https://doi.org/10.3389/fnins.2014.00131

[28] Pinto, D. J., Brumberg, J. C., Simons, D. J., Ermentrout, G. B., & Traub, R. (1996). A quantitative population model of whisker barrels: re-examining the Wilson-Cowan equations. *Journal of computational neuroscience*, *3*(3), 247-264.

[29] Rault, N., Doğan D., Marx, F. E., Jamal, T., Emoghene, A. E., Chandler, F. V., Pridgon, S., Sathani, A., Zeldenrust, F., Celikel, T. (2025). Artificial Human Touch: A Spiking Network Model of the Tactile Periphery. *In prep.*

[30] Bale, M. R., & Petersen, R. S. (2009). Transformation in the neural code for whisker deflection direction along the lemniscal pathway. *Journal of neurophysiology*, *102*(5), 2771-2780.

[31] Minnery, B. S., Bruno, R. M., & Simons, D. J. (2003). Response Transformation and Receptive-Field Synthesis in the Lemniscal Trigeminothalamic Circuit. *Journal Of Neurophysiology*, *90*(3), 1556–1570. https://doi.org/10.1152/jn.00111.2003

[32] Kyriazi, H. T., & Simons, D. J. (1993). Thalamocortical response transformations in simulated whisker barrels. *Journal of Neuroscience*, *13*(4), 1601-1615.

[33] Lo, F., Guido, W., & Erzurumlu, R. S. (1999). Electrophysiological Properties and Synaptic Responses of Cells in the Trigeminal Principal Sensory Nucleus of Postnatal Rats. *Journal Of Neurophysiology*, *82*(5), 2765–2775. https://doi.org/10.1152/jn.1999.82.5.2765

[34] Jamal, T., Yan, X., Da Silva Lantyer, A., Ter Horst, J. G., & Celikel, T. (2024). Experience-dependent regulation of dopaminergic signaling in the somatosensory cortex. *Progress in Neurobiology*, *239*, 102630. https://doi.org/10.1016/j.pneurobio.2024.102630

[35] Simons, D. J., & Carvell, G. E. (1989). Thalamocortical response transformation in the rat vibrissa/barrel system. *Journal Of Neurophysiology*, *61*(2), 311–330. https://doi.org/10.1152/jn.1989.61.2.311

[36] Johansson, R. S., & Vallbo, A. B. (1979). Tactile sensibility in the human hand: relative and absolute densities of four types of mechanoreceptive units in glabrous skin. *The Journal Of Physiology*, *286*(1), 283–300. https://doi.org/10.1113/jphysiol.1979.sp012619

# Supplemental materials

**Supplemental Table 1 -** Parameter values of the Adex model [17] for SA1, SA2, and RA receptors as well as parameters for the elif neurons model for TG and BS.

| Parameters | SA1 | SA2 | RA | TG and BS |
|---|---|---|---|---|
| a | $20.24\ nS$ | $46.11\ nS$ | $59.1\ nS$ | |
| b | $69.65\ pA$ | $3.21\ pA$ | $86.53\ pA$ | |
| $\tau$ | $44.09\ ms$ | $1882.05\ ms$ | $1890.10\ ms$ | |
| $E_{leak}$ | | $-50\ mV$ | | |
| $V_{th}$ | | $-30\ mV$ | | |
| $V_{reset}$ | | $-45\ mV$ | | |
| $C_m$ | | $-0.1\ nF$ | | |
| $g_{leak}$ | | $10\ nS$ | | |
| $\Delta_{th}$ | | $5\ mV$ | | |

**Supplemental Table 2 -** Parameter values for sodium (Na), delayed-rectifier potassium (KDR), slow non-inactivating potassium (M), and leak (L) channels used to model cortical E and I neurons. Values in brackets are default values from [19], which we changed to the outside-bracket values to adjust the neuron frequency-current behaviour (method section).

| Parameter | E values | I values |
|---|---|---|
| $g_{Na}$ | 0.086 [0.056] $S/cm^2$ | 0.078 [0.058] $S/cm^2$ |
| $E_{Na}$ | 50 mV | 50 mV |
| $g_{KDR}$ | 0.006 $S/cm^2$ | 0.0039 $S/cm^2$ |
| $E_{KDR}$ | -90 mV | -90 mV |
| $g_m$ | 18 [7.5] $\times 10^5$ $S/cm^2$ | 5 [7.87] $\times 10^5$ $S/cm^2$ |
| $\tau_{max}$ | 808 [608] ms | 602 [502] ms |
| $g_{leak}$ | 0.85 [2.05] $\times 10^5$ $S/cm^2$ | 3.8 $\times 10^5$ $S/cm^2$ |
| $E_{leak}$ | -69 [-70.3] mV | -70.4 mV |
| $V_T$ | -64 [-56.2] mV | -58 [-57.9] mV |

**Supplemental Table 3 -** Parameter values used for simulating VPM neurons.

| Parameter | Ching et al. (2010) | Pattern-generating | Background |
|---|---|---|---|
| $g_h$ | 0.001 *mS/cm*$^2$ | 0.01 | 0.005 *mS/cm*$^2$ |
| $N$ | 10 | 45 | 24 |
| $g_{In}$ | 0.05 *mS/cm*$^2$ | 0.5 | 0.75 *mS/cm*$^2$ |
| $r$ | 12 *Hz* | 9 | 5 *Hz* |
| $P_{In}$ | 0.5 | 0.3 | 0.1 |
| α | 10 | 14 | 25 |
| $\tau_r$ | 0.5 *ms* | 0.5 | 0.5 *ms* |
| $\tau_d$ | 2 *ms* | 2 | 2 *ms* |

**Supplemental Table 4 -** Synapse-specific weights and connectivity patterns or connection probabilities used in the model. Note that BS neurons send lateral inhibitory connections within BS and excitatory connections to VPM, this structure doesn't contain inhibitory neurons per se.

| Pre-post population | Pre-post neuron type | Weight (mV) | Probability to connect or connectivity pattern |
|---|---|---|---|
| L2-L2 | E-E | 2.8 | 5.6% |
| L3-L2 | E-I | 8.1 | 5.1% |
| L3-L2 | I-E | -17 | 5.9% |
| L3-L3 | I-I | -15 | 5.1% |
| L4-L3 | E-E | 2.4 | 5.8% |
| | E-I | 5.7 | 0.33% |
| | I-E | -14 | 1.7% |
| L4-L4 | E-E | 3.3 | 7.6% |
| | E-I | 7.9 | 4.2% |
| | I-E | -16 | 6.3% |
| | I-I | -14 | 6.2% |
| VPM-L4 | E-E | 7 | 4.3% |
| | E-I | 9 | 5% |
| BS-VPM | | 10 | 30% |
| BS-BS | I-E | -50 | 1% |
| TG-BS | | 25 | one-to-one |
| RA-TG | | 25 | one-to-one |
| SA2-TG | | 25 | one-to-one |
| SA1-TG | | 25 | one-to-one |

**Supplemental Table 5 -** Set of parameters used for whisker deflection simulation. For each set of stimuli, the same set of initial parameters was used: The pole was positioned at 10 mm from the targeted whisker and moved at a speed of 0.3 m/s, with an angle of 0° around the x-axis (along the whisker). The amplitude of the stimulus was 1 mm, and it was held against the whisker for 100 ms at the 10th link of the whisker (middle). Then, only one of these parameters was changed, as shown in the table above.

| | **Amplitude of deflection** | **Direction of deflection** | **Position of deflection along the whisker** | **Velocity of deflection** | **Frequency of vibration at the tip** |
|---|---|---|---|---|---|
| Range of simulation: min to max (step) | 1mm to 22 mm (1mm) | 0° to 350° (10°) | 1st link - 20th link (1) | 0.25 m/s to 0.35 m/s (0.01m/s) | 2 Hz to 32Hz (2Hz) |

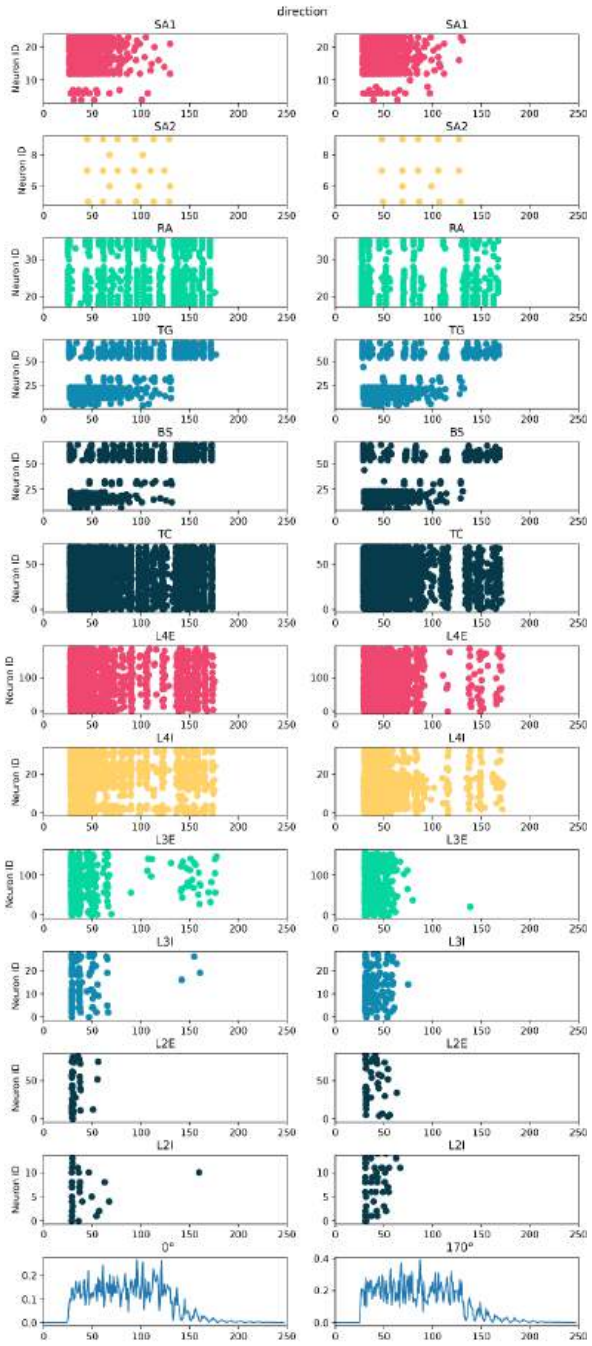


**Supplemental Figure 1** - Population responses and raster plot to a direction of 0 degrees and 170 degrees.

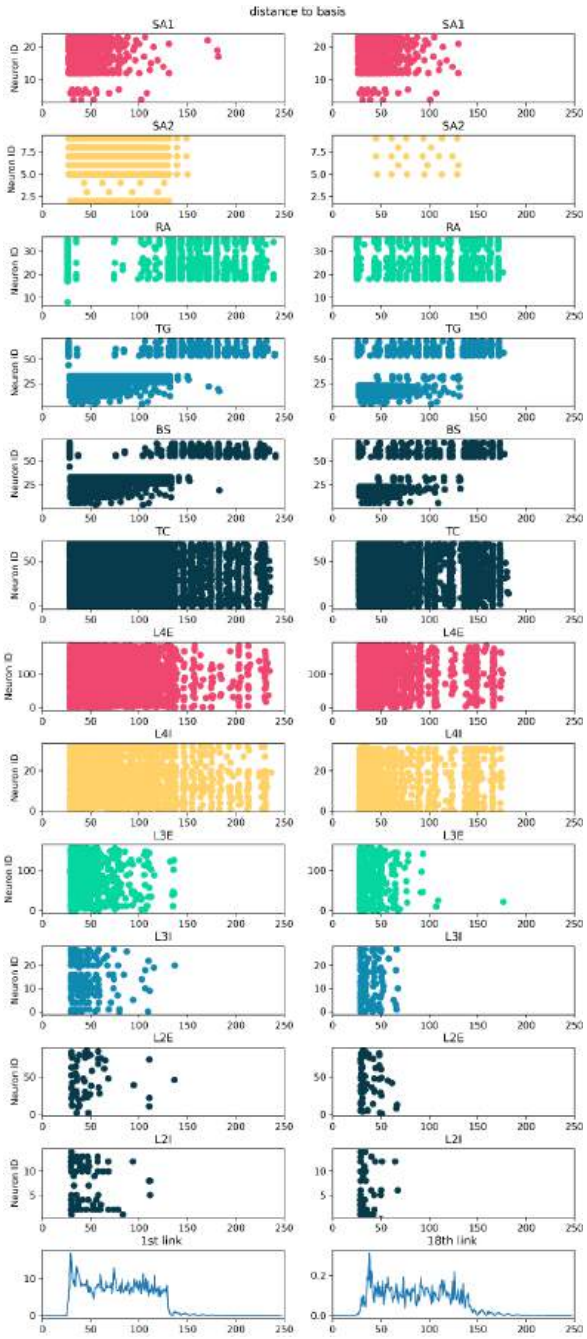


**Supplemental figure 2** - Population response and raster plot for the pole applied to the 1st link (close to the snout) of the whisker and the 18th (close to the tip) link of the whisker.

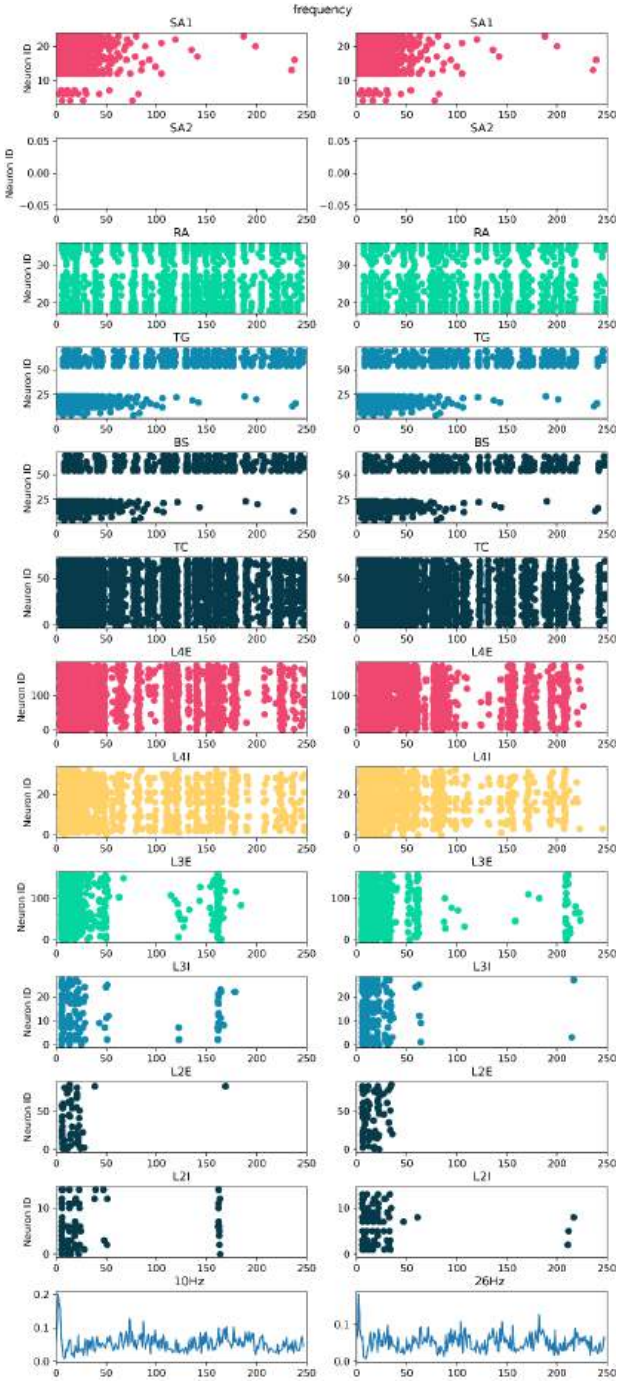


**Supplemental figure 3 -** Population response and raster plot to a frequency of 10 Hz and 26 Hz.

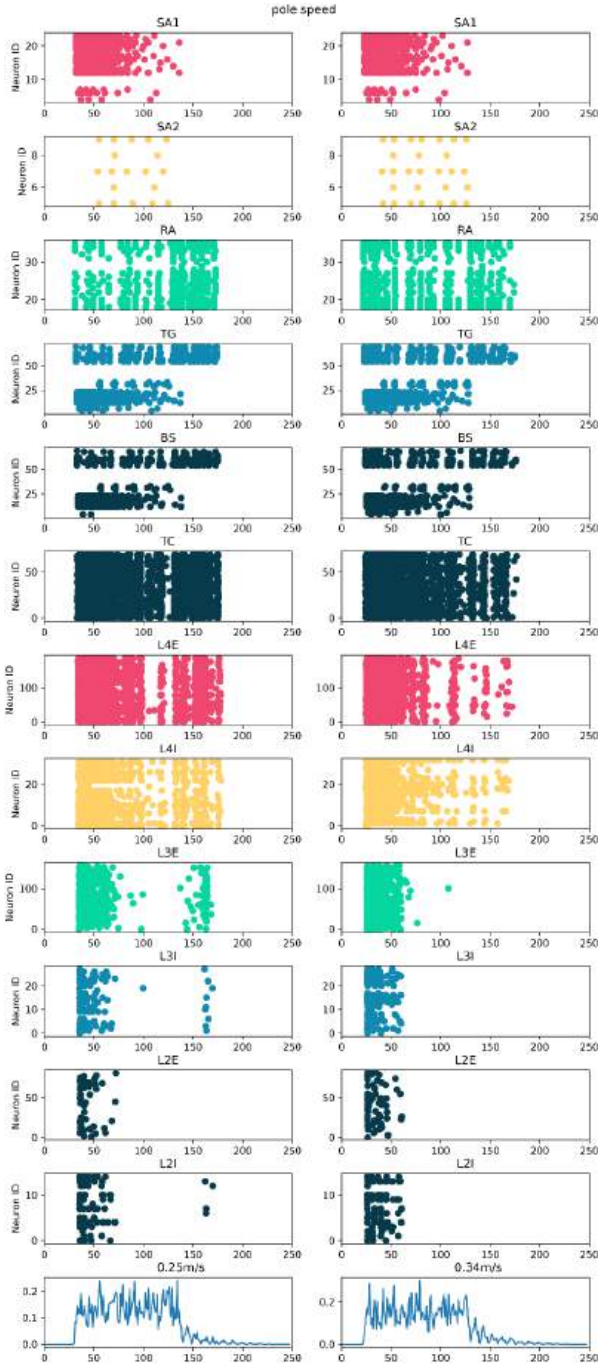


**Supplemental figure 4 -** Population response and raster plot to a pole movement against the whisker of 0.25m/s and 0.34 m/s.

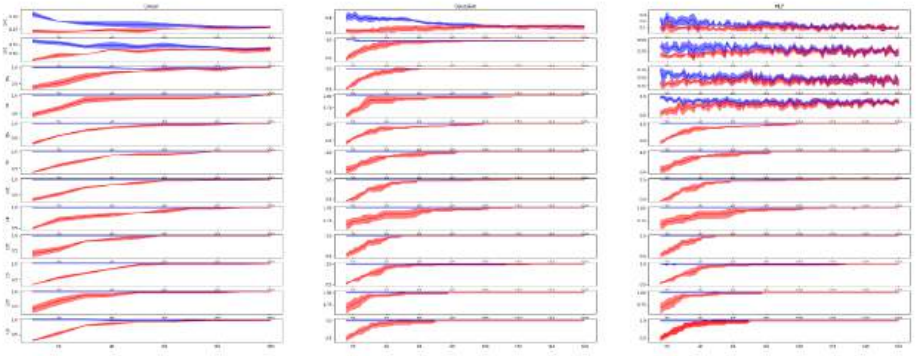

**Supplemental figure 5 -** Learning curve for Linear decoder, MLP and Bayesian when trained to retrieve stimulus amplitude, on whole population activity.

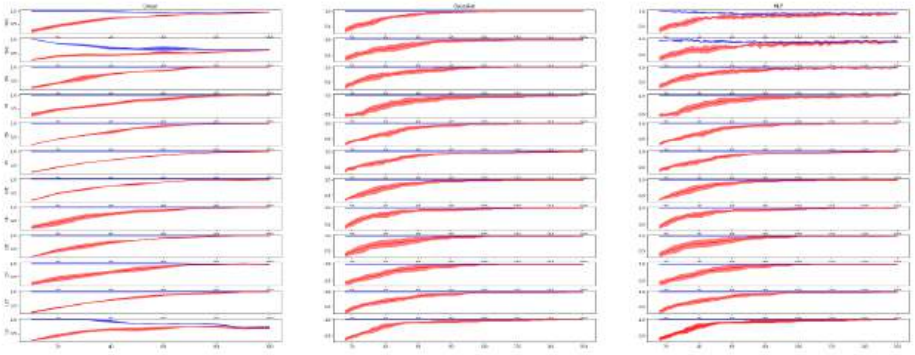

**Supplemental figure 6 -** Learning curve for Linear decoder, MLP and Bayesian when trained to retrieve stimulus direction, on whole population activity.

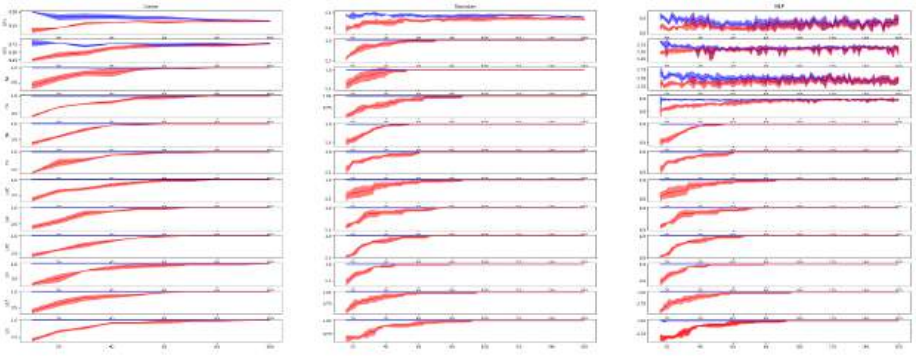

**Supplemental figure 7 -** Learning curve for Linear decoder, MLP and Bayesian when trained to retrieve stimulus distance to whisker basis, on whole population activity.

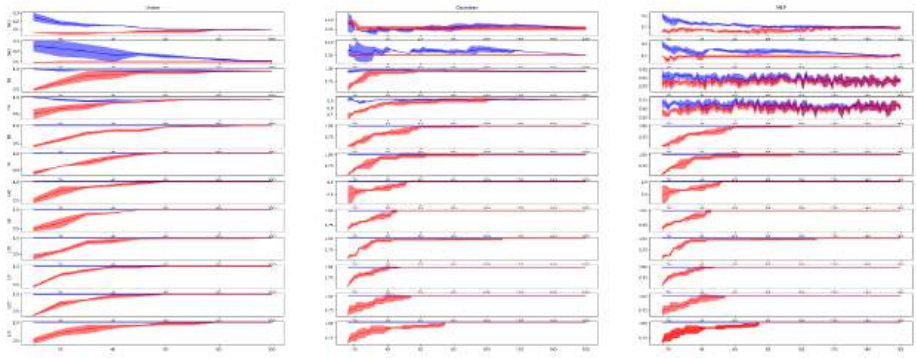

**Supplemental figure 8 -** Learning curve for Linear decoder, MLP and Bayesian when trained to retrieve stimulus frequency, on whole population activity.



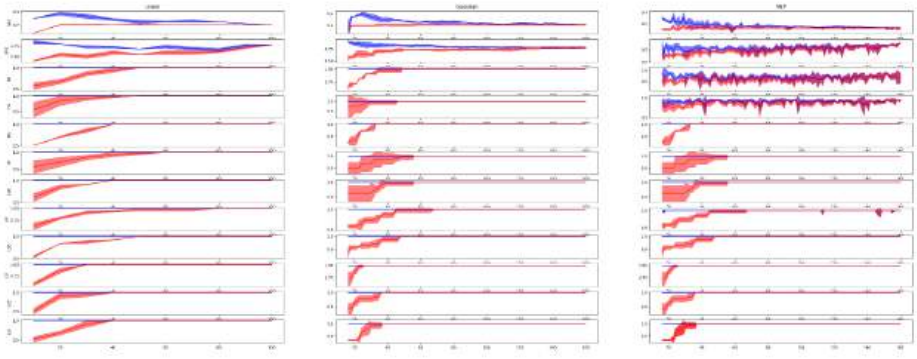

**Supplemental figure 9 -** Learning curve for Linear decoder, MLP and Bayesian when trained to retrieve stimulus speed, on whole population activity.

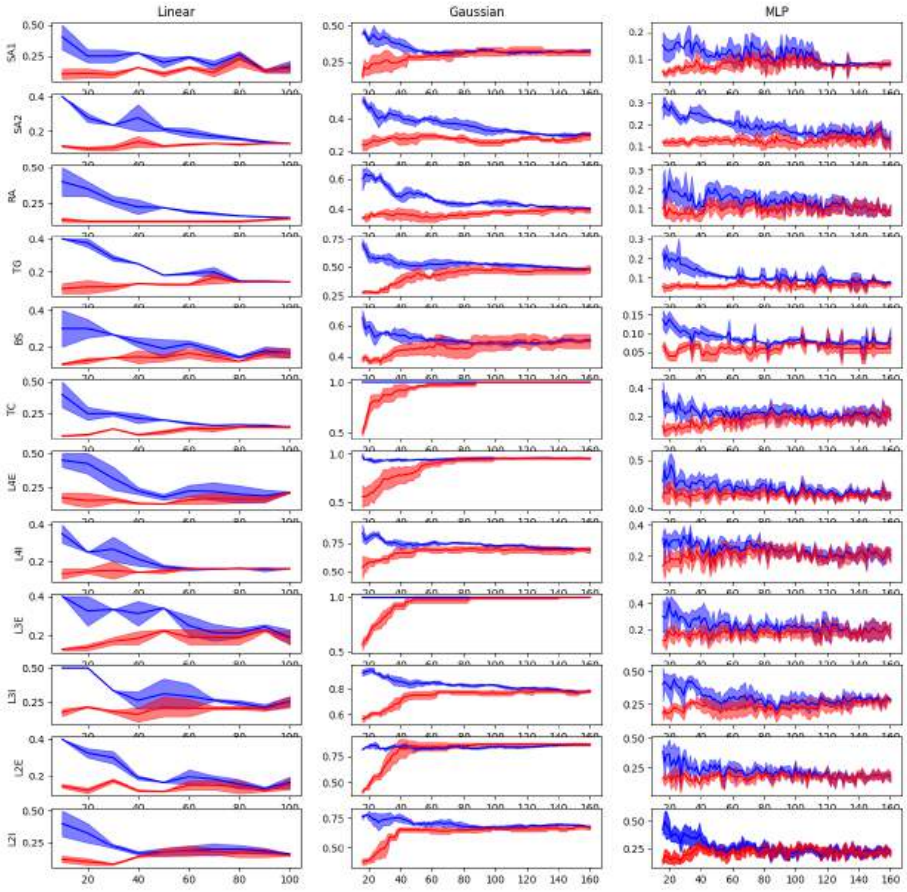


**Supplemental figure 10** - Learning curve for Linear decoder, MLP and Bayesian when trained to retrieve stimulus amplitude, on the firing rate of the most informative neuron of each population.

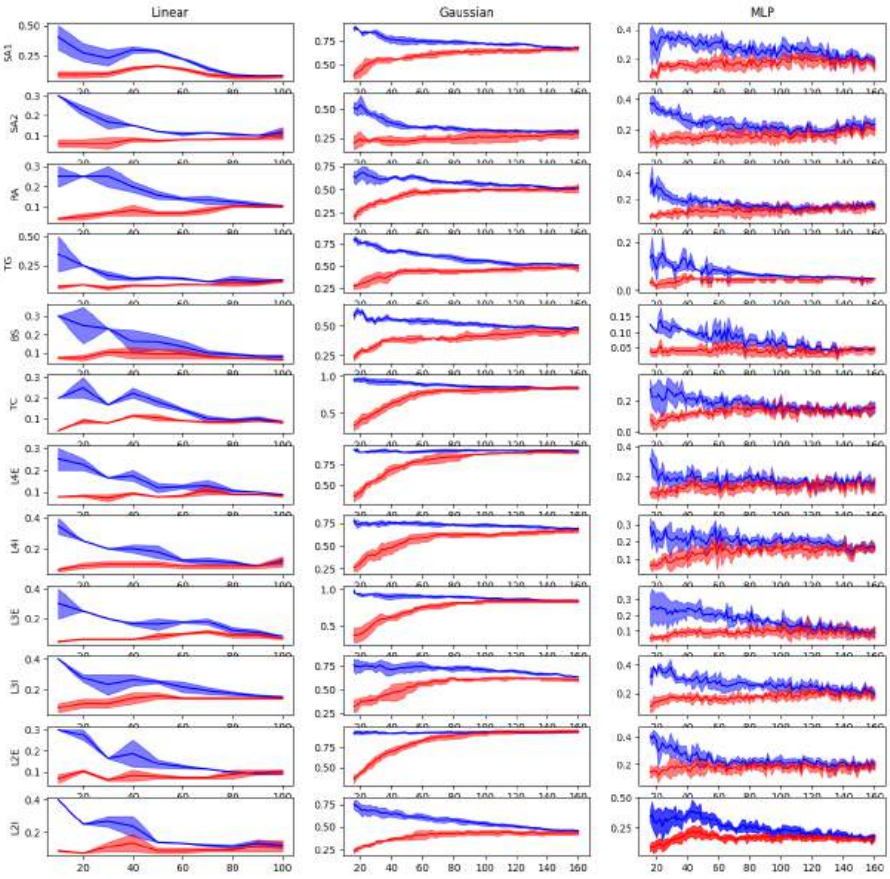


**Supplemental figure 11** - Learning curve for Linear decoder, MLP and Bayesian when trained to retrieve stimulus direction, on the firing rate of the most informative neuron of each population.

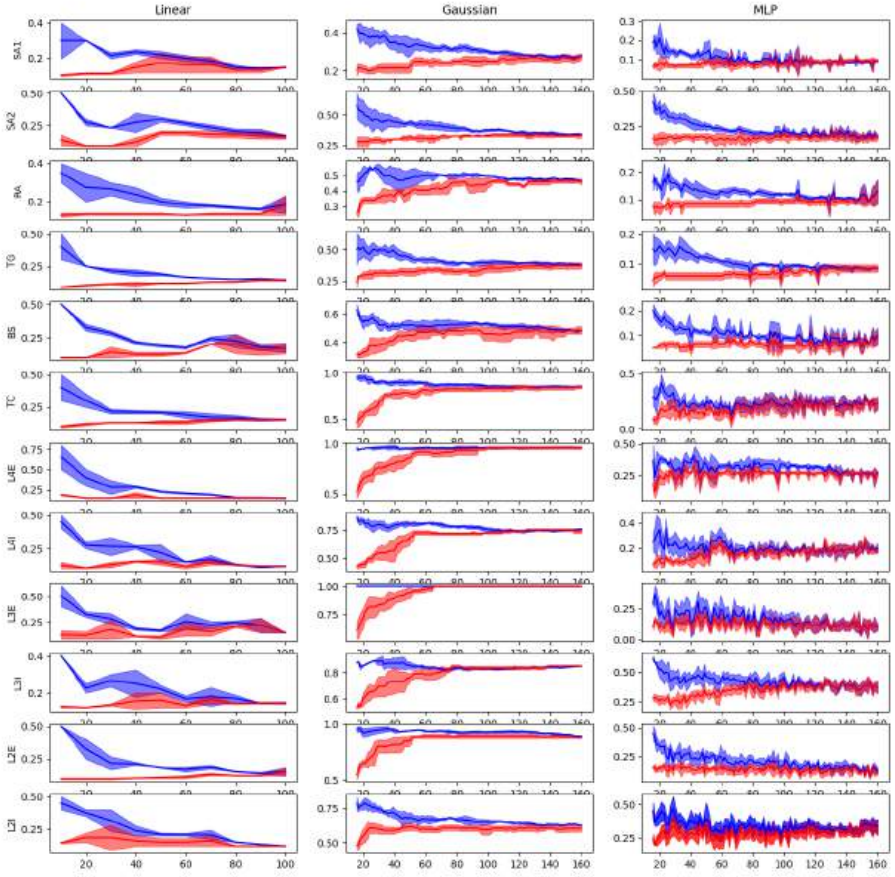


**Supplemental figure 12** - Learning curve for Linear decoder, MLP and Bayesian when trained to retrieve the stimulus distance to whisker basis, on the firing rate of the most informative neuron of each population.

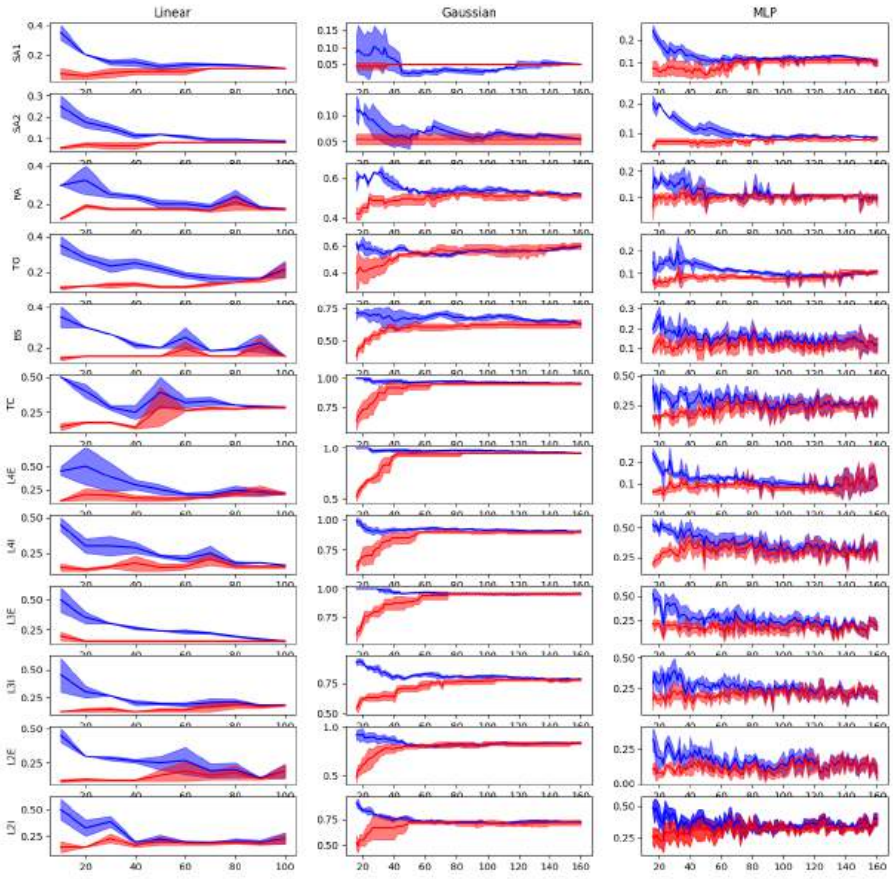


**Supplemental figure 13** - Learning curve for Linear decoder, MLP and Bayesian when trained to retrieve the stimulus frequency, on the firing rate of the most informative neuron of each population.

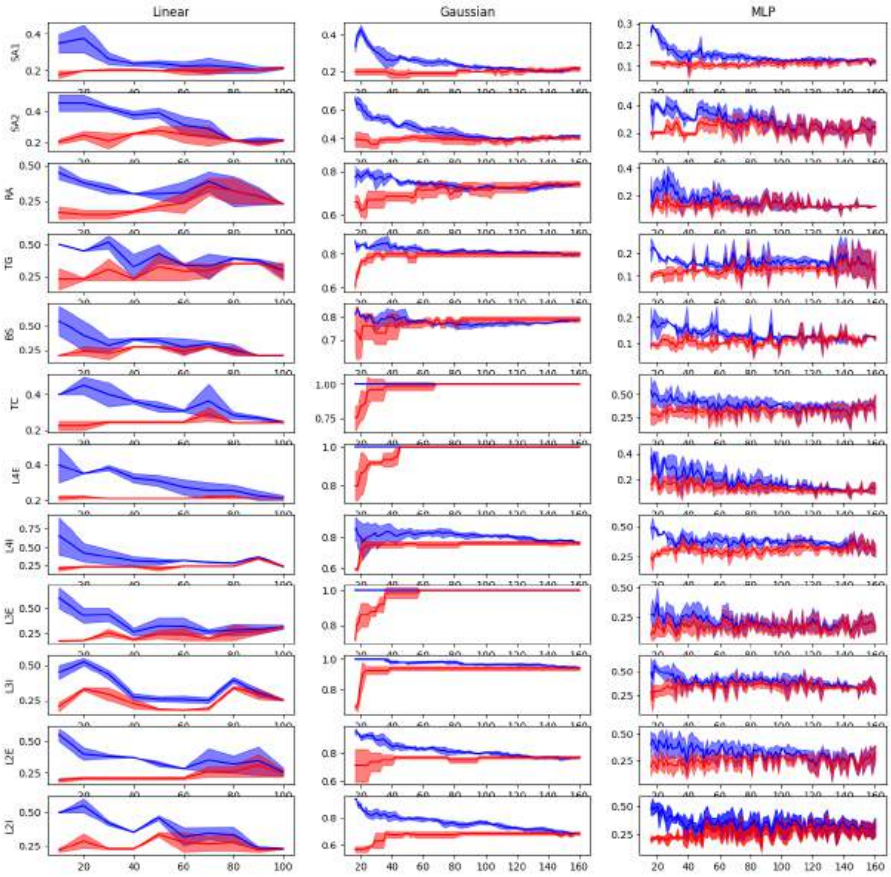


**Supplemental figure 14** - Learning curve for Linear decoder, MLP and Bayesian when trained to retrieve the stimulus speed, on the firing rate of the most informative neuron of each population.

Chapter 6

# Discussion
# Of whiskers, fingertips and prosthetics

Ah, dear reader, how far have we come together? As much as I'd like to press onward, diving deeper in my research, spinning yet more yarns to amuse and enlighten, it is, alas, time for me to wrap up this thesis and for us to part ways. But rejoice, for it is now that we have to draw conclusions from the past experiments and shine a beam of light on the future of this project. It is now that we apply the last coat of varnish and take a step back to contemplate the full picture in its final form. Quite the perilous act when one has spent the last 4 years obsessively drawing fragments of the complete piece. Yet, if you'd allow me to distract you for a last couple of pages, I will, without further ado, tackle this narrative voltige exercise in an attempt to disentangle the storyline underlying sensory integration in the tactile system.

Throughout its history, the field of neuroscience has provided different approaches to stimulate the brain to elicit a percept. From the early reports by Otfrid Foerster in 1929 [1], showing that electrical stimulation of the occipital cortex evoked phosphene, to the fundamental work of André Djourno and Charles Eyriès, who demonstrated that auditory nerve stimulation can be a base for cochlear implants [2], the field has consistently pushed the boundaries of artificial perception. More recently, the repertoire has expanded to median ulnar nerve stimulation to provide tactile sensory feedback in upper limb amputees [3]. Sensory stimulation spans a wide range of applications over the different sensory modalities. However, despite these developments, two fundamental questions remain: *where* along the sensory pathways should one stimulate, and *how* can we do so in a way that is both functionally effective and perceptually meaningful? Until now, accessibility has often been the main driver in choosing stimulation sites—what can be reached is what gets poked. But as stimulation techniques grow increasingly precise, so too must our reasoning. It is within this context, and guided by these dual questions of *where* and *how*, that I would now like to situate this final discussion.

In the second chapter of this thesis, we built upon the Allen brain institute dataset on mouse brain connectivity [4] to draw the connectome of the whisker system. Based on the previously reported connectivity map reviewed in [5], we defined a threshold to apply to the two-photon imaging data made available by the Allen Brain Institute to identify connections between the nodes contributing to the whisker system of the rodent. We leveraged the more than 120 transgenic lines used within the 2700 experiments reported in the dataset to further improve the specification of these connections by identifying the type of presynaptic neuron for each (either excitatory, inhibitory, or uncategorized). With this updated connectome, we demonstrated that the whisker system was composed of highly interconnected nodes, allowing communication between the sensory and motor

pathways at each stage. We also showed the existence of top-down regulation not only from the cortex to the thalamus, but also from the cortex directly to the brainstem, as well as lateral inhibition in the thalamus and brainstem. On top of that already complex network, we showed that neuromodulator releasing nuclei were playing a role in whisker related information integration, as they target all nodes of the whisker system, with structures such as the ventral tegmental area (VTA, core of dopaminergic neurons) sending connections spanning the entire system, or the tuberomammillary nucleus (TM, core of histaminergic neurons) targeting lower structures. Thanks to this analysis, we shed light on the complexity of an often oversimplified early processing system, pointing out the role of the lower structures in sensorimotor integration as being more complicated than that of a simple 'relay station', repeating the information provided by the periphery. While this chapter doesn't offer any insight on how to stimulate the sensory system to produce artificial perception, it certainly deepens our understanding of its structure and gives hints on where to stimulate. Indeed, given the high interconnectivity in the brainstem and the role of neuromodulators, inhibition, and the motor system in this structure, we see that targeting it is not straightforward. Without the knowledge of the contribution of each of these connections to sensory representation, too many unknowns remain in the relationship between the activity of its structure and the stimulus presented to the system for recommending specific stimulation sites or procedures. Targeting the brainstem thus appears to require a lot of assumptions on the contributions of the other structures along the sensorimotor pathway. Sadly, currently the number of assumptions required for effective stimulation of the sensory system only increases as we go further along the pathway, as stimulating the thalamus requires guesses about the activity of the brainstem and stimulating the cortex requires guesses about the activity of the thalamus, and that while considering only the ascending somatosensory pathway and ignoring the connectome of the whisker system in its entirety. As a consequence, if one wants to stimulate the tactile system, one needs to take one step back and take a look at the periphery.



In the third chapter, we explored duration integration of a tactile stimulus within the periphery through the lens of a model and compared it to human behavior. In order to understand the role of each mechanoreceptor, we built upon the recorded data by Sonekatsu and Gu [6] and reproduced the ramp-and-hold paradigm as used by Minnery and Simons [7]. Using this paradigm and dataset, we fitted a neuron model that includes explicitly an adaptation term (Adex [8]), as adaptation is the main property that functionally differentiates three types of mechanoreceptors that exist across systems and species (Slowly Adapting Type 1

(SA1), Slowly Adapting Type 2 (SA2) and Rapidly Adapting (RA)). We connected these three groups of receptors to a layer containing leaky integrate and fire neurons representing the trigeminal ganglion (TG) so that the TG responds by generating a weighted sum of the underlying mechanoreceptor populations. We applied tactile stimuli with different durations to the receptors and recorded the activity of each group of neurons. We then trained decoders on the activity of these neural populations to determine which of the two stimuli was the longest. This revealed that every population was informative about the stimulus duration except for the RA receptors, and that the concatenation of RA activity with that of SAs within TG impaired the decoder capacity to discriminate between two durations within TG. The conclusions of our whisker model were compared to the results of a behavioral task performed by human subjects. They were asked to tell whether or not a tactile stimulus with varying tactile intensities and durations was presented at their fingertips. This experiment showed that the duration of the stimulus was not used by the subjects when the stimulus was longer than 7.8 ms. The model and human results together demonstrate that discrimination and detection are segregated in two different pathways within the sensory system. To conclude this study, we computed the mutual information (MI) and co-information between the spike times and the stimulus duration in the whisker model. This revealed that only the timing of the first spike carries unique information about the stimulus duration. Contrary to the previous chapter, this chapter gives insight into how to stimulate, for it shows that the diverse receptors divide the stimulus information into different streams performing different tasks and that, while one type of receptor could be sufficient to detect and discriminate stimuli, such a homogeneous system would lose accuracy, making the sensory representation less reliable, as shown by the activity of isolated mechanoreceptors and the resulting accuracy of the decoders. Consequently, artificial perception could make use of a heterogeneous system mimicking neural activity to be input into the system to span the entire diversity of a sensory stimulus duration. While this has been shown in this chapter for duration, it is only one of the numerous dimensions of a tactile stimulus.

In the fourth chapter, we leveraged the previously developed model of the tactile periphery. We connected a 3D model of a whisker (WhiskIt [9]) to model a more natural-like whisker stimulus, as the model mimics the elasticity and damping parameters of real whiskers and provides the forces at its base as input to the model. On top of that, we added a model of the brainstem containing leaky exponential integrate and fire neurons (elif) and lateral inhibition. Using this model, we modelled a typical whisker stimulation experiment, where a pole was pushed against the modeled whisker. We varied one of the following dimensions of this

tactile stimulus: the amplitude of the whisker deflection, the direction of deflection, the speed of deflection, the position of the pole along the whisker (distance to the whisker base), and we applied a vibration with different frequencies at the tip of the whisker. We then recorded the activity of each structure within our model (SA1, SA2, RA, TG, BS) in response to these stimuli. We trained decoders to determine the value of one of the dimensions of the applied stimulus (how much the whisker was deflected, in which direction, at what speed, etc). We computed the mutual information between the neural activity of each neuron and the stimulus, and we assessed the correlation across pairs of neurons' firing rates within each population. Moreover, we trained the decoders on a single most informative neuron (based on MI) to determine the stimulus value. This protocol revealed that the different receptor populations were responsible for encoding different parts of the stimulus, while the BS activity could be used to decode every aspect of the tactile stimulus. This also showed that neural activity decorrelates in the BS while the amount of MI at a single neuron level increased compared to the periphery, to the point that the activity of a single neuron was sufficient to determine the applied stimulus features for a decoder. One could interpret that as a single neuron representing the entirety of the stimulus, whereas we see that the fluctuation of activity in a single neuron is sufficient to identify the applied stimulus, as the variability in the neuron's activity is equivalent to the variability within the stimulus. This does not guarantee the ability to reconstruct the stimulus from a single neuron's activity. From a network perspective, to create such a neuron that is informative about the entire range of stimuli, this neuron should receive input from a wide range of afferent neurons, making it a hub. The presence of such hubs is what mainly distinguishes the CNS from the periphery, as the peripheral neurons, receiving input from a limited number of receptors, appear to respond only to particular features of the stimuli, thus, they are specific or specialized in their response. While being more specialized, the activities of peripheral cells demonstrate more overlap with one another than those of the brainstem cells, as shown by the Pearson correlation coefficient. This comes from the probabilistic connection scheme between the trigeminal ganglion and the brainstem, as well as lateral inhibition within the brainstem, which results in the heterogeneization of each neuron within BS as they receive inputs from different receptors and probabilistic inhibition. Then, would it be sufficient to identify the hubs within BS and stimulate them to produce artificial perception? Well, as discussed above, while the hubs provide relatively the most information about the identity of the stimulus, there is no guarantee that their activity is sufficient to reconstruct the stimulus. Although they are informative about the amplitude of deflection of a whisker, here we collapsed the activity for the duration of the simulation into a single value, i.e., the firing rate; thus, this could not be

used to reconstruct the stimulus. Also, which neuron was the most informative in each population was different for each stimulus dimension (amplitude, direction, etc). The process to identify the way to stimulate each neuron to produce artificial perception could thus go as follows: 1) Identify the hubs for each stimulus dimension, 2) Compute the response curve (number of spikes for a given stimulus) for each of these hubs. The issue is that, for a tactile stimulus, we don't really know what information is received by the BS neurons. Thus, we would need to compute the response for each set of stimuli, but also for the combination of all stimuli (for one amplitude, given one duration, given one speed, etc). Meanwhile, the peripheral cells' activities are a direct result of the stimuli, without processing by any other neural units. Thus, their response curve as a function of a stimulus will be a direct transformation from the stimulus, while the BS neurons' response might be irregular with several local maxima, making them more complicated to grasp. Consequently, while considering the production of artificial perception, we are facing a trade-off. Either we do the heavy lifting computationally, trying to guess the relationship between the neural activity of a few hubs given a stimulus within BS, or we leave the heavy lifting in the neural system by focusing on the periphery, by modeling the whole receptor population and stimulating the first order sensory neuron with the given receptor activity. While the first proposition, once again, doesn't guarantee reconstructability of the stimulus, the latter does.

In the fifth chapter, we extended the peripheral network introduced in chapter 4 by adding the thalamocortical layers, thus achieving a complete model of the lemniscal pathway [10, 11]. The added layers comprised the thalamus, excitatory and inhibitory populations in layer 4 of the cortex, excitatory and inhibitory populations in layer 3 of the cortex, and inhibitory and excitatory populations in layer 2 of the cortex. These neuron populations were made of conductance-based neurons following the Hodgkin-Huxley formalism. The peripheral network was downscaled compared to Chapter 4 to ensure computational efficiency. Reproducing the protocol of the previous chapter, relying on WhiskIt [9], we applied the same set of stimuli and recorded the resulting neural activity from each population, which we later used to train decoders. The decoders were trained to identify the applied stimulus. We computed the MI between the neural activity and each stimulus as well as the Pearson correlation coefficient across neurons' firing rate within each population. We ended our analysis by training the decoders on the same task, relying on the activity of the single most informative neuron, based on the MI calculation. The downscaling of the network induced changes in the behaviour of our model of the ascending somatosensory pathway. While decorrelation amongst neurons' firing rate and an increase of MI between a single neuron's activity and a stimulus,

is still present in the network, this process doesn't happen in BS in the reduced model, mostly due to the sparse activity of the population of receptors coupled with a low probability of connection (p=0.01). Rather, we see thalamic neurons and excitatory neurons from layer 4 of the cortex (L4E) taking this role. In fact, while the correlation between neurons' firing rates of the same population remains stable once passed the thalamus, the stimulus information per neuron drops starting from layer 3 of the somatosensory cortex (L3E (excitatory) and L3I (inhibitory)). While this didn't show any impact on the decoders using the entire population activity, the decoders' performance relying on the single most informative neuron dropped in other layers than TC, L4E, and L3E. As we rely on a discretized stimulus, which is a simplification relative to the nuances of environmental cues the whisker system would receive in a real-life situation, the drop of information might not appear that detrimental to the decoders as it would in a realistic setting. In the real system, the information loss might be even more drastic. Recently, an article by Sotomayor-Gómez et al. [12] suggested that the *sequence* of spikes was the most important for stimulus representation, rather than the firing rate. While our results show that the activity of a single neuron is sufficient to identify the stimulus in some layers, there is, similarly to Chapter 4, no guarantee that a single neuron's activity is sufficient to reconstruct the stimulus. Instead, the whole sequence of activation from peripheral neurons to the cortical neurons might be necessary to reconstruct the stimulus. Based on this, we can assume that the best stimulation area to target for artificial perception is, once again, the periphery, for identifying a subset of neurons that are activated in sequence is no easy task, especially with a non-cooperative connectome. Meanwhile, stimulating a TG cell by modeling receptors' activity will send the activity downstream, to the only possible structure in the ascending somatosensory pathway, that is, BS. Similar to the previous chapter, the heavy lifting is left not to the computational model, which would have a lot of parameters to tweak if we stimulated upper structures with higher connectivity, but rather to the already present nervous system. By stimulating the input node of the network, the flow will follow its natural course up to the cortex, thus respecting the sequence of activation, providing an accurate representation of the stimulus.



So, *where should we stimulate* to produce functionally effective and meaningful perception? Based on our discussion, we can answer that the periphery seems to be the most reliable locus to accurately represent a stimulus. While cortical stimulation has been used, in the visual system, the phosphenes produced by such a technique are believed to be the result of the activation of an entire cortical column [13]. Further research on stimulus encoding exhibited representational drift within the cortex [12], making the neural population to target unstable. Building on the

previous point, Sotomayor-Gómez et al. [12] have demonstrated that the sequence of the spikes is what matters for stimulus encoding rather than the firing rate of each neuron, which changes a lot from one trial to another. Furthermore, in their article, Saal et al. demonstrated that the neural activity of cortical neurons in the touch system integrates the activity of several subtypes of receptors [14]. This lets us wonder if the STA, as it is computed for cortical neurons, really has a meaning in such a deep layer. If one targets the periphery to achieve artificial perception, then the sequence of activation of neurons is a mere result of the initial stimulation, since we are stimulating the first node. Stimulating the periphery, such is the idea of cochlear implants [15], artificial retinas [16], or peripheral nerve stimulation to produce touch feedback [3], and, given our results, it seems to be the most straightforward way to achieve artificial perception.

*How should we stimulate* to produce functionally effective and meaningful perception? Cochlear implants mainly use block pulses to stimulate the auditory nerve. While this allows subjects to hear, the resulting auditory percept is perceived as quite robotic, far from natural [17]. Obviously, the shape of the cochlea is an obstacle for accurate stimulation, as the array of electrodes needs to be rolled on itself, which doesn't allow for a lot of electrodes to be integrated in the implant. With artificial retinas, resolution is a common problem because of the high density of ganglion cells present in the retina [18]. For tactile stimuli, peripheral nerve stimulation has been used lately to investigate the role of different stimulation patterns on stimulus localisation [19]. It was demonstrated that by stimulating the nerve at the same place, with a natural-like pattern, one could modify the position of the perceived stimulus on an artificial limb consistently. This result is in agreement with the previously mentioned results showing the importance of the sequence of activation [12], for if one has to respect the relative timing of spikes, then one has to take into consideration the adaptation rate and reproduce the activity of peripheral cells. Indeed, adaptation will change the timing of the next spike as a function of the spiking of the previous spike, thus changing the timing of each spike within a spike train. Altogether, it seems that the future of neuroprosthesis lies within the periphery.

Beyond the theoretical achievements of this thesis, we conclude these 4 years with a set of tools that pave the way for future researchers on sensorimotor integration in the whisker system. The whisker to cortex model gives the possibility to explore different, more dynamic stimuli than those we experimented with so far. The neural network structure connected to it can also be changed to embed more complex neurons, different connectivity patterns, and more structures. The receptor models designed in

this thesis could benefit from more accuracy by integrating the mechanosensitive ion channels or taking more parameters to take into account to determine their position within the whisker follicle. The whole sensorimotor pathway could be replicated based on the Hill muscle model [20] to make the whisker movement biologically accurate. These muscles could be controlled by a model of the facial motor nucleus, thus providing a complete neuromuscular model [21]. In the end, we are left with a model that can be easily modified to explore more sensorimotor paradigms [22]. We also leave with a computationally efficient model of receptors that can easily be integrated in a neuromorphic chip such as Loihi2 [23] and thus used to produce neuromorphic sensors. Their simplicity makes them versatile, and as we saw in the previous chapters, these receptors can encode all aspects of tactile stimuli.

We have shown how the theoretical model developed in this thesis contributes to the understanding of sensory integration and how to build upon our findings to improve neuroprosthetics. We have been through the tools that we provided for future research and the elements that could be pushed forward. Yet, there is still some room for one last discussion point.



Alas, reader, we come to the last part of this thesis, and of them all, not the least, for we embark in our ultimate cavalcade together, once again, on the never ending sea of philosophy, for you know, this thesis wouldn't be mine if it didn't end on a philosophical crescendo. On which journey, you ask? A mere detour, following the foam of Hume, fencing with Descartes, boarding Marleau-Ponty's galleon. What for? Well, for the sole purpose of jousting with the "I". The concept, not me, sheath back your sword and run, for Hume is already gone. This rascal, he played on us a good one. As a philosopher, he was supposed to be the lighthouse in the fog, to enlighten our path. Yet he made us more confused, and we wandered off into the distance, for he said the "I" is an empty vessel that aims only to host the concept of its user, a mere fabrication of our mind to unify our flow of ephemeral perception, thus making "I"'s meaning different for each speaker [24]. But then, who is the speaker? Even more, what is the speaker? To qualify, the speaker is to encage them at a specific time, said the existentialist, for the identity of one is not the same at one time and the following. "I don't have a specific nature, I am a being in the making", answered Heidegger [25]. Such an elusive answer to avoid clarity! Look at us now, surrounded by the fog, lost at sea with no hope for a return! But fear not, for I see a thread of thought, and if we pull it, I bet we'll find our way. "Cogito ergo sum" is written on it, a hair from Descartes' moustache, most likely. Let's follow it, shall we? "I think, therefore, I am", he said. Does it mean that I am my mind? As a dualist, Descartes might have answered yes, as he described the body as an automaton activated by

the mind [26]. But this mind of ours has to interact with the surrounding world, isn't it? Unless you think that the world is within our mind, as George Berkeley did [27], for if not perceived, then it does not exist. Well, we would meet at a dead-end, for are you in my mind or am I in yours, dear reader? Which of us should find his way to the asylum? No, no, after you, please lead the way. Enough with the nonsense! Now that this little argument is settled and we know for sure that I am not a figment of your imagination, nor you of mine, we still haven't answered the question of what you are. Here comes the link with this thesis; it took time, but we finally found it. Let's assume that you are your brain, and, similar to how Descartes described it, your body is an automaton controlled by the central nervous system (CNS). Your CNS still needs to gather information from the outside world, thus, the outside world will shape the activity of the brain. But what else besides the receptors shapes the activity of the brain, given the information gathered from the outside? So, instead of your CNS, are you simply your nervous system, periphery included? Well, what else but the shape of the cornea will dictate the distribution of light amongst the photoreceptors? What else than the lens will propagate the light on the cornea? Similarly, what else but the skin will dampen the intensity of a tactile stimulus? So, are we our body as a whole? What a disappointing conclusion, isn't it? But what if, instead of dissecting the "I" to its minimum, which leads to mistakes as we've seen, we embraced it as a whole? Does it mean that every single part of our body is performing cognition? No, but as discussed by Merleau-Ponty [28], every inch of it influences cognition, for it provides information on a stimulus that will impact our reaction. Thus, our body is our window toward the world, for we exist in the world through it. Without a body, there is no such thing as an "I". As I promised, a joust with the "I", never have I said that we would fend it ourselves. In fact, every battle starts with a good identification of the opponent. And now, I believe we are well prepared. But, dear reader, a battle is more of a moment for actions than for words, and with this new insight, it is time for us to depart to, through our research, tackle the "I". The concept, not me.

# References


[1] Foerster O. (1929). Beitraege zur Pathophysiologie der Sehbahn und der Sehsphaere [Contributions to the pathophysiology of the visual pathway and the visual sphere]. J. Psychol. Neurol. 39 435–463.

[2] Seitz, P. R. (2002). French origins of the cochlear implant. *Cochlear Implants International*, *3*(2), 77–86. https://doi.org/10.1179/cim.2002.3.2.77

[3] Soghoyan, G., Biktimirov, A., Matvienko, Y., Chekh, I., Sintsov, M., & Lebedev, M. A. (2023). Peripheral nerve stimulation enables somatosensory feedback while suppressing phantom limb pain in transradial amputees. *Brain Stimulation*, *16*(3), 756–758. https://doi.org/10.1016/j.brs.2023.04.017

[4] Oh, S. W., Harris, J. A., Ng, L., Winslow, B., Cain, N., Mihalas, S., Wang, Q., Lau, C., Kuan, L., Henry, A. M., Mortrud, M. T., Ouellette, B., Nguyen, T. N., Sorensen, S. A., Slaughterbeck, C. R., Wakeman, W., Li, Y., Feng, D., Ho, A., . . . Zeng, H. (2014). A mesoscale connectome of the mouse brain. *Nature*, *508*(7495), 207–214. https://doi.org/10.1038/nature13186

[5] Bosman, L. W. J., Houweling, A. R., Owens, C. B., Tanke, N., Shevchouk, O. T., Rahmati, N., Teunissen, W. H. T., Ju, C., Gong, W., Koekkoek, S. K. E., & De Zeeuw, C. I. (2011). Anatomical Pathways Involved in Generating and Sensing Rhythmic Whisker Movements. *Frontiers in Integrative Neuroscience*, *5*. https://doi.org/10.3389/fnint.2011.00053

[6] Sonekatsu, M., & Gu, J. G. (2019b). Functional properties of mechanoreceptors in mouse whisker hair follicles determined by the pressure-clamped single-fiber recording technique. *Neuroscience Letters*, *707*, 134321. https://doi.org/10.1016/j.neulet.2019.134321

[7] Minnery, B. S., Bruno, R. M., & Simons, D. J. (2003). Response Transformation and Receptive-Field Synthesis in the Lemniscal Trigeminothalamic Circuit. *Journal Of Neurophysiology*, *90*(3), 1556–1570. https://doi.org/10.1152/jn.00111.2003

[8] Brette, R., & Gerstner, W. (2005b). Adaptive Exponential Integrate-and-Fire Model as an Effective Description of Neuronal Activity. *Journal Of Neurophysiology*, *94*(5), 3637–3642. https://doi.org/10.1152/jn.00686.2005

[9] Zweifel, N. O., Bush, N. E., Abraham, I., Murphey, T. D., & Hartmann, M. J. Z. (2021). A dynamical model for generating synthetic data to quantify active tactile sensing behavior in the rat. *Proceedings Of The National Academy Of Sciences*, *118*(27). https://doi.org/10.1073/pnas.2011905118

[10] Chiaia, N. L., Rhoades, R. W., Bennett-Clarke, C. A., Fish, S. E., & Killackey, H. P. (1991). Thalamic processing of vibrissal information in the rat. I. Afferent input to the medial ventral posterior and posterior nuclei. *The Journal of Comparative Neurology, 314*, 201–216. https://doi.org/10.1002/cne.903140202

[11] Lu, S. M., & Lin, R. C. S. (1993). Thalamic afferents of the rat barrel cortex: A light-and electron-microscopic study using phaseolus vulgaris leucoagglutinin as an anterograde tracer. *Somatosensory & Motor Research, 10*(1), 1–16. https://doi.org/10.3109/08990229309028819

[12] Sotomayor-Gómez, B., Battaglia, F. P., & Vinck, M. (2025). Firing rates in visual cortex show representational drift, while temporal spike sequences remain stable. *Cell Reports*, *44*(4), 115547. https://doi.org/10.1016/j.celrep.2025.115547

[13] Tian, F., Zhang, Y., Schriver, K. E., Hu, J. M., & Roe, A. W. (2024). A novel interface for cortical columnar neuromodulation with multipoint infrared neural stimulation. *Nature Communications*, *15*(1). https://doi.org/10.1038/s41467-024-50375-0

[14] Saal, H. P., & Bensmaia, S. J. (2014). Touch is a team effort: interplay of submodalities in cutaneous sensibility. *Trends in Neurosciences*, *37*(12), 689–697. https://doi.org/10.1016/j.tins.2014.08.012

[15] Deep, N., Dowling, E., Jethanamest, D., & Carlson, M. (2018). Cochlear Implantation: An Overview. *Journal Of Neurological Surgery Part B Skull Base*, *80*(02), 169–177. https://doi.org/10.1055/s-0038-1669411

[16] Chenais, N. A. L., Leccardi, M. J. I. A., & Ghezzi, D. (2021). Photovoltaic retinal prosthesis restores high-resolution responses to single-pixel stimulation in blind retinas. *Communications Materials*, *2*(1). https://doi.org/10.1038/s43246-021-00133-2

[17] Bessen, S. Y., Saunders, J. E., Eisen, E. A., & Magro, I. L. (2021). Perceptions of Sound Quality and Enjoyment After Cochlear Implantation. *OTO open*, *5*(3), 2473974X211031471. https://doi.org/10.1177/2473974X211031471

[18] Miyoshi, T., Morimoto, T., Sawai, H., & Fujikado, T. (2021). Spatial Resolution of Suprachoroidal–Transretinal Stimulation Estimated by Recording Single-Unit Activity From the Cat Lateral Geniculate Nucleus. *Frontiers in Neuroscience*, *15*. https://doi.org/10.3389/fnins.2021.717429

[19] Valle, G., Secerovic, N. K., Eggemann, D., Gorskii, O., Pavlova, N., Petrini, F. M., Cvancara, P., Stieglitz, T., Musienko, P., Bumbasirevic, M., & Raspopovic, S. (2024). Biomimetic computer-to-brain communication enhancing naturalistic touch sensations via peripheral nerve stimulation. *Nature Communications*, *15*(1). https://doi.org/10.1038/s41467-024-45190-6

[20] Göktepe, S., Menzel, A., & Kuhl, E. (2014). The generalized Hill model: A kinematic approach towards active muscle contraction. *Journal Of The Mechanics And Physics Of Solids*, *72*, 20–39. https://doi.org/10.1016/j.jmps.2014.07.015

[21] Rault, N., Bergmans, T., Delfstra, N., Kleijnen, B. J., Zeldenrust, F., & Celikel, T. (2024b). Where Top-Down Meets Bottom-Up: Cell-Type Specific Connectivity Map of the Whisker System. *Neuroinformatics*, *22*(3), 251–268. https://doi.org/10.1007/s12021-024-09658-6

[22] Chaudhary, R., & Rema, V. (2018). Deficits in Behavioral Functions of Intact Barrel Cortex Following Lesions of Homotopic Contralateral Cortex. *Frontiers in Systems Neuroscience*, *12*. https://doi.org/10.3389/fnsys.2018.00057

[23] Uludağ, R. B., Çağdaş, S., İşler, Y. S., Şengör, N. S., & Aktürk, İ. (2024). Bio-realistic neural network implementation on Loihi 2 with Izhikevich neurons. *Neuromorphic Computing And Engineering*, *4*(2), 024013. https://doi.org/10.1088/2634-4386/ad5584

[24] Hume, D. (1978). *Treatise of human nature* (L. A. Selby-Bigge, Ed.; 2nd ed.). Oxford University Press.

[25] Heidegger, M. (1946). Letter on "Humanism". In W. McNeill (Ed. & Trans.), *Pathmarks* (pp. 239–276). Cambridge University Press.

[26] Descartes, R. (1662/1972). Treatise of Man (T. S. Hall, Trans.). Cambridge, MA: Harvard University Press

[27] Berkeley, G. (2003). A Treatise Concerning the Principles of Human Knowledge. Dover Publications.

[28] Merleau-Ponty, M. (1962). *Phenomenology of Perception* (C. Smith, Trans.). London: Routledge & Kegan Paul.

# Appendix

## Acknowledgement

When writing, most of the time, my quill moves on its own. My thoughts, still mere images, get tied together by ink in a landscape that, to my eyes, appears harmonious. Yet, when it comes to acknowledgment, my hand, usually so verbose, stays still, my mind loops over this scene from *Cyrano de Bergerac*, where Edmond Rostand wrote a tirade of "no thanks" ending with "I will rise, maybe not so high, but alone." And yet, I am forced to admit that on my own, this thesis would have been significantly diminished. It is thus with unease that I will engage in this challenge of writing my own monologue of "thanks" in its most uninspired way.

I thus thank Charl Linssen, Mitra Hartmann, and Kevin Kleczka for their invaluable assistance with connecting the virtual whisker model to my neural networks, Tea Tompos for providing a Top-down part of my Bottom-up project, Tousif Jamal, for putting knots in my brain with his gene networks, Nishant Joshi, and Filip Novický for our discussions on methodology, philosophy and music, Arezoo Alizadeh, Farad Razi and all those that were part of the Zeldenrust lab during my PhD and had to suffer my jokes and sarcasm during our weekly meetings.

I shall thank as well the people from the SmartNets project who provided a lot of different perspectives on Neurosciences and organized the workshops, Dario Del Piano and Julijana Gjorgjieva, for hosting me during my secondments.

And finally, my supervisors Fleur Zeldenrust, and Tansu Celikel for allowing me to embark on science, pursuing the projects that I had set my mind to.

This project has received funding from the European Union's Horizon 2020 research and innovation program under the Marie Sklodowska-Curie grant agreement No 860949.

# Thesis Summary

## Computational Mechanics of Sensory Processing: Modelling and Computation for Next-Generation Artificial Sensing

The study of neural computation in the tactile system is fundamental to understanding how the brain interprets and organizes physical interactions with the external environment. Tactile processing begins when mechanoreceptors in the skin transduce physical stimuli into electrical signals, which travel through the peripheral and central nervous systems. Complex neural circuits process these signals to extract key information such as texture, shape, pressure, and movement. Investigating these computations sheds light on how sensory inputs are encoded, integrated, and interpreted in the brain, enhancing our understanding of perception and behavior. The thesis aims to unveil this process with psychophysical experiments performed in humans and computational modeling of the ascending somatosensory system based on available electrophysiological data collected in rodents. Beyond theoretical implications, such research has a significant impact for future applications, including the development of neuroprosthetics, advancements in haptic technology, and treatments for sensory processing disorders. By unraveling the tactile system's mechanisms, we deepen our understanding of human experience and pave the way for innovations that enhance sensory function and quality of life.

The whisker system is an excellent model for studying neural computations in sensory processing. Its somatotopic organization allows researchers to trace information conveyed by a single whisker. Each whisker is represented by the activity of a barrelette in the brainstem, a barreloid in the thalamus, and a barrel in the somatosensory cortex. Additionally, the vibrissae's positions and shapes make them easy to manipulate, enabling precise control over stimuli applied to the tactile system. The whisker system is also a great experimental model for human haptic sensing, due to the preserved organization of the mechanosensitive cells in the periphery and the architecture along the ascending central circuits in the brain.

While the neural architecture of the human nervous system is not easily accessible as an experimental model, the ascending direct path of whisker processing has been extensively studied, including the distributed representations across most sensory and motor circuits in the brain. In Chapter 2 of this thesis, we updated the whisker circuit map (Bosman et al. 2011) using data from the Allen Brain database, which contains two-photon imaging of the mouse connectome to identify projections of targeted neurons expressing fluorescent proteins. By analyzing data from different

transgenic lines to establish cell-type specificity, we first identified the existence and then the type of connectivity between nuclei in the somatosensory pathway, motor pathways, and neuromodulator-releasing nuclei. This study revealed a highly interconnected network with 157 connections across 18 nuclei. Key findings include the existence of low-level inhibition in the brainstem, direct sensory-motor connections at multiple stages, and top-down regulation from the cortex to the thalamus and brainstem. Additionally, neuromodulator-releasing nuclei appear to play a structural role in the architecture of this system, as their presence reduces the average nodal shortest path, thus facilitating communication across the different nodes from the sensorimotor pathway. These results argue that the sense of touch is a "whole brain computation."

In Chapter 2, we showed that the connectome suggests that early sensory processing is more complex than previously thought. To further understand the early processing in the whisker system, we aimed to develop a model of these early processing nuclei. The complexity of the whisker system extends even beyond its connectome, as the mechanoreceptors in the skin already show a large diversity. To understand the initial encoding of duration in tactile information, we developed in Chapter 3 a model of mechanoreceptors based on the different experimentally observed adaptation rates and fitted these to biological recordings (Sonekatsu and Gu, 2020). This model shows how stimuli are dissected into two distinct streams at the receptor level in the mammalian skin. Taking advantage of both the ease of psychophysical quantification of detection and discrimination thresholds in humans and the availability of electrophysiological data in rodents, we developed a species-transcending computational model of the early processing of touch. Using our model, we replicated humans' detection and discrimination performance and proposed that two distinct pathways are responsible for stimulus detection and discrimination, suggesting that parallel processing of touch starts already in the first processing step and hence outside of the central nervous system.

One of the few differences between human and rodent mechanosensation is that before mechanoreceptors detect force in the whisker system, whiskers perform "predermal" filtering, potentially impacting the information available to mechanoreceptors. Thus, in Chapter 4, we integrated *WhiskIt* (Zweifel et al., 2021), a mechanical model of the whisker, into our model of the first two processing stages (i.e., mechanoreceptors and brainstem), enabling simulations of forces and torques as a response to various whisker transformations. We manipulated the virtual whisker with varying directions, amplitudes, speeds, and tip vibrations to analyze all tactile stimulus components. Using information-theoretical analyses,

we quantified how incoming information is transferred and transformed in the periphery (mechanoreceptors) and the brainstem, showing how lateral inhibition in the brainstem controls ascending sensory information.

In Chapter 5, we expanded the computational model to include the thalamus (VPM), as well as the granular and supragranular layers of the somatosensory cortex. We introduced a conductance-based model of thalamic neurons to simulate bursting behavior. We incorporated cortical layers 4 and 2/3 of the somatosensory cortex, quantifying and comparing information transfer and decoding performance at different processing stages, from mechanoreceptors to the cortex. Our findings demonstrate that stimulus identity can already be decoded in the early stages of the ascending pathway. Information quantification revealed the relative contributions of the subcortical and cortical processing to information flow.

Taken together, the research presented in this thesis highlights the complex mechanisms by which biological systems interpret tactile stimuli. It elucidates the role of mechanoreceptor adaptation profiles, the organization of the ascending somatosensory pathway, and the circuitry responsible for tactile integration. These insights contribute to our understanding of sensory processing in particular and its broader applications in neuroscience and technology.

## The list of chapters

**Chapter 1 - Mechanoreceptors: An Overview of the Information Flow in the Periphery**
**Chapter 2 - Where Top-Down Meets Bottom-Up: Cell-Type Specific Connectivity Map of the Whisker System**
**Chapter 3 - A Universal Model of Touch: A Bottom-Up Perspective**
**Chapter 4 - Tactile Integration in the Whisker System: From Whisker to Brainstem**
**Chapter 5 - Thalamocortical Integration of Tactile Stimuli**
**Conclusion - Information Flow in the Ascending Somatosensory System**

# Dutch Thesis Summary

## Computationele mechanica van sensorische verwerking: Modelling and Computation for Next-Generation Artificial Sensing

De fundamentele studie van de berekeningen die de hersenen doen voor onze tastzin vormen het fundament voor het begrip van hoe de hersenen fysieke interacties met de externe omgeving interpreteren en organiseren. Tactiele verwerking begint wanneer mechanoreceptoren in de huid fysieke prikkels omzetten in elektrische signalen, die door het perifere en centrale zenuwstelsel gaan. Complexe neurale circuits verwerken deze signalen om belangrijke informatie zoals textuur, vorm, druk en beweging te extraheren. Het onderzoeken van deze berekeningen werpt licht op hoe zintuiglijke input wordt gecodeerd, geïntegreerd en geïnterpreteerd in de hersenen, wat ons begrip van perceptie en gedrag verbetert. In dit proefschrift wordt dit proces onderzocht aan de hand van psychofysische experimenten bij mensen en het ontwikkelen van computationele modellen van het opgaande somatosensorische systeem op basis van beschikbare elektrofysiologische gegevens verzameld bij knaagdieren. Naast theoretische implicaties heeft dergelijk onderzoek een significante impact op toekomstige toepassingen, waaronder de ontwikkeling van neuroprothesen, vooruitgang in haptische technologie en behandelingen voor sensorische stoornissen. Door de mechanismen achter de tastzin te ontrafelen, verdiepen we ons begrip van de menselijke ervaring en maken we de weg vrij voor innovaties die de sensorische functie en levenskwaliteit verbeteren.

Het systeem van de snorharen is een uitstekend model om neurale berekeningen in sensorische verwerking te bestuderen. De somatotopische organisatie laat het toe om informatie te traceren die door één enkele snorhaar wordt overgebracht. Elke snorhaar wordt vertegenwoordigd door de activiteit van een zogenaamde 'barellette' in de hersenstam, een 'barreloid' in de thalamus en een 'barrel' in de somatosensorische cortex. Bovendien zijn de snorharen door hun positie en vorm eenvoudig te manipuleren, waardoor precieze controle over de stimuli die op het tactiele systeem worden toegepast mogelijk is. Dit snorhaar systeem is een geweldig experimenteel model voor menselijke haptische sensatie, vanwege de organisatie van de mechanosensitieve cellen in de periferie en de architectuur langs de opgaande centrale circuits in de hersenen, een systeem dat vergelijkbaar is in verschillende (zoog)diersoorten.

Hoewel de neurale architectuur van het menselijke zenuwstelsel niet gemakkelijk toegankelijk is als experimenteel model, is het opgaande directe pad van de verwerking van de input die via snorharen de hersenen binnenkomt uitgebreid

bestudeerd, inclusief de gedistribueerde representaties over de meeste sensorische en motorische circuits in de hersenen. In hoofdstuk 2 van dit proefschrift hebben we de bestaande snorhaar circuit-kaart (Bosman et al. 2011) bijgewerkt met behulp van gegevens uit de Allen Brain database, die twee-foton beeldvorming van het muis connectoom bevat, om projecties van specifieke neuronen die fluorescerende eiwitten tot expressie brengen te identificeren. Door gegevens van verschillende transgene lijnen te analyseren om de specificiteit van het celtype vast te stellen, identificeren we eerst het bestaan en vervolgens het type verbinding met tussen kernen in de somatosensorische paden, motorische paden en kernen die neuromodulatoren uitscheiden. Deze studie onthulde een sterk onderling verbonden netwerk met 157 verbindingen tussen 18 kernen. Belangrijke bevindingen zijn onder andere het bestaan van inhibitie op een laag niveau in de hersenstam, directe sensomotorische verbindingen in meerdere kernen en top-down regulatie vanuit de cortex naar de thalamus en hersenstam. Bovendien lijken neuromodulator-uitscheidende kernen een structurele rol te spelen in de architectuur van dit systeem, aangezien hun aanwezigheid de gemiddelde kortste weg van de knooppunten vermindert en zo de communicatie tussen de verschillende knooppunten van het sensorimotorische pad vergemakkelijkt. Deze resultaten suggereren dat tastzin een "whole brain computation" is.

In hoofdstuk 2 hebben we laten zien dat het connectoom suggereert dat de vroege sensorische verwerking complexer is dan eerder gedacht. Om de vroege verwerking in het snorhaarsysteem verder te begrijpen, hebben we een model ontwikkeld van deze vroege verwerkingskernen. De complexiteit van het sonarsysteem gaat zelfs verder dan het connectoom, aangezien de mechanoreceptoren in de huid al een grote diversiteit vertonen. Om de initiële codering van de duur van een tactiele stimulus te begrijpen, ontwikkelden we in hoofdstuk 3 modellen van mechanoreceptoren gebaseerd op hun verschillende experimenteel waargenomen adaptatie snelheden en pasten deze aan door ze te fitten naar op biologische metingen (Sonekatsu en Gu, 2020). Deze modellen laten zien hoe stimuli op receptorniveau in de huid van zoogdieren worden ontleed in twee verschillende stromen. Door gebruik te maken van zowel het gemak van psychofysische kwantificering van detectie- en discriminatiedrempels bij mensen als de beschikbaarheid van elektrofysiologische gegevens bij knaagdieren, ontwikkelden we een soort overstijgend computationeel model van de vroege verwerking van aanraking. Met behulp van ons model bootsten we de detectie- en discriminatieprestaties van mensen na en stelden we voor dat twee verschillende paden verantwoordelijk zijn voor stimulusdetectie en -discriminatie, wat suggereert dat parallelle verwerking van aanraking al in de eerste verwerkingsstap en dus buiten het centrale zenuwstelsel begint.

Één van de weinige verschillen tussen mechano sensatie bij mensen en knaagdieren, is dat voordat mechanoreceptoren kracht detecteren in het snorharen stelsel, snorharen "predermale" filtering uitvoeren, wat mogelijk invloed heeft op de informatie die beschikbaar is voor mechanoreceptoren. Daarom integreerden we in hoofdstuk 4 WhiskIt (Zweifel et al., 2021), een mechanisch model van de snorhaar, in ons model van de eerste twee verwerkingsstadia (d.w.z. mechanoreceptoren en hersenstam), waardoor simulaties van krachten en koppels als reactie op verschillende manipulaties van de snorhaar mogelijk werden. We bewogen de virtuele snorhaar in verschillende richtingen en met verschillende amplitudes, snelheden en tip trillingen om alle tactiele stimuli componenten te analyseren. Met behulp van informatietheoretische analyses hebben we gekwantificeerd hoe inkomende informatie wordt overgedragen en getransformeerd in de periferie (mechanoreceptoren) en de hersenstam, waarbij we hebben laten zien hoe laterale inhibitie in de hersenstam opgaande sensorische informatie bestuurt.

In hoofdstuk 5 hebben we het computationele model van hoofdstuk 4 uitgebreid met de thalamus (VPM) en de granulaire en supra granulaire lagen van de somatosensorische cortex. We introduceerden een conductantie-gebaseerd model van thalamus neuronen om bursting gedrag te simuleren. We voegden ook modellen van corticale lagen 4 en 2/3 van de somatosensorische cortex toe en kwantificeren en vergeleken informatieoverdracht en decodering prestaties in verschillende verwerkingsstadia, van mechanoreceptoren naar de cortex. Onze bevindingen tonen aan dat de stimulus identiteit al in de vroege stadia van het stijgende pad kan worden gedecodeerd. Kwantificering van informatieoverdracht onthulde de relatieve bijdragen van de subcorticale en corticale verwerking aan de informatiestroom.

Alles bij elkaar benadrukt het onderzoek in dit proefschrift de complexe mechanismen waarmee biologische systemen tactiele stimuli interpreteren. Het verduidelijkt de rol van mechanoreceptoradaptatieprofielen, de organisatie van het opgaande somatosensorische pas en het circuit dat verantwoordelijk is voor tactiele integratie. Deze inzichten dragen bij aan ons begrip van sensorische verwerking in het bijzonder en de bredere toepassingen ervan in de neurowetenschappen en technologie.

## Lijst van de hoofdstukken

# Research Data Management

All research presented in this thesis is based solely on computational modeling and analysis. No human or animal subjects were involved in data collection. Simulated data were generated using validated models and processed following reproducible, transparent methods. Ethical considerations focused on data integrity, proper attribution, and open access principles. All code and data are archived following FAIR (Findable, Accessible, Interoperable, Reusable) guidelines.

## Findable Accessible

All code developed for this thesis is openly available in a public repository or will be publicly available after publication. It is documented, version-controlled, and includes instructions for use. The repository is indexed on GitHub to ensure findability. Access does not require authentication or special permissions. This ensures transparency, reproducibility, and long-term availability.

| Chapter | Data/Code availability |
|---|---|
| Chapter 2 | Data: https://connectivity.brain-map.org/ |
| Chapter 3 | Code: https://github.com/Nrault/Universal_model_of_touch |
| Chapter 4 | Code: https://github.com/Nrault/EarlyWhiskerSystem |
| Chapter 5 | Code: https://github.com/Nrault/StimulusRepInAscendingPathway |

## Interoperable, Reusable

All code relies on Python and is given with its corresponding environment, containing all libraries required to run it, thus making it interoperable and reusable.

## Privacy

This thesis involves no collection or processing of personal or sensitive data. All data used are either simulated or publicly available, with no risk to individual privacy. No identifiable information is stored, shared, or analyzed at any stage. Privacy principles were respected in full compliance with data protection standards. The work poses no ethical or legal concerns related to privacy.

*

# CV

27 years old
Driving licence

## Profile

Computational neuroscientist with a focus on low level integration of sensory information

## Languages

TOEIC (900 points)
One year study in Scotland
Fluent english
French

## Hobbies

Guitar, Violin, Piano, Bass, Ukulele, Sport, Programming, Reading

## Contact

n.rault@neurophisiology.nl
+33 (0)6 27 18 93 62

PHD STUDENT IN COMPUTATIONAL NEUROSCIENCE

# Nicolas Rault

DONDERS INSTITUTE FOR BRAIN, COGNITION AND BEHAVIOUR, RADBOUD UNIVERSITY

## Experiences

- PhD Student Apr 2021 - Now
  Sensory integration in the early stages of the somatosensory system
- Internship Feb-Aug 2020
  Spinal-like regulator network implementation for upper limb control with Hybrid team at INCIA (Bordeaux)
- Internship June-Aug 2019
  Post-Stroke rehabilitation BCI with team Neurosys at INRIA (Nancy)
- Robert Gordon University 2018
  Google Hashcode
  Mobile application implementation
  Auction application
  Website pentest
- IUT du Limousin 2017
  Implementation of a website content manager
  Internship on 3D modelling of sound at Napier University (Edinburgh)

## Publication/Conferences

- Conferences
  CNS 2023
  Bernstein 2024
  SFN 2024
- Publications
  Rault, N., Bergmans, T., Delfstra, N. et al. Where Top-Down Meets Bottom-Up: Cell-Type Specific Connectivity Map of the Whisker System. Neuroinform 22, 251–268 (2024). https://doi.org/10.1007/s12021-024-09658-6

## Diplomas

- 2020 - Grenoble (France)
  Research Msc/Master 2 in Cognitive Sciences
- 2019 - Nancy (France)
  Master 1 - Sciences Cognitives
- 2018 - Aberdeen (Scotland)
  Bsc/Licence in Computer Science
  DUETI
- 2017 - Limoges (France)
  DUT informatique
  Baccalauréat Scientifique

## Skills

- Programming Language
  Python
  C++
  Java
  C#
  Bash
- Management
  UML
  Agile
  Waterfall
  GANTT
- Other
  MatLab
  LateX
  BRIAN2
  Sklearn
  Scipy

*

# PhD Portfolio

**Name PhD candidate:** Nicolas Rault
**Graduate School:** Donders Graduate School
**PhD period:** 16-04-2021 – 16-04-2025
**Supervisors:** Fleur Zeldenrust, Tansu Celikel

## Courses & Workshop

| Course | Organizer | Hours |
|---|---|---|
| Data Management | EScience | 7 |
| SmartNets Synaptic Plasticity (2021) | Max Planck Institute of Frankfurt | 21 |
| SmartNets Dendrite modelisation (2021) | IMBB-FORTH | 14 |
| SmartNets NeuroImaging (2022) | Paris Sorbonne | 21 |
| SmartNets Reservoir Computing (2023) | UGent | 21 |
| SmartNets Animal Behaviour (2024) | Max Planck Institute of Animal Behaviour | 21 |
| SmartNets Data Analysis (2024) | Donders institute for brain, cognition and behaviour | 21 |
| Donders School Introduction Day (2022) | Donders Graduate School | 7 |
| Donders Graduate School Day (2023) | Donders Graduate School | 7 |
| Donders Graduate School Day (2024) | Donders Graduate School | 7 |
| Academic Integrity (2025) | Donders Graduate School | 7 |

## Conferences & Summerschools

| Course | Location |
|---|---|
| Dendrites (2021) | Heraklion, Greece |
| CNS (2023) | Leipzig, Germany |
| DNM (2023) | Tiel, The Netherlands |
| DNM (2024) | Tiel, The Netherlands |
| EBrains Baltic-Nordic Summerschool (2024) | Helsinki, Finland and Stockholm, Sweden |
| Bernstein (2024) | Frankfurt, Germany |
| SFN (2024) | Chicago, USA |

## Teaching Activities

| Activity | Study Program |
|---|---|
| Literature Review Supervision<br>Rebekka Brandwijk (4 Months) | Master Medical Biology |
| Teacher Assistant (2022, 2 Months) | Mathematic for Biologists |
| Teacher Assistant (2024, 2 Months) | Mathematic for Biologists |

## Outreach & Societal Impact

| Activity | Location |
|---|---|
| Dutch Brain Olympiad (2021)<br>Writing an Introduction to Brain Computer Interfaces for High School Students | Nijmegen<br>https://hersenolympiade.nl/en/werkgroep-computational-neuroscience-en-ai/ |
| Member of Brain Dutch Olympiad organising team (2023) | Nijmegen |

*

# Donders Graduate School

For a successful research Institute, it is vital to train the next generation of scientists. To achieve this goal, the Donders Institute for Brain, Cognition and Behaviour established the Donders Graduate School in 2009. The mission of the Donders Graduate School is to guide our graduates to become skilled academics who are equipped for a wide range of professions. To achieve this, we do our utmost to ensure that our PhD candidates receive support and supervision of the highest quality.

Since 2009, the Donders Graduate School has grown into a vibrant community of highly talented national and international PhD candidates, with over 500 PhD candidates enrolled. Their backgrounds cover a wide range of disciplines, from physics to psychology, medicine to psycholinguistics, and biology to artificial intelligence. Similarly, their interdisciplinary research covers genetic, molecular, and cellular processes at one end and computational, system-level neuroscience with cognitive and behavioural analysis at the other end. We ask all PhD candidates within the Donders Graduate School to publish their PhD thesis in the Donders Thesis Series. This series currently includes over 600 PhD theses from our PhD graduates and thereby provides a comprehensive overview of the diverse types of research performed at the Donders Institute. A complete overview of the Donders Thesis Series can be found on our website: https://www.ru.nl/donders/donders-series

The Donders Graduate School tracks the careers of our PhD graduates carefully. In general, the PhD graduates end up at high-quality positions in different sectors, for a complete overview see https://www.ru.nl/donders/destination-our-former-phd. A large proportion of our PhD alumni continue in academia (>50%). Most of them first work as a postdoc before growing into more senior research positions. They work at top institutes worldwide, such as University of Oxford, University of Cambridge, Stanford University, Princeton University, UCL London, MPI Leipzig, Karolinska Institute, UC Berkeley, EPFL Lausanne, and many others. In addition, a large group of PhD graduates continue in clinical positions, sometimes combining it with academic research. Clinical positions can be divided into medical doctors, for instance, in genetics, geriatrics, psychiatry, or neurology, and in psychologists, for instance as healthcare psychologist, clinical neuropsychologist, or clinical psychologist. Furthermore, there are PhD graduates who continue to work as researchers outside academia, for instance at non-profit or government organizations, or in pharmaceutical companies. There are also PhD graduates who work in education, such as teachers in high school, or as lecturers in higher

education. Others continue in a wide range of positions, such as policy advisors, project managers, consultants, data scientists, web- or software developers, business owners, regulatory affairs specialists, engineers, managers, or IT architects. As such, the career paths of Donders PhD graduates span a broad range of sectors and professions, but the common factor is that they almost all have become successful professionals.

For more information on the Donders Graduate School, as well as past and upcoming defences please visit: http://www.ru.nl/donders/graduate-school/phd/

This thesis explores how the brain interprets touch by tracing the transformation of physical stimuli into neural representations. From mechanoreceptors in the skin to cortical networks, it combines psychophysical experiments in humans with computational modeling of the rodent whisker system to uncover how tactile information is encoded, transmitted, and decoded. Updating the connectome of the whisker pathway reveals a dense network of sensory, motor, and modulatory nuclei—supporting the view that touch is a "whole-brain computation." Biophysical models of mechanoreceptors show that tactile signals divide into parallel detection and discrimination streams even before reaching the central nervous system. Integrating mechanical and neural models, the work quantifies how information flows from the periphery through brainstem, thalamus, and cortex, highlighting the roles of inhibition and top-down regulation. By linking human perception to detailed neural mechanisms, this research deepens our understanding of sensory computation and lays foundations for advances in neuroprosthetics, haptic technologies, and sensory-disorder treatments while providing insight into our perception of the world.

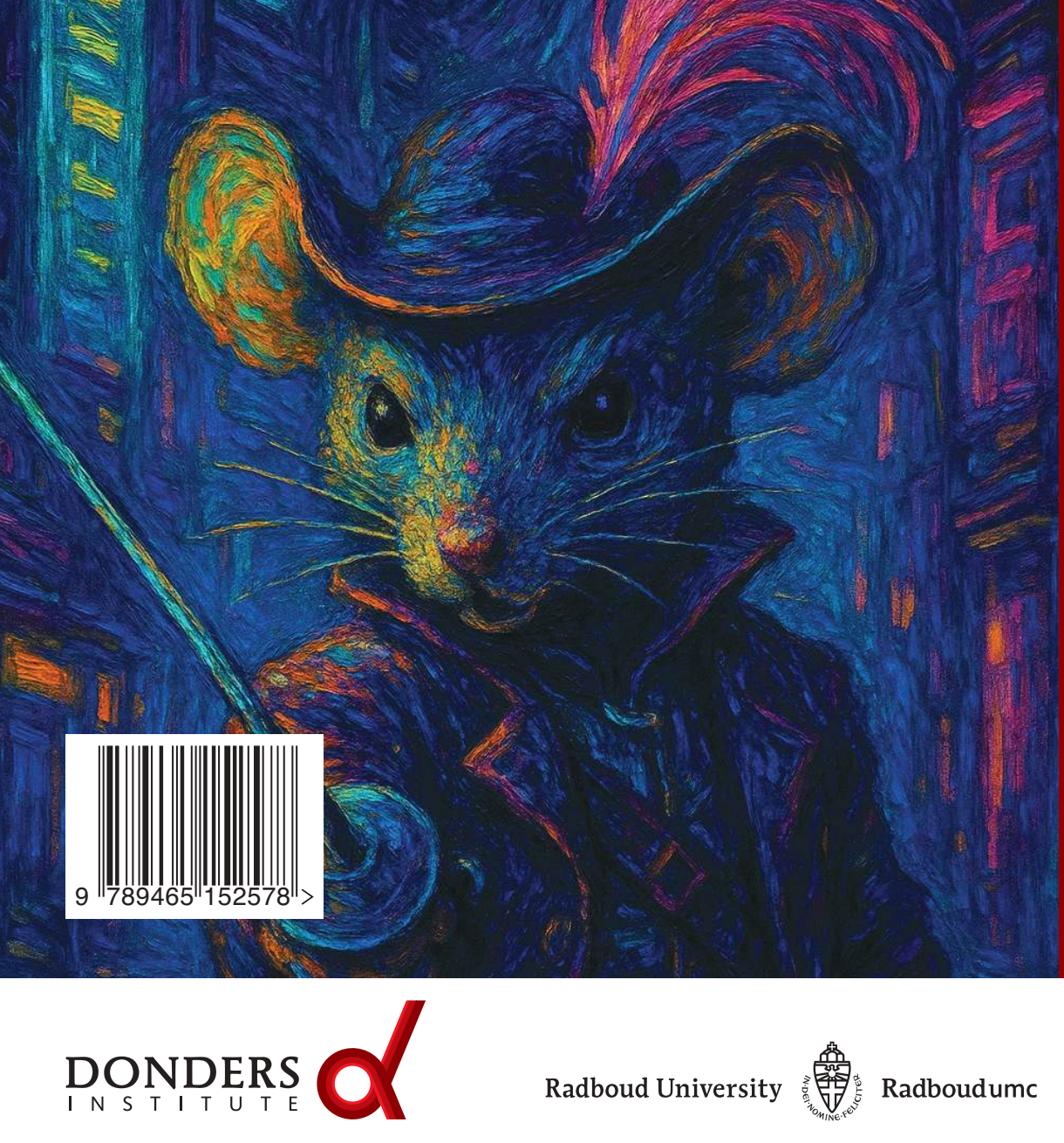

9 789465 152578 >

DONDERS INSTITUTE

Radboud University

Radboudumc